

EISSN 1305-3612

DIR

Diagnostic and Interventional
Radiology



Editor in Chief

Mehmet Ruhi Onur, MD

Department of Radiology, Hacettepe University Faculty of Medicine, Ankara, Türkiye

ORCID ID: 0000-0003-1732-7862

Section Editors and Scientific Editorial Board

Abdominal Imaging

İlkay S. İdilman, MD 

Department of Radiology, Hacettepe University Faculty of Medicine, Ankara, Türkiye

ORCID ID: 0000-0002-1913-2404

Sonay Aydin, MD 

Department of Radiology, Erzincan Binali Yıldırım University Faculty of Medicine, Erzincan, Türkiye

ORCID ID: 0000-0002-3812-6333

Artificial Intelligence and Informatics

Burak Koçak, MD 

Department of Radiology, Başakşehir Çam and Sakura City Hospital, İstanbul, Türkiye

ORCID ID: 0000-0002-7307-396X

Tuğba Akıncı D'Antonoli, MD 

Institute of Radiology and Nuclear Medicine, Cantonal Hospital Baselland, Liestal, Switzerland

ORCID ID: 0000-0002-7237-711X

Breast Imaging

Serap Gültekin, MD 

Department of Radiology, Gazi University Faculty of Medicine, Ankara, Türkiye

ORCID ID: 0000-0001-6349-3998

Chest and Cardiovascular Imaging

Furkan Ufuk, MD 

Department of Radiology, The University of Chicago, Chicago, USA

ORCID ID: 0000-0002-8614-5387

Hybrid Imaging and Nuclear Medicine

Evrim Bengi Türkbeyp, MD 

Radiology and Imaging Sciences, Clinical Center, National Institutes of Health Bethesda, Maryland, United States

ORCID ID: 0000-0002-5216-3528

Interventional Radiology

Barbaros Çil, MD, FCIRSE 

Department of Radiology, Koç University School of Medicine, İstanbul, Türkiye

ORCID ID: 0000-0003-1079-0088

Bahri Üstünsöz, MD 

Department of Radiology, LSUHSC (Louisiana State University Health Science Center) School of Medicine, New Orleans, United States

ORCID ID: 0000-0003-4308-6708

James Milburn, MD 

Department of Radiology, Ochsner Medical System, New Orleans, Louisiana, USA

ORCID ID: 0000-0003-3403-2628

Musculoskeletal Imaging

Zeynep Maraş Özdemir, MD 

Department of Radiology, İnönü University Faculty of Medicine, Malatya, Türkiye

ORCID ID: 0000-0003-1085-8978

Neuroradiology

Gülgün Yılmaz Ovalı, MD 

Department of Radiology, Celal Bayar University Faculty of Medicine, Manisa, Türkiye

ORCID ID: 0000-0001-8433-5622

Erkan Gökçe, MD 

Department of Radiology, Tokat Gaziosmanpaşa University Faculty of Medicine, Tokat, Türkiye

ORCID ID: 0000-0003-3947-2972

Pediatric Radiology

Meltem Ceyhan Bilgici, MD 

Department of Radiology, 19 Mayıs University Faculty of Medicine, Samsun, Türkiye

ORCID ID: 0000-0002-0133-0234

Evrim Özmen, MD 

Department of Radiology, Koç University Hospital, İstanbul, Türkiye

ORCID ID: 0000-0003-3100-4197

Publication Coordinator

Nermin Tunçbilek, MD 

Department of Radiology, Trakya University Faculty of Medicine, Edirne, Türkiye

ORCID ID: 0000-0002-8734-1849

Biostatistical Consultant

İlker Ercan, PhD 

Department of Biostatistics, Uludağ University School of Medicine, Bursa, Türkiye

ORCID ID: 0000-0002-2382-290X

Social Media Lead Editor

Tümay Bekçi, MD 

Department of Radiology, Giresun University Faculty of Medicine, Giresun, Türkiye

Social Media Editors

Mahmut Bilal Doğan, MD 

Department of Radiology, Marmara University Faculty of Medicine, İstanbul, Türkiye

Kendal Erincik, MD 

Department of Radiology, İstanbul Medeniyet University Faculty of Medicine, İstanbul, Türkiye

Şule Gümürdü, MD 

Department of Radiology, İstanbul Medeniyet University Faculty of Medicine, İstanbul, Türkiye

Gürsel Karacaoğlu, MD 

Department of Radiology, İstanbul Medeniyet University Faculty of Medicine, İstanbul, Türkiye

Publication Services

Galenos Publishing, İstanbul, Türkiye

Past Editors

Editors in Chief

Mustafa Seçil, MD (2016-2023)

Nevzat Karabulut, MD (2011-2016)

Üstün Aydingöz, MD (2010-2011)

Okan Akhan, MD (2001-2010)

Ferhun Balkancı, MD (1999-2001)

Aytekin Besim, MD (1994-1999)*

*Aytekin Besim, MD, actually served as the General Coordinator. His work in this capacity, however, was in effect that of an Editor in Chief.

Editors

Ayşenur Cila, MD (2001-2002)

Suat Kemal Aytaç, MD (1997-2001)

Erhan İlgit, MD (1994-2001)

Okan Akhan, MD (1994-2001)

Ferhun Balkancı, MD (1994-2000)

Serdar Akyar, MD (1994-1997)

Section Editors

Section Editorship was established in 2002 at the tenure of Okan Akhan, MD, Editor in Chief.

Abdominal Imaging

Bengi Gürses, MD (2020-2023)
Mehmet Ruhi Onur, MD (2016-2023)
Barış Türkbey, MD (2014-2020)
Mustafa N. Özmen, MD (2012-2018)
Murat Acar, MD (2015-2016)
Mustafa Seçil, MD (2011-2016)
Ahmet Tuncay Turgut, MD (2011)
Deniz Akata, MD (2007-2011)
Ayşe Erden, MD (2002-2011)
Okan Akhan, MD (2002-2010)
Hakan Özdemir, MD (2002-2010)

Artificial Intelligence and Informatics

Barış Türkbey, MD (2020-2023)

Breast Imaging

Mustafa Erkin Arıbal, MD (2016-2023)
Sibel Kul (2015-2018)
Ayşenur Oktay, MD (2009-2014)
Ayşegül Özdemir, MD (2004-2009)

Cardiovascular Imaging

Uğur Bozlar, MD (2016-2023)
Muşturay Karçaaltıncaba, MD (2007-2010)
Mecit Kantarcı (2010-2016)

Chest Imaging

Nevzat Karabulut, MD (2010-2014)
Çetin Atasoy, MD (2007-2010)
Macit Arıyürek, MD (2002-2007)
Figen Demirkazık, MD, (2014-2018)

General Radiology

Ersin Öztürk, MD (2014-2017)
Utku Şenol, MD (2010-2013)
Oğuz Dicle, MD (2007-2010)

Interventional Radiology

Cüneyt Aytekin, MD (2016-2023)
Bora Peynircioğlu, MD (2012-2015)
Levent Oğuzkurt, MD (2011-2014)
Fatih Boyvat, MD (2007-2010)
İsmail Oran, MD (2015-2019)

Musculoskeletal Imaging

Hatice Tuba Sanal, MD (2016-2023)
Fatih Kantarcı, MD (2014-2016)
Ayşenur Oktay, MD (2011-2013)
Üstün Aydıngöz, MD (2002-2011)
Berna Dirim Mete (2016-2017)

Neuroradiology and Head & Neck Imaging

Kubilay Aydın, MD (2016-2023)
Nafi Aygün, MD (2016-2023)
Kader Karlı Oğuz, MD (2011-2015)
Süleyman Men, MD (2007-2013)
Muhteşem Ağıldere, MD (2002-2011)

Nuclear Medicine

A. Cahid Civelek, MD (2016-2023)
Oktay Sarı, MD (2015)
Akin Yıldız, MD (2011-2014)

Pediatric Radiology

Korgün Koral, MD (2016-2023)
Murat Kocaoğlu, MD (2016-2023)
Ensar Yekeler, MD (2014-2016)
Suat Fitöz, MD (2007-2013)

Diagnostic and Interventional Radiology (Diagn Interv Radiol) is a bimonthly periodical of the Turkish Society of Radiology and the content of the journal is available at <https://www.dirjournal.org/>. It is peer-reviewed and adheres to the highest ethical and editorial standards. The editors of the journal endorse the Editorial Policy Statements Approved by the Council of Science Editors Board of Directors (<https://cse.memberclicks.net/>). The journal is in compliance with the Recommendations for the Conduct, Reporting, Editing and Publication of Scholarly Work in Medical Journals published by the International Committee of Medical Journal Editors (updated May 2022, www.icmje.org).

First ten volumes of Diagnostic and Interventional Radiology have been published in Turkish under the name of *Tanısal ve Girişimsel Radyoloji* (MEDLINE abbreviation: *Tanı Girişim Radyol*), the current title's exact Turkish translation.

Diagnostic and Interventional Radiology is an open access publication, and the journal's publication model is based on Budapest Open Access Initiative (BOAI) declaration. All published content is available online, free of charge at <https://www.dirjournal.org/>. Authors retain the copyright of their published work in Diagnostic and Interventional Radiology. The journal's content is licensed under a Creative Commons Attribution-NonCommercial (CC BY-NC) 4.0 International License which permits third parties to share and adapt the content for non-commercial purposes by giving the appropriate credit to the original work.

Please refer to the journal's webpage (<https://dirjournal.org/>) for "Aims and Scope", "Instructions to Authors" and "Instructions to Reviewers".

The editorial and publication processes of the journal are shaped in accordance with the guidelines of the ICMJE, WAME, CSE, COPE, EASE, and NISO.

Diagnostic and Interventional Radiology is indexed in **SCI-Expanded, Pubmed/Medline, Pubmed Central, TUBITAK ULAKBIM TR Index, Scopus, DOAJ, EBSCO, HINARI, EMBASE, CINAHL, ProQuest, Gale and CNKI**.

The journal is published online.

Owner: Turkish Society of Radiology

Responsible Manager: Mehmet Ruhi Onur

Contact Information

Diagnostic and Interventional Radiology Turkish Society of Radiology

Hoşdere Cad., Güzelkent Sok., Çankaya Evleri, F/2, 06540
Ankara, Türkiye
E-mail: info@dirjournal.org
Phone: +90 (312) 442 36 53 Fax: +90 (312) 442 36 54

Publisher Contact

Address: Molla Gürani Mah. Kaçamak Sk.

No: 21/1 34093 İstanbul, Türkiye

Phone: +90 (530) 177 30 97

E-mail: info@galenos.com.tr yayin@galenos.com.tr

Web: www.galenos.com.tr **Publisher Certificate Number:** 14521

Online Publication Date: January 2026

EISSN 1305-3612

International scientific journal published bimonthly.



Contents

ABDOMINAL IMAGING

1 **Original Article** Diagnostic sensitivity and specificity of enhanced computed tomography in colorectal tumors: a meta-analysis and systematic review *Chuanxian Liu, Chao Yuan, Shaocui Huang*

8 **Original Article** The role of T1 hyperintensity in differentiating granulomatous prostatitis from prostate cancer: a retrospective analysis of 31 lesions *Selahattin Durmaz, Mert Kılıç, Bilgen Coşkun, Sergen Akpek, Bariş Bakır, Tarık Esen, Metin Vural, Emre Altınmakas*

16 **Original Article** Magnetic resonance T1p relaxation in patients with liver fibrosis: a systematic review and meta-analysis *Xiaoyu Liu, Yinzhang Wang, Caihua Xu, Yixiang Li, Junqiang Lei*

ARTIFICIAL INTELLIGENCE AND INFORMATICS

25 **Letter to the Editor Reply:** evaluating text and visual diagnostic capabilities of large language models on questions related to the Breast Imaging Reporting and Data System (BI-RADS) Atlas 5th edition *Yasin Celal Güneş, Turay Cesur, Eren Çamur, Leman Günbey Karabekmez*

27 **Original Article** Artificial intelligence in radiology: diagnostic sensitivity of ChatGPT for detecting hemorrhages in cranial computed tomography scans *Olga Bayar-Kapıcı, Erman Altunışık, Feyza Musabeyoğlu, Şeyda Dev, Ömer Kaya*

33 **Original Article** Automated evaluation of pulmonary lesion changes on chest radiograph during follow-up using semantic segmentation *Youngjae Kim, Yura Ahn, Sang Min Lee, Han Na Noh, Jongjun Won, Chaewon Kim, Hyunna Lee*

BREAST IMAGING

40 **Original Article** New lens on breast health: harnessing high-b-value synthetic diffusion-weighted imaging for breast lesion characterization *Serap Karabiyik, Saima Ramadan, Emil Settarzade, Ali İlker Filiz, Hatice Ozturkmen Akay*

CARDIOVASCULAR IMAGING

47 **Invited Review** Recent advances in vascular ultrasound imaging technology and their clinical implications *Suna Özhan Oktar, Mahi Nur Cerit, Halit Nahit Şendur, Atiye Cenay Karabörk Kılıç*

EMERGENCY RADIOLOGY

57 **Review Article** Emergency radiology in displaced populations: imaging and practical challenges *Vefa Çakmak, Pınar Çakmak, Duygu Herek, Sonay Aydin*

GENERAL RADIOLOGY

65 **Original Article** Radiologists' tendency to collaborate with referring physicians in managing contrast media-related risk factors *Burak Öztürk, Özgür Karabiyık*

71 **Original Article** Bibliometric analysis of radiology residency theses in Türkiye: publication metrics and trends *Ali Salbas, Ali Murat Koc*

HYBRID IMAGING AND NUCLEAR MEDICINE

81 **Pictorial Essay** Normal physiological variants and benign conditions in pelvic oncologic fluorodeoxyglucose positron emission tomography/magnetic resonance imaging *Ayşe Erden, Diğdem Kuru Öz, Nuriye Özlem Küçük*

INTERVENTIONAL RADIOLOGY

91 **Original Article** Possible use of digital variance angiography in uterine fibroid embolization: a retrospective observational study *Viktor Bérczi, Szuzina Fazekas, István Gó, Marcell Gyánó, Ambrus Tóth, Ákos Bérczi, Osama Habeeballah, Krzysztof Pyra, Zoltán Harmat, Dat Tin Nguyen*

96 **Original Article** Combined therapy with microwave ablation and conventional transarterial chemoembolization for hepatocellular carcinoma tumors larger than five centimetres: a prospective study *Hui Liu, Zhuoyang Fan, Ranying Zhang, Xingwei Zhang, Jianhua Wang*

104 **Original Article** Factors influencing diagnostic yield and complication risk in computed tomography fluoroscopy-guided lung biopsies: a 10-year single-center study *Nabeel Mansour, Hannah Gildein, Frederik F. Strobl, Osman Öcal, Tobias Geith, Daniel, Puhr-Westerheide, Matthias Stechele, Sinan Deniz, Muzaffer R. Ümütlu, Nicola Fink, Dirk Mehrens, Moritz Wildgruber, Max Seidensticker, Maximilian F. Reiser, Jens Ricke, Philipp M. Paprottka, Matthias P. Fabritius*

Contents

115 Technical Note Computed tomography-guided irreversible electroporation for a pubic bone metastasis: a technical note and early experience *Claudio Pusceddu, Eliodoro Faiella, Claudio Cau, Pierluigi Rinaldi, Paolo Cossu, Salvatore Marsico*

119 Original Article Factors affecting the difficulty of transurethral double J stent removal in patients with renal transplants *Elisabeth R. Seyferth, Gregory J. Nadolski, Jeffrey I. Mondschein, Ryan M. Cobb, Scott O. Trerotola*

PEDIATRIC RADIOLOGY

125 Original Article Gastrostomy tube check radiographs: performance of an alternative diagnostic exam

Muhammad Y. Hameed, Charles A. James, Kevin Wong, Paul S. Lewis, Paula K. Roberson, Kelli R. Schmitz, Sateesh Jayappa, Amy C. Rowell, Marcene McVay-Gillam, Mary B. Moore

Dear Reviewers,

Thank you for your invaluable contributions as reviewers to Diagnostic and Interventional Radiology in 2025. Your expertise and insightful feedback have helped to maintain our journal's high standards and ensure the quality of the articles we publish. We appreciate your interest in our journal and wish you every success in your academic career.

Sincerely,

Ahmed Maiter	Rui Duarte Armindo	Begümhan Baysal
Hatice Öztürkmen Akay	Muhammet Arslan	Tumay Bekçi
Sabri Abuş	Sevtap Arslan	Elena Belloni
Saad Abuzahra	Arzu Arslan	Muhammed Said Beşler
Berat Acu	Hakan Artaş	Murat Beyhan
Leyla Acu	Christoph Artzner	Ambarish Bhat
Nuno Adubeiro	Yoshiki Asayama	Rupsa Bhattacharjee
Ayaz Aghayev	Akram M. Asbeutah	Pierpaolo Biondetti
Tuğçe Ağırılar Trabzonlu	Aydan Avdan Aslan	Ivan Blokhin
Serpil Ağlamış	Serdar Aslan	Matteo Bonatti
Awais Ahmed	Özge Aslan	Giacomo Bonito
Ayşegül Akdoğan Gemici	Kerim Aslan	Alessandra Borgheresi
İsmail Akdulum	Gökçe Kaan Ataç	Murat Fani Bozkurt
Erol Akgül	Fırat Atak	Keno Bressem
Fatih Akın	Başak Atalay	Torkel Brismar
Hüseyin Akkaya	Ömer Ateş	Nima Broomand Lomer
Zehra Akkaya	Ece Ateş Kuş	Özüm Yüksel Buğdaycı
Meltem Gülsün Akpınar	Kazuo Awai	Onur Buğdaycı
Direnç Özlem Aksoy	Ercan Ayaz	Nail Bulakbaşı
Recai Aktay	Ramazan Aydın	Emre Utkan Büyükeren
Seda Aladağ Kurt	Elçin Aydın	Matthew G. Cable
Deniz Alis	Hale Aydın	Burçak Çakır Pekoz
José Almeida	Mohamed M.K. Badreldine	Vefa Cakmak
Canan ALTAY	Sinan Bahadır	Lucio Calandriello
Ayşegül Altunkeser	Derya Bako	İlkay Çamlıdağ
Angela Ammirabile	Ali Balcı	Döndü Üsküdar Cansu
Choirul Anam	Ayşe Özlem Balık	Semihha Canverenler
Yonca Anık	Serdar Balsak	Romain Carron
Uri Arad	Mustafa Mahmut Barış	Nurdan Çay
Tetsuro Araki	Hakan Bas	Ferdi Çay
Selin Ardalı Düzgün	İşil Başara Akın	Manuela Cesaretti
Bilgin Kadri Aribal	Figen Başaran Demirkazık	Türkhun Çetin
Erkin Aribal	Cihat Çınar Basekim	Naim Ceylan
Serkan Aribal	Burak Bayraktar	Kai-Lun Cheng
Nikolaos-Achilleas Arkoudis	Selen Bayraktaroğlu	Sophie Chopinet

Atilla Hikmet Çilengir	Erkan Gökçe	Volkan Kızılgöz
Helena Cindrič	Ozan Gökhan	Volkan Kızılgöz
Gabriele Ciuti	Dilek Gökharcman	Ural Koç
Esra Çıvgın	Jose Andres Guirola	Ali Murat Koç
Cenk Conkbayır	Ezgi Güler	Murat Kocaoğlu
Andrea Corsi	Ekim Gümeler	Mustafa Koplay
Fabio Corvino	Yasin Celal Güneş	Muhammed Köroğlu
Renato Cuocolo	Jia Guo	Özlem Öztürk Köse
Gennaro D'Anna	Defne Gürbüz	Sibel Kul
Mario D'Oria	Merve Gürsoy	Luis Landeras
Surjeet Dalal	Christopher Gutjahr	Wen Li
Kavitha Danabal	Martin Weng Chin Hng	Guihan Lin
Rafael De Freitas	Muhammad Taha Hagar	Ojaswita Lokre
Lucio Dell'Attì	Safouane M. Hamdi	Xuefeng Luo
Eftychia Demerouti	Gül Hatipoğlu	Pierre Yves Marcy
Aydın Demircioğlu	Türkan İkizceli	Paolo Marra
Sinan Deniz	Mehmet Fatih İncekili	Tomohiro Matsumoto
Safiye Sanem Dereli Bulut	Akitoshi Inoue	Naofumi Matsunaga
Berna Dirim Mete	Nilgun Işıksalan Özbulbul	Kemal Buğra Memis
Görkem Durak	Bharathi Jagadeesan	Bökebatur Ahmet Raşit Mendi
Gamze Durhan	Sriram Jaganathan	İsmail Meşe
Mehmet Sedat Durmaz	Rupi Jamwal	Kenkichi Michimoto
Irmak Durur-Subaşı	Frederick Jan Anton Meijer	Omeed Moaven
David D. E.	Kader K. Oğuz	Rajesh Mohandas
Bunyamin Ece	Esat Kaba	Kyle J. Morgan
Filiz Elbüken	Adnan Kabaalioğlu	Hippocrates Moschouris
Gonca Eldem	Gökhan Kahraman	Michael Moser
İlker Ercan	Güven Kahriman	Emanuele Muscogiuri
Ahmet Erdemir	Bora Kalaycıoğlu	Yulian Mytsyk
Fatma Bilge Ergen	Sedat Kandemirli	Takhesi Nakaura
Duygu Erkal Tonkaz	Mecit Kantarcı	Mehmet Ali Nazlı
Şükrü Mehmet Ertürk	Kamil Karaali	Emilia Niemiec
Şehnaz Evrímler	M. Yasemin Karadeniz	Zachary Nuffer
David Fallmar	Oğuz Karahan	Osman Öcal
Richard Fine	Can Zafer Karaman	Yılmaz Onal
Marco Fronda	Gülbiz Kartal	Mehmet Hamdi Örüm
Moawia Gameraddin	Yiğit Can Kartal	Ebru Özan
Fazıl Gelal	Ömer Kaya	H. Nursun Özcan
Barış Genç	Yasemin Kayadibi	Alper Özel
Rohini Gupta Ghasi	Ülkü Kerimoğlu	Cemre Özenbaş
Francesco Giurazza	Abidin Kilinçer	Halil Özer
Matthew D. Givens	Yavuz Selim Kiyak	Gözde Özer
Mustafa Gök	İnci Kızıldağ Yirgin	Hamit Özgül

Cihan Özgür
Suna Özhan Oktar
Orhan Şeref Özkan
Serçin Özkok
Murat Alp Öztek
Fırat Öztepe
Muhsin Özgün Öztürk
Onural Öztürk
Figen Palabiyık
Nicolas Papalexis
Mehmet Emin Parlak
Uday Patel
Yeliz Pekçevik
Jan Petr
Sebastiano Piana
Berhan Pirimoğlu
Ferhat Can Pişkin
Ahmet Kürşad Poyraz
Ciro Princiotta
Li-Ting Qian
Babak Rafiee
Clare Rainey
R Rajagopal
Kumaresan Ramanathan
Sanjay Rastogi
Pedro Ravizzini
Liqiang Ren
Martin Rössle
Dilek Sağlam
Semih Sağlık
Ergin Sağtaş
Aliaksei Salei
Artur Salmaslioğlu
João Santinha
Babak Saravi

Burcu Savran
Ayşe Say
Suzan Şaylısoy
Samia Khaled Sayyid
Mustafa Ege Seker
Yıldız Şengül
Pankaj Sharma
Susan Shelmerdine
Sweta Singh
Pasqualino Sirignano
Sinan Sözütok
Enrico Spinias
Paolo Spinnato
Arnaldo Stanzione
Martin Svaton
Tatsuro Takei
Aslı Tanrıvermiş Sayit
Bilge Han Taş
Onur Taydaş
Ali Fuat Tekin
Muhammed Tekinhatun
Gizem Timoçin Yiğman
Nil Tokgöz
Oğuzhan Tokur
Osman Melih Topçuoğlu
Çağdaş Topel
Uğur Toprak
Ulysses S. Torres
Özgür Tosun
Matthaios Triantafyllou
Satvik Tripathi
Cenk Turba
Bariş Türkbe
Furkan Ufuk
Lorenzo Ugga

Emre Ünal
Bogdan Silviu Ungureanu
José Urbano
Nihal Uslu
Bahri Üstünsöz
Michael Valente
Murat Velioğlu
Nuray Voyvoda
Qizheng Wang
Zhongmin Wang
Dajie Wang
Chen Jiang Wu
Xiang Wu
Ahmet Baki Yağcı
Burak Yağdiran
Masahiro Yanagawa
Erdem Yanar
Lei Yang
Aytül Hande Yardımcı
Hüseyin Yavaş
Zeynep Yazıcı
Hasan Yerli
Hasan Yiğit
Adalet Elçin Yıldız
Şeyma Yıldız
Ahmet Yasin Yitik
Düzungün Yıldırım
Jie Yu
Qian Yu
Murat Yüce
Nursel Yurtutan
Sabahattin Yüzkan
Banafsheh Zeinali-Rafsanjani
Jingyu Zhong



Diagnostic sensitivity and specificity of enhanced computed tomography in colorectal tumors: a meta-analysis and systematic review

✉ Chuanxian Liu
✉ Chao Yuan
✉ Shaocui Huang

Jiaxing University Affiliated TCM Hospital,
Department of Radiology, Jiaxing, China

PURPOSE

Early detection of colorectal cancer (CRC) is crucial for improving patient prognosis and survival outcomes. In contemporary clinical practice, computed tomography (CT) has become an established diagnostic modality and a reference standard for CRC evaluation. This meta-analysis systematically evaluates the diagnostic performance of contrast-enhanced CT imaging in detecting and characterizing colorectal neoplasms, providing evidence-based recommendations to optimize clinical decision-making and therapeutic strategies in CRC management.

METHODS

A systematic literature search was performed across multiple electronic databases, including PubMed, Medline, EMBASE, the Cochrane Library, ClinicalTrials.gov, CNKI, Wanfang, and Weipu, covering studies from database inception through November 25, 2024. The search strategy was designed to identify all relevant studies investigating the diagnostic accuracy of contrast-enhanced CT imaging in colorectal neoplasms. For each eligible study, diagnostic performance parameters—specifically, sensitivity and specificity—were extracted and analyzed. All statistical analyses were conducted using RevMan software.

RESULTS

A total of nine studies involving 4,857 patients were included. The meta-analysis revealed that the pooled sensitivity of enhanced CT imaging for diagnosing colorectal tumors was 76% [95% confidence interval (CI): 70%–79%] and the pooled specificity reached 87% (95% CI: 84%–89%). Furthermore, the area under the curve for the diagnostic test was 0.89 (95% CI: 0.85–0.92), indicating strong discriminatory capability in differentiating colorectal tumors. Subgroup analysis revealed no statistically significant differences in diagnostic sensitivity and specificity between intravenously administered and orally administered contrast agents in enhanced CT scans.

CONCLUSION

Contrast-enhanced CT imaging is an effective and reliable method for the clinical diagnosis of colorectal tumors.

CLINICAL SIGNIFICANCE

Contrast-enhanced CT scanning demonstrates high sensitivity and specificity in the diagnosis of CRC.

KEYWORDS

Clinical, computed tomography, colorectal tumor, diagnosis, treatment

Corresponding author: Shaocui Huang

E-mail: caai34@sina.com

Received 19 December 2024; revision requested 09 February 2025; accepted 22 February 2025.



Epub: 28.04.2025

Publication date: 02.01.2026

DOI: 10.4274/dir.2025.243185

Colorectal cancer (CRC) is a globally prevalent malignant neoplasm of the digestive system, with incidence and mortality rates among the highest compared with all malignant tumors.^{1,2} Global cancer statistics indicate that in 2020, approximately 1,932 million new CRC cases were reported worldwide, resulting in nearly 935,000 fatalities.^{3,4} Over the past decade, the global incidence of CRC has increased, with a marked rise in cases in devel-

You may cite this article as: Liu C, Yuan C, Huang S. Diagnostic sensitivity and specificity of enhanced computed tomography in colorectal tumors: a meta-analysis and systematic review. *Diagn Interv Radiol*. 2026;32(1):1-7.

oping regions such as China and Southeast Asia.⁵ In China, CRC has become the second most frequently occurring malignant tumor, with an annual incidence of approximately 517,100 cases—307,700 in men and 209,400 in women.^{6,7}

Risk factors associated with CRC include advanced age, being a man, unhealthy dietary habits (such as high consumption of fats, sugars, alcohol, red meat, and processed meats), obesity, tobacco use, and physical inactivity.⁸ Notably, the lifetime risk of developing and dying from gastrointestinal cancers is estimated at 8.20% and 6.17%, respectively, with CRC posing the highest risk, accounting for 38.5% of the incidence risk and 28.2% of the mortality risk among gastrointestinal cancers.⁹ Patients with early-stage CRC who undergo radical surgery have improved long-term survival rates and better prognoses, considerably enhancing their survival prospects.¹⁰ Conversely, patients with late-stage CRC, who often forgo surgical intervention, rely predominantly on chemotherapy and radiotherapy—treatments with limited efficacy that require frequent hospital visits and consume substantial medical resources.^{11,12} Therefore, early diagnosis of CRC is crucial for improving patient outcomes and conserving healthcare resources.

For early-stage CRC, the prognosis following diagnosis and surgical intervention is relatively favorable. However, the five-year survival rate for patients with advanced metastatic disease remains low.^{13,14} Enhanced computed tomography (CT), known for its non-invasive and rapid imaging capabilities, is widely used in the early diagnosis of CRC.¹⁵ However, significant heterogeneity exists in the literature regarding the diagnostic performance of contrast-enhanced CT for colorectal neoplasms, particularly in terms of reported sensitivity and specificity values. This study adopts an evidence-based medi-

cine approach to systematically evaluate the diagnostic efficacy of contrast-enhanced CT imaging in detecting colorectal tumors, aiming to establish a strong evidence base for optimizing clinical decision-making in CRC diagnosis and management.

Methods

This meta-analysis was conducted in strict accordance with the Preferred Reporting Items for Systematic Reviews and Meta-Analyses guidelines.¹⁶ Given the nature of our study as a meta-analysis, neither ethical approval nor patient consent was required.

Inclusion and exclusion criteria

This study explicitly defined the inclusion and exclusion criteria to ensure the homogeneity of the included studies and the reliability of the results. The specific criteria were as follows: (1) Study type: the study included diagnostic trials that utilized enhanced CT imaging technology for the diagnosis of CRC. To ensure data extractability and comparability, only studies providing fourfold table (2 × 2 contingency table) data were included. There was no lower age limit for study participants; however, participants had to be over 18 years of age, with no restrictions on gender or ethnicity, to enhance the generalizability of the study results. (2) Diagnostic test methods: the study focused on CT imaging techniques enhanced with intravenous and oral contrast agents. Both methods are commonly used radiological tools for diagnosing CRC, providing vital information about tumor location, size, and the extent of invasion. (3) Measurement indicators: the primary measurement indicators in this study included sensitivity, specificity, and the diagnostic odds ratio. Sensitivity and specificity are core indicators for evaluating the accuracy of diagnostic tests, reflecting the test's ability to identify genuine cases and exclude non-cases, respectively. The diagnostic odds ratio integrates information from both sensitivity and specificity, providing a metric for the overall performance of the diagnostic test.

Main points

- Enhanced computed tomography (CT) scanning with contrast agents is recognized for its high sensitivity and specificity in diagnosing colorectal cancer.
- There is no statistically significant difference in diagnostic sensitivity and specificity between intravenously and orally administered contrast agents.
- When performing contrast-enhanced CT scans for patients with suspected colorectal tumors, orally administered contrast agents should be given preferential consideration due to their comparable diagnostic efficacy.

Literature search

This study followed a predefined literature search strategy to ensure the comprehensiveness and accuracy of the data collected. The search strategy, which incorporated Boolean operators, was as follows: ("computed tomography" or "CT") and ("colorectal tumors" or "rectal cancer" or "colon cancer") and ("diagnosis" or "sensitivity" or "specificity"). Searches were conducted across PubMed,

Medline, EMBASE, the Cochrane Library, ClinicalTrials.gov, CNKI, Wanfang, and Weipu databases, covering studies from the database inception to November 25, 2024. Additionally, we reviewed the references of included articles and relevant systematic reviews to identify additional relevant studies, ensuring a broader scope of related research within our analysis.

Literature screening and data extraction

In this study, a cross-checking methodology was employed for the comprehensive evaluation and selection of literature. Adhering to predefined inclusion and exclusion criteria, we systematically reviewed the titles, abstracts, and full texts of the identified studies, making inclusion decisions based on this sequential assessment. For the selected articles, an exhaustive data extraction process was conducted, capturing fundamental information such as author details, study locations, publishing journals, and study populations—key elements in understanding the research context. Furthermore, for diagnostic data, we extracted fourfold tables (2 × 2 contingency tables) and implemented a dual-reviewer cross-checking mechanism to ensure the precision and reliability of the extracted data.

Quality assessment of included studies

This study employed the Quality Assessment of Diagnostic Accuracy Studies (QUADAS) tool,¹⁷ as recommended by the Cochrane Library, to systematically evaluate the methodological quality of diagnostic accuracy studies. The QUADAS-2 instrument encompasses four key domains: patient selection, index test, reference standard, and flow and timing, collectively comprising 18 items. Within these domains, reviewers assessed the risk of bias for each, with the first three also undergoing an evaluation of clinical applicability. During the assessment process, reviewers categorized the risk of bias as "low," "high," or "unclear" based on responses to domain-specific questions, which could be "yes," "no," or "unclear." This methodological approach helped identify potential biases within the studies and provided an objective assessment of their reliability. By applying the QUADAS-2 tool, this study conducted a meticulous analysis of the methodological quality of diagnostic accuracy research, ensuring the scientific rigor and validity of the conclusions drawn.

Statistical analysis

This meta-analysis utilized RevMan software for data analysis (Review Manager,

RevMan, The Cochrane Collaboration, Nordic). Statistical heterogeneity was assessed using the I^2 statistic and Cochran's Q test. Studies were considered to exhibit significant heterogeneity if the I^2 value exceeded 50% or if Cochran's Q test yielded statistically significant results ($P < 0.05$). In such cases, a random-effects model was employed to account for the observed variability.

We calculated the sensitivity, specificity, and area under the summary receiver operating characteristic curve for enhanced CT scans in diagnosing colorectal tumors. Additionally, studies were stratified into two subgroups based on the route of contrast agent administration: intravenous and oral. Sensitivity and specificity were calculated for each subgroup, followed by a comparative analysis to determine whether differences existed between them. Egger's regression test was conducted to assess publication bias in the synthesized outcomes. In this study, a P value of less than 0.05 was considered the threshold for statistical significance.

Results

As indicated in Figure 1, an initial electronic search identified 694 articles relevant to the study's theme. After reviewing abstracts and titles, 626 articles were excluded for not meeting the inclusion criteria. Further examination of full texts led to the exclusion of an additional 36 studies that did not fulfill the research requirements. Ultimately, nine studies met all eligibility criteria and were included in this analysis.

As summarized in Table 1, this meta-analysis includes nine studies¹⁸⁻²⁶ involving 4,857 patients. These articles were published between 2000 and 2019, with sample sizes ranging from 71 to 2,541 participants. Among the nine included studies, five used intravenous contrast enhancement, and four employed oral contrast enhancement. These data provide an overview of the application of different contrast enhancement techniques in studies diagnosing colorectal tumors and form the basis for subsequent analysis.

In this diagnostic meta-analysis, the QUADAS tool was used to assess the quality of the included studies, which were collectively rated as moderate in quality (Figures 2 and 3). Regarding patient selection, most studies provided consecutive or random patient samples, thereby reducing potential biases associated with case-control designs and minimizing inappropriate patient exclusions. However, some studies did not fully blind

the interpretation of diagnostic test results from the reference standard, potentially introducing performance bias. In terms of the reference standard, most studies employed methods capable of accurately classifying the target condition, but in some cases, the interpretation of results was conducted with knowledge of the diagnostic test outcomes, potentially affecting the accuracy of the findings.

With respect to flow and timing, although all patients underwent reference standard testing, inconsistencies were observed in the intervals and interventions between the index test and the reference standard across different studies. Overall, despite some methodological limitations, the included studies demonstrated a reasonable level of reliability in assessing diagnostic accuracy, and these moderately rated studies provided valuable data for this meta-analysis.

In this diagnostic meta-analysis, we selected the sensitivity and specificity of enhanced CT imaging as the primary evaluation metrics. Statistical findings revealed that the I^2 values for sensitivity and specificity were 93.8% and 89.0%, respectively—both exceeding 50%—and that Cochran's Q test results were statistically significant (all $P <$

0.009), indicating substantial heterogeneity among the included studies. Consequently, a random-effects model was employed to account for this heterogeneity in the pooled analysis. The results of the meta-analysis demonstrated that the pooled sensitivity of enhanced CT imaging for the diagnosis of colorectal tumors was 76% [95% confidence interval (CI): 70%–79%], as shown in Figure 1; the pooled specificity was 87% (95% CI: 84%–89%), as depicted in Figure 4. Furthermore, the area under the diagnostic test's receiver operating characteristic curve (AUC) was 0.89 (95% CI: 0.85–0.92), as illustrated in Figure 5, suggesting that enhanced CT imaging possesses good accuracy in diagnosing colorectal tumors. The Egger's regression test demonstrated no significant evidence of publication bias across the synthesized outcomes ($P = 0.082$).

Based on the contrast methods used, we stratified the included studies into two subgroups for analysis. For studies utilizing intravenous contrast-enhanced CT scans, sensitivity was 0.65 (95% CI: 0.60–0.72) and specificity was 0.86 (95% CI: 0.82–0.90). By contrast, for studies employing oral contrast-enhanced CT scans, sensitivity was 0.78 (95% CI: 0.74–0.81) and specificity was 0.86 (95% CI: 0.84–0.87).

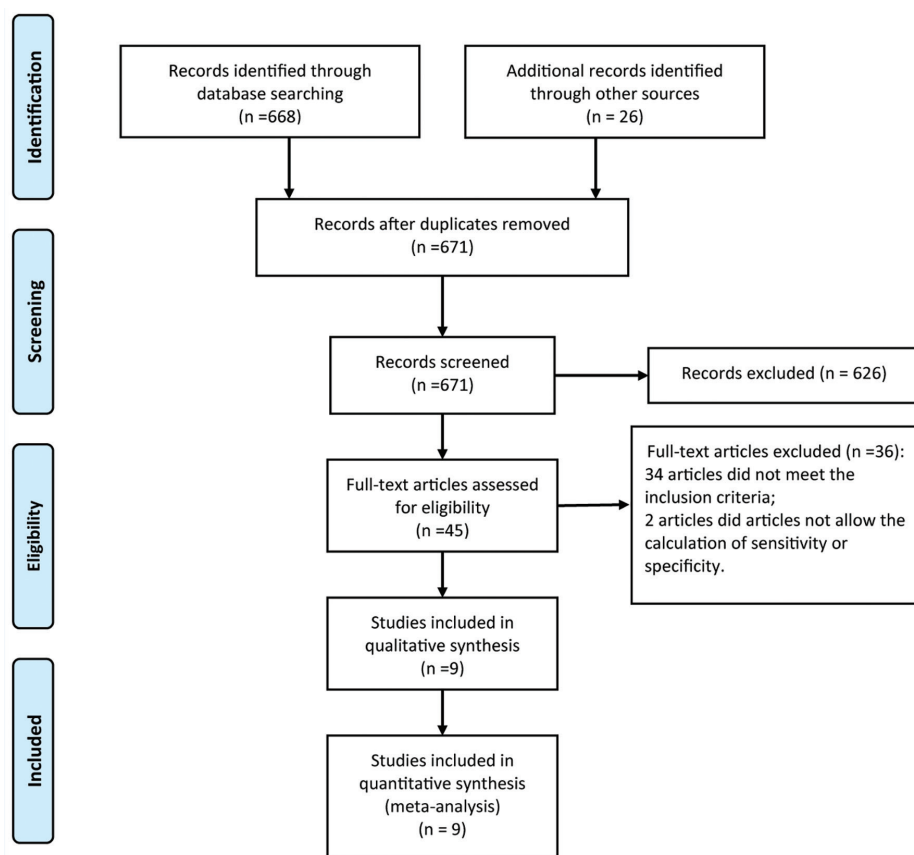


Figure 1. PRISMA flow diagram of the study selection. PRISMA, Preferred Reporting Items for Systematic Reviews and Meta-Analyses.

Table 1. Characteristics of the included studies

Study ID	Country	Cases	Diagnostic gold standard	Enhanced CT scanning		True positive	False positive	False negative	True negative	Enhanced method for CT imaging
Sensitivity Specificity										
Cao et al. ¹⁸ (2016)	China	120	Colonoscopy	0.65	0.66	24	28	13	55	Intravenous contrast agents
Dai ¹⁹ (2019)	China	205	Colonoscopy	0.84	0.83	38	27	7	133	Oral contrast agents
Fletcher et al. ²⁰ (2000)	USA	180	Colonoscopy	0.88	0.72	114	14	16	36	Oral contrast agents
Hoppe et al. ²¹ (2004)	Switzerland	92	Colonoscopy	0.76	0.88	26	7	8	51	Intravenous contrast agents
Johnson et al. ²² (2008)	USA	2541	Colonoscopy	0.66	0.89	193	248	99	2001	Oral contrast agents
Kim et al. ²³ (2008)	Korea	214	Colonoscopy	0.69	0.89	37	21	17	166	Intravenous contrast agents
Miao et al. ²⁴ (2003)	UK	201	Colonoscopy	0.24	0.89	14	16	45	126	Intravenous contrast agents
Pickhardt et al. ²⁵ (2003)	USA	1233	Colonoscopy	0.89	0.80	149	217	19	848	Oral contrast agents
Wong et al. ²⁶ (2002)	China	71	Colonoscopy	0.59	0.93	16	3	11	41	Intravenous contrast agents

CT, computed tomography; USA, United States of America; UK, United Kingdom of Great Britain and Northern Ireland.

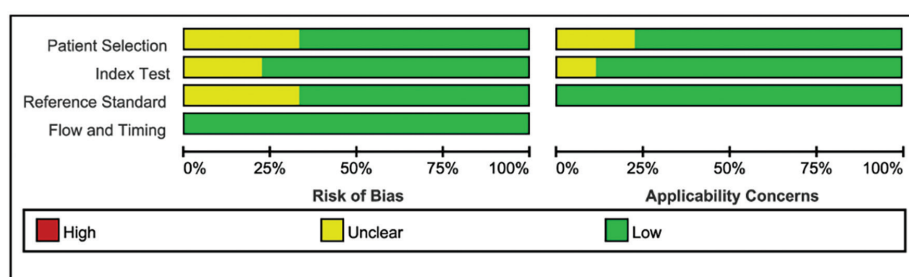


Figure 2. Cumulative bar plot of risk of bias and applicability concerns across all studies.

Comparing sensitivity ($P = 0.152$) and specificity ($P = 0.230$) between the two contrast methods, we found no statistically significant differences. These findings suggest that both contrast methods exhibit similar diagnostic accuracy, each demonstrating a reasonable level of reliability.

Discussion

Over the past decade, the global incidence of CRC has shown an upward trend, particularly in developing regions such as China and Southeast Asia, where cases have increased considerably.²⁷ CRC ranks fourth among new cancer cases worldwide, accounting for 11% of all cancer diagnoses, with approximately 1,096 million new cases of colon cancer and 704,000 new cases of rectal cancer, totaling 1.8 million new CRC cases.²⁸ The incidence rate of CRC is higher in men than in women and is more common in developed countries than in developing ones, with age-standardized incidence rates of 30.1 per 100,000 for men and 16.3 per 100,000 for women.²⁹ Moreover, the incidence of CRC among women in Southeast Asia has increased notably, with mortality rates also rising in this region, particularly among women.⁵ These trends may be associated with rapid economic development in these regions, which in turn affects lifestyle and dietary habits.³⁰ For instance, there has been a shift from a grain-based diet to one richer in protein.³¹ Given the high incidence

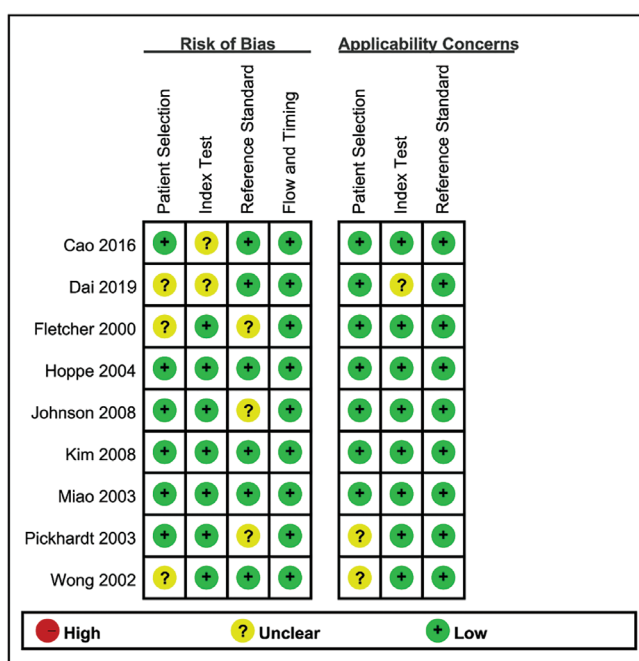


Figure 3. Summary of risk of bias and applicability concerns.

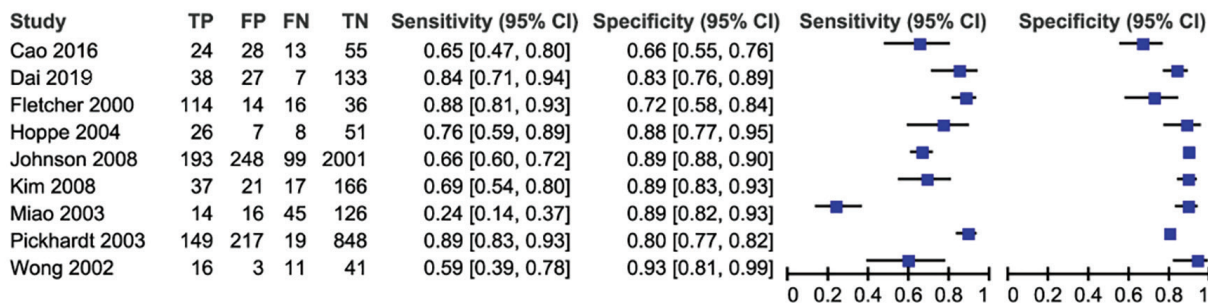


Figure 4. Forest plot of the sensitivity and specificity of enhanced CT in the diagnosis of colorectal tumors. CT, computed tomography; CI, confidence interval.

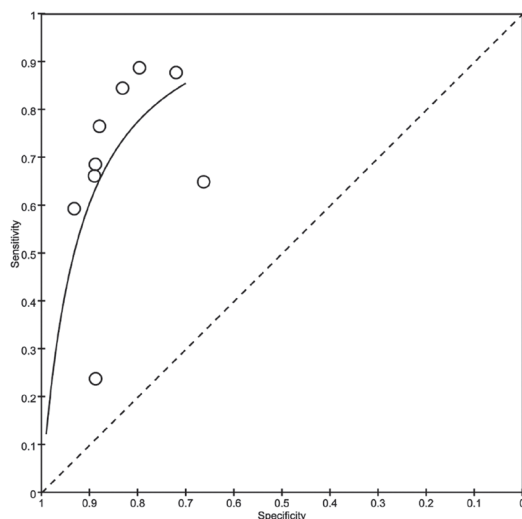


Figure 5. SROC plot curve of the sensitivity of enhanced CT in the diagnosis of colorectal tumors. SROC, summary receiver operating characteristic; CT, computed tomography.

and increasing prevalence of CRC in younger populations, early screening in the general population or large-scale settings becomes particularly important.³²

Patients diagnosed with CRC at an early stage can undergo potentially curative surgical treatment, leading to higher long-term survival rates and better prognoses, thereby significantly improving survival.³³ By contrast, patients presenting with advanced-stage CRC are typically ineligible for surgical intervention, with treatment primarily limited to palliative chemotherapy and radiotherapy, which demonstrate limited therapeutic efficacy.³⁴ These patients frequently require repeated hospital admissions, resulting in substantial healthcare resource consumption. Consequently, early CRC detection is crucial not only for optimizing patient prognosis but also for enhancing healthcare resource utilization efficiency.

Enhanced CT scanning, characterized by its speed, non-invasiveness, and relatively low cost, has become a crucial tool for the early diagnosis of CRC.³⁵ In addition to as-

sessing the location of CRC and its relationship with surrounding tissues, enhanced CT provides essential diagnostic information and valuable details for surgical assessment.^{36,37} However, heterogeneity in study design, population demographics, and the technical parameters of CT imaging protocols among different diagnostic trials has resulted in considerable variability in reported outcomes. Our meta-analysis demonstrates that contrast-enhanced CT imaging exhibits superior diagnostic performance in CRC detection, with high sensitivity and specificity, thereby establishing its clinical utility as a reliable diagnostic modality.

These findings align with the existing literature. A previous investigation evaluating the diagnostic efficacy of multi-slice spiral CT enhancement in lung cancer differentiation reported enhanced scanning parameters with 91.4% sensitivity, 88.1% specificity, and 90.0% accuracy, demonstrating statistically significant improvements over non-enhanced scanning protocols.³⁸ Additionally, fecal DNA methylation testing, a non-invasive

molecular method, has been applied to the early diagnosis of CRC. One study showed that the combined detection of SDC2/ADH-FE1/PPP2R5C methylation predicted CRC with a sensitivity of 84.8%, a specificity of 98.0%, and an AUC of 0.930 (95% CI: 0.889–0.970).³⁹ These data further confirm the value of enhanced CT imaging in the early diagnosis of CRC and demonstrate its high accuracy and potential in comparison to other non-invasive screening methods. Therefore, enhanced CT imaging plays an indispensable role in early CRC diagnosis, significantly contributing to improved patient survival rates and reduced healthcare resource consumption.

Enhanced CT scanning plays a pivotal role in the diagnosis of CRC, offering considerable advantages while also presenting certain limitations. Its utility is underscored by its ability to accurately delineate the location and extent of CRC, providing crucial data for tumor staging and size assessment.^{40,41} It enhances tumor detection rates and minimizes missed diagnoses by offering detailed insights into lesion vascularity, which is instrumental in characterizing pathology.⁴² As a non-invasive diagnostic modality, it employs specialized X-ray equipment to generate cross-sectional images that reveal internal structures with high diagnostic value.

The strengths of enhanced CT scanning include its high sensitivity and specificity, particularly for detecting larger colonic adenomas and tumors over 10 mm, with sensitivity reaching up to 90%.⁴³ Its rapid imaging capability reduces the impact of respiratory and bowel motion artifacts, yielding clear images.⁴⁴ Technological advancements in resolution, image reconstruction, and scanning speed further enhance the accuracy of CRC diagnosis with CT. However, the use of ionizing radiation in CT scans poses risks, particularly for patients requiring multiple scans or long-term follow-ups.⁴⁵ Additionally, its ability to detect small lesions (≤ 1 cm)

is limited, making accurate differentiation of T1–2 stage intestinal wall layers challenging.

Potential for misdiagnosis and missed diagnoses exist due to factors such as inadequate bowel preparation or peritoneal fat turbidity, which may lead to confusion between pathological and physiological stenosis or misinterpretation of tumor invasion.⁴⁶ Furthermore, assessing lymph node metastasis remains a limitation, as CT primarily relies on lymph node size, which is prone to diagnostic errors.⁴⁷ Although enhanced CT scanning is invaluable for tumor localization, staging, and vascular assessment in CRC, its limitations in detecting small lesions, radiation risks, and accurate lymph node metastasis assessment must be considered.^{48,49}

This meta-analysis investigating the diagnostic utility of contrast-enhanced CT scanning in CRC identification has several inherent limitations that warrant consideration. The primary limitation stems from the substantial heterogeneity observed in sensitivity and specificity metrics across the included studies, likely due to variations in diagnostic protocols, reference standards, and imaging parameters. Although we implemented a random-effects model to account for this heterogeneity, its potential impact on the overall findings remains non-negligible.

Furthermore, dataset limitations prevented a comprehensive stratified analysis of CT diagnostic efficacy across different CRC stages, constraining our ability to evaluate stage-specific diagnostic performance. Methodologically, the predominance of cohort studies, particularly those conducted within the Chinese population, may affect the generalizability of our conclusions, as these study designs generally provide lower levels of clinical evidence compared with prospective diagnostic trials. These limitations highlight the need for future large-scale, prospective multicenter studies to further validate the diagnostic role of contrast-enhanced CT scanning in CRC, thereby strengthening the evidence base for clinical decision-making in CRC diagnosis and management.

In conclusion, this meta-analysis demonstrates that contrast-enhanced CT scanning exhibits superior diagnostic performance in CRC detection, with high sensitivity and specificity, thereby establishing its clinical utility as a reliable diagnostic modality. Notably, our findings reveal comparable diagnostic efficacy between intravenous and oral contrast administration ($P > 0.05$), suggesting that oral contrast agents may serve as a preferable alternative in clinical practice. The

preferential use of oral contrast agents offers multiple advantages, including reduced healthcare expenditures, streamlined examination procedures, and maintained diagnostic accuracy while also improving therapeutic efficiency and alleviating patient financial burdens.

Looking ahead, future research should focus on three key areas: (1) optimizing contrast-enhanced CT protocols for CRC detection across different disease stages; (2) developing integrated diagnostic frameworks that combine CT with emerging modalities such as artificial intelligence-based image analysis and molecular biomarkers; and (3) exploring multimodal imaging strategies to enhance tumor characterization and improve precision in therapeutic decision-making. These advancements have the potential to revolutionize CRC diagnosis and management, ultimately improving patient outcomes.

Footnotes

Conflict of interest disclosure

The authors declared no conflicts of interest.

Funding

This study was funded by Science and Technology Plan Project of Jiaxing, Zhejiang Province (no.: 2023AD11006 and 2024AD10014).

References

1. Murphy CC, Zaki TA. Changing epidemiology of colorectal cancer - birth cohort effects and emerging risk factors. *Nat Rev Gastroenterol Hepatol.* 2024;21(1):25-34. [\[CrossRef\]](#)
2. Patel SG, Dominitz JA. Screening for colorectal cancer. *Ann Intern Med.* 2024;177(4):49-64. [\[CrossRef\]](#)
3. Liu SC, Zhang H. Early diagnostic strategies for colorectal cancer. *World J Gastroenterol.* 2024;30(33):3818-3822. [\[CrossRef\]](#)
4. Metaxas G, Papachristou A, Stathaki M. Colorectal cancer screening: modalities and adherence. *World J Gastroenterol.* 2024;30:3048-3051. [\[CrossRef\]](#)
5. Tamraz M, Al Ghossaini N, Temraz S. Optimization of colorectal cancer screening strategies: new insights. *World J Gastroenterol.* 2024;30(28):3361-3366. [\[CrossRef\]](#)
6. Cao W, Chen HD, Yu YW, Li N, Chen WQ. Changing profiles of cancer burden worldwide and in China: a secondary analysis of the global cancer statistics 2020. *Chin Med J (Engl).* 2021;134(7):783-791. [\[CrossRef\]](#)
7. Qu R, Ma Y, Zhang Z, Fu W. Increasing burden of colorectal cancer in China. *Lancet Gastroenterol Hepatol.* 2022;7(8):700. [\[CrossRef\]](#)
8. Li N, Lu B, Luo C, et al. Incidence, mortality, survival, risk factor and screening of colorectal cancer: a comparison among China, Europe, and northern America. *Cancer Lett.* 2021;522:255-268. [\[CrossRef\]](#)
9. Winkels RM, Kampman E, Wu M. Learning from East to West and vice versa: clinical epidemiology of colorectal cancer in China. *Cancer.* 2021;127(11):1736-1738. [\[CrossRef\]](#)
10. Xu L, Zhao J, Li Z, et al. National and subnational incidence, mortality and associated factors of colorectal cancer in China: a systematic analysis and modelling study. *J Glob Health.* 2023;13:04096. [\[CrossRef\]](#)
11. Li Q, Yu M, Lv H, Zhang L, Deng Y, Yu H. Burden of early-onset colorectal cancer along with attributable risk factors from 1990 to 2019: a comparative study between China and other G20 countries. *BMC Public Health.* 2023;23(1):1463. [\[CrossRef\]](#)
12. Cenin D, Li P, Wang J, et al. Optimising colorectal cancer screening in Shanghai, China: a modelling study. *BMJ Open.* 2022;12(5):48156. [\[CrossRef\]](#)
13. Jacobsson M, Wagner V, Kanneganti S. Screening for colorectal cancer. *Surg Clin North Am.* 2024;104(3):595-607. [\[CrossRef\]](#)
14. Brenner H, Heisser T, Cardoso R, Hoffmeister M. Reduction in colorectal cancer incidence by screening endoscopy. *Nat Rev Gastroenterol Hepatol.* 2024;21(2):125-133. [\[CrossRef\]](#)
15. Li J, Li ZP, Ruan WJ, Wang W. Colorectal cancer screening: the value of early detection and modern challenges. *World J Gastroenterol.* 2024;30(20):2726-2730. [\[CrossRef\]](#)
16. Page MJ, McKenzie JE, Bossuyt PM, et al. The PRISMA 2020 statement: an updated guideline for reporting systematic reviews. *BMJ.* 2021;372:71. [\[CrossRef\]](#)
17. Whiting PF, Rutjes AW, Westwood ME, et al. QUADAS-2: a revised tool for the quality assessment of diagnostic accuracy studies. *Ann Intern Med.* 2011;155(8):529-536. [\[CrossRef\]](#)
18. Cao W, Rong Y, Liu H. Analysis of the Clinical value of CT in preoperative diagnosis and staging of rectal cancer. *Journal of Practical Cancer.* 2016;13(11):1851-1854. [\[CrossRef\]](#)
19. Dai Y. Analysis of the clinical value of CT plain scan and enhanced scan in preoperative diagnosis of colorectal cancer. *Primary Care Medical Forum.* 2019;23(26):2-6. [\[CrossRef\]](#)
20. Fletcher JG, Johnson CD, Welch TJ, et al. Optimization of CT colonography technique: prospective trial in 180 patients. *Radiology.* 2000;216(3):704-711. [\[CrossRef\]](#)
21. Hoppe H, Quattropani C, Spreng A, Mattich J, Netzer P, Dinkel HP. Virtual colon dissection with CT colonography compared with axial interpretation and conventional colonoscopy: preliminary results. *AJR Am J Roentgenol.* 2004;182(5):1151-1158. [\[CrossRef\]](#)

22. Johnson CD, Chen MH, Toledano AY, et al. Accuracy of CT colonography for detection of large adenomas and cancers. *N Engl J Med.* 2008;359(12):1207-1217. [\[CrossRef\]](#)

23. Kim YS, Kim N, Kim SH, et al. The efficacy of intravenous contrast-enhanced 16-row multidetector CT colonography for detecting patients with colorectal polyps in an asymptomatic population in Korea. *J Clin Gastroenterol.* 2008;42(7):791-798. [\[CrossRef\]](#)

24. Miao YM, Amin Z, Healy J, et al. A prospective single centre study comparing computed tomography pneumocolon against colonoscopy in the detection of colorectal neoplasms. *Gut.* 2000;47(6):832-837. [\[CrossRef\]](#)

25. Pickhardt PJ, Choi JR, Hwang I, et al. Computed tomographic virtual colonoscopy to screen for colorectal neoplasia in asymptomatic adults. *N Engl J Med.* 2003;349(23):2191-2200. [\[CrossRef\]](#)

26. Wong BC, Wong WM, Chan JK, et al. Virtual colonoscopy for the detection of colorectal polyps and cancers in a Chinese population. *J Gastroenterol Hepatol.* 2002;17(12):1323-1327. [\[CrossRef\]](#)

27. O'Leary TJ. Colorectal Cancer Screening: Increasing the Options. *J Mol Diagn.* 2024;26(8):669-672. [\[CrossRef\]](#)

28. Shaukat A, Crockett SD. Colorectal cancer screening: time to spring forward. *Am J Gastroenterol.* 2024;119(3):395-396. [\[CrossRef\]](#)

29. Wang Y, Wu ZL, Wang YG, Wang H, Jia XY. Early colorectal cancer screening-no time to lose. *World J Gastroenterol.* 2024;30(23):2959-2963. [\[CrossRef\]](#)

30. Li YJ, Wang X, Wu YJ, et al. Access to colorectal cancer screening in populations in China, 2020: a coverage-focused synthesis analysis. *Int J Cancer.* 2024;155(3):558-568. [\[CrossRef\]](#)

31. Liu J, Liao F, Dong W. Research progress on risk factors associated with early-onset colorectal cancer. *Journal of Medical Research.* 2022;51(5):4-6. [\[CrossRef\]](#)

32. Laine C, Qaseem A, Moyer DV. Controversies in colorectal cancer screening. *Ann Intern Med.* 2024;177(1):83-84. [\[CrossRef\]](#)

33. Tanadi C, Tandarto K, Stella MM, et al. Colorectal cancer screening guidelines for average-risk and high-risk individuals: a systematic review. *Rom J Intern Med.* 2024;62(2):101-123. [\[CrossRef\]](#)

34. Ness RM, Llor X, Abbass MA, et al. NCCN Guidelines(R) Insights: Colorectal Cancer Screening, version 1.2024. *J Natl Compr Canc Netw.* 2024;22(7):438-446. [\[CrossRef\]](#)

35. Chen S, Du W, Cao Y, et al. Preoperative contrast-enhanced CT imaging and clinicopathological characteristics analysis of mismatch repair-deficient colorectal cancer. *Cancer Imaging.* 2023;23(1):97. [\[CrossRef\]](#)

36. Crimi F, Zanon C, Cabrelle G, et al. Contrast-enhanced ct texture analysis in colon cancer: correlation with genetic markers. *Tomography.* 2022;8(5):2193-2201. [\[CrossRef\]](#)

37. Kong Y, Xu M, Wei X, et al. CT imaging-based radiomics signatures improve prognosis prediction in postoperative colorectal cancer. *J Xray Sci Technol.* 2023;31(6):1281-1294. [\[CrossRef\]](#)

38. Ren B, Zhou Q. Clinical value of multi-slice spiral CT enhanced scanning in differentiating lung cancer. *China Journal of CT and MRI.* 2016;14(4):3-7. [\[CrossRef\]](#)

39. Li W, Li B. Application value of DNA methylation based on peripheral blood circulation and fecal samples in early screening of colorectal cancer. *Medical Theory and Practice.* 2022;35(7):3-7. [\[CrossRef\]](#)

40. Zhao Y, Yang J, Luo M, et al. Contrast-enhanced CT-based textural parameters as potential prognostic factors of survival for colorectal cancer patients receiving targeted therapy. *Mol Imaging Biol.* 2021;23(3):427-435. [\[CrossRef\]](#)

41. Sali L, Falchini M, Taddei A, Mascalchi M. Role of preoperative CT colonography in patients with colorectal cancer. *World J Gastroenterol.* 2014;20(14):3795-3803. [\[CrossRef\]](#)

42. Bae H, Lee H, Kim S, et al. Radiomics analysis of contrast-enhanced CT for classification of hepatic focal lesions in colorectal cancer patients: its limitations compared to radiologists. *Eur Radiol.* 2021;31(11):8786-8796. [\[CrossRef\]](#)

43. Liu H. Meta-analysis on enhancing the sensitivity and specificity of CT in the diagnosis of colorectal tumors. *Jilin Medicine.* 2023;44(2):375-378. [\[CrossRef\]](#)

44. Tan L, Liu S, Liu X. The diagnostic value of multi-phase dynamic enhanced CT in preoperative prediction of vascular tumor thrombus in colorectal cancer. *Journal of Medical Imaging.* 2022;32(4):630-633. [\[CrossRef\]](#)

45. Zhang X, Wang Q, Cheng Y. Current status and progress of the application of artificial intelligence in endoscopic and imaging diagnosis of colorectal cancer. *Chinese Journal of Digestive Surgery.* 2024;23(4):622-628. [\[CrossRef\]](#)

46. Liu Y, Zhao Y, Li P. Quantitative CT analysis of changes in body composition and risk factors in patients with colorectal cancer before and after treatment. *Chinese Journal of Osteoporosis.* 2023;29(4):10-14. [\[CrossRef\]](#)

47. Qiao Y. Application of enhanced CT scanning and three-dimensional reconstruction combined with CT angiography in the diagnosis and staging of colorectal cancer. *Practical Journal of Cancer.* 2023;38(11):1868-1871. [\[CrossRef\]](#)

48. Gong S, Chen W. Current status and progress of preoperative application of PET/CT in colorectal cancer. *Gastroenterology.* 2022;27(10):618-22. [\[CrossRef\]](#)

49. Hu K, Qian W. The diagnostic value of CT combined with MR diffusion-weighted imaging in preoperative staging and lymph node positive for rectal cancer. *Henan Journal of Surgery.* 2023;31(7):10-14. [\[CrossRef\]](#)



The role of T1 hyperintensity in differentiating granulomatous prostatitis from prostate cancer: a retrospective analysis of 31 lesions

Selahattin Durmaz¹

Mert Kılıç^{2,3}

Bilgen Coşkun⁴

Sergin Akpek⁴

Barış Bakır⁵

Tarık Esen^{2,3}

Metin Vural⁴

Emre Altınmakas^{6,7}

¹Gaziosmanpaşa Training and Research Hospital, Clinic of Radiology, İstanbul, Türkiye

²American Hospital, Clinic of Urology, İstanbul, Türkiye

³Koç University School of Medicine, Department of Urology, İstanbul, Türkiye

⁴American Hospital, Clinic of Radiology, İstanbul, Türkiye

⁵İstanbul University İstanbul Faculty of Medicine, Department of Radiology, İstanbul, Türkiye

⁶ICahn School of Medicine at Mount Sinai, Department of Diagnostic, Molecular and Interventional Radiology, New York, USA

⁷Koç University School of Medicine Department of Radiology, İstanbul, Türkiye

Corresponding author: Selahattin Durmaz

E-mail: drselahattindurmaz@gmail.com

Received 06 February 2025; revision requested 19 March 2025; accepted 05 April 2025.



Epub: 20.05.2025

Publication date: 02.01.2026

DOI: 10.4274/dir.2025.253242

PURPOSE

To investigate the multiparametric magnetic resonance imaging (mpMRI) characteristics of granulomatous prostatitis (GP) and share our experience with 31 pathologically confirmed GP lesions in 19 patients.

METHODS

This two-center retrospective study reviewed the pathological and imaging data of 856 patients who underwent prostate biopsy between January 2012 and April 2024. Of these, 19 patients with available prebiopsy mpMRI and a pathologically confirmed diagnosis of GP were included. Additionally, 280 biopsy-naïve patients diagnosed with clinically significant prostate cancer (csPCa) were included as a control group for comparative analysis. Prebiopsy mpMR images of patients with GP were assessed by consensus between two of three radiologists (M.V., B.C., S.D.), evaluating lesion location, size, shape, multifocality, extraprostatic extension (EPE), signal characteristics on T1-, T2-, and diffusion-weighted imaging (DWI), the mean apparent diffusion coefficient (ADC_{mean}) value, enhancement patterns, and prostate imaging reporting and data system (PI-RADS) scores. Statistical analyses were conducted using SPSS version 30.0.

RESULTS

In 19 patients, 31 pathologically confirmed GP lesions were identified on prebiopsy mpMRI. Twenty-six lesions were located in the peripheral zone and five in the transitional zone. Multifocal involvement was observed in nine patients (47.3%). Thirty of 31 lesions were hypointense on T2-WI, and seven showed capsular bulging and/or irregularity, suggesting EPE. DWI revealed markedly impeded diffusion in all lesions. The median ADC_{mean} value was $825 \times 10^{-3} \text{ mm}^2/\text{s}$ (IQR: $230 \times 10^{-3} \text{ mm}^2/\text{s}$). On dynamic contrast-enhanced sequences, 25 lesions showed early enhancement, five showed prolonged enhancement, and one showed prolonged ring enhancement. Based on mpMRI findings, 17 lesions were assigned a PI-RADS score of 4, and 13 lesions were assigned a PI-RADS score of 5. Notably, 22 lesions (71%) in 14 patients with GP (73.7%) exhibited hyperintensity on T1-WI despite no prior prostate biopsy history. Statistical analysis comparing the GP and csPCa groups revealed that hyperintensity on T1-WI was significantly more frequent in GP, both on a per-patient basis (73.7% vs. 3.2%) and a per-lesion basis (71.0% vs. 3.1%) ($P < 0.0001$ for both).

CONCLUSION

GP shares overlapping imaging features with prostate cancer on mpMRI. However, hyperintensity on T1-WI may serve as a distinguishing feature, potentially reducing unnecessary prostate interventions. Radiologists should consider GP in PI-RADS ≥ 4 lesions exhibiting T1-WI hyperintensity. Furthermore, given the high incidence of GP following intravesical Bacillus Calmette-Guérin (BCG) therapy, a thorough history of BCG treatment should be obtained.

CLINICAL SIGNIFICANCE

GP is recognized for its tendency to mimic PCa on mpMRI, a finding corroborated by this study. However, T1-WI hyperintensity emerged as a promising distinguishing feature for GP. Incorporating this marker into mpMRI interpretation criteria may help reduce unnecessary prostate interventions and improve patient outcomes.

KEYWORDS

Bacillus Calmette-Guérin, granulomatous prostatitis, magnetic resonance imaging, prostate cancer, T1-weighted imaging

You may cite this article as: Durmaz S, Kılıç M, Coşkun B, et al. The role of T1 hyperintensity in differentiating granulomatous prostatitis from prostate cancer: a retrospective analysis of 31 lesions. *Diagn Interv Radiol.* 2026;32(1):8-15.

Granulomatous prostatitis (GP) is a rare, benign inflammatory condition estimated to account for 3.3% of all inflammatory lesions of the prostate. It has long been recognized that GP lesions can mimic prostate cancer (PCa) in both clinical and laboratory presentations.¹ Typical clinical features include elevated serum prostate-specific antigen (PSA) levels and a firm, nodular prostate on digital rectal examination (DRE).^{1,2} On multiparametric magnetic resonance imaging (mpMRI), GP lesions often appear hypointense on T2-weighted images and exhibit markedly impeded diffusion on diffusion-weighted imaging (DWI), closely resembling PCa.^{1,3}

The specificity and positive predictive value of mpMRI in detecting PCa have been reported to be limited following intravesical *Bacillus Calmette-Guérin* (BCG) therapy.⁴ In a prospective study, Ogreden et al.⁵ compared PSA levels, PSA density (PSAd), DRE findings, and the number of PI-RADS ≥ 3 lesions detected on mpMRI before and after intravesical BCG therapy in 10 patients. They observed substantially higher PSA and PSAd levels, more frequent abnormal DRE findings, and an increased number of PI-RADS ≥ 3 lesions after BCG therapy.

The clinical and radiological similarities between GP and PCa often complicate patient management. Most GP lesions receive a high cancer suspicion score (PI-RADS 4 or 5), resulting in unnecessary biopsies.^{3,6} Identifying specific mpMRI features of GP may help reduce the number of unnecessary biopsies and their associated complications.

To date, only a limited number of studies—with small patient cohorts—have investigated the MRI characteristics of GP. In this study, we aim to review the existing MRI literature on GP and share our experience with a series of 31 pathologically confirmed GP lesions in 19 patients.

Main points

- Granulomatous prostatitis (GP) shares overlapping imaging characteristics with prostate cancer (PCa) on multiparametric magnetic resonance imaging.
- Hyperintensity on T1-weighted imaging is frequently observed in GP and may assist in distinguishing it from PCa.
- In cases of caseous necrosis or abscess formation, early and prolonged ring enhancement on dynamic contrast-enhanced imaging can support the diagnosis of GP.

Methods

Patients

Koc University Institutional Review Board approved this retrospective observational study and waived the requirement for written informed consent (decision number: 2022.394.IRB1.149, approval date: 10/17/2022). Between January 2012 and April 2024, we reviewed the pathological records of 856 patients who had undergone prostate biopsy due to a high suspicion of clinically significant PCa (csPCa). From this cohort, patients with available prebiopsy mpMRI who were diagnosed with GP through MRI-targeted biopsy—either transrectal MRI-guided in-bore biopsy or MRI-directed cognitive fusion-guided biopsy—were identified and included. Two patients diagnosed with GP via biopsy were excluded due to the absence of detectable lesions on mpMRI.

Additionally, 280 biopsy-naïve patients from the same cohort, diagnosed with csPCa (ISUP grade group ≥ 2) via biopsy, were included as a control group for comparative analysis. A study flowchart is presented in Figure 1. Clinical data, including age, PSA levels, and PSAd, were also collected for patients with GP.

Magnetic resonance imaging technique

This study included MRI scans from two different hospitals. mpMRI examinations were performed on a 3.0 Tesla scanner (MAGNETOM® Skyra, Siemens AG, Munich, Germany) in 8 patients and a 1.5 Tesla scanner (MAGNETOM® Aera, Siemens AG, Munich, Germany) in 11 patients using a 30-channel phased-array body coil. Prior to imaging, seven patients received an intravenous (IV) injection of 20 mg butylscopolamine (Buscopan®; Boehringer Ingelheim) to suppress bowel peristalsis.

All patients underwent mpMRI due to elevated serum PSA levels and/or suspicious findings on DRE. The imaging protocol included axial T1-WI of the pelvis, high-resolution T2-WI in axial, coronal, and sagittal planes, axial DWI, and axial dynamic contrast-enhanced (DCE) sequences, performed according to the recommendations of the European consensus meeting on prostate mpMRI standardization.⁷ DCE images were obtained using 9–10 mL of gadolinium-based contrast agent (gadoterate meglumine 0.5 mmol/mL; DOTAREM®, Guerbet, Villepinte, France), administered at a rate of 3.5 mL/s via power injector. MRI protocols for both centers are summarized in Table 1.

Image analysis

All MRI were reviewed in consensus by two of three radiologists (M.V., B.C., S.D.) with 4–16 years of experience in prostate MRI. The reviewers were blinded to the pathological results. Each GP lesion was evaluated for location, shape, size, multifocality, signal intensity (SI) on T1-WI, T2-WI, and DWI, mean apparent diffusion coefficient (ADC_{mean}) value, presence of extraprostatic extension (EPE), enhancement patterns on DCE, and PI-RADS score. The PI-RADS scores were assigned according to the criteria outlined in PI-RADS version 2.1.⁸ Lesion shape was assessed on T2-WI using the shape patterns described by Suzuki et al.⁹

SI on T1-WI, T2-WI, and DWI was assessed by visual comparison with the residual healthy peripheral zone (PZ). Mean ADC values were measured by placing a region of interest over the largest area of the lesion, avoiding the tumor edges. For comparative analysis, the T1-WI signal characteristics of csPCa lesions in the control group were also retrospectively assessed and recorded.

Statistical analysis

Statistical analyses were performed using SPSS version 30.0 (IBM Corp., Armonk, NY, USA). Continuous variables were assessed for normality using the Shapiro-Wilk test. Non-normally distributed variables were summarized as median with interquartile range (IQR), whereas normally distributed variables were reported as mean \pm standard deviation. Categorical variables were presented as frequencies and percentages. The presence of hyperintensity on T1-WI was compared between the csPCa and GP groups using Fisher's exact test on both a per-patient and per-lesion basis. A *P* value of < 0.05 was considered statistically significant.

Results

A total of 31 pathologically proven GP lesions in 19 patients were included in this study. The overall incidence of GP in our cohort was 21/856 (2.4%). Eleven patients had a history of intravesical BCG therapy and were considered to have BCG-induced GP, whereas the remaining patients had no identifiable predisposing factors and were thus classified as having idiopathic (non-specific) GP. In all patients, the interval between the last BCG administration and the mpMRI examination was less than 3 months.

The median age was 65 years (IQR: 13.5 years), the median PSA level was 6.25 ng/

mL (IQR: 2.8 ng/mL), the median PSAd was 0.14 ng/mL/mL (IQR: 0.08 ng/mL/mL), and the median prostate volume was 47 mL (IQR: 22 mL). mpMRI evaluation identified 26 lesions in the PZ and five in the transition zone. Both zones were involved in three patients (Figure 2). Lesions were classified by shape as nodular ($n = 25$), diffuse ($n = 5$), or cystic ($n = 1$). The median lesion size was 14 mm (IQR: 11.25 mm). Multifocal involvement was present in nine patients (Figures 2 and 3).

Regardless of lesion shape, 22 lesions (71%) in 14 patients with GP (73.7%) demonstrated increased SI on T1-WI (Figures 2 and 4). In the control group, only nine lesions (3.1%) in nine patients (3.2%) exhibited mild to moderate T1 hyperintensity. Statistical analysis showed that hyperintensity on T1-WI was significantly more frequent in GP compared with csPCa, both on a per-patient basis [14/19 (73.7%) vs. 9/280 (3.2%), $P < 0.0001$] and on a per-lesion basis [22/31 (71.0%) vs. 9/294 (3.1%), $P < 0.0001$].

On DWI, all lesions demonstrated markedly impeded diffusion. The median ADC_{mean} value was 825×10^{-3} mm²/s (IQR: 230×10^{-3} mm²/s). On T2-WI, 30 lesions were hypointense, whereas the remaining lesion was iso- to hyperintense compared with the PZ. Capsular bulging and/or irregularity suggestive of EPE was noted in seven lesions (Figures 3 and 4). Following IV contrast administration, 25 lesions showed early enhancement (Figures 2 and 4), five showed prolonged enhancement, and one demonstrated prolonged ring enhancement (Figure 5). The characteristics of the patients and the main mpMRI findings of the lesions are presented in Table 2.

Based on imaging findings, 13 lesions were assigned a PI-RADS 5 score, and 17 lesions were scored as PI-RADS 4. The remaining lesion's MRI features were consistent with abscess formation. Due to the high clinical suspicion of PCa, seven patients underwent MRI-guided in-bore biopsy, and 11 underwent MRI-directed cognitive fusion-guided biopsy. The remaining patient—suspected to have a prostate abscess—was also sampled by MRI-directed cognitive fusion-guided biopsy to confirm the diagnosis and rule out coexisting PCa.

Histopathological examination confirmed the diagnosis of GP in all patients. Concomitant PCa was detected outside the targeted lesion in four patients: three with a Gleason score of 6 (3+3) (cases 7, 13, and 17) and one with a Gleason score of 8 (4+4) (case 14).

Figure 1. The study flowchart. MRI, magnetic resonance imaging; mpMRI, multiparametric magnetic resonance imaging.

Table 1. Multiparametric magnetic resonance imaging protocols of two centers

Parameter	Center	T2-WI	DWI	DCE	T1-WI
TR (ms)	1	5290	4800	9	445
	2	7500	4700	4.27	578
TE (ms)	1	111	98	1.76	9.80
	2	101	59	1.64	10
Field of view (mm)	1	200 × 200	260 × 260	260 × 260	300 × 400
	2	200 × 200	192 × 192	200 × 200	200 × 200
Matrix size	1	512 × 297	192 × 154	192 × 155	384 × 297
	2	320 × 230	128 × 128	192 × 134	192 × 256
Slice thickness/gap (mm)	1	3/0.6	3.6/0	3.6/0	6/1.2
	2	3	3	3	3
Flip angle (°)	1	180	180	15	120
	2	160		12	160
Scan time (mins)	1	03:23	05:38	04:38	1:16
	2	04:17	08:34	04:53	2:31
Temporal resolution (s)	1	-	-	8	-
	2	-	-	8	-
B value	1	-	1600	-	-
	2	-	1400	-	-

TR, repetition time; TE, echo time; T2-WI, T2-weighted imaging; DWI, diffusion-weighted imaging; T1-WI, T1-weighted imaging; DCE, Dynamic contrast-enhanced.

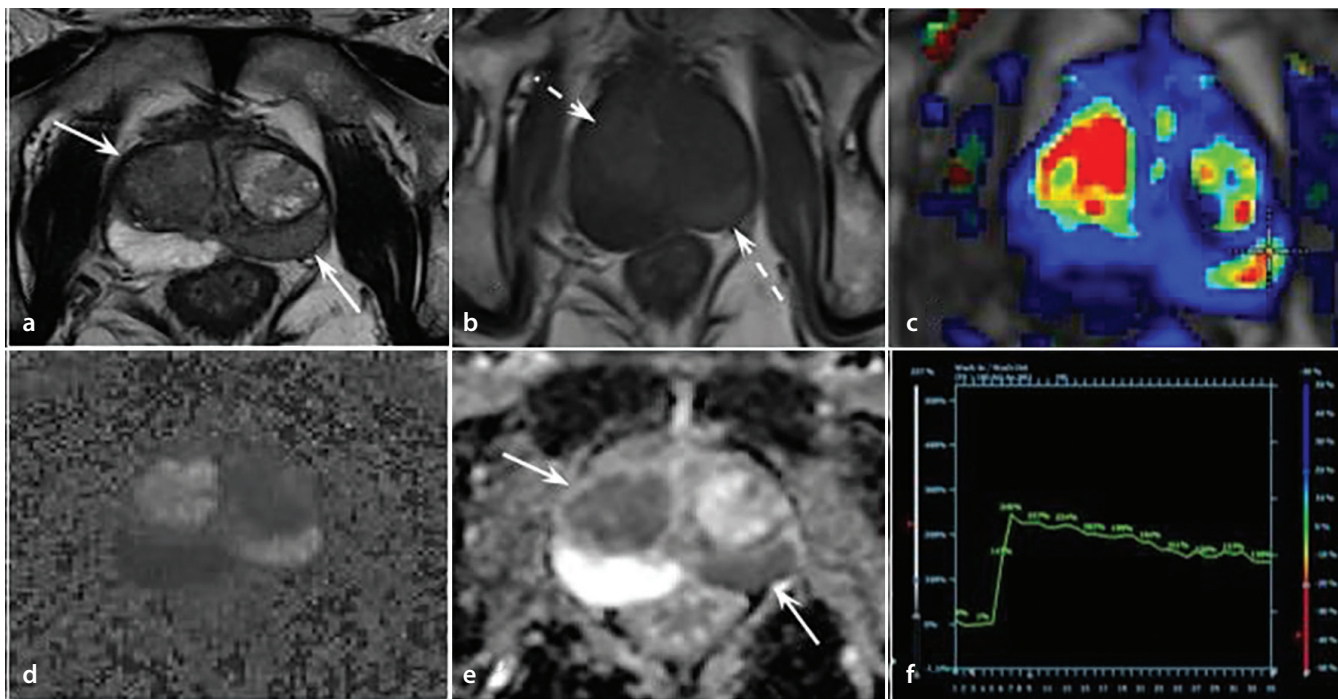


Figure 2. A 76-year-old biopsy-naïve patient (case 4) with a history of intravesical BCG administration for non-muscle-invasive bladder cancer presented with elevated PSA (9.79 ng/mL) and abnormal digital rectal examination. The prostate volume and PSA density were 76 mL and 0.13 ng/mL², respectively. Subsequent mpMRI demonstrated 21 mm left peripheral zone and 29 mm right transition zone lesions. Both lesions showed a hypointense signal on T2-WI (arrows) (a) and a hyperintense signal on T1-WI (dashed arrows) (b), with marked restricted diffusion on DWI and ADC maps (ADC values: 825 and 758 × 10⁻³ mm²/s) (d, e). On DCE imaging (c, f), both lesions showed early enhancement relative to the background prostate gland and were classified as PI-RADS 5. BCG, Bacillus Calmette-Guérin; PSA, prostate-specific antigen; mpMRI, multiparametric magnetic resonance imaging; T1-WI, T1-weighted imaging; T2-WI, T2-weighted imaging; DWI, Diffusion-weighted imaging; ADC, apparent diffusion coefficient; PI-RADS, prostate imaging reporting and data system; DCE, dynamic contrast-enhanced.

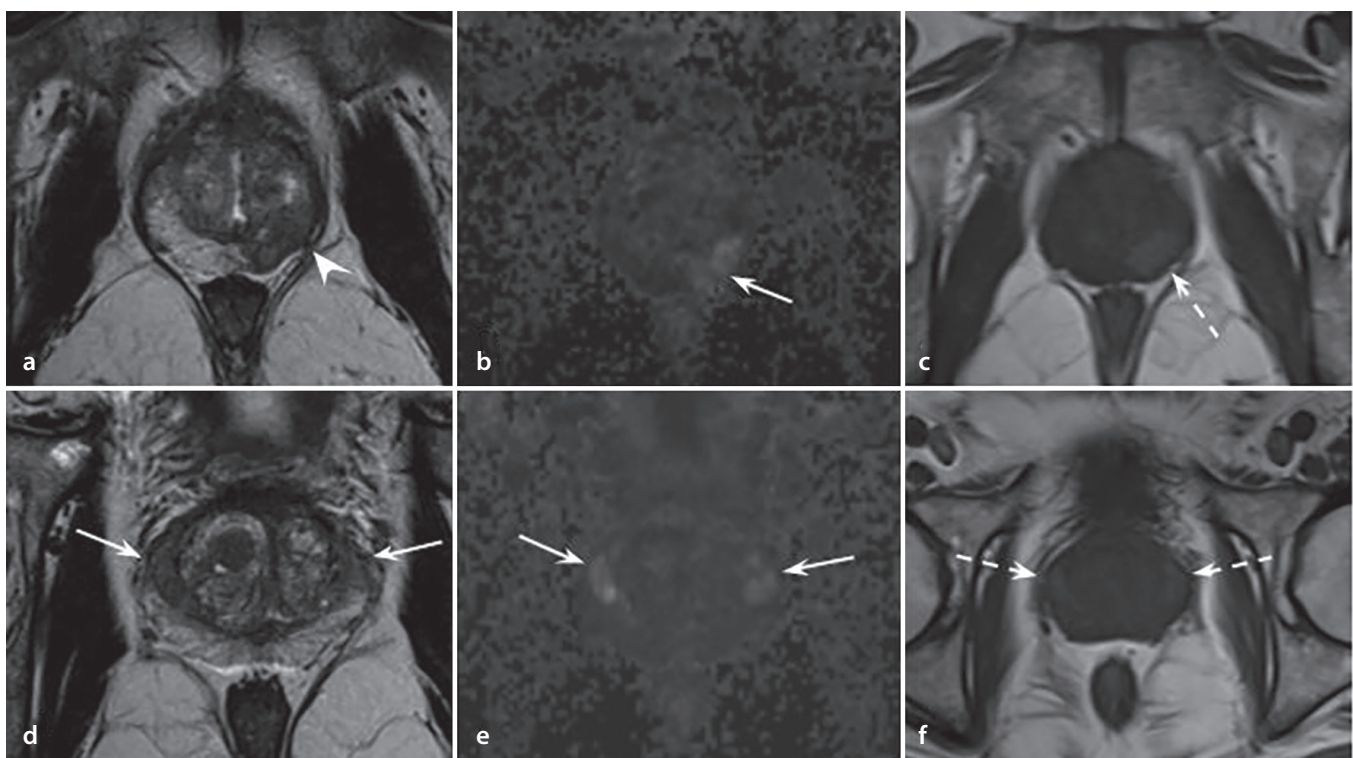


Figure 3. A 76-year-old biopsy-naïve patient (case 7) with a history of intravesical BCG administration for non-muscle-invasive bladder cancer presented with elevated PSA (5.2 ng/mL) and abnormal digital rectal examination findings. The prostate volume and PSA density were 37 mL and 0.14 ng/mL², respectively. Subsequent mpMRI demonstrated three peripheral zone lesions measuring 11 mm, 12 mm, and 19 mm. The lesions showed a hypointense signal on T2-WI (a, d) and a hyperintense signal on T1-WI (c, f) (dashed arrows), with marked impeded diffusion (ADC values: 737, 925, and 675 × 10⁻³ mm²/s) (b, e). Note capsular bulging and mild irregularity on T2-WI (a) (arrowhead), suggesting EPE. BCG, Bacillus Calmette-Guérin; PSA, prostate-specific antigen; T2-WI, T2-weighted imaging; T1-WI, T1-weighted imaging; ADC, apparent diffusion coefficient; EPE, extraprostatic extension.

Table 2. The summary of the clinical, demographic, and multiparametric magnetic resonance imaging features of the patients

Case	Age (years)	PSA (ng/mL)	PSAd (ng/mL ²)	BCG history	Number of lesions	Location	Shape	SI on T2-WI	SI on DWI	SI on T1-WI	Enhancement pattern	PI-RADS score
1	62	9	0.1	+	1	PZ	Cystic	Iso-high	High	Iso	Prolonged-ring	-
2	54	3.6	0.06	+	1	PZ	Diffuse	Low	High	High	Prolonged	5
3	72	6	0.23	+	2	PZ	Nodular	Low	High	High	Early	4
4	76	9.79	0.13	+	2	PZ TZ	Nodular	Low	High	High	Early	5
5	74	4.4	0.1	+	1	PZ	Nodular	Low	High	High	Early	4
6	73	4.11	0.1	+	1	PZ	Nodular	Low	High	High	Early	5
												4
7	76	5.2	0.14	+	3	PZ	Nodular	Low	High	High	Early	4
												5
8	74	5	0.19	+	2	PZ	Nodular	Low	High	High	Early Prolonged	4
9	63	7	0.032	-	1	PZ	Diffuse	Low	High	High	Early	5
10	51	4	0.2	-	2	PZ	Nodular	Low	High	Iso	Early	4
11	70	6.52	0.1	-	1	PZ	Nodular	Low	High	High	Early	5
						PZ	Nodular					5
12	57	9.9	0.24	-	3	TZ TZ	Diffuse Diffuse	Low	High	High	Early	4 (3 + 1) 4 (3 + 1)
13	68	5.54	0.13	-	1	PZ	Diffuse	Low	High	Iso	Early	5
14	65	10	0.16	-	1	PZ	Nodular	Low	High	High	Early	5
15	53	6.5	0.14	-	2	TZ	Nodular	Low	High	Iso	Early	5
16	65	11.23	0.24	+	1	PZ	Nodular	Low	High	High	Prolonged	4
17	61	5.23	0.1	-	1	PZ and TZ	Nodular	Low	High	Iso	Early	5
18	56	6.5	0.16	+	3	PZ	Nodular	Low	High	High	Early	4
										Iso		
19	62	8.1	0.16	+	2	PZ	Nodular	Low	High	High	Prolonged	4

PSA, prostate-specific antigen; PSAd, prostate-specific antigen density; BCG, Bacillus Calmette-Guérin; PZ, peripheral zone; TZ, transition zone; SI, signal intensity; T2-WI, T2-weighted imaging; DWI, diffusion-weighted imaging; T1-WI, T1-weighted imaging; PI-RADS, prostate imaging reporting and data system.

Table 3. Reported case series of granulomatous prostatitis in the English literature

First author (reference)	Year	Patient (n)	BCG history (n%)	Age (years)	PSA (ng/ml)	PSAd (ng/mL ²)	Lesion size (mm)	Location PZ (n)/TZ (n)	Low SI on T2WI (n%)	High SI on DWI (n%)	High SI on T1-WI (n%)
Naik et al. ¹⁶	1998	10	0	68	11	-	-	-	40	-	0
Ma et al. ¹⁷	2009	5	100	-	-	-	-	5/0	100	-	-
Bour et al. ¹⁵	2012	5	60	-	-	-	-	5/4	80	100	0
Suzuki et al. ⁹	2013	10	100	70.2	7.39	-	-	10/2	90	90	70
Kawada et al. ²²	2015	5	100	70.4	-	-	21.2	5/3	40	100	100
Gottlieb et al. ²	2017	6	100	68.7	-	-	-	6/0	100	17	0
Rais-Bahrami et al. ¹⁹	2017	5	40	66	7.4	0.20	19.2	3/2	100	100	-
Lee et al. ¹	2019	16	0	62.5	7.7	0.15	-	16/14	100	100	-
Wang et al. ²⁴	2021	8	100	63.6	5.7	-	-	8/0	100	100	12.5
Lee et al. ²³	2022	24	100	66	-	-	22	-	100	92	-
Bertelli et al. ¹⁴	2022	11	36	68	8.74	0.12	-	10/4	100	100	-
Ogreden et al. ⁵	2024	10	100	66.9	4.3	0.10	-	-	-	-	-
Guerra et al. ²⁶	2024	12	100	62	7.26	0.13	10	9/7	83	100	-
Avudaiappan et al. ⁴	2024	7	100	-	6.9	-	-	5/0	-	-	-

BCG, Bacillus Calmette-Guérin; PSA, prostate-specific antigen; PSAd, prostate-specific antigen density; PZ, peripheral zone; TZ, transition zone; SI, signal intensity; T2-WI, T2-weighted imaging; DWI, Diffusion-weighted imaging; T1-WI, T1-weighted imaging.

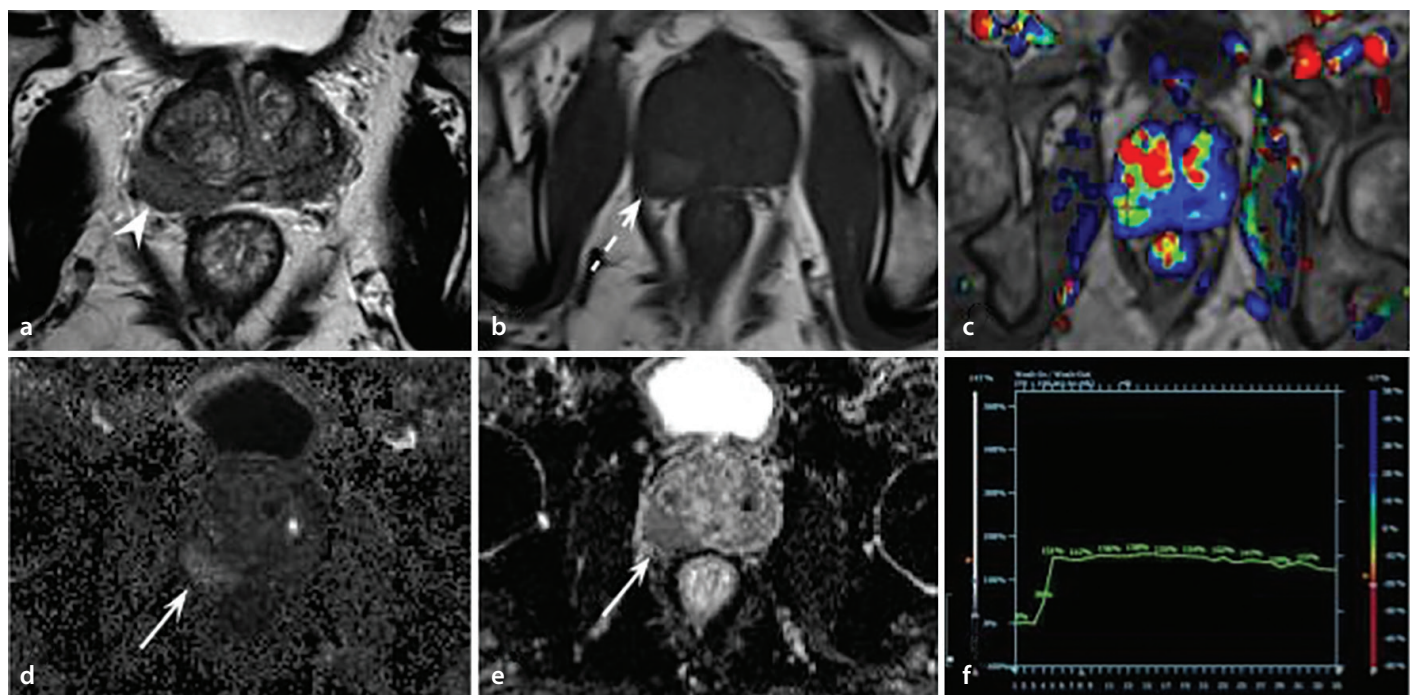


Figure 4. A 73-year-old biopsy-naïve patient (case 6) with a history of intravesical BCG administration for non-muscle-invasive bladder cancer presented with elevated PSA (4.11 ng/mL) and abnormal digital rectal examination findings. The prostate volume and PSA density were 47 mL and 0.10 ng/mL², respectively. Subsequent mpMRI revealed a 25 mm right peripheral zone lesion. The lesion demonstrated a hypointense signal on T2-WI (a) and a hyperintense signal on T1-WI (b) (dashed arrow), with marked impeded diffusion (ADC value: 814×10^{-3} mm²/s) (d, e). On DCE imaging (c, f), the enhancement pattern resembled that of prostate cancer. Note the capsular bulging and irregularity on T2-WI (a) (arrowhead), suggestive of EPE. BCG, *Bacillus Calmette-Guérin*; PSA, prostate-specific antigen; mpMRI, multiparametric magnetic resonance imaging; T2-WI, T2-weighted imaging; T1-WI, T1-weighted imaging; ADC, apparent diffusion coefficient; DCE, dynamic contrast-enhanced.

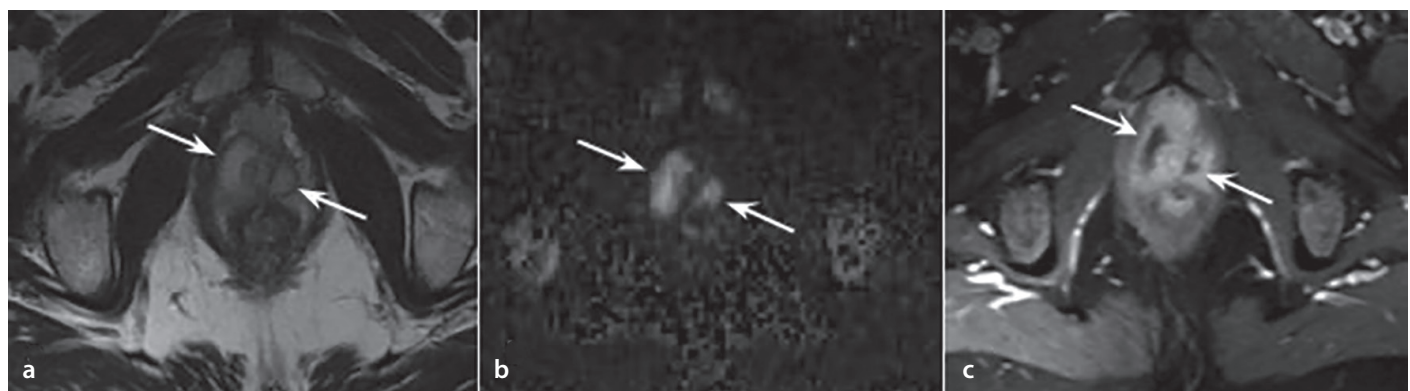


Figure 5. A 62-year-old biopsy-naïve patient (case 1) with a history of intravesical BCG administration for non-muscle-invasive bladder cancer presented with elevated PSA (9 ng/mL) and abnormal digital rectal examination. The prostate volume and PSA density were 86 mL and 0.10 ng/mL², respectively. Subsequent mpMRI demonstrated a peripheral zone lesion located at the apex (arrows). The lesion appeared iso- to hyperintense on T2-WI (a) and isointense on T1-WI (not shown). On DCE imaging (c), peripheral rim-like enhancement was observed (arrowhead). The avascular central portion of the lesion demonstrated marked impeded diffusion (ADC value: 715×10^{-3} mm²/s) (b). BCG, *Bacillus Calmette-Guérin*; PSA, prostate-specific antigen; mpMRI, multiparametric magnetic resonance imaging; T2-WI, T2-weighted imaging; T1-WI, T1-weighted imaging; ADC, apparent diffusion coefficient; DCE, dynamic contrast-enhanced.

Discussion

In this study, we found that GP and PCA have overlapping imaging features on mpMRI; however, we also identified hyperintensity on T1-WI as a promising distinguishing feature for GP.

GP can be idiopathic (non-specific) or secondary to infective (intravesical BCG therapy)

etiologies, iatrogenic factors [transurethral resection of the prostate (TUR-P), prostate biopsy], or systemic diseases.^{1,10} According to reported series, non-specific GP comprises 60%–77.7% of all GP cases.¹⁰ However, in our patient group, the proportions of non-specific and BCG-induced GP cases were 42% (8/19) and 58% (11/19), respectively. This discrepancy, compared with a more extensive

series, can be attributed to our small sample size and the high proportion of patients with a history of intravesical BCG therapy for the treatment of bladder cancer. The incidence of GP following intravesical BCG therapy is reported to be 41%.¹

Oppenheimer et al.¹¹ reported the incidence of GP to be 0.36% in a series of 25,000

men who underwent prostate biopsy. However, based on more recent studies, the incidence has been increasing due to the widespread use of intravesical BCG therapy, the growing number of TUR-P procedures, and the increasing frequency of extensive prostate biopsies.^{3,12,13} Similar to these more recent studies,^{1,13,14} the GP incidence in our cohort was 2.4%.

GP lesions are usually asymptomatic, except for infectious GP, which generally does not require treatment.^{14,15} However, the primary concern lies in the potential for these lesions to be misinterpreted as PCa on mpMRI, leading to unnecessary biopsy. A limited number of studies have explored the MRI characteristics of GP to address this radiology-pathology discordance and improve the positive predictive value of MRI. Table 3 summarizes the reported GP case series in the English literature.

Naik and Carey¹⁶ were among the first to investigate the imaging characteristics of GP in an attempt to identify specific features. They evaluated the transrectal ultrasound and MRI (T2-WI, pre- and post-contrast T1-WI) findings of 10 patients diagnosed with GP. They concluded that no reliable clinical, laboratory, US, or MRI findings could be used to differentiate GP from PCa. Ma et al.¹⁷ evaluated MRI findings in five patients with GP and observed diffuse or focal-nodular decreased SI on T2-WI. Since neither the clinical nor imaging findings could reliably exclude the possibility of PCa, the researchers stated that a biopsy was necessary for a definitive diagnosis.¹⁷

Five biopsy-proven patients with GP (three of whom had a history of BCG therapy) were reported by Bour et al.¹⁵ Based on mpMRI findings, two distinct manifestations of GP were described. The first and more frequent type had a tumor-like appearance that could not be distinguished from that of PCa. In contrast, the second type was suggestive of abscess formation induced by a severe caseating necrotic process. Furthermore, the authors observed periprostatic or seminal vesicle wall infiltration in four patients, simulating locally advanced PCa.¹⁵

Lee et al.¹ evaluated the MRI findings of 16 patients with GP and reported suspicious EPE findings in 15 of them. All patients were assigned a PI-RADS score of five according to PI-RADS version 2.¹⁸ In another study, Rais-Bahrami et al.¹⁹ compared the clinical and mpMRI findings of five biopsy-proven patients with GP (two with a history of BCG therapy) to 15 biopsy-proven csPCa patients. In contrast to

the findings of Lee et al.¹ and Bour et al.,¹⁵ they reported significantly higher ADC values in patients with GP compared to those with PCa and suggested that high-stage features such as EPE are more indicative of PCa than GP. Another study comparing BCG-exposed and non-BCG-exposed groups reported a lower risk of csPCa in PI-RADS ≥ 3 lesions among BCG-exposed patients.²⁰

Our findings were consistent with those of Lee et al.¹ and Bour et al.¹⁵ In our cohort, 30 lesions exhibited a tumor-like appearance with low ADC_{mean} values, seven of which showed capsular bulging and/or irregularity suggestive of EPE (Figures 3 and 4). The remaining lesion displayed imaging findings consistent with the second manifestation described by Bour et al.¹⁵

GP tends to show variable diffusion characteristics. Since the degree of impeded diffusion reflects cellular density, it is thought that more acute manifestations of GP tend to exhibit greater diffusion restriction.^{2,3,21} Gotthlieb et al.² evaluated the mpMRI findings of six patients with BCG-induced GP. Based on the diffusion characteristics of the lesions, the authors described acute and chronic patterns, which were believed to reflect the acute and chronic phases of prostatitis, respectively. The chronic pattern was more common and demonstrated less impeded diffusion, whereas the acute pattern was indistinguishable from aggressive PCa.² A case report by Logan et al.¹² evaluated the serial MRI changes in BCG-induced GP from the completion of BCG therapy to the development of GP. The authors noted that the manifestation of chronic GP took more than 12 months following the completion of BCG therapy.¹² In our cohort, the interval between the last BCG administration and mpMRI examination was less than 3 months in all patients. Accordingly, we observed marked impeded diffusion in all cases, corresponding to the acute manifestation of GP.

The dynamic contrast enhancement pattern of BCG-induced GP lesions was first evaluated by Kawada et al.²² in five patients. They reported that early and prolonged ring enhancement may help differentiate GP from PCa. Additionally, the authors noted T1-WI hyperintensity in all patients. Another study involving four BCG-induced GP and seven non-specific GP patients also observed prolonged ring enhancement in the BCG-induced cases.¹⁴ In our study group, prolonged ring enhancement was observed in one patient (case 1) with a history of intravesical BCG therapy (Figure 5). Among the re-

maining patients, 25 out of 30 lesions (83%) demonstrated early enhancement similar to PCa, whereas five lesions showed prolonged enhancement.

The largest group of BCG-induced GP patients (n = 24) was reported by Lee et al.²³ Based on imaging findings from contrast-enhanced T1-WI and DWI, the authors categorized GP lesions into three types: type A, type B, and type C. Types A and B were reported to correspond to the acute phase of BCG-induced GP, whereas type C represented the chronic phase. As previously stated by Gotthlieb et al.,² the acute manifestation—particularly type A lesions—was reported to be more challenging to differentiate from PCa. According to the imaging patterns proposed by Lee et al.,²³ 30 lesions in our cohort could be classified as type A, and the remaining lesion as type B.

Suzuki et al.⁹ performed a bi-parametric MRI on ten patients with BCG-induced GP and identified three main lesion patterns based on shape: diffuse, nodular, and cystic with a mural nodule. In all diffuse lesions, the authors observed hyperintensity on T1-WI.⁹ In another study, 12.5% (n = 2/8) of BCG-induced GP cases were reported to show hyperintensity on T1-WI.²⁴ Supporting this, Lim et al.²⁵ also noted hyperintensity on T1-WI in a case of mass-forming splenic tuberculosis.

In our patient group, 31 pathologically confirmed GP lesions were identified. Similar to a recently published study,²⁶ the majority of GP lesions in our cohort (n = 25/31, 80.6%) were nodular in shape. Regardless of lesion shape, 22 lesions (71%) demonstrated hyperintensity on T1-WI. All patients in our cohort were biopsy-naïve, and histopathological examination did not reveal any findings that could account for this hyperintensity. Previous studies have attributed the hyperintense appearance of granulomatous lesions on T1-WI to the presence of paramagnetic substances, such as macrophage-laden oxygen free radicals produced during phagocytosis by activated macrophages.^{6,9,27,28}

To the best of our knowledge, this study reports the mpMRI characteristics of the largest number of GP lesions. On a per-patient basis, our study includes one of the largest groups of patients with GP. Based on the mpMRI findings in our patient group, we suggest that hyperintensity on T1-WI can be helpful in the differentiation of GP from PCa. As discussed above, hyperintensity on T1-WI has been observed in three previous studies as an MRI finding in some GP lesions.^{9,22,24} However, to our knowledge, this is the first

time it is being reported and highlighted as a possible differentiator of GP from PCa.

We acknowledge that this study had several limitations. First, our cohort is relatively small; however, this can be attributed to the low incidence of GP. Furthermore, as far as we can tell, it is one of the most extensive series among published studies on the MRI findings of GP. Second, there may be increased patient selection bias owing to the retrospective design and the recruitment period spanning 12 years.

In conclusion, despite advances in MRI technology and imaging techniques, differentiating GP from PCa based on mpMRI findings remains challenging. However, we propose hyperintensity on T1-WI as a promising feature in this differentiation. To avoid unnecessary prostate interventions, radiologists should consider the possibility of GP in PI-RADS ≥ 4 lesions that exhibit hyperintensity on T1-WI. Additionally, given the high incidence of GP following intravesical BCG therapy, a detailed history of BCG treatment should be carefully investigated. Prospective studies with larger patient cohorts are needed to validate the diagnostic value of our findings.

Footnotes

Conflict of interest disclosure

The authors declared no conflicts of interest.

References

1. Lee SM, Wolfe K, Acher P, Liyanage SH. Multiparametric MRI appearances of primary granulomatous prostatitis. *Br J Radiol*. 2019;92(1098):20180075. [\[Crossref\]](#)
2. Gottlieb J, Princenthal R, Cohen MI. Multiparametric MRI findings of granulomatous prostatitis developing after intravesical bacillus calmette-guérin therapy. *Abdom Radiol (NY)*. 2017;42(7):1963-1967. [\[Crossref\]](#)
3. Gaudiano C, Renzetti B, De Fino C, et al. Multiparametric magnetic resonance imaging for the differential diagnosis between granulomatous prostatitis and prostate cancer: a literature review to an intriguing diagnostic challenge. *Front Oncol*. 2023;13:1178430. [\[Crossref\]](#)
4. Avudaiappan AP, Prabhakar P, Siretskiy R, Renshaw A, Eldefrawy A, Manoharan M. Reliability of mpMRI in diagnosing cancer prostate following intravesical BCG for bladder cancer. *BJUI Compass*. 2024;5(11):1090-1094. [\[Crossref\]](#)
5. Ogreden E, Oguz U, Demirelli E, et al. The role of multiparametric magnetic resonance imaging in the diagnosis of granulomatous prostatitis mimicking prostate cancer. *Abdom Radiol (NY)*. 2024;49(7):2305-2310. [\[Crossref\]](#)
6. Han C, Zhu L, Liu X, Ma S, Liu Y, Wang X. Differential diagnosis of uncommon prostate diseases: combining mpMRI and clinical information. *Insights Imaging*. 2021;12(1):79. [\[Crossref\]](#)
7. Dickinson L, Ahmed HU, Allen C, et al. Magnetic resonance imaging for the detection, localisation, and characterisation of prostate cancer: recommendations from a European consensus meeting. *Eur Urol*. 2011;59(4):477-494. [\[Crossref\]](#)
8. Turkbey B, Rosenkrantz AB, Haider MA, et al. Prostate imaging reporting and data system version 2.1: 2019 update of prostate imaging reporting and data system version 2. *Eur Urol*. 2019;76(3):340-351. [\[Crossref\]](#)
9. Suzuki T, Takeuchi M, Naiki T, et al. MRI findings of granulomatous prostatitis developing after intravesical Bacillus Calmette-Guérin therapy. *Clin Radiol*. 2013;68(6):595-599. [\[Crossref\]](#)
10. Kitzing YX, Prando A, Varol C, Karczmar GS, Maclean F, Oto A. Benign conditions that mimic prostate carcinoma: MR imaging features with histopathologic correlation. *Radiographics*. 2016;36(1):162-175. [\[Crossref\]](#)
11. Oppenheimer JR, Kahane H, Epstein JI. Granulomatous prostatitis on needle biopsy. *Arch Pathol Lab Med*. 1997;121(7):724-729. [\[Crossref\]](#)
12. Logan JK, Walton-Diaz A, Rais-Bahrami S, et al. Changes observed in multiparametric prostate magnetic resonance imaging characteristics correlate with histopathological development of chronic granulomatous prostatitis after intravesical Bacillus Calmette-Guérin therapy. *J Comput Assist Tomogr*. 2014;38(2):274-276. [\[Crossref\]](#)
13. Shukla P, Gulwani HV, Kaur S. Granulomatous prostatitis: clinical and histomorphologic survey of the disease in a tertiary care hospital. *Prostate Int*. 2017;5(1):29-34. [\[Crossref\]](#)
14. Bertelli E, Zantonelli G, Cinelli A, et al. Granulomatous prostatitis, the great mimicker of prostate cancer: can multiparametric MRI features help in this challenging differential diagnosis? *Diagnostics (Basel)*. 2022;12(10):2302. [\[Crossref\]](#)
15. Bour L, Schull A, Delongchamps NB, et al. Multiparametric MRI features of granulomatous prostatitis and tubercular prostate abscess. *Diagn Interv Imaging*. 2013;94(1):84-90. [\[Crossref\]](#)
16. Naik KS, Carey BM. The transrectal ultrasound and MRI appearances of granulomatous prostatitis and its differentiation from carcinoma. *Clin Radiol*. 1999;54(3):173-175. [\[Crossref\]](#)
17. Ma W, Kang SK, Hricak H, Gerst SR, Zhang J. Imaging appearance of granulomatous disease after intravesical Bacille Calmette-Guerin (BCG) treatment of bladder carcinoma. *AJR Am J Roentgenol*. 2009;192(6):1494-1500. [\[Crossref\]](#)
18. Weinreb JC, Barentsz JO, Choyke PL, et al. PI-RADS Prostate imaging - reporting and data system: 2015, version 2. *Eur Urol*. 2016;69(1):16-40. [\[Crossref\]](#)
19. Rais-Bahrami S, Nix JW, Turkbey B, et al. Clinical and multiparametric MRI signatures of granulomatous prostatitis. *Abdom Radiol (NY)*. 2017;42(7):1956-1962. [\[Crossref\]](#)
20. Rodríguez Cabello MA, Méndez Rubio S, Vázquez Alba D, Aulló González C, Platas Sancho A. Effect of Bacillus Calmette-Guerin exposure on prostate cancer detection using magnetic resonance imaging: a cohort study. *Clin Genitourin Cancer*. 2024;22(5):102130. [\[Crossref\]](#)
21. Green DB, Kawashima A, Menias CO, et al. Complications of Intravesical BCG immunotherapy for bladder cancer. *Radiographics*. 2019;39(1):80-94. [\[Crossref\]](#)
22. Kawada H, Kanematsu M, Goshima S, et al. Multiphase contrast-enhanced magnetic resonance imaging features of Bacillus Calmette-Guerin-induced granulomatous prostatitis in five patients. *Korean J Radiol*. 2015;16(2):342-348. [\[Crossref\]](#)
23. Lee S, Oh YT, Kim HM, Jung DC, Hong H. Imaging patterns of Bacillus Calmette-Guérin-related granulomatous prostatitis based on multiparametric MRI. *Korean J Radiol*. 2022;23(1):60-67. [\[Crossref\]](#)
24. Wang Z, Han C, Xu Y, et al. The role of prostate-specific antigen and multiparametric magnetic resonance imaging in the diagnosis of granulomatous prostatitis induced by intravesical Bacillus Calmette-Guérin vaccine therapy in patients with nonmuscle invasive bladder cancer. *J Cancer Res Ther*. 2021;17(3):625-629. [\[Crossref\]](#)
25. Lim J, Yu JS, Hong SW, Chung JJ, Kim JH, Kim KW. A case of mass-forming splenic tuberculosis: MRI findings with emphasis of diffusion-weighted imaging characteristics. *J Korean Med Sci*. 2011;26(3):457-460. [\[Crossref\]](#)
26. Guerra J, Pina JM, Andrade V, Lança M, Campos Pinheiro L. Bacillus Calmette-Guérin instillations may mimic prostate cancer on multiparametric magnetic resonance imaging. *Cureus*. 2024;16(9):e69890. [\[Crossref\]](#)
27. Chung MH, Lee HG, Kwon SS, Park SH. MR imaging of solitary pulmonary lesion: emphasis on tuberculomas and comparison with tumors. *J Magn Reson Imaging*. 2000;11(6):629-637. [\[Crossref\]](#)
28. Sze G, Zimmerman RD. The magnetic resonance imaging of infections and inflammatory diseases. *Radiol Clin North Am*. 1988;26(4):839-859. [\[Crossref\]](#)



Magnetic resonance T1p relaxation in patients with liver fibrosis: a systematic review and meta-analysis

✉ Xiaoyu Liu^{1,2}
 ✉ Yinzhen Wang²
 ✉ Caihua Xu³
 ✉ Yixiang Li^{1,2}
 ✉ Junqiang Lei^{1,2}

¹Lanzhou University, Department of First Clinical Medical College, Lanzhou, China

²First Hospital of Lanzhou University, Department of Radiology, Lanzhou, China

³Lanzhou University School of Basic Medical Sciences, Evidence-Based Medicine Center, Lanzhou, China

PURPOSE

This study aimed to evaluate the diagnostic performance of T1p relaxation in distinguishing patients with liver fibrosis (LF) from those without.

METHODS

A systematic review was conducted using PubMed, EMBASE, Cochrane, and Web of Science databases up to February 2025 to identify studies assessing T1p for LF diagnosis.

RESULTS

Eleven studies involving 792 patients were included. T1p values were significantly higher in cirrhotic versus normal livers [weighted mean difference (WMD): 6.69, $P < 0.001$], and in fibrotic versus normal livers (WMD: 7.17, $P = 0.006$). Patients with Child-Pugh classes A, B, and C showed significantly higher T1p values compared with normal liver ($P < 0.001$). T1p values in LF stages F1–F3 were not significantly different from normal liver ($P = 0.18$), but stage F4 showed significant differences (WMD: 10.48, $P = 0.02$).

CONCLUSION

T1p relaxation differentiates high-grade LF from normal liver tissue.

CLINICAL SIGNIFICANCE

As a non-invasive imaging technique, T1p shows potential for use in the diagnosis and follow-up of LF and to optimize the assessment and management of chronic liver disease.

KEYWORDS

Liver fibrosis, cirrhosis, imaging biomarker, meta-analysis, T1p relaxation

Corresponding author: Junqiang Lei

E-mail: leijq2011@126.com

Received 06 March 2025; revision requested 18 May 2025; last revision received 11 June 2025; accepted 28 June 2025.



Epub: 22.09.2025

Publication date: 02.01.2026

DOI: 10.4274/dir.2025.253325

Liver fibrosis (LF) progression occurs in almost all cases of chronic liver disease (CLD) and represents the most common consequence of these conditions.¹ During the healing process, excessive protein deposition in the extracellular matrix leads to scarring that connects the adjacent portal triad to the central vein, ultimately resulting in cirrhosis.^{2,3} The main clinical manifestations of cirrhosis include impaired liver function, portal hypertension, and the development of hepatocellular carcinoma.^{4–6} End-stage LF is typically considered irreversible, with limited effective treatment options; however, complications of early or intermediate stages are often treatable.^{2,7–9} Therefore, early LF detection and accurate staging are crucial for therapeutic decisions and prognosis determination.

Currently, liver biopsy serves as the gold standard for LF diagnosis, but its clinical adoption is limited due to its highly invasive nature, variability in patient and physician acceptance, risk of serious complications, and potential sampling errors.^{10–12} Consequently, non-invasive imaging techniques such as magnetic resonance (MR) elastography and ultrasound elastography have been developed to assess hepatic fibrosis.^{13–15} However, MR elastography requires specific hardware and software, and ultrasound elastography is operator-dependent and less repro-

You may cite this article as: Liu X, Wang Y, Xu C, Li Y, Lei J. Magnetic resonance T1p relaxation in patients with liver fibrosis: a systematic review and meta-analysis. *Diagn Interv Radiol*. 2026;32(1):16–24.

ducible.¹⁴⁻¹⁷ Therefore, there is a clear clinical need for a simpler, more objective method to non-invasively assess LF staging.

$T1\rho$ refers to the spin-lattice relaxation time (ms) constant in the rotating coordinate frame, which describes the decay of transverse magnetization under a spin-locked radiofrequency field.^{18,19} As $T1\rho$ is sensitive to the macromolecular components of the tissue, $T1\rho$ MR imaging shows potential for evaluating LF.²⁰⁻²⁴ This meta-analysis aims to assess the diagnostic value of $T1\rho$ in patients with CLD.

Methods

This systematic evaluation followed the Preferred Reporting Items for Systematic Evaluation and Meta-Analysis (PRISMA) guidelines^{25,26} and was registered with PROSPERO (ID: CRD42024498897). Ethics approval and informed consent were not required, as systematic reviews synthesize and summarize existing literature rather than directly involving human or animal participants.

Literature search

Databases searched included PubMed, Cochrane Library, Web of Science, and Embase initially up to October 2023, using the search terms "liver" OR "hepatic" OR "hepar" AND "T1rho mapping" OR "T1rho relaxation" OR "T1ρ mapping" OR "T1ρ relaxation" (Supplementary file 1). Reference lists of all eligible studies were also screened for additional relevant publications. The search was updated in February 2025 in the same databases, and the results were screened according to the inclusion criteria.

Study selection

Eligible studies included English-language publications reporting liver $T1\rho$ relaxation times and featuring at least two participant groups, one of which had cirrhosis or

LF. Specific inclusion criteria were 1) patients with a definitive diagnosis of cirrhosis or hepatic fibrosis via pathological or clinical evaluation, 2) reported liver $T1\rho$ values, and 3) a control group consisting of healthy individuals or patients without hepatic fibrosis. Exclusion criteria were 1) articles lacking valid data, 2) duplicate publications, 3) non-original research, and 4) non-English language literature. Two reviewers independently screened all titles and abstracts identified by the search. Articles judged eligible by at least one reviewer were retrieved as full-text manuscripts for further evaluation. Articles meeting the inclusion criteria after full-text review were included in the review. Conflicts of opinion at any stage were resolved through consensus.

Data extraction

Two investigators independently extracted the following data from the included literature: $T1\rho$ relaxation times for cirrhosis and LF (combined if liver function grading or pathological stage grading was reported separately for cirrhosis), authors, year of publication, study design type, number of patients, mean age, MR imaging (MRI) hardware, pulse sequence and parameters, Child-Pugh classification²⁷ or pathological stage grading, $T1\rho$ relaxation time, and standard deviation. When data were unclear or unavailable, the original authors were contacted via email. If no response was received, data were extracted from charts, if available.

Quality assessment

Two researchers evaluated the quality of the included literature using the Newcastle-Ottawa Scale (NOS)²⁸ quality assessment tool for observational studies as recommended in the Cochrane Handbook. The NOS scale includes two scales for assessing cohort and case-control study quality, covering study population selection, comparability, and exposure or outcome assessment. Each study was scored on a scale from 0 to 9. A score of ≥ 6 was considered indicative of high quality, whereas studies scoring ≤ 3 were regarded as low quality and were excluded from the analysis due to critical methodological limitations. Higher scores reflected higher study quality. Any disagreement between the two investigators was resolved through discussion, with a third researcher acting as final arbiter if necessary.

Statistical analysis

Statistical analysis was performed using Review Manager 5.4 (Cochrane), and

the results were compared using pooled estimates of weighted mean differences (WMDs) and 95% confidence intervals (CIs) for the MRI component data, with $P < 0.05$ deemed statistically significant. Sensitivity analyses and publication bias assessments were performed using Stata 15.0 (StataCorp LLC). In calculating the combined effect sizes, we weighted all WMDs according to the sample size of the respective studies. For the $T1\rho$ relaxation time, WMD was calculated as the difference between a normal liver and patients with cirrhosis or LF divided by the pooled standard deviation. The heterogeneity of the results was verified using the Q-test and I^2 statistic.²⁸ $P \geq 0.01$ and $I^2 < 50\%$ indicated low statistical heterogeneity among study results, warranting the use of a fixed-effects model for meta-analysis; conversely, higher statistical heterogeneity supported a random-effects model. Potential sources of heterogeneity (methodological, statistical, or clinical) were analyzed, with subgroup analyses conducted as appropriate. Descriptive analysis was used if the heterogeneity between groups was too large or not easily combined clinically. Positive values indicated patients with prolonged $T1\rho$ relaxation times. Publication bias was assessed using Egger's test, with $P > 0.1$ suggesting no significant bias. The robustness of the pooled results was tested with leave-one-out sensitivity analyses: each study was sequentially excluded from the meta-analysis, and the pooled WMD and I^2 were recalculated. The results were considered stable if the recalculated WMD remained within the 95% CI of the overall effect estimate, and the I^2 value did not fluctuate by more than 10% compared with the original value.

Results

Study selection and article screening

An initial search was conducted in October 2023 and updated in February 2025 by two researchers who each developed a search strategy. The initial search yielded 231 potentially eligible documents. After removing 99 duplicates, 132 titles and abstracts were screened, and 45 of these were excluded. After full-text review, another 76 documents were excluded (22 reviews, commentaries, or editorials; 39 animal experiments; 12 irrelevant articles; and 3 with no available data). The updated search did not identify any additional eligible publications. Ultimately, 11 articles²⁹⁻³⁹ with a total of 792 participants were included. The literature screening flowchart is shown in Figure 1.

Main points

- This study constitutes a pioneering advancement as the first systematic review and meta-analysis assessing the diagnostic efficacy of magnetic resonance imaging $T1\rho$ relaxation for liver fibrosis (LF).
- This meta-analysis concludes that $T1\rho$ can identify LF in patients with chronic liver disease, providing a new idea for non-invasive assessment of LF.
- Differences and limitations should be noted when using biomarker imaging to diagnose disease.

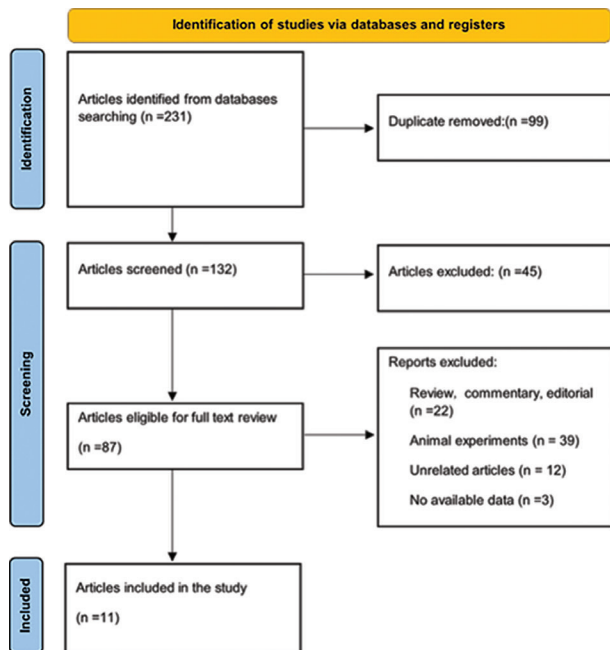


Figure 1. The PRISMA flowchart quantifies the studies accepted and rejected within the different review stages and explains the reasons for the different review stage.

Study characteristics

The characteristics of all included studies are shown in Tables 1 and 2. $T1\mu$ values were reported as outcome metrics in all 11 studies, with six assessing $T1\mu$ values in patients with cirrhosis, six in patients with fibrosis, and one reporting both Child–Pugh scores and $T1\mu$ values corresponding to their pathological classifications.

Quality assessment

All 11 articles included were case–control studies. Six were high-quality articles and five were medium-quality articles, as shown in Supplementary Table 1.

Descriptive analysis

Of the 11 studies, nine observed a significant increase in $T1\mu$ relaxation times in pa-

tients with fibrosis or cirrhosis compared with normal liver. Specifically, all six studies evaluating cirrhosis reported significantly longer $T1\mu$ relaxation times, and four of the six studies assessing patients with LF reported significantly longer $T1\mu$ relaxation times. Supplementary Table 2 provides the individual P values and Z-scores derived from forest plots.

Meta-analysis

Data on $T1\mu$ values from patients with cirrhosis or LF were collected, and the combined WMD forest plots are shown in Figures 2 and 3, respectively. The differences between the two groups were statistically significant: cirrhosis group WMD: 6.69 [95% CI (4.14, 9.25); $P < 0.001$; Figure 2] and LF group WMD: 7.17 [95% CI (2.08, 12.26); $P = 0.006$; Figure 3].

Subgroup analysis

Two subgroup analyses were performed to assess the impact of disease severity. Statistically significant differences in $T1\mu$ values were observed in patients with cirrhosis with different Child–Pugh scores when compared with controls: Child–Pugh stage A WMD 4.73 [95% CI (2.26, 7.20); $P < 0.001$], Child–Pugh stage B WMD 9.17 [95% CI (7.21, 11.13); $P < 0.001$], and Child–Pugh stage C WMD 15.97 [95% CI (9.30, 22.64); $P < 0.001$] (Figure 4). Comparison of $T1\mu$ values of patients with different fibrosis stages showed no significant difference for stages F1–F3 [WMD: 4.38; 95% CI (−2.04, 10.80); $P = 0.18$]. However, stage F4 showed a significant increase [WMD: 10.48; 95% CI (1.61, 19.36); $P = 0.02$] (Figure 5). We also analyzed the difference in $T1\mu$ values between patients with stage F1 fibrosis and healthy controls. Although the mean $T1\mu$ values were higher in the F1 group, the difference was not statistically significant [WMD: 3.06, 95% CI (−1.39, 7.51); $P = 0.18$].

Publication bias

Egger's test showed no significant publication bias for either the cirrhosis or fibrosis meta-analyses.

Sensitivity analysis

Leave-one-out sensitivity analyses showed that removing individual studies did not significantly impact the results, affirming the stability and reliability of the random-effects calculations. In addition, I^2 values varied by no more than 5% across all recalculated models, indicating that no single study exerted undue influence on the overall results. Detailed results are presented in Supplementary Figures 1 and 2, and the corresponding I^2 values are shown in Supplementary Tables 3, 4.

Table 1. Description of studies included in the systematic review

Study	Country	Duration of patient recruitment	Age (mean/range)	Gender	Study design	Reference standard	Disease spectrum
Chen et al. ³⁵ 2018	China	2014.03–2016.11	Patient: 51 (28–75) Control: 38 (23–64)	16 F/17 M 9 F/24 M	Prospective	Clinical	HBV, HCV, ALD
Allkemper et al. ²⁹ 2014	Germany	2012.07–2013.07	Patient: 59.7 (28–74) Control: 49 (29–76)	12 F/22 M 9 F/16 M	Prospective	Pathology	HCV, ALD, NASH, AIH, unknown
Takayama et al. ³⁹ 2022	Japan	2015.10–2018.07	73.8 (22–86)	29 F/53 M	Retrospective	Pathology	HBV, HCV, ALD, NASH, AIH, glycogenosis, Non-B/C hepatitis, unknown
Singh et al. ³¹ 2015	India	NA	Patient: 40–70 Control: 27–65	NA	Prospective	Pathology	HCV

Table 1. Continued

Study	Country	Duration of patient recruitment	Age (mean/range)	Gender	Study design	Reference standard	Disease spectrum
Takayama et al. ³² 2014	Japan	2012.05–2013.07	65.2 (35–86)	18 F/35 M	Retrospective	Pathology	HBV, HCV, ALD, NAFLD, AIH, NASH, PBC, unknow
Xie et al. ³⁴ 2017	China	2015.07–2016.03	Patient: 41.7 (21–63) Control: 51.8 (35–74)	5 F/13 M 5F/13 M	Prospective	Clinical	HBV
Hou et al. ³⁸ 2022	China	2019.04–2019.10	58	NA	Retrospective	Pathology	NAFLD
Suyama et al. ³⁷ 2021	Japan	2016.07–2017.01	Patient: 68 (36–87) Control: 30 (26–46)	NA	Prospective	Clinical	HBV, HCV, AIH, NAFLD, ALD
Rauscher et al. ³⁰ 2014	Germany	2012.01–2012.11	Patient: 56.6 (23–80) Control: 42.7 (27–65)	NA 6 F/4 M	NA	Clinical	HBV, HCV, ALD
Yang et al. ³³ 2016	China	2014.03–2015.11	Patient: 48.47 (34–70) Control: 41.44 (22–64)	3 F/14 M 19 F/21 M	NA	Pathology	HBV, HCV, ALD
Stief 2019	Germany	2016.05–2017.03	65.2 (23–88)	129 F/84 M	Retrospective	Clinical	NA

HBV, hepatitis B virus; HCV, hepatitis C virus; ALD, alcoholic liver disease; NAFLD, non-alcoholic fatty liver disease; NASH, non-alcoholic steatohepatitis; AIH, autoimmune hepatitis; PBC, primary biliary cholangitis; F, female; M, male; NA, not available.

Table 2. Description of studies included in the systematic review

Study	Scanner	TSL/frequency	Coil	TR/TE	Slices of T1ρ sequence	Shape of ROIs	Location of ROIs	Breath-control technique
Chen et al. ³⁵ 2018	3.0 T Philips	0, 10, 20, 40, 60/500	16-Ch sense XL Torso	5.1/2.55	NA	NA	Eight functionally independent segments	Respiratory-triggered 3D whole-liver coverage sequence
Allkemper et al. ²⁹ 2014	1.5T Philips	10, 20, 40, 80/500	16-Ch Torso	9.1/4.6	26	Circle	Liver parenchyma	Respiratory belt
Takayama et al. ³⁹ 2022	3.0 T Philips	0, 20, 40, 60/500	32-Ch Torso-cardiac phased-array	1.6/5.4	3	Polygonal regions	Liver parenchyma	Breath-hold
Singh et al. ³¹ 2015	1.5T Siemens	0, 10, 20, 30/500	Body and spine array	5.1/2.4	1	NA	Liver parenchyma	Breath-hold
Takayama et al. ³² 2014	3.0 T Philips	1, 20, 40, 60/500	32-Ch Torso-cardiac phased-array	2.1/0.98	3	Circle; oval	Right lobe or segment IV of the left lobe	Breath-hold
Xie et al. ³⁴ 2017	3.0 T Philips	1, 10, 20, 30, 40, 50/500	16-Ch phased-array	3.8/1.82	8		Left lobes; right lobes	Breath-hold
Hou et al. ³⁸ 2022	3.0 T Philips	0, 10, 30, 50/NA	Invivo 32-Ch cardiac	2000/20	3	NA	Liver parenchyma	Breath-hold
Suyama et al. ³⁷ 2021	3.0 T Philips	0, 10, 20, 40, 60/1000	32-Ch torso	4.3/2.2	11	Focal	Right lobe	Breath-hold
Rauscher et al. ³⁰ 2014	1.5T Siemens	4, 8, 16, 32, 48/NA	body and spine matrix	3/1.31	1	Circle/irregular	Right lobe	Breath-hold
Yang et al. ³³ 2016	3.0 T Philips	1, 27, 54/500	16-Ch sense XL torso	2.1/1.02	3	Oval	NA	Breath-hold
Stief et al. ³⁶ 2019	1.5T Siemens	0, 10, 20, 30, 40, 50/500	One-Ch body coil and 8-Ch surface coils	5.1/2.4	2	Circle	Right lobe	NA

TSL, time of spin-lock; TR, repetition time; TE, echo time; Ch, channel; ROI, region of interest; NA, not available.

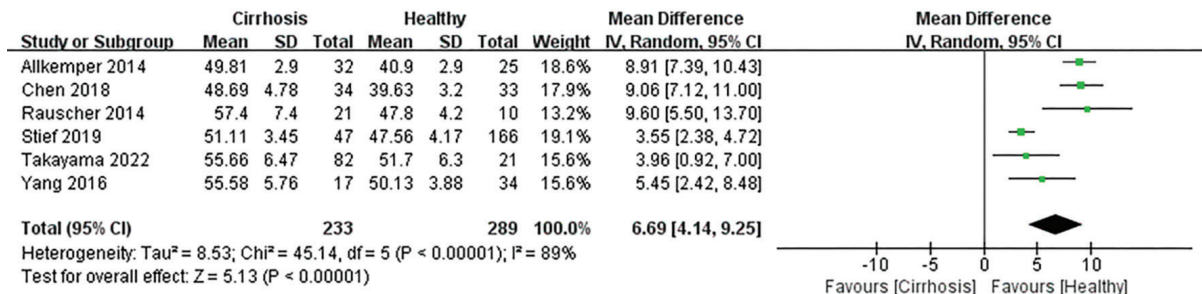


Figure 2. Forest plot showing individual differences and pooled mean standard deviation of T1p relaxation times (ms) in healthy controls and patients with cirrhosis. CI, confidence interval; SD, standard deviation; IV, inverse variance.

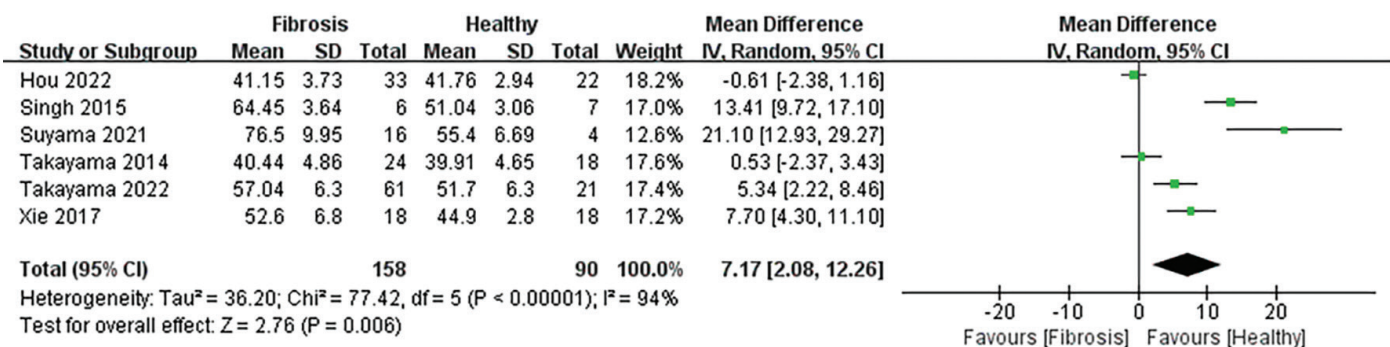


Figure 3. Forest plot showing individual differences and pooled mean standard deviation of T1p relaxation times (ms) for healthy controls and patients with fibrosis. CI, confidence interval; SD, standard deviation; IV, inverse variance.

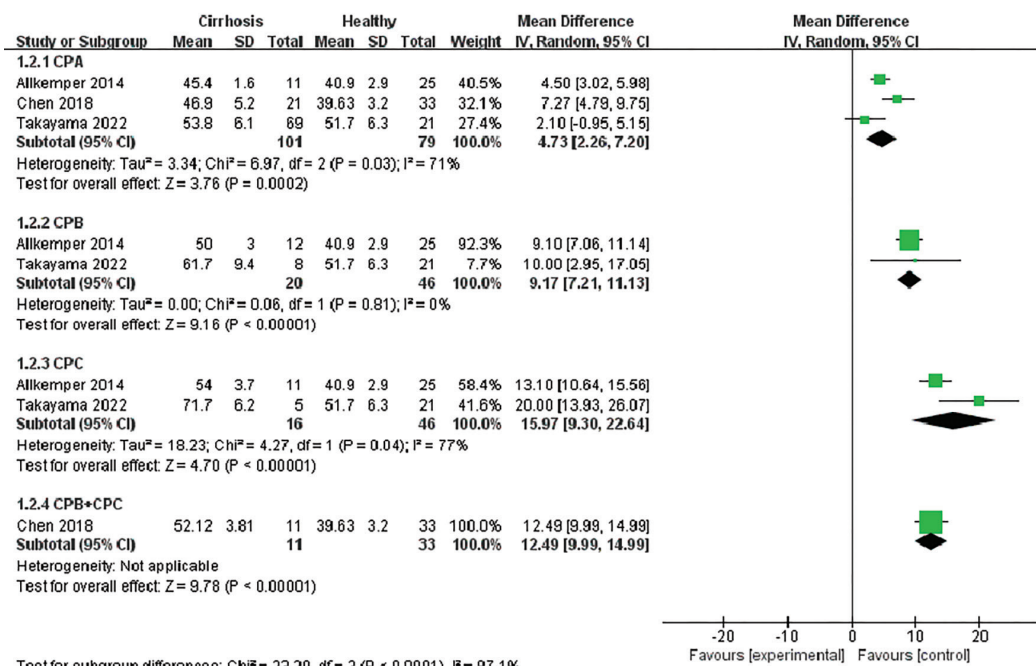


Figure 4. Forest plots showing individual differences in T1p relaxation times (ms) and pooled mean standard deviations for healthy controls and patients with cirrhosis with different Child-Pugh scores. SD, standard deviation; CI, confidence interval; CPA, Child-Pugh A; CPB, Child-Pugh B; CPC, Child-Pugh C; IV, inverse variance.

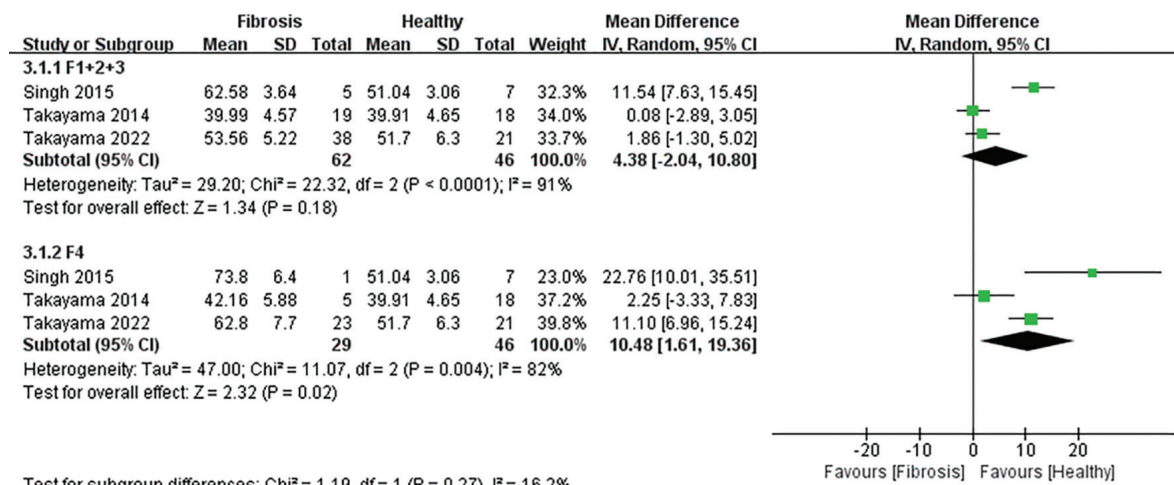


Figure 5. Forest plots showing individual differences in T1p relaxation times (ms) and pooled mean standard deviations for healthy controls and patients with different degrees of liver fibrosis. CI, confidence interval; IV, inverse variance; SD, standard deviation.

Discussion

Cirrhosis represents the advanced stage of various CLDs, and several imaging techniques facilitate direct diagnosis and staging of LF, including state or shear wave elastography, perfusion or dual-energy computed tomography, liver-specific contrast-enhanced MRI, diffusion-weighted MRI, and MR elastography.⁴⁰⁻⁴⁵ T1p imaging, an emerging imaging technique, is currently used to detect macromolecular levels, and its diagnosis of LF may depend on the overall loss of macromolecule content and an increase in water fraction.⁴⁶ Our study, based on data from 11 studies involving 792 participants, showed that T1p relaxation time was effective in differentiating between normal livers and patients with LF. These findings align with previous animal studies⁴⁷⁻⁵⁰ and underscore the potential of T1p values in reflecting the severity of LF.

The results of the subgroup analyses further indicated that T1p relaxation times showed a significant advantage in differentiating between varying degrees of cirrhosis as the disease progressed. Specifically, there was a significant difference between T1p values for cirrhosis across Child–Pugh stages compared with normal liver, and this difference increased with higher Child–Pugh scores. Furthermore, in the comparison of different fibrosis stages, although patients in stages F1–F3 did not show statistically significant differences, in stage F4 (i.e., advanced LF or cirrhosis), the difference in T1p values was statistically significant. Multiple subgrouping strategies were attempted—including by individual fibrosis stages and early (F1–2) versus advanced (F3–4) groupings—but most

comparisons did not reach statistical significance due to limited data and high variability. Therefore, stages F1–3 were combined to examine overall T1p trends in early-to-moderate fibrosis.

The Child–Pugh classification for assessing liver reserve function in cirrhosis evaluates the overall functional status of the liver based on five clinical and biochemical parameters (bilirubin, albumin, coagulation time, ascites, and hepatic encephalopathy), whereas LF responds to histological alterations of the liver only. Previous studies have reported a negative correlation between T1p and liver iron concentration (LIC), suggesting that LIC may confound T1p measurements.^{51,52} Moreover, changes in T1p values do not always directly reflect structural changes in hepatic tissues,^{53,54} indicating that T1p values are sensitive to a wide range of biological and physical factors. T1p values may also be affected by unknown factors, such as inflammation, venous congestion, or lymphoedema, all of which could alter T1p signals, leading to increased differences in T1p signals in various regions of the liver, thus affecting fibrosis assessment. In addition, comorbidities such as diabetes and obesity may also interfere with the interpretation of the T1p signal, further increasing the variability of the signal. Therefore, more studies are needed to understand the effect of LF on liver T1p values.

One strength of this study is that it is the first meta-analysis of the effectiveness of T1p in differentiating normal liver from CLD-related fibrosis, conducted in accordance with established guidelines for systematic reviews and meta-analyses.²⁵ This included consensus among multiple reviewers at each step

of the literature search, study selection, and data extraction; quality assessment of the studies; publication bias assessment and adjustment; and preplanned meta-analyses, including sensitivity analyses based on a priori assumptions in the event of substantial heterogeneity. However, the analysis encountered high heterogeneity among the included studies (>50% for the primary outcome), with the source of this heterogeneity remaining unidentified despite subgroup analyses. Moreover, the limited number of T1p studies on LF and small sample sizes further emphasize the need for additional research to strengthen confidence in the results.

Considerable variation was noted between MRI methods in the included studies, including scanners, coils, software, and pulse sequences, all of which can affect T1p relaxation. In this review alone, two brands of scanners, two magnet strengths, and seven different coils were identified (Table 2). Choice of pulse sequence can also significantly affect relaxation time, with a difference of as much as 10 ms observed across commonly used sequences.^{55,56} Post-processing and segmentation can also affect T1p values, such as how the assessor defines the region of interest (ROI), differences in the ROI between studies, the number of slices included in the ROI,⁵⁷ the proximity of the border to other tissues, and partial volume effects.⁵⁸ Continued use of the recommended standardized terminology and ROI definitions will improve the comparability of ROIs across studies and study sites.⁵⁹ This study identified substantial differences in methods across testing sites, suggesting that considerable caution should be adopted when making comparisons across studies and highlighting

the limitations in the current state of T1p relaxation as an imaging biomarker.

Improving the reliability of compositional MRI as an imaging biomarker requires comparability across scanners and research institutions. The results of this study support current international efforts by researchers and vendors to improve sequencing, calibration, and standardization,⁶⁰ for example, the use of a calibration phantom to develop calibration functions to account for the different hardware and software used in different institutions.^{60,61} Meanwhile, the findings from this study suggest that the future use of MRI component measurements as potential biomarkers would benefit from a deeper understanding of the impact of different testing methods and more standardization of data collection and analysis methods.^{62,63}

Although this study provides a systematic analysis of the effectiveness of hepatic fibrosis detection with T1p by integrating the existing literature, there are still some limitations. First, the small number of original studies included limits our ability to draw more generalizable conclusions. Second, the different studies involved different groups of patients who varied in disease severity, LF etiology, age, and gender ratio, which may have affected T1p performance and thus the generalizability of the results. Third, the imaging parameters used in different studies (different settings of the T1p imaging sequence, different models of imaging equipment, different breathing control techniques, location of the ROIs, etc.) may have also contributed to the heterogeneity of the results.

The significant heterogeneity observed in the combined effect size of T1p relaxation times underscores the need for further investigation, particularly on the impact of different CLD stages. Subgroup analyses hint at varying degrees of heterogeneity across LF stages, suggesting the need for standardized assessment criteria and additional prospective studies to minimize bias and validate the diagnostic utility of T1p for LF staging. Although T1p values exhibited slight differences across fibrosis stages, they demonstrated limited ability to differentiate early-stage fibrosis from a normal liver, yet hold promise in differentiating F4 stage fibrosis from cirrhosis. This limitation is likely due to the subtle histological changes present in early-stage fibrosis, which may be below the detection threshold of T1p mapping techniques. At stages F1–F3, collagen deposition and extracellular matrix remodeling remain relatively limited, leading to only minor alterations in tissue macromolecular content and

water interaction that may not significantly affect T1p relaxation times. This observation is consistent with prior studies using MR elastography and diffusion-weighted MRI, which have also demonstrated reduced sensitivity in differentiating early-stage LF.^{64,65}

In conclusion, based on these results, hepatic T1p relaxation measurements show great potential in identifying LF in patients with CLD. This study provides a more plausible scientific basis for the validity of T1p for detecting LF and a new idea for the non-invasive assessment of LF.

Footnotes

Conflict of interest disclosure

The authors declared no conflicts of interest.

Acknowledgments

The authors thank all investigators and supporters involved in this study. This work was supported by the Health Industry Scientific Research Program of Gansu Province (GSWSKY2023-10).

Supplementary: <https://d2v96fxpocvxx.cloudfront.net/51ec7646-9122-48c7-1d99-90e9cb16981b/content-images/b0ff08a2-ecaa-4d23-bb16-25e503ca9f5a.pdf>

References

1. Tsouchatzis EA, Bosch J, Burroughs AK. Liver cirrhosis. *Lancet*. 2014;383(9930):1749-1761. [\[Crossref\]](#)
2. Wallace K, Burt AD, Wright MC. Liver Fibrosis. *Biochem J*. 2008;411(1):1-18. [\[Crossref\]](#)
3. Su TH, Kao JH, Liu CJ. Molecular mechanism and treatment of viral hepatitis-related liver fibrosis. *Int J Mol Sci*. 2014;15(6):10578-10604. [\[Crossref\]](#)
4. D'Amico G, Garcia-Tsao G, Pagliaro L. Natural history and prognostic indicators of survival in cirrhosis: a systematic review of 118 studies. *J Hepatol*. 2006;44(1):217-231. [\[Crossref\]](#)
5. Sebastiani G, Gkouvatsos K, Pantopoulos K. Chronic hepatitis C and liver fibrosis. *World J Gastroenterol*. 2014;20(32):11033-11053. [\[Crossref\]](#)
6. Friedman SL. Hepatic fibrosis -- overview. *Toxicology*. 2008;254(3):120-129. [\[Crossref\]](#)
7. Schuppan D, Afdhal NH. Liver cirrhosis. *Lancet*. 2008;371(9615):838-851. [\[Crossref\]](#)
8. Marcellin P, Gane E, Buti M, et al. Regression of cirrhosis during treatment with tenofovir disoproxil fumarate for chronic hepatitis B: a 5-year open-label follow-up study. *Lancet*. 2013;381(9865):468-475. [\[Crossref\]](#)
9. Chang TT, Liaw YF, Wu SS, et al. Long-term entecavir therapy results in the reversal of fibrosis/cirrhosis and continued histological improvement in patients with chronic hepatitis B. *Hepatology*. 2010;52(3):886-893. [\[Crossref\]](#)
10. Janes CH, Lindor KD. Outcome of patients hospitalized for complications after outpatient liver biopsy. *Ann Intern Med*. 1993;118(2):96-98. [\[Crossref\]](#)
11. Regev A, Berho M, Jeffers LJ, et al. Sampling error and intraobserver variation in liver biopsy in patients with chronic HCV infection. *Am J Gastroenterol*. 2002;97(10):2614-2618. [\[Crossref\]](#)
12. Cadranel JF, Rufat P, Degos F. Practices of liver biopsy in France: results of a prospective nationwide survey. For the Group of Epidemiology of the French Association for the Study of the Liver (AFEF). *Hepatology*. 2000;32(3):477-481. [\[Crossref\]](#)
13. Manduca A, Oliphant TE, Dresner MA, et al. Magnetic resonance elastography: non-invasive mapping of tissue elasticity. *Med Image Anal*. 2001;5(4):237-254. [\[Crossref\]](#)
14. Boll DT, Merkle EM. Diffuse liver disease: strategies for hepatic CT and MR imaging. *Radiographics*. 2009;29(6):1591-1614. [\[Crossref\]](#)
15. Yoshioka K, Hashimoto S. Can non-invasive assessment of liver fibrosis replace liver biopsy? *Hepatol Res*. 2012;42(3):233-240. [\[Crossref\]](#)
16. Arda K, Ciledag N, Aktas E, Aribas BK, Kose K. Quantitative assessment of normal soft-tissue elasticity using shear-wave ultrasound elastography. *AJR Am J Roentgenol*. 2011;197(3):532-536. [\[Crossref\]](#)
17. Yin M, Chen J, Glaser KJ, Talwalkar JA, Ehman RL. Abdominal magnetic resonance elastography. *Top Magn Reson Imaging*. 2009;20(2):79-87. [\[Crossref\]](#)
18. Deng M, Zhao F, Yuan J, Ahuja AT, Wang YX. Liver T1p MRI measurement in healthy human subjects at 3 T: a preliminary study with a two-dimensional fast-field echo sequence. *Br J Radiol*. 2012;85(1017):590-595. [\[Crossref\]](#)
19. Wang YX, Yuan J, Chu ES, et al. T1rho MR imaging is sensitive to evaluate liver fibrosis: an experimental study in a rat biliary duct ligation model. *Radiology*. 2011;259(3):712-719. [\[Crossref\]](#)
20. Duvvuri U, Goldberg AD, Kranz JK, et al. Water magnetic relaxation dispersion in biological systems: the contribution of proton exchange and implications for the noninvasive detection of cartilage degradation. *Proc Natl Acad Sci U S A*. 2001;98(22):12479-12484. [\[Crossref\]](#)
21. Haris M, McArdle E, Fenty M, et al. Early marker for Alzheimer's disease: hippocampus T1rho (T1rho) estimation. *J Magn Reson Imaging*. 2009;29(5):1008-1012. [\[Crossref\]](#)
22. Nestrasil I, Michaeli S, Liimatainen T, et al. T1rho and T2rho MRI in the evaluation of Parkinson's disease. *J Neurol*. 2010;257(6):964-968. [\[Crossref\]](#)

23. Nguyen AM, Johannessen W, Yoder JH, et al. Noninvasive quantification of human nucleus pulposus pressure with use of T1rho-weighted magnetic resonance imaging. *J Bone Joint Surg Am.* 2008;90(4):796-802. [\[Crossref\]](#)

24. Szyperski T, Luginbühl P, Otting G, Güntert P, Wüthrich K. Protein dynamics studied by rotating frame 15n spin relaxation times. *J Biomol NMR.* 1993;3(2):151-164. [\[Crossref\]](#)

25. Moher D, Liberati A, Tetzlaff J, Altman DG; PRISMA Group. Preferred reporting items for systematic reviews and meta-analyses: the PRISMA statement. *PLoS Med.* 2009;6:e1000097. [\[Crossref\]](#)

26. Wells GA, Wells G, Shea B, et al. The Newcastle-Ottawa Scale (Nos) for assessing the quality of nonrandomised studies in meta-analyses. 2014. [\[Crossref\]](#)

27. de Franchis R; Baveno VI Faculty. Expanding consensus in portal hypertension: Report of the Baveno VI Consensus Workshop: stratifying risk and individualizing care for portal hypertension. *J Hepatol.* 2015;63(3):743-752. [\[Crossref\]](#)

28. Higgins JP, Thompson SG, Deeks JJ, Altman DG. Measuring inconsistency in meta-analyses. *BMJ.* 2003;327(7414):557-560. [\[Crossref\]](#)

29. Allkemper T, Sagmeister F, Cincinnati V, et al. Evaluation of fibrotic liver disease with whole-liver T1r MR imaging: a feasibility study at 1.5 T. *Radiology.* 2014;271(2):408-415. [\[Crossref\]](#)

30. Rauscher I, Eiber M, Ganter C, et al. Evaluation of T1p as a potential MR biomarker for liver cirrhosis: comparison of healthy control subjects and patients with liver cirrhosis. *Eur J Radiol.* 2014;83(6):900-904. [\[Crossref\]](#)

31. Singh A, Reddy D, Haris M, et al. T1p MRI of healthy and fibrotic human livers at 1.5 T. *J Transl Med.* 2015;13:292. [\[Crossref\]](#)

32. Takayama Y, Nishie A, Asayama Y, et al. T1 P relaxation of the liver: a potential biomarker of liver function. *J Magn Reson Imaging.* 2015;42(1):188-195. [\[Crossref\]](#)

33. Yang Q, Yu T, Yun S, et al. Comparison of multislice breath-hold and 3d respiratory triggered T1 P imaging of liver in healthy volunteers and liver cirrhosis patients in 3.0 T MRI. *J Magn Reson Imaging.* 2016;44(4):906-913. [\[Crossref\]](#)

34. Xie S, Li Q, Cheng Y, et al. Impact of liver fibrosis and fatty liver on t1rho measurements: a prospective study. *Korean J Radiol.* 2017;18(6):898-905. [\[Crossref\]](#)

35. Chen W, Chen X, Yang L, et al. Quantitative assessment of liver function with whole-liver T1rho mapping at 3.0t. *Magn Reson Imaging.* 2018;46:75-80. [\[Crossref\]](#)

36. Stief JD, Haase M, Lüdemann L, et al. Combined morphological and functional liver MRI using spin-lattice relaxation in the rotating frame (T1p) in conjunction with gadoteric acid-enhanced MRI. *Sci Rep.* 2019;9:2083. [\[Crossref\]](#)

37. Suyama Y, Tomita K, Soga S, et al. T1p magnetic resonance imaging value as a potential marker to assess the severity of liver fibrosis: a pilot study. *Eur J Radiol Open.* 2021;8:100321. [\[Crossref\]](#)

38. Hou J, Wong VW, Qian Y, et al. Detecting early-stage liver fibrosis using macromolecular proton fraction mapping based on spin-lock MRI: preliminary observations. *J Magn Reson Imaging.* 2023;57(2):485-492. [\[Crossref\]](#)

39. Takayama Y, Nishie A, Ishimatsu K, et al. Diagnostic Potential of T1p and T2 relaxations in assessing the severity of liver fibrosis and necro-inflammation. *Magn Reson Imaging.* 2022;87:104-112. [\[Crossref\]](#)

40. Tsochatzis EA, Gurusamy KS, Ntaoula S, Cholongitas E, Davidson BR, Burroughs AK. Elastography for the diagnosis of severity of fibrosis in chronic liver disease: a meta-analysis of diagnostic accuracy. *J Hepatol.* 2011;54(4):650-659. [\[Crossref\]](#)

41. Ronot M, Asselah T, Paradis V, et al. Liver fibrosis in chronic hepatitis C virus infection: differentiating minimal from intermediate fibrosis with perfusion CT. *Radiology.* 2010;256(1):135-142. [\[Crossref\]](#)

42. Wang L, Fan J, Ding X, Sun J, Zhang M. Assessment of liver fibrosis in the early stages with perfusion CT. *Int J Clin Exp Med.* 2015;8(9):15276-15282. [\[Crossref\]](#)

43. Ding Y, Rao S, Yang L, Chen C, Zeng M. Comparison of the effect of region-of-interest methods using gadoteric acid-enhanced MR imaging with diffusion-weighted imaging on staging hepatic fibrosis. *Radiol Med.* 2016;121(11):821-827. [\[Crossref\]](#)

44. Watanabe H, Kanematsu M, Goshima S, et al. Staging hepatic fibrosis: comparison of gadoxetate disodium-enhanced and diffusion-weighted MR imaging—preliminary observations. *Radiology.* 2011;259(1):142-150. [\[Crossref\]](#)

45. Venkatesh SK, Wang G, Lim SG, Wee A. Magnetic resonance elastography for the detection and staging of liver fibrosis in chronic hepatitis B. *Eur Radiol.* 2014;24(1):70-78. [\[Crossref\]](#)

46. Wang P, Zhu H, Kang H, Gore JC. R_{1p} dispersion and sodium imaging in human calf muscle. *Magn Reson Imaging.* 2017;42:139-143. [\[Crossref\]](#)

47. Koon CM, Zhang X, Chen W, Chu ES, San Lau CB, Wang YX. Black blood T1rho MR imaging may diagnose early stage liver fibrosis: a proof-of-principle study with rat biliary duct ligation model. *Quant Imaging Med Surg.* 2016;6(4):353-363. [\[Crossref\]](#)

48. Hu G, Zhang X, Liang W, et al. Assessment of liver fibrosis in rats by MRI with apparent diffusion coefficient and T1 relaxation time in the rotating frame. *J Magn Reson Imaging.* 2016;43(5):1082-1089. [\[Crossref\]](#)

49. Li J, Lai B, Zhang F, Liang B, Yang Q. Value of T1rho in Quantitative Diagnosis of Liver Fibrosis in Rats. *Chinese Journal of Medical Imaging Technology.* 2019;35(10):1445-1449. [\[Crossref\]](#)

50. Lu Y, Wang Q, Zhang T, et al. Staging liver fibrosis: comparison of native T1 mapping, T2 mapping, and T1p: an experimental study in rats with bile duct ligation and carbon tetrachloride at 11.7 T MRI. *J Magn Reson Imaging.* 2022;55(2):507-517. [\[Crossref\]](#)

51. Wang YXJ, Chen W, Deng M. How liver pathologies contribute to T1rho contrast require more careful studies. *Quant Imaging Med Surg.* 2017;7(5):608-613. [\[Crossref\]](#)

52. Qian Y, Hou J, Jiang B, et al. Characterization and correction of the effects of hepatic iron on T_{1p} relaxation in the liver at 3.0T. *Magn Reson Med.* 2022;88(4):1828-1839. [\[Crossref\]](#)

53. Zhao F, Wang YX, Yuan J, et al. Mr T1p as an imaging biomarker for monitoring liver injury progression and regression: an experimental study in rats with carbon tetrachloride intoxication. *Eur Radiol.* 2012;22(8):1709-1716. [\[Crossref\]](#)

54. Gilani IA, Sepponen R. Quantitative rotating frame relaxometry methods in MRI. *NMR Biomed.* 2016;29(6):841-861. [\[Crossref\]](#)

55. Eckstein F, Cicuttin F, Raynaud JP, Waterton JC, Peterfy C. Magnetic resonance imaging (MRI) of articular cartilage in knee osteoarthritis (OA): morphological assessment. *Osteoarthritis Cartilage.* 2006;14(Suppl A):46-75. [\[Crossref\]](#)

56. Pai A, Li X, Majumdar S. A comparative study at 3 T of sequence dependence of T2 quantitation in the knee. *Magn Reson Imaging.* 2008;26(9):1215-1220. [\[Crossref\]](#)

57. Crawley AP, Henkelman RM. Errors in T2 estimation using multislice multiple-echo imaging. *Magn Reson Med.* 1987;4(1):34-47. [\[Crossref\]](#)

58. Eckstein F, Heudorfer L, Faber SC, Burgkart R, Englmeier KH, Reiser M. Long-term and resegmentation precision of quantitative cartilage MR imaging (qMRI). *Osteoarthritis Cartilage.* 2002;10(12):922-928. [\[Crossref\]](#)

59. Eckstein F, Ateshian G, Burgkart R, et al. Proposal for a nomenclature for magnetic resonance imaging based measures of articular cartilage in osteoarthritis. *Osteoarthritis Cartilage.* 2006;14(10):974-983. [\[Crossref\]](#)

60. Link TM, Li X. Establishing compositional MRI of cartilage as a biomarker for clinical practice. *Osteoarthritis Cartilage.* 2018;26(9):1137-1139. [\[Crossref\]](#)

61. Keenan KE, Ainslie M, Barker AJ, et al. Quantitative magnetic resonance imaging phantoms: a review and the need for a system phantom. *Magn Reson Med.* 2017;79(1):48-61. [\[Crossref\]](#)

62. Li X, Pedoia V, Kumar D, et al. Cartilage T1p and T2 relaxation times: longitudinal reproducibility and variations using different coils, MR systems and sites. *Osteoarthritis*

Cartilage. 2015;23(12):2214-2223. [\[Crossref\]](#)

63. Roemer F, Kijowski R, Guermazi A. Editorial: from theory to practice - the challenges of compositional MRI in osteoarthritis research. *Osteoarthritis Cartilage.* 2017;25(12):1923-1925. [\[Crossref\]](#)

64. Huwart L, Peeters F, Sinkus R, et al. Liver fibrosis: non-invasive assessment with MR elastography. *NMR Biomed.* 2006;19(2):173-179. [\[Crossref\]](#)

65. Taouli B, Tolia AJ, Losada M, et al. Diffusion-weighted MRI for quantification of liver fibrosis: preliminary experience. *AJR Am J Roentgenol.* 2007;189(4):799-806. [\[Crossref\]](#)



Reply: evaluating text and visual diagnostic capabilities of large language models on questions related to the Breast Imaging Reporting and Data System (BI-RADS) Atlas 5th edition

Yasin Celal Güneş¹

Turay Cesur²

Eren Çamur³

Leman Günbey Karabekmez⁴

¹Kırıkkale Yüksek İhtisas Hospital, Clinic of Radiology, Kırıkkale, Türkiye

²Mamak State Hospital, Clinic of Radiology, Ankara, Türkiye

³Ankara 29 Mayıs State Hospital, Clinic of Radiology, Ankara, Türkiye

⁴Ankara Yıldırım Beyazıt University, Ankara Bilkent City Hospital, Department of Radiology, Ankara, Türkiye

KEYWORDS

BI-RADS, breast radiology, ChatGPT, large language models, retrieval-augmented generation

Dear Editor,

We sincerely thank the author for their insightful comments¹ and valuable suggestions regarding our manuscript titled "Evaluating text and visual diagnostic capabilities of large language models on questions related to the Breast Imaging Reporting and Data System Atlas 5th edition.² We appreciate the author's interest and the constructive proposal to incorporate retrieval-augmented generation (RAG) methodologies.¹

We fully agree that employing RAG could enhance the accuracy, contextual relevance, and reliability of responses generated by large language models (LLMs), particularly when addressing complex clinical scenarios such as those encountered in breast radiology.² As noted, RAG effectively mitigates limitations inherent in static models, including knowledge gaps and the risk of hallucinations, by dynamically retrieving relevant external information.^{3,4}

The examples provided by the author, including the promising results reported by Tozuka et al.⁵ in lung cancer tumor, node, metastasis staging using Google's NotebookLM with RAG, clearly demonstrate the considerable potential of this approach in radiological contexts.

Given these compelling points, we agree that incorporating RAG methodologies in future research would be highly valuable. Our current study did not include RAG, as its initial scope was limited to evaluating the inherent capabilities of standalone LLMs compared with radiologists based solely on the models' existing training data. Nonetheless, we acknowledge that future investigations involving retrieval-based augmentation could yield further insights into enhancing LLM performance in clinical radiology decision-making and guideline adherence.⁶

We appreciate the constructive input and believe that combining LLMs with RAG techniques in future work could substantially advance radiology education and clinical practice.

Thank you again for your thoughtful recommendations and contribution to this important discussion.

Footnotes

Conflict of interest disclosure

The authors declared no conflicts of interest.

Corresponding author: Yasin Celal Güneş

E-mail: gunesyasin cel@gmail.com

Received 24 March 2025; accepted 20 April 2025.



Epub: 20.05.2025

Publication date: 02.01.2026

DOI: 10.4274/dir.2025.253360

You may cite this article as: Güneş YC, Cesur T, Çamur E, Günbey Karabekmez L. Reply: evaluating text and visual diagnostic capabilities of large language models on questions related to the Breast Imaging Reporting and Data System (BI-RADS) Atlas 5th edition. *Diagn Interv Radiol.* 2026;32(1):25-26.

References

1. Kaba E. Retrieval-augmented generation for answering breast imaging reporting and data system (BI-RADS)-related questions with large language models. *Diagn Interv Radiol.* 2025. [\[Crossref\]](#)
2. Güneş YC, Cesur T, Çamur E, Günbey Karabekmez L. Evaluating text and visual diagnostic capabilities of large language models on questions related to the Breast Imaging Reporting and Data System (BI-RADS) Atlas 5th edition. *Diagn Interv Radiol.* 2025;31(2):111-129. [\[Crossref\]](#)
3. Zakka C, Shad R, Chaurasia A, et al. Almanac - retrieval-augmented language models for clinical medicine. *NEJM AI.* 2024;1(2):10. [\[Crossref\]](#)
4. Steybe D, Poxleitner P, Aljohani S, et al. Evaluation of a context-aware chatbot using retrieval-augmented generation for answering clinical questions on medication-related osteonecrosis of the jaw. *J Craniomaxillofac Surg.* 2025;53(4):355-360. [\[Crossref\]](#)
5. Tozuka R, Johno H, Amakawa A, et al. Application of NotebookLM, a large language model with retrieval-augmented generation, for lung cancer staging. *Jpn J Radiol.* 2025;43(4):706-712. [\[Crossref\]](#)
6. Liu S, Wright AP, Patterson BL, et al. Using AI-generated suggestions from ChatGPT to optimize clinical decision support. *J Am Med Inform Assoc.* 2023;30(7):1237-1245. [\[Crossref\]](#)



Artificial intelligence in radiology: diagnostic sensitivity of ChatGPT for detecting hemorrhages in cranial computed tomography scans

✉ Olga Bayar-Kapıcı¹
 ✉ Erman Altunışık²
 ✉ Feyza Musabeyoğlu²
 ✉ Şeyda Dev²
 ✉ Ömer Kaya³

¹Seyhan State Hospital, Clinic of Radiology, Adana, Türkiye

²University of Health Sciences Türkiye, Gaziantep City Hospital, Clinic of Neurology, Gaziantep, Türkiye

³Çukurova University Faculty of Medicine, Department of Radiology, Adana, Türkiye

PURPOSE

Chat Generative Pre-trained Transformer (ChatGPT)-4V, a large language model developed by OpenAI, has been explored for its potential application in radiology. This study assesses ChatGPT-4V's diagnostic performance in identifying various types of intracranial hemorrhages in non-contrast cranial computed tomography (CT) images.

METHODS

Intracranial hemorrhages were presented to ChatGPT using the clearest 2D imaging slices. The first question, "Q1: Which imaging technique is used in this image?" was asked to determine the imaging modality. ChatGPT was then prompted with the second question, "Q2: What do you see in this image and what is the final diagnosis?" to assess whether the CT scan was normal or showed pathology. For CT scans containing hemorrhage that ChatGPT did not interpret correctly, a follow-up question—"Q3: There is bleeding in this image. Which type of bleeding do you see?"—was used to evaluate whether this guidance influenced its response.

RESULTS

ChatGPT accurately identified the imaging technique (Q1) in all cases but demonstrated difficulty diagnosing epidural hematoma (EDH), subdural hematoma (SDH), and subarachnoid hemorrhage (SAH) when no clues were provided (Q2). When a hemorrhage clue was introduced (Q3), ChatGPT correctly identified EDH in 16.7% of cases, SDH in 60%, and SAH in 15.6%, and achieved 100% diagnostic accuracy for hemorrhagic cerebrovascular disease. Its sensitivity, specificity, and accuracy for Q2 were 23.6%, 92.5%, and 57.4%, respectively. These values improved substantially with the clue in Q3, with sensitivity rising to 50.9% and accuracy to 71.3%. ChatGPT also demonstrated higher diagnostic accuracy in larger hemorrhages in EDH and SDH images.

CONCLUSION

Although the model performs well in recognizing imaging modalities, its diagnostic accuracy substantially improves when guided by additional contextual information.

CLINICAL SIGNIFICANCE

These findings suggest that ChatGPT's diagnostic performance improves with guided prompts, highlighting its potential as a supportive tool in clinical radiology.

KEYWORDS

Artificial intelligence, intracranial hemorrhages, ChatGPT, computed tomography, hematoma

Corresponding author: Olga Bayar-Kapıcı

E-mail: olgasahbayar@gmail.com

Received 24 May 2025; revision requested 10 June 2025; accepted 28 June 2025.



Epub: 21.07.2025

Publication date: 02.01.2026

DOI: 10.4274/dir.2025.253456

Artificial intelligence (AI) is increasingly being used across various fields to assist humans in quickly accessing information and supporting decision-making processes.¹ One of the subcategories of AI, large language models (LLMs), is a type of generative AI capable of processing, understanding, and generating human knowledge. LLMs are trained using self-supervised learning, which enables them to predict missing or hidden elements within a text.² Among these LLMs, Chat Generative Pre-trained Transformer (ChatGPT) is built on the GPT-4 architecture. ChatGPT is a text-based model that supports decision-making

You may cite this article as: Bayar-Kapıcı O, Altunışık E, Musabeyoğlu F, Dev Ş, Kaya Ö. Artificial intelligence in radiology: diagnostic sensitivity of ChatGPT for detecting hemorrhages in cranial computed tomography scans. *Diagn Interv Radiol.* 2026;32(1):27-32.

across a wide range of domains. OpenAI's ChatGPT model operates using a supervised learning process in which it predicts the next element in a sequence of text.³

In November 2023, OpenAI updated the ChatGPT model to GPT-4V, which introduced the ability not only to communicate through text but also to interpret and generate images. GPT-4V is an enhanced version of ChatGPT with capabilities for processing visual data, allowing it to analyze and comment on images. This development expands its utility beyond text-based tasks, enabling performance in image-related contexts as well.⁴ However, the visual capabilities of ChatGPT remain in development and currently have certain limitations.

There has been considerable discussion in the literature regarding the potential use of AI in radiology.⁵ In acute settings, where rapid decision-making is critical, AI's ability to detect pathologies in radiological imaging may help reduce patient morbidity and mortality. It has been proposed that ChatGPT, in particular, could support the diagnosis of patients with time-sensitive conditions such as stroke.⁶ In such cases, where timely intervention substantially lowers the risk of long-term disability, ChatGPT's diagnostic capabilities could offer valuable support.

In this study, we presented ChatGPT-4V with computed tomography images (CTI) of epidural hematoma (EDH), subdural hematoma (SDH), subarachnoid hemorrhage (SAH), hemorrhagic cerebrovascular disease (HSVD), and normal brain scans [non-contrast CT (NCT)], and asked it a series of questions. We aimed to evaluate its diagnostic

sensitivity and specificity in detecting hemorrhages based on the responses it provided.

Methods

Study design

This study was conducted at the Neurology Clinic of Gaziantep City Hospital. Approval was obtained from the Non-Interventional Clinical Research Ethics Committee of Gaziantep City Hospital (IRB number: 159/2025, decision date: March 19, 2025). All participants provided signed informed consent.

Participants were required to meet specific inclusion criteria. Only adults aged 18 years and older with available cranial CT scans were included. These scans needed to show either intracranial hemorrhages—such as EDH, SDH, SAH, or HSVD—or a normal brain. Additionally, the CTIs had to be clear and non-contrast, enabling accurate detection and classification of hemorrhages.

Exclusion criteria included pediatric patients under the age of 18, as well as participants with unclear CTIs or imaging artifacts that interfered with hemorrhage detection. Patients with a history of cognitive impairment or conditions that prevented them from providing informed consent were also excluded, as were individuals with a history of brain trauma or prior neurosurgical procedures, as these could influence the interpretation of current CT findings. Finally, cases involving chronic hemorrhages, where the acute nature of the pathology could not be confirmed, were excluded. A flowchart of the study is presented in Figure 1.

Chat Generative Pre-trained Transformer assessment

Intracranial hemorrhages were presented to ChatGPT using the clearest 2D imaging slices. In Q1, ChatGPT was asked to identify the imaging technique (Figure 2). In Q2, it was prompted to determine whether the CTI was normal or to identify any pathology, if present (Figure 3). For scans showing hemorrhage that ChatGPT failed to interpret accurately, a follow-up prompt—Q3—was used to assess whether its response changed when guided to identify the type of bleeding (Figure 4).

Statistical analysis

The analysis of ChatGPT's diagnostic performance was conducted using descriptive statistics to evaluate the model's success rates in answering questions related to

various hemorrhage types (EDH, SDH, SAH, HSVD, and NCT) presented in cranial CT scans. The success rates for each question (Q1, Q2, Q3) were calculated and reported as frequencies and percentages for each condition.

To determine the sensitivity, specificity, positive predictive value (PPV), negative predictive value (NPV), and accuracy of the model in identifying hemorrhages, 2 × 2 contingency tables were constructed for each question. Sensitivity (true positive rate) and specificity (true negative rate) were calculated for Q2 and Q3 to evaluate ChatGPT's diagnostic performance in detecting hemorrhages.

Further analysis involved comparing sensitivity and specificity across different hemorrhage types and questions (Q1, Q2, Q3). Additionally, the relationship between hemorrhage size and diagnostic accuracy was examined using *P* values derived from statistical tests (e.g., Mann–Whitney *U* test) to assess whether hemorrhage size influenced diagnostic outcomes.

Results

ChatGPT correctly identified the imaging technique (Q1) in all images. When asked what it saw in the image without any clues (Q2), ChatGPT failed to correctly diagnose EDH, SDH, and SAH. However, when the image was identified as showing hemorrhage and the task was to determine the type, ChatGPT correctly identified EDH in 16.7%, SDH in 60%, and SAH in 15.6% of cases. For HSVD, ChatGPT achieved an 86.7% correct diagnosis rate in Q2 and reached 100% diagnostic accuracy in Q3. It also correctly identified negative findings in 92.5% of normal CT scans (Table 1 and Figure 5).

The sensitivity and specificity of ChatGPT for detecting intracranial hemorrhages are summarized in Table 2. For Q2, sensitivity was 23.6%, specificity was 92.5%, PPV was 76.5%, NPV was 53.8%, and overall accuracy was 57.4%. With the diagnostic clue provided in Q3, sensitivity increased to 50.9%, PPV to 87.5%, NPV to 64.5%, and accuracy to 71.3%.

The relationship between correct diagnoses of EDH and SDH in Q3 and hemorrhage size is shown in Table 3. According to these results, in EDH and SDH images, the hemorrhage size was statistically significantly larger in cases correctly diagnosed by ChatGPT compared with false negatives (*P* = 0.038 and *P* = 0.030, respectively).

Discussion

The main findings of this study are as follows: (i) ChatGPT correctly identified the imaging modality in all images; (ii) it failed to provide accurate diagnoses in cases of EDH, SDH, and SAH, with the exception of HSVD; (iii) it was able to generate correct diagnoses when appropriately guided; and (iv) in EDH and SDH images, the hemorrhage diameter was larger in cases where ChatGPT provided the correct diagnosis.

This study evaluated the diagnostic capabilities of ChatGPT in identifying various types of intracranial hemorrhages using non-contrast cranial CTIs. The results highlight both the potential and the current

limitations of this large language and vision model in the context of neuroimaging interpretation.

The first key finding is that ChatGPT successfully identified the imaging modality as CT in 100% of cases. This suggests that the model is reliably capable of recognizing basic imaging types, even when presented with isolated slices and no clinical context. However, when tasked with identifying specific pathologies—particularly acute hemorrhages—its diagnostic performance was notably limited. The model was only able to correctly diagnose HSVD with high accuracy, whereas it consistently failed to detect EDH, SDH, and SAH without guidance.

These findings are important, as they reveal that while ChatGPT possesses a degree of image interpretation capacity, its baseline performance in detecting life-threatening hemorrhages remains suboptimal. A key secondary observation, however, is that the model's diagnostic accuracy improved considerably when guided with targeted questions (Q3). Prior research has suggested that LLMs such as ChatGPT tend to perform better in complex clinical tasks when questions are framed in open-ended or context-rich formats, which enhance the relevance and depth of their responses.⁷

Supporting our findings, a recent study by Kahalian et al.⁸ evaluated ChatGPT-4V's diagnostic performance in interpreting oral and maxillofacial radiographic images. The authors reported that the correct pre-diagnosis rate was only 30.7% when no clues were provided, but this rate substantially increased to 56.9% with the inclusion of structured prompts, such as internal lesion features or anatomical context. These results confirm that providing domain-relevant cues can substantially enhance the diagnostic accuracy of GPT-4V in medical imaging tasks. Notably, similar to our study, the authors found that the model struggled to differentiate closely located anatomical structures and failed to generate comprehensive differential diagnoses in complex cases. This parallel reinforces the conclusion that, while ChatGPT-4V demonstrates baseline interpretive ability, its effective use in clinical radiology depends heavily on contextual scaffolding and targeted prompting strategies.

Recent literature has further emphasized the growing potential of LLMs in radiology, highlighting their capacity to support tasks ranging from protocol selection to diagnostic reasoning and structured reporting. Akinci D'Antonoli et al.⁹ provided a comprehensive overview of how LLMs, such as GPT-4, may be integrated into radiological workflows to improve clinical decision-making.

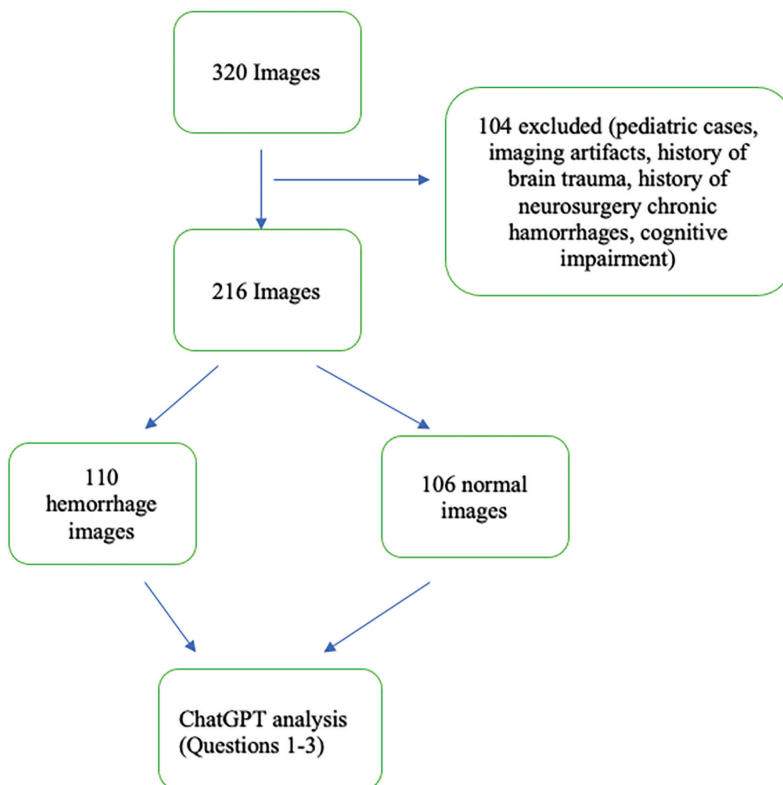
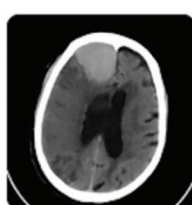


Figure 1. Flowchart of the study. ChatGPT, Chat Generative Pre-trained Transformer.



Which imaging technique is used in this image?

The imaging technique used in this image is **non-contrast cranial computed tomography (CT)**.

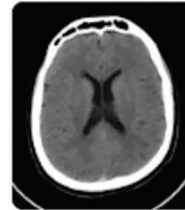
Figure 2. Q1: Which imaging technique is used in this image?

ing and enhance the efficiency of data interpretation. Although our study demonstrates that GPT-4V continues to underperform in detecting subtle hemorrhagic pathologies on cranial CT scans—particularly in the absence of contextual prompts—these broader applications suggest that LLMs may still contribute meaningfully when used for textual analysis, report structuring, or as conversational assistants in radiology departments. Future iterations of such models, especially those fine-tuned for radiological image data and integrated with clinical metadata, may

hold transformative potential in diagnostic radiology.

In contrast to our findings, which revealed diagnostic limitations of ChatGPT on cranial CTs, Kuzan et al.¹⁰ observed improved performance in stroke diagnosis when diffusion-weighted imaging (DWI) magnetic resonance imaging (MRI) was utilized. In their study, ChatGPT-4V demonstrated a sensitivity of 79.5% and a specificity of 84.9% in detecting acute ischemic stroke using DWI and apparent diffusion coefficient maps. Although our results showed that ChatGPT-4V

struggled particularly with identifying EDH, SDH, and SAH, its success in HSVD cases and its improvement after guided prompts suggest that diagnostic performance is strongly influenced by the nature and clarity of radiological findings. The relatively high accuracy reported by Kuzan et al.¹⁰ may be attributed to the more conspicuous radiologic features of diffusion restriction on MRI, compared with the often subtle or variable appearance of hemorrhages on CT. These findings underscore the importance of tailoring AI applications to specific imaging modalities



What do you see in this image? What is your final diagnosis?



This axial non-contrast CT scan of the brain appears relatively normal. Here's what I observe:

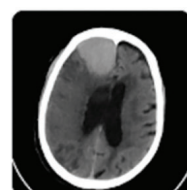
Key findings:

- **Symmetric lateral ventricles** without midline shift
- **No hyperdense (acute blood)** or hypodense (edema or infarct) areas
- **No mass effect**, sulcal effacement, or herniation signs
- **Gray-white matter differentiation** is preserved
- **No evidence of skull fracture or extracranial soft tissue swelling**

Final Diagnosis:

Normal cranial CT — no acute intracranial pathology is visible in this slice.

Figure 3. Q2: What do you see in this image, and what is the final diagnosis? CT, computed tomography.



There is a bleeding in this image. Which type of bleeding do you see?

This CT image shows a **hyperdense (bright) crescent-shaped area** along the **left cerebral hemisphere**, causing a midline shift and compression of the lateral ventricle. These findings are characteristic of a **subdural hematoma (SDH)**.

Figure 4. Q3: There is bleeding in this image. Which type of bleeding do you see?

and reinforce the potential of ChatGPT as a supportive tool when used within defined clinical and technical contexts.

Furthermore, the study showed that in EDH and SDH cases, the hemorrhage diameter was substantially greater in the true pos-

itive group than in the false negative group. This suggests that the model may be more adept at recognizing larger and more prominent pathologies and may struggle with subtle or borderline findings. This size-related variability in diagnostic accuracy has impor-

tant implications for clinical practice, where early detection of small-volume hemorrhages is often critical for timely intervention.

A recent study by Koyun et al.¹¹ evaluated the diagnostic capabilities of ChatGPT-4V in identifying various types of intracranial hemorrhages on NCT and reported promising results, with a sensitivity of 79.2% and an accuracy of 68.3% in hemorrhage detection. However, their findings also revealed notable limitations in localizing hemorrhages and identifying subarachnoid and epidural types, particularly in the absence of clear density differences. These results are consistent with our study, which demonstrated that ChatGPT's performance was markedly better for hemorrhages with larger diameters and distinct features (e.g., HSVD), whereas its diagnostic accuracy was considerably lower in cases of EDH, SDH, and SAH. Notably, both studies found that the model was highly consistent in identifying the imaging modality but often failed in complex classification tasks without tailored prompting. Together, these findings highlight the current strengths and limitations of general-purpose LLMs in radiologic interpretation and reinforce the need for multimodal training and task-specific tuning for clinical use.

One of the most comprehensive assessments of GPT-4V's performance in neuro-imaging was recently conducted by Zhang et al.¹², who analyzed the model's ability to detect and annotate cerebral hemorrhages on non-contrast cranial CTs. In their retrospective evaluation of 208 CT scans, GPT-4V achieved an overall identification completeness of 72.6%, with the highest performance observed in epidural and intraparenchymal hemorrhages (89.0% and 86.9%, respectively). However, it showed substantially lower performance in chronic SDH and SAH, mirroring the diagnostic gaps also noted in our study. Their results also indicated that GPT-4V was more accurate in identifying massive hemorrhages than minor ones, supporting our finding that larger bleeding volumes in EDH and SDH were associated with better diagnostic accuracy. Together, these findings underscore the model's dependence on the visual salience of hemorrhagic lesions and reaffirm the need for multimodal refinement and clinical oversight if GPT-4V is to be integrated into routine radiologic workflows.

In addition to our findings on image-based diagnostic limitations, recent research has also highlighted concerns regarding the textual output of AI models. Güll et al.¹³ conducted a cross-sectional study eval-

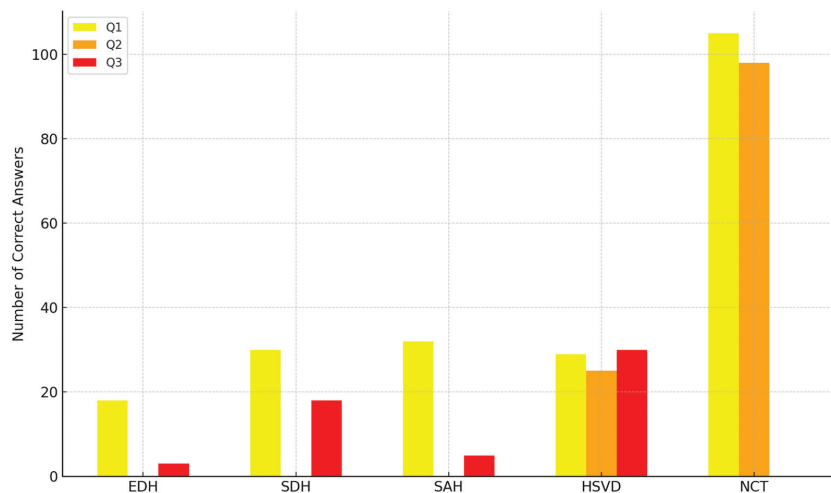


Figure 5. Number of correct responses by ChatGPT. ChatGPT, Chat Generative Pre-trained Transformer; EDH, epidural hematoma; SDH, subdural hematoma; SAH, subarachnoid hemorrhage; HSVD, hemorrhagic cerebrovascular disease; NCT, non-contrast computed tomography.

Table 1. ChatGPT's success rates in answering the questions

	Q1 n (%)	Q2 n (%)	Q3 n (%)
EDH (n = 18)	18 (100)	0 (0)	3 (16.7)
SDH (n = 30)	30 (100)	0 (0)	18 (60)
SAH (n = 32)	32 (100)	0 (0)	5 (15.6)
HSVD (n = 30)	30 (100)	26 (86.7)	30 (100)
NCT (n = 106)	106 (100)	98 (92.5)	

ChatGPT, Chat Generative Pre-trained Transformer; EDH, epidural hematoma; SDH, subdural hematoma; SAH, subarachnoid hemorrhage; HSVD, hemorrhagic cerebrovascular disease; NCT, normal cranial computed tomography images.

Table 2. Sensitivity and specificity analysis of ChatGPT

Q2	TP	TN	FP	FN	Sensitivity	Specificity	PPV	NPV	Accuracy
n	26	98	8	84	26/110	98/106	26/34	98/182	124/216
%					23.6	92.5	76.5	53.8	57.4
Q3	TP	TN	FP	FN	Sensitivity	Specificity	PPV	NPV	Accuracy
n	56	98	8	54	56/110	98/106	56/64	98/152	154/216
%					50.9	92.5	87.5	64.5	71.3

Sensitivity = TP / (TP + FN), Specificity = TN / (TN + FP), PPV = TP / (TP + FP), NPV = TN / (TN + FN), Accuracy = (TP + TN) / (TP + TN + FP + FN).

TP, true positives; TN, true negatives; FP, false positives; FN, false negatives; NPV, negative predictive value.

Table 3. Comparison of ChatGPT's results based on hemorrhage size

Q3	FN median (min.–max.)	TP median (min.–max.)	P value
EDH diameter (mm)	10 (3–32)	17 (16–20)	0.038
SDH diameter (mm)	19 (10–35)	22.5 (12–41)	0.030

The Mann–Whitney U test was used. A P value <0.05 was considered statistically significant.

EDH, epidural hematoma; SDH, subdural hematoma; mm, millimeter; FN, false negatives; TP, true positives; min.–max., minimum–maximum.

uating the quality, reliability, and readability of ChatGPT, Bard, and Perplexity responses to patient-centered questions on SDH. They found that all three AI tools produced answers that substantially exceeded the recommended sixth-grade reading level, making the content difficult for general users to understand. Moreover, ChatGPT's responses were rated lower in readability than Bard and Perplexity, and its DISCERN and JAMA quality scores indicated deficiencies in transparency, citation, and clarity. These findings reinforce the need for optimization not only in visual diagnostic performance, as shown in our study, but also in natural language output, especially for patient education. They further support the idea that while LLMs show potential in clinical contexts, their use must be accompanied by careful oversight and task-specific calibration to avoid misleading or inaccessible information.

These limitations align with the understanding that GPT-4V, although capable of processing visual inputs, has not been trained on annotated radiologic datasets and lacks the spatial learning capabilities typical of convolutional neural networks.¹⁴ As a result, its ability to detect subtle radiographic features remains inherently limited.

Nevertheless, the model's capacity to engage in guided reasoning and improve diagnostic performance when provided with contextual prompts presents promising potential. With further domain-specific training and integration of multimodal clinical data—such as patient history, symptoms, and laboratory results—LLMs may evolve into useful adjunct tools in emergency and diagnostic radiology.

This study has several limitations that should be considered. First, the sample size for each hemorrhage type was relatively small, which may limit the generalizability of the results. Second, the accuracy of ChatGPT-4V was influenced by the clarity and quality of the CTIs, as some scans contained artifacts or poor resolution, potentially affecting performance. Third, the retrospective nature of the study means the findings are based on historical data, and real-time clinical valida-

tion is needed to confirm the model's practical utility. Additionally, although ChatGPT-4V showed improved diagnostic accuracy when given clues, its performance in more complex or subtle hemorrhage cases remains uncertain, suggesting the need for further refinement. Lastly, the lack of comparison with other AI models or radiologists limits the ability to fully assess ChatGPT's relative effectiveness in diagnosing intracranial hemorrhages.

In conclusion, while ChatGPT demonstrates basic competence in identifying imaging modalities and limited ability in hemorrhage detection—particularly in HSVD—it is not yet suitable for autonomous radiologic interpretation. However, its interactive design and improved performance under guidance suggest that LLMs may serve a valuable supportive role in the future, particularly when embedded within supervised or hybrid diagnostic systems.

Footnotes

Conflict of interest disclosure

The authors declared no conflicts of interest.

References

1. Giordano C, Brennan M, Mohamed B, Rashidi P, Modave F, Tighe P. Assessing artificial intelligence for clinical decision-making. *Front Digit Health.* 2021;3:645232. [\[Crossref\]](#)
2. Elkassem AA, Smith AD. Potential use cases for ChatGPT in radiology reporting. *AJR Am J Roentgenol.* 2023;221(3):373-376. [\[Crossref\]](#)
3. Kim JK, Chua M, Rickard M, Lorenzo A. ChatGPT and large language model (LLM) chatbots: the current state of acceptability and a proposal for guidelines on utilization in academic medicine. *J Pediatr Urol.* 2023;19(5):598-604. [\[Crossref\]](#)
4. Horiuchi D, Tatekawa H, Oura T, et al. ChatGPT's diagnostic performance based on textual vs. visual information compared to radiologists' diagnostic performance in musculoskeletal radiology. *Eur Radiol.* 2025;35(1):506-516. [\[Crossref\]](#)
5. Boeken T, Feydy J, Lecler A, et al. Artificial intelligence in diagnostic and interventional radiology: where are we now? *Diagn Interv Imaging.* 2023;104(1):1-5. [\[Crossref\]](#)
6. Gilotra K, Swarna S, Mani R, Basem J, Dashti R. Role of artificial intelligence and machine learning in the diagnosis of cerebrovascular disease. *Front Hum Neurosci.* 2023;17:1254417. [\[Crossref\]](#)
7. Kung TH, Cheatham M, Medenilla A, et al. Performance of ChatGPT on USMLE: potential for AI-assisted medical education using large language models. *PLOS Digit Health.* 2023;2(2):e0000198. [\[Crossref\]](#)
8. Kahalian S, Rajabzadeh M, Özbe M, Medisoglu MS. ChatGPT-4.0 in oral and maxillofacial radiology: prediction of anatomical and pathological conditions from radiographic images. *Folia Med (Plovdiv).* 2024;66(6):863-868. [\[Crossref\]](#)
9. Akinci D'Antonoli T, Stanzione A, Bluethgen C, et al. Large language models in radiology: fundamentals, applications, ethical considerations, risks, and future directions. *Diagn Interv Radiol.* 2024;30(2):80-90. [\[Crossref\]](#)
10. Kuzan BN, Meşe İ, Yaşar S, Kuzan TY. A retrospective evaluation of the potential of ChatGPT in the accurate diagnosis of acute stroke. *Diagn Interv Radiol.* 2025;31(3):187-195. [\[Crossref\]](#)
11. Koyun M, Cevval ZK, Reis B, Ece B. Detection of intracranial hemorrhage from computed tomography images: diagnostic role and efficacy of ChatGPT-4o. *Diagnostics (Basel).* 2025;15(2):143. [\[Crossref\]](#)
12. Zhang D, Ma Z, Gong R, et al. Using natural language processing (GPT-4) for computed tomography image analysis of cerebral hemorrhages in radiology: retrospective analysis. *J Med Internet Res.* 2024;26:e58741. [\[Crossref\]](#)
13. Güll Ş, Erdemir İ, Hancı V, Aydoğmuş E, Erkoç YS. How artificial intelligence can provide information about subdural hematoma: Assessment of readability, reliability, and quality of ChatGPT, BARD, and perplexity responses. *Medicine (Baltimore).* 2024;103(18):e38009. [\[Crossref\]](#)
14. OpenAI. GPT-4 technical report. 2023. [\[Crossref\]](#)



Automated evaluation of pulmonary lesion changes on chest radiograph during follow-up using semantic segmentation

✉ **Youngjae Kim**^{1,2*}
Yura Ahn^{3*}
Sang Min Lee³
Han Na Noh⁴
Jongjun Won²
Chaewon Kim²
Hyunna Lee⁵

¹University of Ulsan Faculty of Medicine, Department of Biomedical Engineering, AMIST, Asan Medical Center, Seoul, Republic of Korea

²University of Ulsan Faculty of Medicine, Department of Convergence Medicine, Asan Medical Institute of Convergence Science and Technology, Asan Medical Center, Seoul, Republic of Korea

³University of Ulsan Faculty of Medicine, Department of Radiology and Research Institute of Radiology, Asan Medical Center, Seoul, Republic of Korea

⁴University of Ulsan Faculty of Medicine, Health Screening and Promotion Center, Asan Medical Center, Seoul, Republic of Korea

⁵Bigdata Research Center, Asan Institute for Life Science, Asan Medical Center, Seoul, Republic of Korea

PURPOSE

To develop and validate a deep learning-based model utilizing lesion-specific segmentation to determine the changed/unchanged status of consolidation and pleural effusion in paired chest radiographs (CRs).

METHODS

The model was trained using 5,178 CRs from a single institution for lesion segmentation. Paired CRs from the emergency department (ED) and intensive care unit (ICU) were used to determine the thresholds for change and temporal validation. Model performance was evaluated through the area under the receiver operating characteristic curve (AUC), and its accuracy was compared with that of a thoracic radiologist.

RESULTS

In the ED, the model achieved AUCs of 0.988 and 0.883 for consolidation and pleural effusion, respectively, with accuracies of 0.900 (36/40) and 0.825 (33/40). The radiologist showed accuracies of 0.975 (39/40) and 0.950 (38/40), respectively. In the ICU, model AUCs were 0.970 (consolidation) and 0.955 (pleural effusion), with accuracies of 0.875 (35/40) and 0.800 (32/40), respectively. Radiologist performance was 0.975 (39/40) for consolidation and 1.000 (40/40) for pleural effusion. No significant accuracy differences were observed between the model and radiologist for consolidation in the ICU or both targets in the ED (all $P > 0.05$), except for pleural effusion in the ICU ($P = 0.01$).

CONCLUSION

The lesion-specific deep learning model was feasible for identifying interval changes in consolidation and pleural effusion on follow-up CRs.

CLINICAL SIGNIFICANCE

It could potentially be utilized for prioritizing interpretation, generating alerts, and extracting time-series data from multiple follow-up CRs.

KEYWORDS

Radiography, thoracic, follow-up studies, diagnosis, computer-assisted, artificial intelligence, segmentation

*Joint first authors

Corresponding author: Sang Min Lee

E-mail: sangmin.lee.md@gmail.com

Received 22 July 2025; revision requested 24 August 2025; accepted 23 September 2025.



Publication date: 02.01.2026

DOI: 10.4274/dir.2025.253567

Chest radiography is a widely used medical imaging modality due to its cost-effectiveness and low radiation exposure. Chest radiographs (CRs) detect thoracic abnormalities and track changes during follow-ups. Monitoring abnormalities such as pleural effusion or consolidation is crucial for evaluating disease progression and treatment response.¹⁻⁴ However, frequent follow-up CRs increase workload. For example, in intensive care units (ICUs), CR is often performed daily for patients who are critically ill or after device adjustments, generating millions of ICU CRs annually in the United States.^{5,6} Consequently, the timely and accurate interpretation of follow-up CRs is becoming more challenging.

You may cite this article as: Kim Y, Ahn Y, Lee SM, et al. Automated evaluation of pulmonary lesion changes on chest radiograph during follow-up using semantic segmentation. *Diagn Interv Radiol*. 2026;32(1):33-39.

Since follow-up CRs primarily detect changes between exams, analyzing CR pairs rather than relying solely on single-image abnormality detection is necessary. One line of currently developed deep learning methods detects overall changes using image registration to identify all CR findings.^{7,8} It operates independently of detectable abnormality types and lesion-specific segmentation performance. However, it lacks information on which lesions have changed and the nature of these changes, which are essential in clinical practice. Furthermore, in settings such as the ICU, where various medical devices are attached, even simple repositioning, addition, or removal of a device may be recorded as a change, making it difficult to accurately determine whether a true change has occurred in the finding of interest.

Some methods have targeted specific abnormalities. For example, Li et al.⁹ compared lung infiltration on serial CRs of patients with Coronavirus Disease-19, Huang et al.¹⁰ quantified pleural effusion severity on individual CRs, and Lim et al.¹¹ estimated lung nodule volume from serial CRs. Although these studies demonstrated the feasibility or potential applicability of abnormality-specific monitoring, their scope was restricted to a single lesion type. An alternative approach that enables the simultaneous tracking of different abnormalities is lesion segmentation. Singh et al.¹² developed a deep learning algorithm that segments specific abnormalities and determines their changed/unchanged status based on the persistence of segmentation masks for lesions. The study reported an area under the receiver operating characteristic curve (AUC) of 0.758 for evaluating changes in pulmonary opacities over follow-up CRs. However, the algorithm was unable to deter-

mine the changed/unchanged status when their extent varied despite persistence. Despite its limitations, an algorithm that autonomously detects, segments, and assesses the changed/unchanged status of various abnormalities based on the degree of observed changes would be valuable.

Therefore, this study aims to develop a deep learning-based classifier for determining changed/unchanged status in paired CRs, using automatic lesion segmentation and extent comparison for consolidation and pleural effusion, and to validate its feasibility.

Methods

This retrospective study was approved by the institutional review board of Asan Medical Center, which waived the requirement for written informed consent (approval number: 2023-0810, date: 2023-07-01). Of the 5,178 CRs used for training, 4,593 were utilized in a previous study to develop a model for detecting five abnormalities.¹³ However, our model is not related to the model from that study.

Training and validation datasets

In the classifier pipeline, the training set for abnormality segmentation was derived from CRs of adult patients (≥ 18 years) obtained at a tertiary referral hospital between January 2015 and December 2018 (Figure 1). The training set consisted of three types: normal CR, abnormal CR (with consolidation or pleural effusion), and CR with medical devices (Appendix S1). Radiologist-labeled lesion masks that had been developed and validated in the previous work were used.¹³ However, the lesion segmentation algorithm, the paired radiograph comparison, and the change-detection framework were newly developed in this study. During the training process for the segmentation component of the model, the training set was further divided into a 9:1 ratio for model development and tuning.

After developing a lesion segmentation algorithm, CRs obtained from the emergency department (ED) and ICU between January 2019 and December 2019 were collected to determine the changed/unchanged classifier threshold. For each patient, one pair of CRs was randomly selected while maintaining the chronological order. The pairing principle was applied regardless of the CR projection type (posteroanterior or antero-posterior). However, due to the nature of the ED and ICU settings with patients who are critically ill, most radiographs were antero-

posterior. Two thoracic radiologists (BLINDED and BLINDED, with 7 and 17 years of experience in thoracic imaging, respectively), blinded to the radiologic report, interpreted the changed/unchanged status, as well as the presence of target abnormality (i.e., consolidation and pleural effusion), in queried CR pairs in a random order until the target number of each dataset was reached. Both the changed/unchanged status and type of abnormality were determined in consensus by the two radiologists.

For temporal validation of the changed/unchanged classifier, CRs obtained from the ED and ICU between January 2020 and December 2020 were collected, each containing a single abnormality (consolidation or pleural effusion). To compare the performance between the model and radiologist, another thoracic radiologist (BLINDED, with 27 years of experience in thoracic imaging) independently reviewed the temporal validation set and determined the changed/unchanged status. This review was conducted blinded to the reference standard result but with knowledge of the target abnormality type (consolidation vs. pleural effusion).

Architecture of the lesion-specific classifier

Our model included two pipelines: 1) abnormality segmentation and 2) lesion area quantification and decision-making within pairs (Figure 2). First, the nnU-Net, a U-Net-based medical segmentation model known for its robust and high performance, served as the base model. Its structure and training options were modified for enhanced pulmonary lesion segmentation performance.¹⁴ To improve the model's generalization ability, a multi-task learning (MTL) approach that jointly performs segmentation and classification was adopted, thereby improving the model's capability to differentiate between lesions in similar anatomical locations and medical devices and reducing potential segmentation errors. Two auxiliary classifiers were incorporated at the nnU-Net bottleneck for MTL: one for lesion presence classification and the other for lesion type classification (Appendix S2). The modified nnU-Net was trained for 1,000 epochs using 5-fold cross-validation, and the final lesion segmentation masks were generated by ensembling the inferred masks from each fold.

In the changed/unchanged classifier, lesion areas in each generated mask were quantified by multiplying the number of pixels in each lesion class by the pixel spacing of the corresponding CR. Changes in lesion quantities were calculated as the absolute

Main points

- Using lesion-specific segmentation, a deep-learning model determines consolidation and pleural effusion changes in chest radiographs (CRs) by assessing changes in their extent.
- A deep-learning model achieved an area under the curve of 0.970–0.988 for determining the changed/unchanged status of consolidation and 0.883–0.955 for pleural effusion in follow-up CRs from emergency department and intensive care unit datasets.
- With a predefined threshold, the model demonstrated an accuracy of 0.875–0.900 for changed/unchanged determination in consolidation and 0.800–0.825 for pleural effusion.

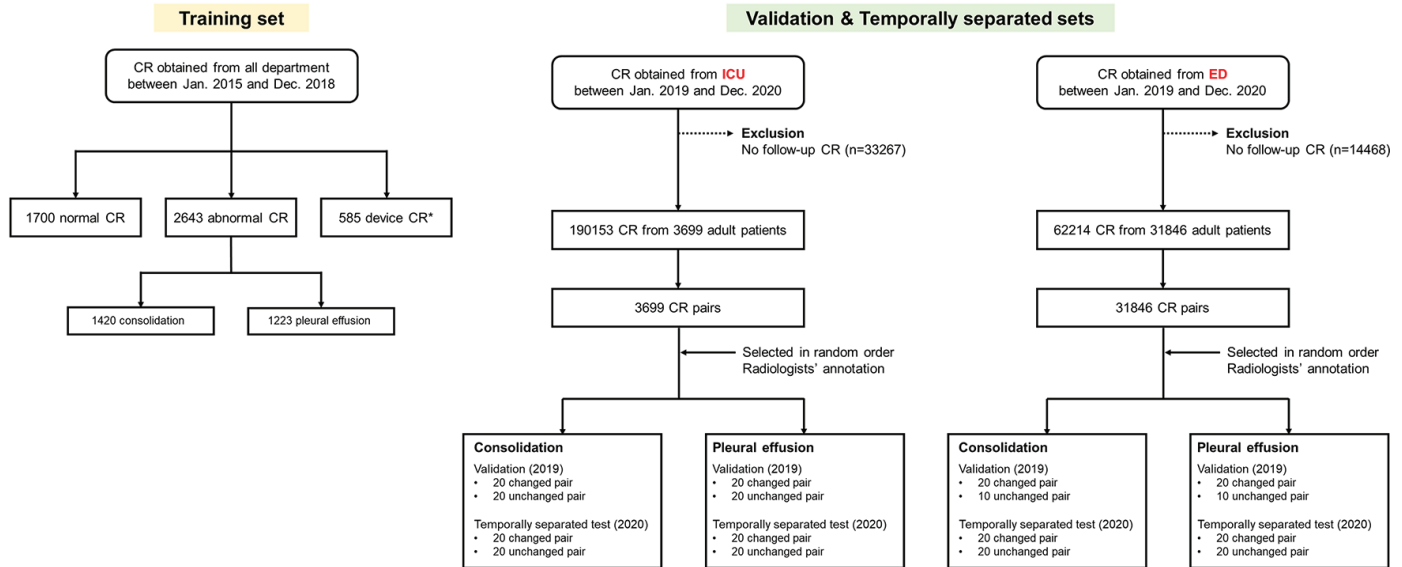


Figure 1. Flowchart illustrating dataset inclusion. *CRs containing medical devices include endotracheal tubes, drainage catheters, central lines, peripherally inserted central catheters, nasogastric tubes, chemoports, and electrocardiogram leads. CR, chest radiograph; ED, emergency department; ICU, intensive care unit.

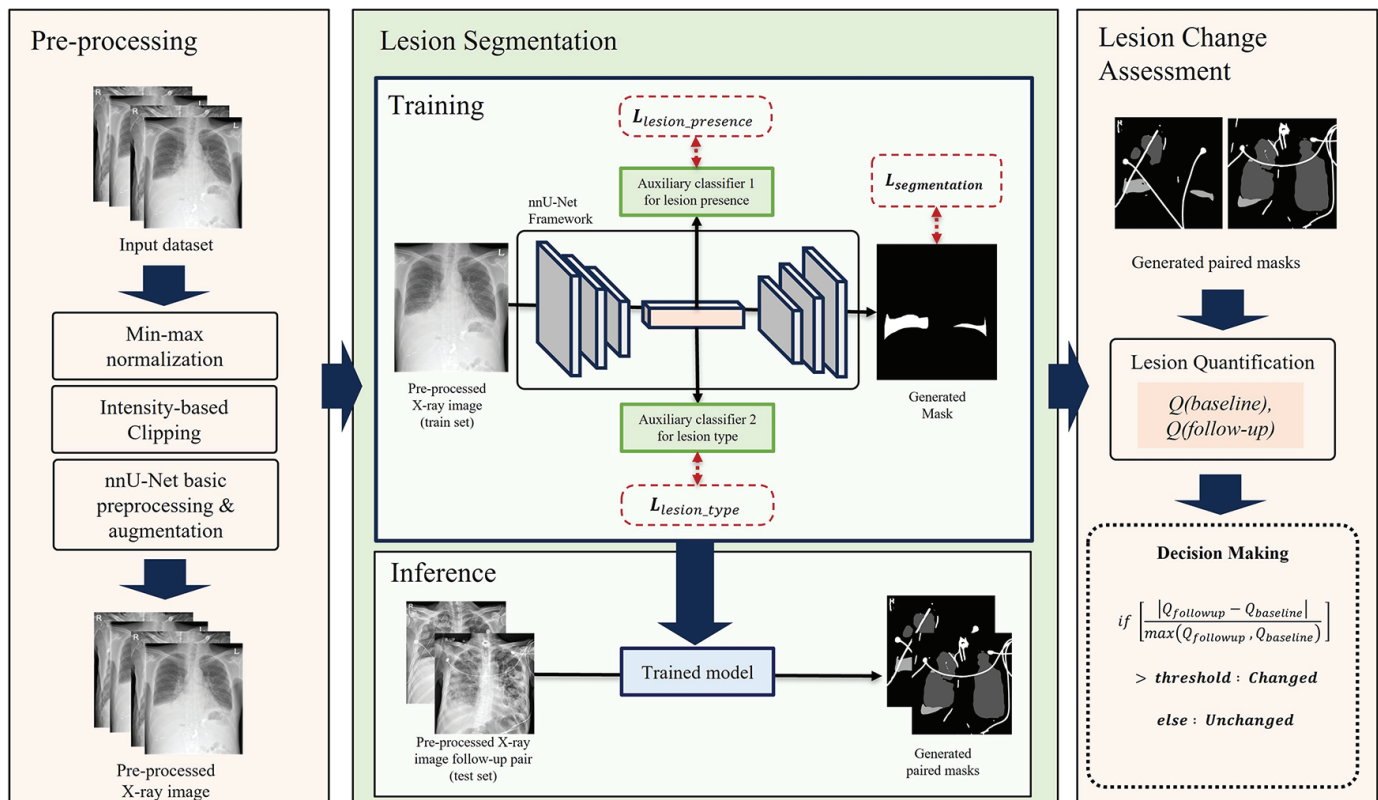


Figure 2. Schematic illustrating the model workflow. The process includes three stages: preprocessing (image normalization and augmentation), lesion segmentation (using a modified nnU-Net with auxiliary classifiers to generate lesion masks), and lesion change assessment (quantifying lesion changes to classify them as changed or unchanged).

difference in quantified lesion areas divided by the larger of the two values to determine the relative change. The tuning set was used to optimize the threshold for changed/unchanged decision-making (Appendix S3). The calculated ratio was then used to classify each paired image as changed/unchanged based on a predefined threshold (Supplementary Figure 1).

$$\text{if } \left[\frac{|Q_{\text{followup}} - Q_{\text{baseline}}|}{\max(Q_{\text{followup}}, Q_{\text{baseline}})} \right] > \text{threshold} : \text{"changed"} \\ \text{else} : \text{"unchanged"}$$

Model training was done using the PyTorch framework and NVIDIA NVIDIA TITAN RTX 24GB GPU (NVIDIA Corporation, Santa Clara, CA, USA). The code for the model architecture is available on GitHub (https://github.com/provbs/CR_DL_FU).

Statistical analysis

The segmentation performance of the model for consolidation and pleural effusion was evaluated using Dice scores. T-tests were conducted to compare models, and *P* values were calculated for their differences. The performance of the model in classifying changed/unchanged was evaluated using the radiologists' results as the reference

standard. The AUC was calculated, and the optimal threshold was determined using the Youden index based on the tuning set results. The accuracy, sensitivity, specificity, positive predictive value, negative predictive value, and F1 score of the temporal validation set were then calculated using the predetermined threshold. The model and radiologist accuracy were compared using the McNemar test. All statistical analyses were conducted using R version 4.3.1 (R Foundation for Statistical Computing).

Results

Dataset characteristics

The training dataset consisted of 1,700 normal CRs, 1,223 with pleural effusion, 1,420 with consolidation, and 585 with medical devices. For the changed/unchanged classifier tuning and temporal validation, 3,699 CR pairs from the ICU and 31,846 from the ED were generated after excluding single CRs without follow-up.

In the ED dataset, 30 pleural effusion pairs (20 changed, 10 unchanged) and 30 consolidation pairs (20 changed, 10 unchanged) from 2019 were included for the changed/unchanged classifier tuning. For temporal validation, 40 pleural effusion pairs (20 changed, 20 unchanged) and 40 consolidation pairs (20 changed, 20 unchanged) from 2019 were selected. In the ICU dataset, 40 pleural effusion pairs (20 changed, 20 unchanged) and 40 consolidation pairs (20 changed, 20 unchanged) from 2019 were used for the changed/unchanged classifier tuning, whereas the same numbers of pleural effusion and consolidation pairs from 2020 were used for temporal validation.

The median interval between CR pairs was 10 days (interquartile range: 1–100 days) in the tuning set and 15 days (interquartile range: 1–72 days) in the temporal validation set. Table 1 shows the demographics in detail.

Performance of lesion segmentation

The nnU-Net with MTL (using two auxiliary classifiers) and medical equipment masks in the training dataset was the best-performing segmentation model, with Dice scores of 0.848 for pleural effusion and 0.841 for consolidation (Table 2 and Supplementary Figure 2).

Incorporating medical equipment labels during training enhanced the Dice score for consolidation by approximately 0.044, although it decreased that for pleural effusion by 0.043, resulting in no major change in the average Dice score. Nevertheless, the qualitative results showed that the model trained with medical equipment labelling considerably reduced misclassification of medical equipment as lesions, a critical distinction in ICU and ED settings. Furthermore, integrating MTL and medical equipment labels improved the average Dice score by 0.015, reducing the difference between lesion types

and achieving a more balanced performance (Figure 3).

Performance of lesion-specific change detection

In the tuning set, the AUCs of the model were 0.747 for consolidation and 0.850 for pleural effusion in the ED, and 0.980 for consolidation and 0.800 for pleural effusion in the ICU (Supplementary Figure 3). To account for different clinical settings, thresholds were determined separately for the ED and ICU. The optimal thresholds derived from the tuning set were 0.26 for consolidation and 0.29 for pleural effusion in the ED and 0.40 for consolidation and 0.55 for pleural effusion in the ICU.

In the temporal validation set, the AUCs of the model were 0.988 for consolidation and 0.883 for pleural effusion in the ED and 0.970 for consolidation and 0.955 for pleural effusion in the ICU (Figure 4). The AUC for consol-

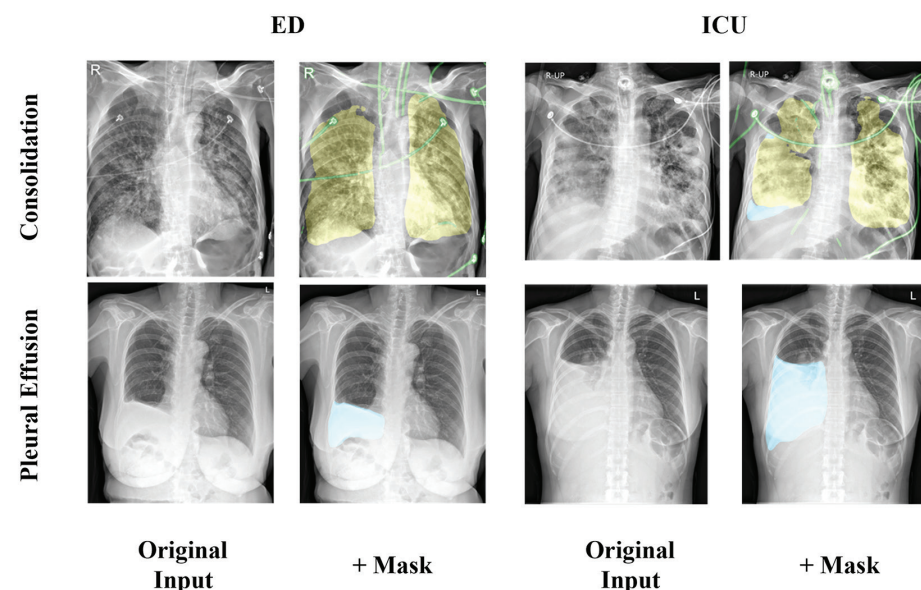


Figure 3. Lesion segmentation results using the best-performing model. The first column shows the original images, and the second column shows the model output in the emergency department (ED) and intensive care unit (ICU). Yellow indicates consolidation, and sky blue indicates pleural effusion.

Table 1. Baseline characteristics for the tuning and temporal validation sets

Characteristics	Tuning set		Temporal validation set	
	ED	ICU	ED	ICU
Number of patients	80	60	80	80
Age, years ^a	66.8 ± 13.7	64.4 ± 13.6	72.0 ± 14.2	61.3 ± 12.6
Sex				
Male	49 (61.2%)	29 (48.3%)	50 (62.5%)	51 (63.8%)
Female	31 (38.8%)	31 (51.7%)	30 (37.5%)	29 (36.2%)
Interval between baseline and follow-up CR ^b	4.0 (1.0, 84.5)	23.0 (5.5, 156.5)	13.5 (1.0, 124.0)	15.5 (3.5, 44.0)

^aData are mean ± standard deviation.

^bData are median with interquartile range in parentheses.

CR, chest radiograph; ED, emergency department; ICU, intensive care unit.

idation was similar between the ED and ICU, whereas the AUC for pleural effusion in the ED was slightly lower than that in the ICU.

Comparisons between the model and the thoracic radiologist

In the ED, the model achieved an accuracy of 0.900 (36/40) for consolidation, with a sensitivity of 1.000 for “changed” and a specificity of 0.800 for “unchanged.” For pleural effusion, the accuracy was 0.825 (33/40), with a sensitivity of 0.850 and specificity of 0.800 (Figure 5). The accuracy of the thoracic radiologist was 0.975 (39/40) for consolidation and 0.950 (38/40) for pleural effusion (Table 3).

In the ICU, the model achieved an accuracy of 0.875 (35/40) for consolidation, with a sensitivity of 0.900 for “changed” and a specificity of 0.850 for “unchanged.” For pleural effusion, the accuracy of the model was 0.800 (32/40), with a sensitivity of 0.600 and specificity of 1.000 (Supplementary Figures 4 and 5). The accuracy of the thoracic radiologist was 0.975 (39/40) for consolidation and 1.000 (40/40) for pleural effusion (Table 3 and Supplementary Figure 5).

When comparing the accuracy of the model and the thoracic radiologist, no significant difference was found for consolidation in the ED [0.900 (36/40) vs. 0.975 (39/40), $P = 0.371$], pleural effusion in the ED [0.825 (33/40) vs. 0.950 (38/40), $P = 0.182$], and consolidation in the ICU [0.875 (35/40) vs. 0.975 (39/40), $P = 0.221$]. However, for pleural effusion in the ICU, the radiologist outperformed the model [1.000 (40/40) vs. 0.800 (32/40), $P = 0.013$] (Supplementary Figure 6).

Discussion

Multiple CRs for follow-up are common in clinical practice. However, current interpretation techniques are largely limited to single images, and automated methods for follow-up CR analysis remain underdeveloped. In this study, we developed and validated a deep-learning model for assessing the changed/unchanged status through lesion-specific segmentation. In validation within the ED and ICU settings, the model classified the changed/unchanged status with an accuracy of 0.875–0.900 for consolidation and 0.800–0.825 for pleural effusion,

comparable to that of the radiologist, except for pleural effusion in the ICU.

Interpreting follow-up CRs poses challenges for both radiologists and deep-learning algorithms due to changes in the thoracic cage caused by variations in posture or inspiration status, as well as background changes such as alterations in medical devices. Consequently, few studies focus on the automated interpretation of CR pairs.^{7,8,12} The approach of determining changes or no changes in the overall image landscape can help prioritize worklists and improve workflow efficiency,^{7,8} although it lacks details on the specific objects involved or the extent of the changes. Unlike previous approaches, we aimed to develop a model that identifies specific abnormal changes. Lesion-specific interpretation is straightforward and enables the detection of clinically relevant changes, such as consolidation increases in patients with pneumonia. With further refinement, it could become a component of an autonomous reporting system. To achieve this, we focused on two major abnormalities—consolidation and pleural effusion—that are commonly monitored for treatment response. These abnormalities were tested in the ED and ICU settings, where they are more prevalent and dynamic than in outpatient clinics or general wards.

Our model achieved an AUC of 0.883–0.988, outperforming a previous study (AUC: 0.687 for pulmonary opacity changes and 0.782 for pleural effusion changes) that determined changed/unchanged status sole-

Table 2. Comparison of lesion segmentation performance across different training settings

Learning method	Dice score		
	Consolidation	Pleural effusion	Average
nnU-Net (without device labels)	0.821*	0.838	0.830
nnU-Net (with device labels)	0.866**	0.794***	0.830
nnU-Net + MTL (with device labels)	0.841	0.848	0.845

* $P < 0.10$, ** $P < 0.05$, *** $P < 0.001$. MTL, multi-task learning.

Table 3. Evaluation metrics assessed on the temporal validation set

Evaluator	Lesion type	AUC	Accuracy	Sensitivity	Specificity	PPV	NPV	F1 score
ED								
Model	Consolidation	0.988 [0.968, 1.000]	0.900 (36/40) [0.763, 0.972]	1.000 (20/20) [0.832, 1.000]	0.800 (16/20) [0.563, 0.943]	0.833 (20/24) [0.626, 0.953]	1.000 (16/16) [0.794, 1.000]	0.909
	Pleural effusion	0.883 [0.800, 0.993]	0.825 (33/40) [0.672, 0.927]	0.850 (17/20) [0.621, 0.968]	0.800 (16/20) [0.563, 0.943]	0.810 (17/21) [0.581, 0.946]	0.842 (16/19) [0.604, 0.966]	0.829
Radiologist	Consolidation	-	0.975 (39/40) [0.868, 0.999]	1.000 (20/20) [0.832, 1.000]	0.950 (19/20) [0.751, 0.999]	0.952 (20/21) [0.762, 0.999]	1.000 (19/19) [0.824, 1.000]	0.976
	Pleural effusion	-	0.950 (38/40) [0.831, 0.994]	0.950 (19/20) [0.751, 0.999]	0.950 (19/20) [0.751, 0.999]	0.950 (19/20) [0.751, 0.999]	0.950 (19/20) [0.751, 0.999]	0.950
ICU								
Model	Consolidation	0.970 [0.931, 1.000]	0.875 (35/40) [0.732, 0.958]	0.900 (18/20) [0.683, 0.988]	0.850 (17/20) [0.621, 0.968]	0.857 (18/21) [0.637, 0.970]	0.895 (17/19) [0.669, 0.987]	0.878
	Pleural effusion	0.955 [0.908, 1.000]	0.800 (32/40) [0.644, 0.909]	0.600 (12/20) [0.361, 0.809]	1.000 (20/20) [0.832, 1.000]	1.000 (12/12) [0.735, 1.000]	0.714 (20/28) [0.513, 0.868]	0.750
Radiologist	Consolidation	-	0.975 (39/40) [0.868, 0.999]	1.000 (20/20) [0.832, 1.000]	0.950 (19/20) [0.751, 0.999]	0.952 (20/21) [0.762, 0.999]	1.000 (19/19) [0.824, 1.000]	0.976
	Pleural effusion	-	1.000 (40/40) [0.912, 1.000]	1.000 (20/20) [0.832, 1.000]	1.000 (20/20) [0.832, 1.000]	1.000 (20/20) [0.832, 1.000]	1.000 (20/20) [0.832, 1.000]	1.000

Data in the parentheses are the number of CR pairs. AUC, area under curve; ED, emergency department; ICU, intensive care unit; NPV, negative predictive value; PPV, positive predictive value.

ly based on lesion persistence.¹² It was also similar to prior non-lesion-specific models, which have AUCs of 0.800–0.858.^{7,8} This performance may be due to the accurate lesion segmentation of our model, achieving a Dice score of up to 0.845 in the training set, and its

reduced misclassification of medical devices as lesions. Singh et al.¹² reported that the mis-segmentation of medical devices as pulmonary opacities is a challenge. To address this, we specifically trained our model on CRs with medical devices, ensuring robust per-

formance in the ICU and ED settings where they are almost always present.

The accuracy of our model was similar to that of the radiologist for consolidation in the ICU and ED and for pleural effusion in the ED, though slightly lower. The decision of the radiologist on whether a condition had changed or remained unchanged closely aligns with the reference standard. Although consolidation and pleural effusion are typically assessed qualitatively in routine practice, the threshold of readers may be interchangeable. Our model showed considerably lower performance than that of the radiologist for pleural effusion in the ICU. This may be related to the position of the patient in the ICU. In patients in the supine position, both consolidation and pleural effusion can appear as diffusely increased opacity, making differentiation difficult. Pleural fluid tends to spread under gravity, making the margins of effusion indistinct. Radiologists also assess changes in pleural effusion while considering positional changes, which may be challenging for our model. Notably, all incorrect ICU pleural effusion classifications occurred in “changed” cases, whereas the model correctly identified all stable cases. We therefore consider that the model can

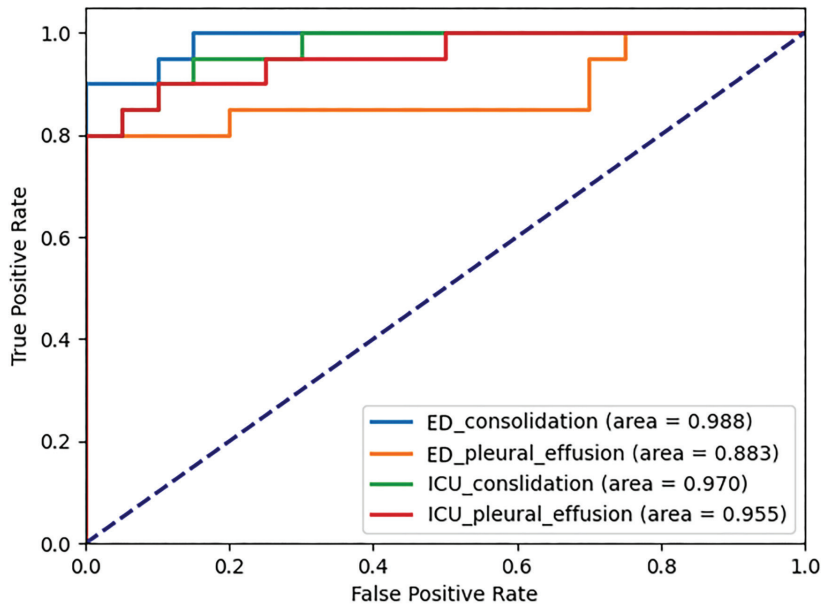


Figure 4. ROC curves illustrating algorithm performance for each department and lesion type in the temporal validation set. The shaded areas represent the area under the ROC curves. ED, emergency department; ICU, intensive care unit; ROC, receiver operating characteristic.

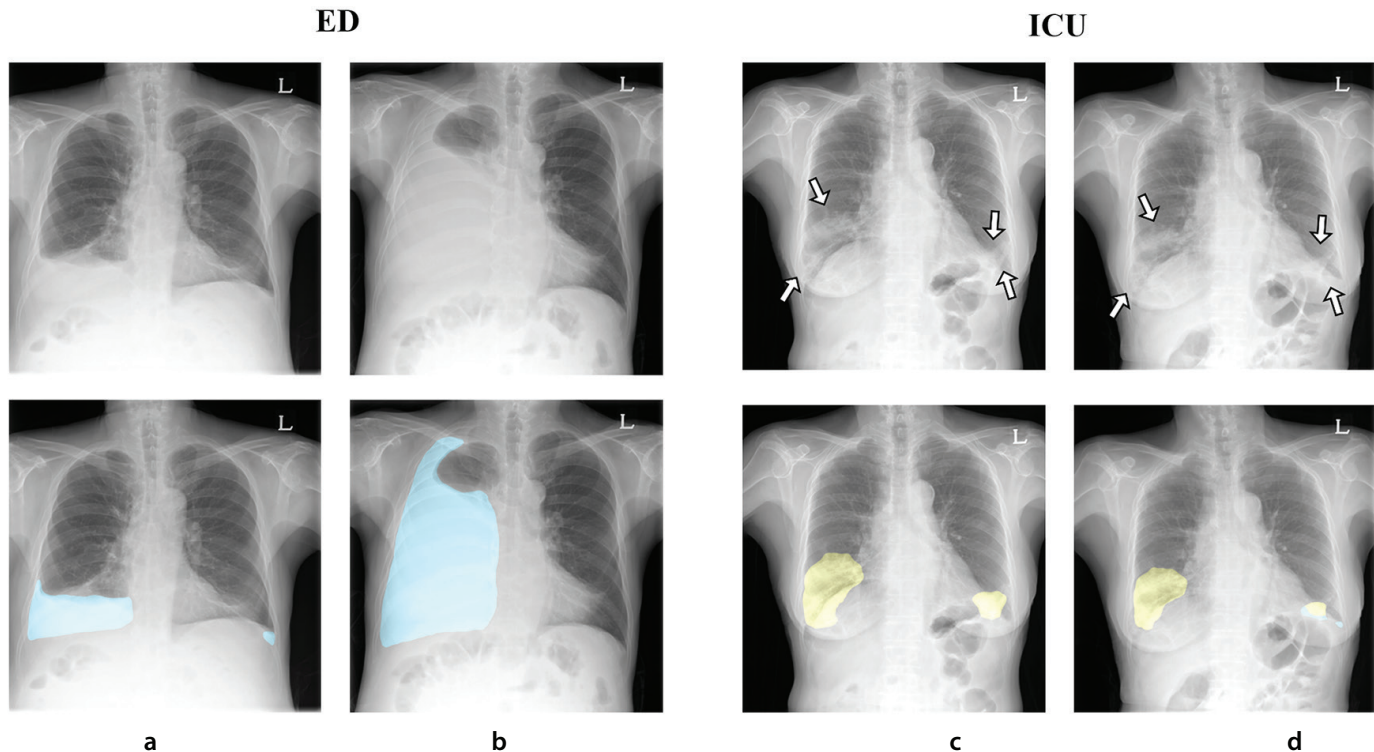


Figure 5. Examples of determining changed/unchanged status in the emergency department (ED) and intensive care unit (ICU). (a, b) In the ED, a right pleural effusion increased between baseline (a) and follow-up chest radiograph (CR) (b). The model detected and segmented the effusion (sky-blue areas) and classified it as changed. The pixel difference was 19.299 (75% ratio). (c, d) In the ICU, patchy consolidation in both lower lobes (arrows) remained unchanged between baseline (c) and follow-up CR (d), matching the reference standard. The model segmented the consolidation (yellow areas) and classified it as unchanged. The pixel difference was -2.253 (36.9% ratio).

adequately triage stable pleural effusion, but reduced sensitivity in supine patients remains an important limitation that warrants further refinement. In addition, the limited size of the tuning set (40 pairs) may have led to overfitting of the threshold for pleural effusion, contributing to skewed results. Although this should be addressed in future studies, our findings provide proof of concept for the feasibility of lesion-specific segmentation in change status detection.

Unlike preexisting non-lesion-specific models, which primarily filter grossly stable CR pairs, our lesion-specific model offers dual functionality. It can inform and prioritize changes for physician review while simultaneously filtering stable cases. Previous approaches based on registration and subtraction within pairs are limited compared with a segmentation-based method, which has the potential to be applied to multiple CRs in longitudinal follow-up, enabling the extraction of lesion extent as time-series data with quantification. Recent advances in language models have enabled training on large-scale, weakly labeled data for multi-label, multi-class change detection and even automated report generation.^{15,16} In contrast, our model leverages radiologist-provided hard labeling, which ensures disease-specific accuracy and offers interpretable, intuitive visual explanations of the degree of change. These strengths may provide potential applicability, working synergistically with text generation models as part of automated reporting systems. However, our model is currently limited to two abnormalities: consolidation and pleural effusion. Expanding its capabilities to include other major abnormalities, such as nodules or interstitial opacities, may be a valuable next step. Furthermore, improving lesion segmentation and consideration of position change are warranted.

Our study has some limitations. First, as a single-center retrospective study, it may have selection bias and limited generalizability. Second, the experiment was conducted using datasets from the same institution. Although the datasets do not overlap, true external validation was not performed. Third, the tuning and temporal validation sets were relatively small. Since our model was designed specifically for consolidation and pleural effusion, only patients with at least

one of these abnormalities were eligible. This may contribute to the performance differences between the tuning and temporal validation sets. Further validation in a larger population is necessary.

In conclusion, lesion-specific segmentation enables the deep-learning-based model to determine the changed/unchanged status of consolidation and pleural effusion based on changes in their extent.

Footnotes

Conflict of interest disclosure

The authors declared no conflicts of interest.

Funding

This work was supported by the Korea Medical Device Development Fund grant funded by the Korea government (the Ministry of Science and ICT, the Ministry of Trade, Industry and Energy, the Ministry of Health & Welfare, the Ministry of Food and Drug Safety) (Project Number: 2710002589, RS-2023-00254209).

Supplementary: <https://d2v96fxpocvxx.cloudfront.net/51ec7646-9122-48c7-a1d9-90e9cb16981b/content-images/bb9cdf66-d592-417d-84f0-0c36bf3fe5b3.pdf>

Appendix: <https://d2v96fxpocvxx.cloudfront.net/51ec7646-9122-48c7-a1d9-90e9cb16981b/content-images/62a39fef-d33a-4a92-9e80-9f838b46a779.pdf>

References

1. Expert Panel on Thoracic Imaging; Morris MF, Henry TS, Raptis CA, et al. ACR appropriateness criteria® workup of pleural effusion or pleural disease. *J Am Coll Radiol.* 2024;21(6S):S343-S352. [\[Crossref\]](#)
2. Krishna R, Antoine MH, Alahmadi MH, Rudrappa M. Pleural Effusion. 2024 Aug 31. In: StatPearls [Internet]. Treasure Island (FL): StatPearls Publishing; 2025 Jan-. [\[Crossref\]](#)
3. Karkhanis VS, Joshi JM. Pleural effusion: diagnosis, treatment, and management. *Open Access Emerg Med.* 2012;4:31-52. [\[Crossref\]](#)
4. Little BP, Gilman MD, Humphrey KL, Alkasab TK, Gibbons FK, Shepard JA, et al. Outcome of recommendations for radiographic follow-up of pneumonia on outpatient chest radiography. *AJR Am J Roentgenol.* 2014;202(1):54-9. [\[Crossref\]](#)
5. Gershengorn HB, Wunsch H, Scales DC, Rubenfeld GD. Trends in use of daily chest radiographs among us adults receiving mechanical ventilation. *JAMA Netw Open.* 2018;1(4):e181119. [\[Crossref\]](#)
6. Oba Y, Zaza T. Abandoning daily routine chest radiography in the intensive care unit: meta-analysis. *Radiology.* 2010;255(2):386-95. [\[Crossref\]](#)
7. Cho K, Kim J, Kim KD, et al. Music-ViT: a multi-task Siamese convolutional vision transformer for differentiating change from no-change in follow-up chest radiographs. *Med Image Anal.* 2023;89:102894. [\[Crossref\]](#)
8. Yun J, Ahn Y, Cho K, et al. Deep learning for automated triaging of stable chest radiographs in a follow-up setting. *Radiology.* 2023;309(1):e230606. [\[Crossref\]](#)
9. Li MD, Arun NT, Gidwani M, et al. Automated assessment and tracking of COVID-19 pulmonary disease severity on chest radiographs using convolutional siamese neural networks. *Radiol Artif Intell.* 2020;2(4):e200079. [\[Crossref\]](#)
10. Huang T, Yang R, Shen L, et al. Deep transfer learning to quantify pleural effusion severity in chest X-rays. *BMC Med Imaging.* 2022;22(1):100. [\[Crossref\]](#)
11. Lim CY, Cha YK, Chung MJ, et al. Estimating the volume of nodules and masses on serial chest radiography using a deep-learning-based automatic detection algorithm: a preliminary study. *Diagnostics (Basel).* 2023;13(12):2060. [\[Crossref\]](#)
12. Singh R, Kalra MK, Nitiwarangkul C, et al. Deep learning in chest radiography: detection of findings and presence of change. *PLoS One.* 2018;13(10):e0204155. [\[Crossref\]](#)
13. Park B, Cho Y, Lee G, et al. A curriculum learning strategy to enhance the accuracy of classification of various lesions in chest-PA X-ray screening for pulmonary abnormalities. *Sci Rep.* 2019;9(1):15352. [\[Crossref\]](#)
14. Isensee F, Jaeger PF, Kohl SAA, Petersen J, Maier-Hein KH. nnU-Net: a self-configuring method for deep learning-based biomedical image segmentation. *Nat Methods.* 2021;18(2):203-211. [\[Crossref\]](#)
15. Yu K, Ghosh S, Liu Z, Deible C, Poynton CB, Batmanghelich K. Anatomy-specific progression classification in chest radiographs via weakly supervised learning. *Radiol Artif Intell.* 2024;6(5):e230277. [\[Crossref\]](#)
16. Wang Z, Deng Q, So TY, Chiu WH, Lee K, Hui ES. Disease probability-enhanced follow-up chest X-ray radiology report summary generation. *Sci Rep.* 2025;15(1):26930. [\[Crossref\]](#)

Appendix S1. Medical equipment data in final segmentation training

Using the 4.593 chest radiographs (CRs) of general patients, we trained a nnU-Net model with default settings for lesion segmentation. The training was conducted for 1.000 epochs using the Pytorch framework on an NVIDIA TITAN RTX 24GB GPU. The 250 images from the additional CR dataset, containing only labeled medical devices from patients in the intensive care unit (ICU), were then processed using the trained segmentation model. This inference generated 250 CR images with both pulmonary lesions and medical devices altogether.

We did not evaluate or optimize the lesion segmentation performance specifically for this 250 CR dataset, as it represents a relatively small proportion of the entire training dataset in terms of lesion data. Its primary purpose is to provide the final model with explicit information on medical devices rather than lesion-related information.

By including this dataset in our final training dataset, we aimed to enable the model to semantically learn to better differentiate medical equipment from lesions in ICU and emergency department (ED) datasets, thereby reducing the misclassification of medical devices as lesions, resulting in better segmentation performance in general. As shown in Table 1, this additional dataset contributed to improving the performances of our final segmentation model by addressing this challenge effectively.

Appendix S2. Details of the segmentation model

Input preprocessing

The CRs in the training/tuning/temporal validation datasets were all preprocessed with the following steps: Firstly, intensi-

ty-based clipping was implemented, where the top and bottom 0.5% of pixel intensities were clipped. This was done to mitigate the influence of high-intensity outliers, such as L&R markers or other unexpected artifacts on the CR. Secondly, min-max normalization was conducted to scale pixel values of the images within the range of 0–1. Both steps were done to ensure consistency and facilitated convergence during the segmentation model training explained after. Other preprocessing and augmentations were conducted in accordance with the nnU-Net methodology, accounting for median shape, distribution of spacings, intensity distribution, and image modality within the training dataset.

Model structure and training details

The model employed in this study is a modified nnU-Net with two auxiliary classifiers incorporated between the encoder and segmentation decoder. The auxiliary classifiers used here are quite simple: two fully connected layers with a ReLu activation in between. These auxiliary classifiers are intended to enable the shared encoder to progressively focus on features related to lesion type and presence during its training, thereby passing more pertinent information to the segmentation decoder. The total loss was calculated as the sum of the original nnU-Net segmentation loss and the losses from the auxiliary classifiers, lesion presence and lesion type classifier, as follows:

$$L_{\text{total}} = L_{\text{seg}} + (L_{\text{lesion_presence}} + L_{\text{lesion_type}}) \quad (1)$$

Severe augmentations, including Gaussian noise and Gaussian blur transformations, were adopted to enhance segmentation performance on the noisier ICU/ED CRs.

During inference, we excluded regions with fewer than 50 pixels in the predicted mask to eliminate insignificant noise, as most mask sizes exceed 2000 × 2000 pixels,

with some surpassing 3000 pixels on one side. This threshold was chosen based on the observation that smaller regions often represent false positives or artifacts rather than meaningful predictions.

Appendix S3. Optimal threshold determination for assessment decision-making

To select the optimal threshold, we employed Youden's J statistic, which measures the effectiveness of a threshold in terms of maximizing the true positive rate while minimizing the false positive rate. For each threshold t_i , where t_i increases by 0.01 from 0.00 to 1.00, the true positive ratio (TPR) and false positive ratio (FPR) can be computed, and the value of J at t_i is calculated as:

$$J(t) = TPR(t) - FPR(t) \quad (2)$$

The optimal threshold can be determined by identifying the highest value of J, representing the most balanced threshold between sensitivity and specificity:

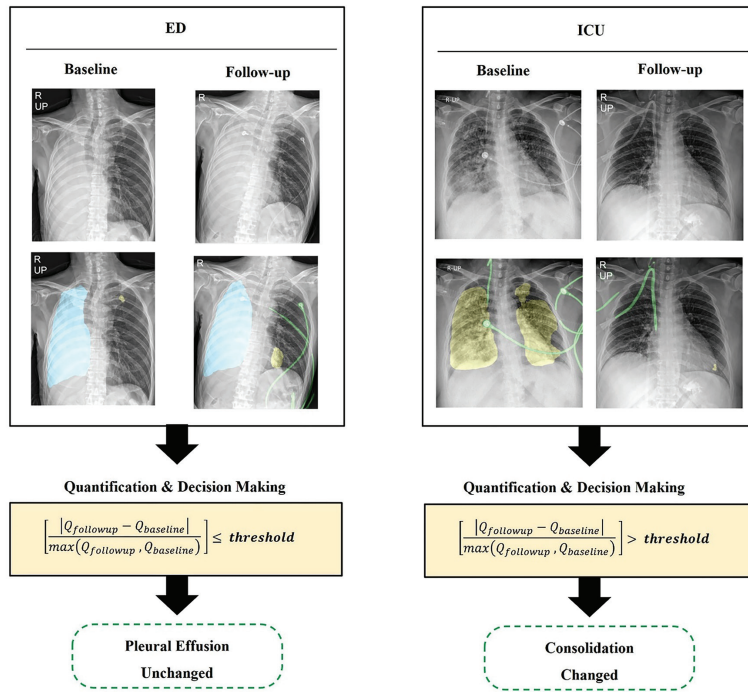
$$t_{\text{optimal}} = \text{argmax}_{t_i} J(t_i) \quad (3)$$

If multiple values of t_{optimal} exist, we selected the lowest threshold value to increase sensitivity and reduce the chance of false negatives:

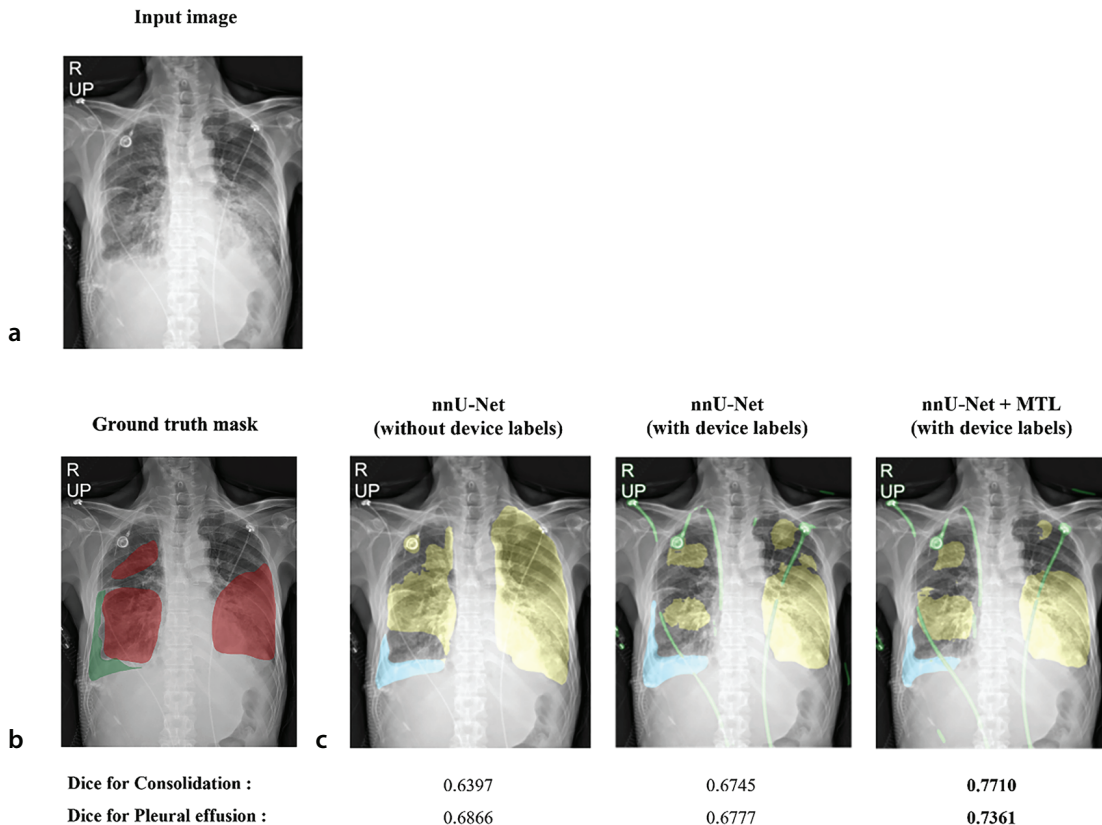
$$t_{\text{selected}} = \min(t_{\text{optimal},i}), \text{ for } i = 1, 2, \dots, n \quad (4)$$

This approach minimizes the misclassification of true positives as negatives, which is crucial in settings such as the ICU/ED, where timely intervention is essential. We have inferred the tuning set using the trained segmentation model and then calculated the optimal threshold accordingly.

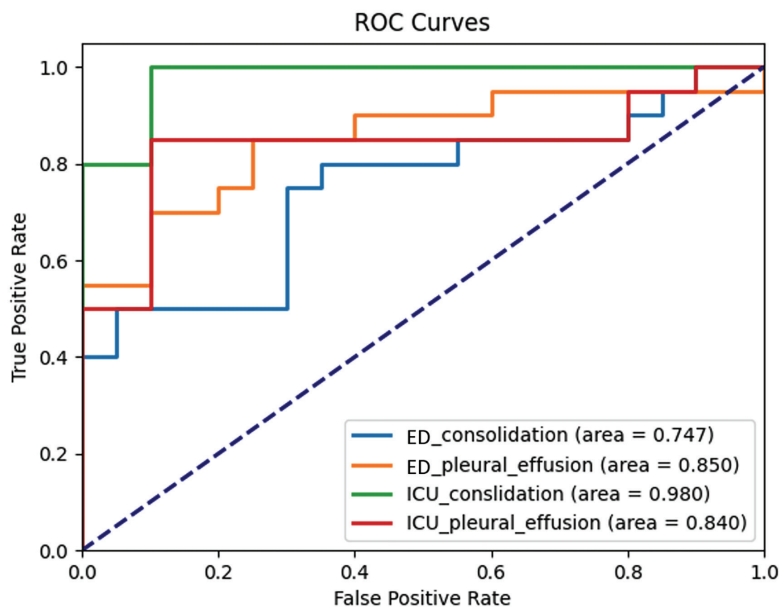
Supplementary Figures



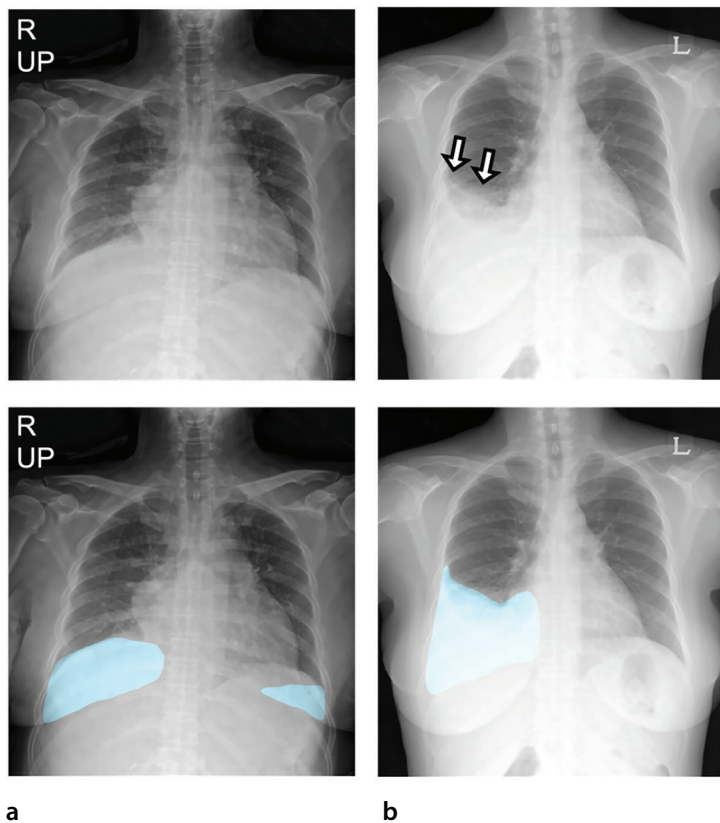
Supplementary Figure 1. Determination of unchanged/changed in the ED and ICU. The yellow area represents consolidation, while the sky-blue area indicates pleural effusion. ED, emergency department; ICU, intensive care unit.



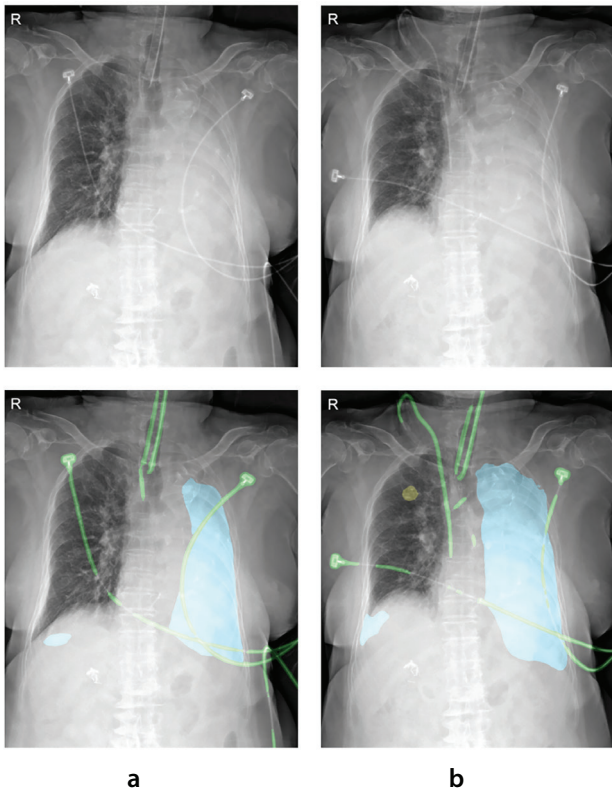
Supplementary Figure 2. Segmentation results across models with various training settings. (a) Original input image. (b) The ground-truth mask by a thoracic radiologist. The red area represents a consolidation, while the green area indicates pleural effusion. (c) Segmentation results from three different settings. The yellow area represents consolidation, while the sky-blue area indicates pleural effusion. Green areas represent the segmentation of medical devices. The Dice score was calculated for each abnormality. MTL, multi-task learning.



Supplementary Figure 3. Receiver operating characteristic (ROC) curves show the performance of the algorithm for each department and the abnormality lesion in the tuning set. Area means the area under the ROC curves. ED, emergency department; ICU, intensive care unit.



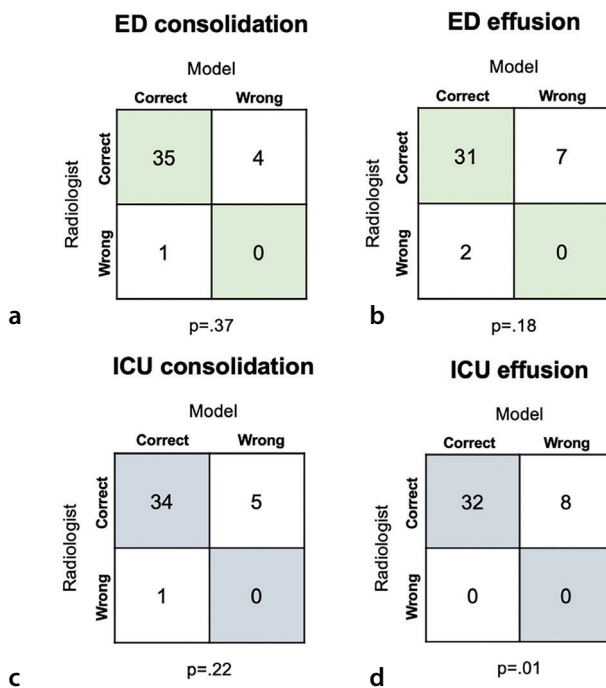
Supplementary Figure 4. Example of failure in detecting “changed” in pleural effusion in the intensive care unit. (a) Baseline chest radiograph (CR) obtained in a semi-supine position showed no clear fluid level, but the model segmented increased opacity along both hemidiaphragms as pleural effusion (sky-blue areas). The presence of true effusion could not be confirmed on CR alone. (b) In the follow-up CR acquired in an upright position, overt right pleural effusion (arrows) was evident and correctly segmented by the model (sky-blue areas). The radiologist interpreted this case as “changed,” whereas the model classified it as “unchanged.”



a

b

Supplementary Figure 5. Example of failure in detecting “unchanged” pleural effusion in the intensive care unit. (a) Baseline chest radiograph (CR) and (b) follow-up CR obtained in the supine position both showed diffuse left pleural effusion opacifying the left hemithorax. Due to slight rightward rotation on the baseline CR, the segmented area for pleural effusion (sky-blue areas) appeared smaller, leading the model to classify the case as “changed,” whereas the radiologist interpreted it as “unchanged.”



Supplementary Figure 6. Comparisons between the model and radiologist in assessing change/unchanged status of consolidation or pleural effusion. (a) for consolidation in the emergency department (ED), (b) for effusion in the ED, (c) for consolidation in the intensive care unit (ICU), and (d) for effusion in the ICU. *P* values were calculated using the McNemar test to compare accuracy.



New lens on breast health: harnessing high-b-value synthetic diffusion-weighted imaging for breast lesion characterization

✉ Serap Karabiyik¹
 ✉ Saime Ramadan²
 ✉ Emil Settarzade³
 ✉ Ali İlker Filiz⁴
 ✉ Hatice Ozturkmen Akay⁵

¹Istanbul Training and Research Hospital, Clinic of Radiology, İstanbul, Türkiye

²Baskent University Istanbul Hospital, Department of Pathology, İstanbul, Türkiye

³Zollernalb Klinikum, Radiologie Abteilung, Balingen, Germany

⁴Baskent University Istanbul Hospital, Department of General Surgery, İstanbul, Türkiye

⁵Baskent University Istanbul Hospital, Department of Radiology, İstanbul, Türkiye

PURPOSE

This study aims to evaluate the diagnostic efficacy of synthetic diffusion-weighted imaging (sDWI) at various high b-values in distinguishing malignant from benign breast lesions and to compare its performance with that of conventional DWI (cDWI).

METHODS

After the exclusion of 22 lesions, 63 women (age range, 24–99 years; mean age, 53.7 ± 15.1 years) with 68 suspicious breast lesions on ultrasound who underwent multiparametric breast magnetic resonance imaging before biopsy between January 2021 and April 2023 were included in this retrospective study. According to the pathological results, lesions were classified as malignant or benign. Volumetric mask images were defined. The lesion signal/normal breast signal ratio [relative signal intensity (rSI)] was measured on different diffusion-weighted images (cDWI at $b = 800$ and 1500 s/mm^2 ; sDWI at $b = 1500$ – 5000 s/mm^2), and lesion SI on apparent diffusion coefficient (ADC) 0– 800 and ADC 0 – 1500 maps (mADC) was calculated. The diagnostic performances of these parameters were evaluated using a receiver operating characteristic curve analysis and the DeLong test in both the mass and non-mass lesion groups.

RESULTS

A total of 32 (47.06%) benign and 36 (52.94%) malignant lesions were identified. Malignant lesions exhibited significantly higher rSI values on cDWI 800 , cDWI 1500 , sDWI 1500 , sDWI 2000 , and sDWI 3000 (P values: <0.001 , <0.001 , <0.001 , <0.001 , 0.03) and lower mADC 800 and mADC 1500 values (P values: 0.01 and 0.03). In mass lesions, synthetic b 1500 and conventional b 1500 demonstrated diagnostic accuracy comparable with that of routine mADC 800 and mADC 1500 . However, in non-mass lesions, high-b-value DWI maps ($b \geq 2000$ s/mm^2) significantly outperformed mADC and cDWI in differentiating malignant from benign lesions. The highest diagnostic accuracy in non-mass lesions was observed with rSIC 4000 [area under the curve (AUC) = 0.87], whereas in mass lesions, rSIC 1500 exhibited the highest diagnostic performance (AUC = 0.79).

CONCLUSION

The optimal b-value for DWI differs between mass and non-mass breast lesions, emphasizing the need for separate evaluation protocols. Although high-b-value sDWI provides limited added diagnostic value in mass lesions, it significantly improves malignancy detection in non-mass lesions, outperforming cDWI and ADC mapping.

CLINICAL SIGNIFICANCE

This study underscores the need for a tailored DWI protocol for optimal breast lesion characterization, particularly for non-mass lesions, where high-b-value synthetic imaging enhances diagnostic accuracy.

KEYWORDS

Breast, synthetic diffusion-weighted imaging, high-b-value, breast cancer, magnetic resonance imaging

Corresponding author: Serap Karabiyik

E-mail: serapyucl@gmail.com

Received 21 December 2024; revision requested 27 January 2025; last revision received 26 March 2025; accepted 08 April 2025



Epub: 20.05.2025

Publication date: 02.01.2026

DOI: 10.4274/dir.2025.253190

You may cite this article as: Karabiyik S, Ramadan S, Settarzade E, Filiz Al, Ozturkmen Akay H. New lens on breast health: harnessing high-b-value synthetic diffusion-weighted imaging for breast lesion characterization. *Diagn Interv Radiol.* 2026;32(1):40-46.

Magnetic resonance imaging (MRI) is an imaging modality with high sensitivity, frequently used in breast imaging.¹ Diffusion-weighted imaging (DWI) is routinely added to protocols worldwide.² The addition of DWI to dynamic contrast-enhanced MRI (DCE-MRI) has been shown to improve the differentiation between malignant and benign breast lesions, thereby increasing specificity.^{3,4} However, the optimal b-values for DWI and the appropriate number of b-values to acquire remain subjects of debate.⁵⁻⁷ At low b-values, benign lesion signals cannot be sufficiently suppressed, whereas at high b-values, the signal-to-noise ratio (SNR) decreases. Taking both images simultaneously increases the acquisition time.⁸⁻¹⁰ The European Society of Breast Imaging recommends acquiring at least two b-values for breast DWI: a low b-value (0–50 s/mm²) and a high b-value (800 s/mm²). The selection of 800 s/mm² as the high b-value represents a balanced compromise, ensuring standardized imaging quality while maintaining sufficient SNR and diagnostic accuracy.⁶ Meanwhile, the Quantitative Imaging Biomarkers Alliance (QIBA) suggests acquiring a minimum of two b-values: a low b-value (0–50 s/mm²), an intermediate b-value (~100 s/mm²), and a high b-value (600–800 s/mm²). The QIBA emphasizes the inclusion of an intermediate b-value to enhance the precision of ADC measurements.¹¹

Synthetic DWI (sDWI) is derived from conventional DWI (cDWI) directly acquired using at least two distinct b-values. It has the potential to address the limitations of cDWI by effectively suppressing background signal at very high b-values, all without the need for additional scanning time.^{10,12} There are numerous studies on sDWI conducted on other organs, such as the liver and prostate.

Main points

- The optimal b-value for diffusion-weighted imaging (DWI) differs between mass and non-mass breast lesions.
- High-b-value synthetic DWI ($b \geq 2000$ s/mm²) demonstrated superior diagnostic performance in non-mass breast lesions compared with conventional apparent diffusion coefficient (ADC) maps and DWI ($b = 800$ s/mm²), whereas in mass lesions, it offered no diagnostic advantage over conventional DWI and ADC mapping.
- There is a need for tailored DWI protocols for mass and non-mass lesions to optimize breast cancer detection and lesion characterization.

However, a limited number of studies have investigated the diagnostic performance of sDWI.^{9,12-15}

The diagnostic utility of DWI in non-mass lesions is more variable, as non-mass enhancement often exhibits overlapping ADC values between benign and malignant cases, reducing specificity.^{16,17} Consequently, optimizing DWI protocols, including the selection of appropriate b-values and synthetic imaging techniques, is essential for improving lesion differentiation, with a particular focus on the mass or non-mass features of the lesions.

Therefore, the present study aims to investigate the diagnostic efficacy of sDWI with different high b-values for differentiating malignant breast lesions from benign ones and compare it with cDWI.

Methods

Study population and magnetic resonance imaging protocol

This single-center retrospective study was approved by the institutional review board (project no.: KA23/73) on March 2, 2023, and was conducted in compliance with the Health Insurance Portability and Account-

ability Act. Informed consent was waived due to the retrospective nature of the study.

Eighty-five women with 90 suspicious mass and non-mass breast lesions (Breast Imaging Reporting and Data System 4A–5) who underwent tru-cut biopsies between January 2021 and April 2023 were retrospectively evaluated. The patients underwent breast MRI either 1 month before or after the biopsy procedure. Indications for breast MRI included preoperative staging, high-risk patient screening, or equivocal mammogram and ultrasound results. After excluding 22 lesions, 68 consecutive suspicious lesions in 63 patients (age range: 24–99 years; mean age: 53.7 ± 15.1 years) were included in the study (Figure 1). The lesions were classified as malignant or benign based on pathological results from tru-cut or excisional biopsy.

All MRIs were performed in the prone position using a 4-channel breast coil on a 1.5T MRI scanner (MAGNETOM Avanto, Siemens Healthcare, Erlangen, Germany). As part of the routine clinical protocol, the following sequences were acquired: axial turbo spin-echo T1, turbo inversion recovery magnitude, and DCE-MRI (3D fat-saturated gradient-echo axial sequence) after intravenous injection of 0.2 mL/kg gadoterate meglumine (Dotarem).

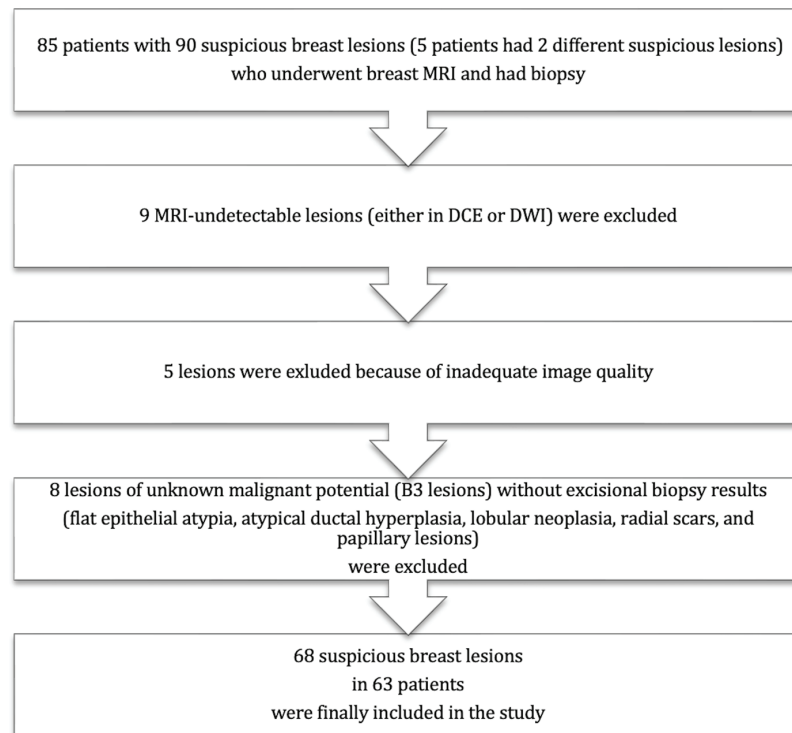


Figure 1. Flowchart of the patient inclusion and exclusion criteria. MRI, magnetic resonance imaging; DCE, dynamic contrast-enhanced; DWI, diffusion-weighted imaging.

Conventional and synthetic diffusion-weighted imaging and image analysis

DWI was acquired using spin-echo planar imaging with spectral attenuated inversion recovery fat suppression and b-values of 0, 100, 800, and 1500 s/mm² (repetition time/echo time: 7,400/78 ms; slice thickness: 4 mm; number of excitations: 5; matrix size: 63 × 164; field of view: 340 × 390 mm; acquisition time: 6 minutes 32 seconds).

All DWI images were converted from DICOM format using the dcm2niix (Rorden, 2021). Noise was removed using the “dwide-noise” command in the MRtrix utility. Images with b-values of 0, 100, 800, and 1500 s/mm² were extracted using fslroi. Synthetic images with calculated b-values of 1500, 2000, 3000, 4000, and 5000 s/mm² were created using a monoexponential decay model via FSL 6.0.5 (FMRIB Software Library).¹⁸ Apparent diffusion coefficient maps (mADC) were also created with the same software.

A radiologist with 4 years of experience in breast radiology manually segmented the lesions on each slice of b = 0 DWI images, with the aid of DCE-MRI, avoiding necrotic, hemorrhagic, or cystic components using ITK-SNAP software (developed by the Penn Image Computing and Science Laboratory, University of Pennsylvania).¹⁹ For multifocal or multicentric tumors, only the index lesion was segmented. Volumetric mask images of the lesion and contralateral normal breast fibroglandular tissue were generated using the volume of interest (VOI) method based on b = 0 images and DCE with ITKs-SNAP (Figure 2). The VOI of the contralateral normal breast was carefully selected to minimize fatty tissue inclusion and match the volume of the mass lesion as closely as possible.

The average SI in the segmented lesion and contralateral normal breast was automatically calculated for each sDWI and cDWI image and mADC using “fslmaths.” relative signal intensity (rSI) for each DWI was calculated as follows:

$$rSI = \frac{(\text{mean SI of lesion})}{(\text{mean SI of contralateral normal breast})}$$

Both rSI values for different DWI maps and the mean SI for different mADC were analyzed.

Statistical analysis

The mean and standard deviation were calculated for each cDWI and sDWI in both

benign and malignant lesions, as well as in mass and non-mass subgroups. Based on the normality of the data, the Kolmogorov-Smirnov test was performed, followed by independent samples t-tests or Mann-Whitney U tests for between-group comparisons. Using receiver operating characteristic (ROC) curve analysis, the diagnostic efficacy of these values in malignant and benign lesions was evaluated. The DeLong test was used to assess whether sDWI images exhibited diagnostic superiority over cDWI and conventional mADC. Statistical analysis were performed using SPSS 22.0 and RStudio.

Results

The mean tumor size was 17.54 ± 5.23 mm (range: 6–80 mm). A total of 32 (47.06%) benign and 36 (52.94%) malignant lesions were identified. The characteristics of the tumors and patients are summarized in Table 1.

Malignant lesions exhibited significantly higher rSI values in cDWI800, cDWI1500, sDWI1500, sDWI2000, and sDWI3000 images and lower ADC800 and ADC1500 values (Table 2). Among the evaluated parameters, rSIC1500 demonstrated the highest diagnostic performance in ROC curve analysis [area under the curve (AUC) = 0.79], followed by rSIS1500 (AUC = 0.77). However, the DeLong test analysis revealed no statistically significant difference in AUC values between rSIC1500, rSIS1500, rSIS2000, ADC800, and ADC1500. Nevertheless, rSIC1500 was superior to rSIC800 and other high-b-value synthetic images (Table 2).

When mass lesions were analyzed separately, ADC800 and ADC1500 values were significantly lower in the malignant group, whereas rSIC800, rSIC1500, rSIS1500, and rSIS2000 were significantly higher (Figure 3). ROC curve analysis identified rSIC1500 as the most effective diagnostic parameter (AUC = 0.79), followed by rSIS1500 (AUC = 0.78). The DeLong test results indicated no significant differences in AUC values between cDWI1500, ADC800, ADC1500, rSIC800, rSIS1500, and rSIS2000. However, rSIC1500 was found to be superior to other high-b-value synthetic maps (Table 3).

For non-mass lesions, high-b-value images (b ≥ 2000 s/mm²) outperformed other parameters in distinguishing malignant from benign lesions. Among these, rSIC4000 exhibited the highest diagnostic accuracy (AUC = 0.87). The DeLong test analysis confirmed that rSIC4000 was significantly superior to mADC800 and mADC1500 and rSIC800 and rSIC1500 maps, although no significant differences were found between rSIC4000 and other synthetic maps (Table 3).

For mass lesions, the optimal cut-off value for rSIC1500 was 1.90 based on ROC curve analysis. At this threshold, rSIC1500 achieved a sensitivity of 61.3% and a specificity of 78.0%, with a positive predictive value (PPV) of 70.4% and a negative predictive value (NPV) of 55.6%.

For non-mass lesions, the optimal cut-off value for rSIC4000 was 5.73. At this threshold, rSIS4000 demonstrated a sensitivity of 75% and a specificity of 83.3%, with PPV and NPV values of 75% and 83.3%, respectively.

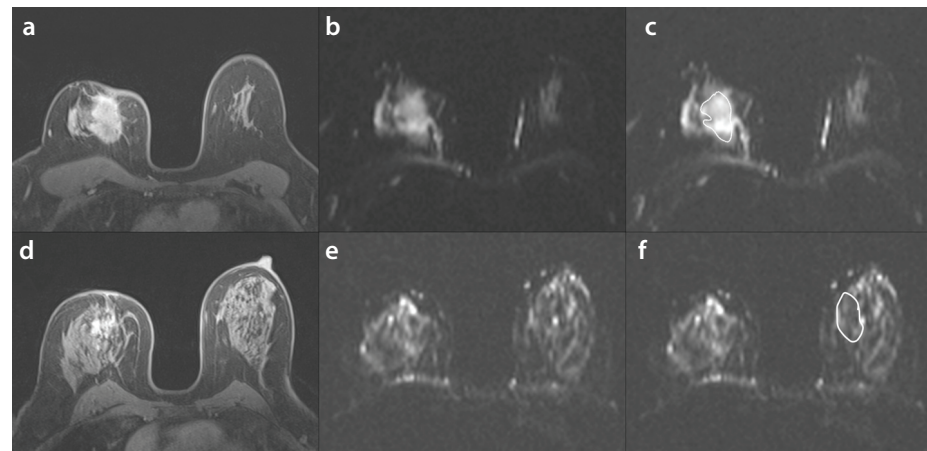


Figure 2. Segmentation process: An irregular mass in the upper quadrant of the right breast is visible in the contrast-enhanced axial image (a) and the b = 0 diffusion-weighted imaging (DWI) (b). The segmented area of the lesion in the b = 0 DWI sequence, used to create the mask image, is outlined with a white line (c). Additionally, the contrast-enhanced axial image (d) and the b = 0 DWI map (e) of the contralateral normal breast tissue, along with its segmentation marked by a white line, are shown (f).

Table 1. Characteristics of the tumors

	Malignant lesions: no. (%)	Benign lesions: no. (%)
Frequency	36 (52.94)	32 (47.06)
Mean diameter (mm) (min.-max.)	13.69 ± 6.46 (7–33)	27.64 ± 16.13 (6–80)
Shape		
Mass	31 (45.6)	26 (38.2)
Non-mass	5 (7.3)	6 (8.8)
Histopathological subtype	Invasive carcinoma of no special type 22 (32.3) Invasive lobular carcinoma 4 (5.9) 1 mixed IDC/ILC (1.5) Mucinous carcinoma 1 (1.5) Tubular carcinoma 1 (1.5) Mucoepidermoid carcinoma 1 (1.5) Ductal carcinoma <i>in situ</i> 5 (7.3) Focal microinvasive carcinoma on a background of papillary DCIS 1 (1.5)	Fibroadenoma 12 (17.6) Fibrocystic changes 10 (14.7) Apocrine metaplasia 2 (2.9) Florid ductal hyperplasia 3 (4.4) Focal granulomatous mastitis 3 (4.4) Lobulocentric mastitis 1 (1.5) Papilloma 3 (4.4)
Grade		
1	3 (4.4)	-
2	15 (22.1)	
3	12 (17.6)	
Her-2 status		
Positive	5 (7.3)	-
Negative	31 (45.6)	
Hormone receptor		
Positive	35 (51.5)	-
Negative	1 (1.5)	
Number of lesions		
Multifocal	10 (14.7)	-
Multicentric	4 (5.9)	
One mass	14 (20.6)	

min.-max., minimum-maximum; no., number; IDC, invasive ductal carcinoma; ILC, invasive lobular carcinoma; DCIS, ductal carcinoma *in situ*.**Table 2.** Comparison of the diagnostic values of synthetic and conventional diffusion-weighted imaging

	Benign (mean ± SD)	Malignant (mean ± SD)	P	AUC (95% CI)	P ⁺
rSIC1500	1.4 ± 0.66	2.45 ± 1.24	<0.001*	0.79 (0.68–0.90)	-
rSIS1500	1.63 ± 1.04	2.93 ± 1.72	<0.001*	0.77 (0.66–0.88)	0.27
rSIS2000	1.76 ± 1.21	3.57 ± 2.87	<0.001*	0.73 (0.61–0.85)	0.08
rSIC800	1.64 ± 1.12	2.44 ± 1.19	<0.001*	0.72 (0.57–0.83)	0.03
ADC ₈₀₀ × 10 ⁻³	1.3 ± 0.42	1.06 ± 0.28	0.01 ^t	0.69 (0.56–0.82)	0.31
ADC ₁₅₀₀ × 10 ⁻³	1.02 ± 0.37	0.85 ± 0.24	0.03 ^t	0.68 (0.55–0.82)	0.31
rSIS3000	2.64 ± 2.6	6.28 ± 8.63	0.03*	0.66 (0.53–0.79)	0.03
rSIS4000	6.16 ± 10.02	13.23 ± 25.15	0.10*	0.62 (0.48–0.75)	0.02
rSIS5000	21.89 ± 48.29	30.99 ± 71.97	0.30*	0.57 (0.43–0.71)	0.01

*P values of the Mann–Whitney U test; ^tP values of the t-test; ⁺P values of the DeLong test comparing rSIC1500 with other parameters. AUC, area under the curve; CI, confidence interval; SD, standard deviation.

Discussion

The present study demonstrates that the optimal b-values for DWI differ between mass and non-mass breast lesions and that high-b-value synthetic images exhibit better diagnostic performance in non-mass breast lesions. In mass lesions, synthetic b1500 and conventional b1500 yielded comparable di-

agnostic performance to routine ADC800 and ADC1500 values. However, in non-mass lesions, high-b-value ($b \geq 2000 \text{ s/mm}^2$) DWI maps outperformed both mADC and cDWI images in diagnostic performance.

Previous research has suggested that higher b-values (1200–1800 s/mm^2) enhance cancer detection and lesion conspicuity due

to the improved suppression of fibro-glandular tissue and benign lesion signals at higher diffusion weightings. Choi et al.⁹ reported that increasing b-values (800–1500 s/mm^2) improved cancer detection rates and cancer-to-parenchyma contrast ratios (CPCR) for both sDWI and cDWI, with sDWI1500 demonstrating superior lesion conspicuity

Table 3. Comparison of the diagnostic values of synthetic and conventional diffusion-weighted imaging in mass and non-mass lesions

	Mass lesions				Non-mass lesions				<i>P</i> ⁺	
	Benign (mean \pm SD)	Malignant (mean \pm SD)	<i>P</i>	AUC (95% CI)	Benign (mean \pm SD)	Malignant (mean \pm SD)	<i>P</i>	AUC (95% CI)		
rSIC800	1.92 \pm 1.29	3.66 \pm 3.01	0.08*	0.72 (0.58–0.86)	0.23	1.34 \pm 1.01	3.49 \pm 1.69	0.33*	0.70 (0.40–0.91)	0.03
rSIC1500	1.43 \pm 0.73	2.47 \pm 1.27	<0.001*	0.79 (0.66–0.88)	-	1.28 \pm 0.47	2.65 \pm 0.95	0.55	0.73 (0.43–0.92)	0.04
rSIS1500	1.70 \pm 1.12	2.97 \pm 1.76	0.001*	0.78 (0.65–0.88)	0.5	1.46 \pm 0.96	3.02 \pm 1.41	0.88	0.7 (0.36–0.93)	0.09
rSIS2000	1.92 \pm 1.29	3.66 \pm 3.01	0.008*	0.72 (0.59–0.83)	0.11	1.34 \pm 1.01	3.49 \pm 1.69	0.03	0.77 (0.43–0.96)	0.07
rSIS3000	3.17 \pm 2.82	6.64 \pm 9.21	0.17*	0.63 (0.49–0.75)	0.03	1.18 \pm 1.11	4.80 \pm 1.20	0.03	0.83 (0.43–0.96)	0.09
rSIS4000	7.98 \pm 11.30	14.45 \pm 26.91	0.35*	0.58 (0.44–0.71)	0.01	1.08 \pm 1.15	6.79 \pm 3.86	0.02	0.87 (0.54–0.99)	-
rSIS5000	29.66 \pm 55.28	34.69 \pm 77.03	0.97*	0.53 (0.39–0.66)	0.005	1.02 \pm 1.12	9.85 \pm 6.34	0.03	0.80 (0.46–0.97)	0.25
ADC _{800 \times 10⁻³}	1.27 \pm 0.37	1.02 \pm 0.27	0.007 ^t	0.70 (0.57–0.82)	0.45	1.35 \pm 0.36	1.07 \pm 0.34	0.39	0.60 (0.28–0.87)	0.02
ADC _{1500 \times 10⁻³}	0.99 \pm 0.33	0.81 \pm 0.23	0.023 ^t	0.70 (0.56–0.81)	0.43	1.07 \pm 0.34	1.07 \pm 0.09	0.67	0.63 (0.30–0.89)	0.02

**P* values of the Mann–Whitney *U* test, ^t*P* values of the *t*-test, ⁺*P* values of the DeLong test analysis. AUC, area under the curve; CI, confidence interval; SD, standard deviation; ADC, apparent diffusion coefficient.

and CPCR. Similarly, Bickel et al.¹⁴ found a significant increase in CPCR with b-values between 1000 and 2000 s/mm², identifying 1200–1800 s/mm² as optimal for image quality and lesion visibility. Park et al.¹³ reported that sDWI1500 enhances sensitivity without affecting predictive value, whereas Ahn et al.²⁰ observed that cDWI1000 provided better image quality compared with cDWI2000 and sDWI2000, despite superior lesion detection at cDWI2000. Naranjo et al.²¹ noted that synthetic b-values of 1200–1500 s/mm² offered the best lesion conspicuity, albeit with lower image quality. Additionally, Yilmaz et al.¹⁵ demonstrated that sDWI1500 outperformed cDWI800 in differentiating malignant from benign lesions, yielding higher sensitivity, specificity, and accuracy with fewer false positives. However, they did not compare higher b-values between sDWI and cDWI.¹⁵ None of these studies specifically analyzed mass and non-mass lesions separately. DWI may perform differently in distinguishing malignant lesions in mass versus non-mass lesions.^{16,17} Additionally, most studies in the literature have not used the DeLong test to compare differences in AUC values, limiting statistical insights into diagnostic performance.

Although there is still no universal consensus on the ideal b-value, our findings highlight the necessity of developing sepa-

rate DWI protocols for mass and non-mass lesions. Specifically, our results suggest that routine mADC and b800 DWI images provide diagnostic accuracy comparable with conventional b1500 and sDWI maps in mass lesions, questioning the added diagnostic value of high-b-value synthetic images in these cases. Conversely, our findings support the use of high-b-value DWI in non-mass lesions, as they demonstrated superior diagnostic performance in this subgroup. Incorporating sDWI images into routine breast MRI protocols may enhance diagnostic accuracy without extending acquisition times. Although not evaluated in the present study, prior research suggests that patient-related factors, such as breast density, may influence breast cancer detection rates on DWI.^{20,21} Moreover, sDWI offers radiologists greater flexibility by allowing lesion-specific and patient-specific selection of optimal b-values, thereby enhancing tailored imaging approaches.

Several limitations of this study should be acknowledged. First, its retrospective, single-center design and relatively small sample size limit the generalizability of the findings. Additionally, some patients underwent breast MRI after biopsy, which may have influenced the diffusion signal and affected imaging interpretation. The study population was also inherently biased, as it com-

prised patients undergoing breast biopsy for suspected breast cancer, potentially skewing the proportion of malignant lesions and impacting the study's sensitivity and specificity. Moreover, the predominance of hormone receptor-positive luminal-type tumors restricted the ability to perform subgroup analyses across different tumor subtypes. Lastly, the study focused solely on index lesions, which may not fully capture the complexities of multifocal or multicentric disease patterns.

In conclusion, the optimal b-values and the diagnostic performance of sDWI differ between mass and non-mass breast lesions. Although routine mADC and conventional b800 images offered diagnostic accuracy comparable with high-b-value synthetic images in mass lesions, high-b-value (b \geq 2000) DWI maps significantly outperformed cDWI and ADC images in non-mass lesions. These findings suggest that a tailored DWI protocol is necessary for optimal lesion characterization, particularly for non-mass lesions where high-b-value imaging provides added diagnostic value. This study highlights the need for further research involving large patient populations and separate evaluations for mass and non-mass lesions to clarify the role of high-b-value sDWI in breast lesion assessment and to determine the optimal b-value for accurate diagnosis.

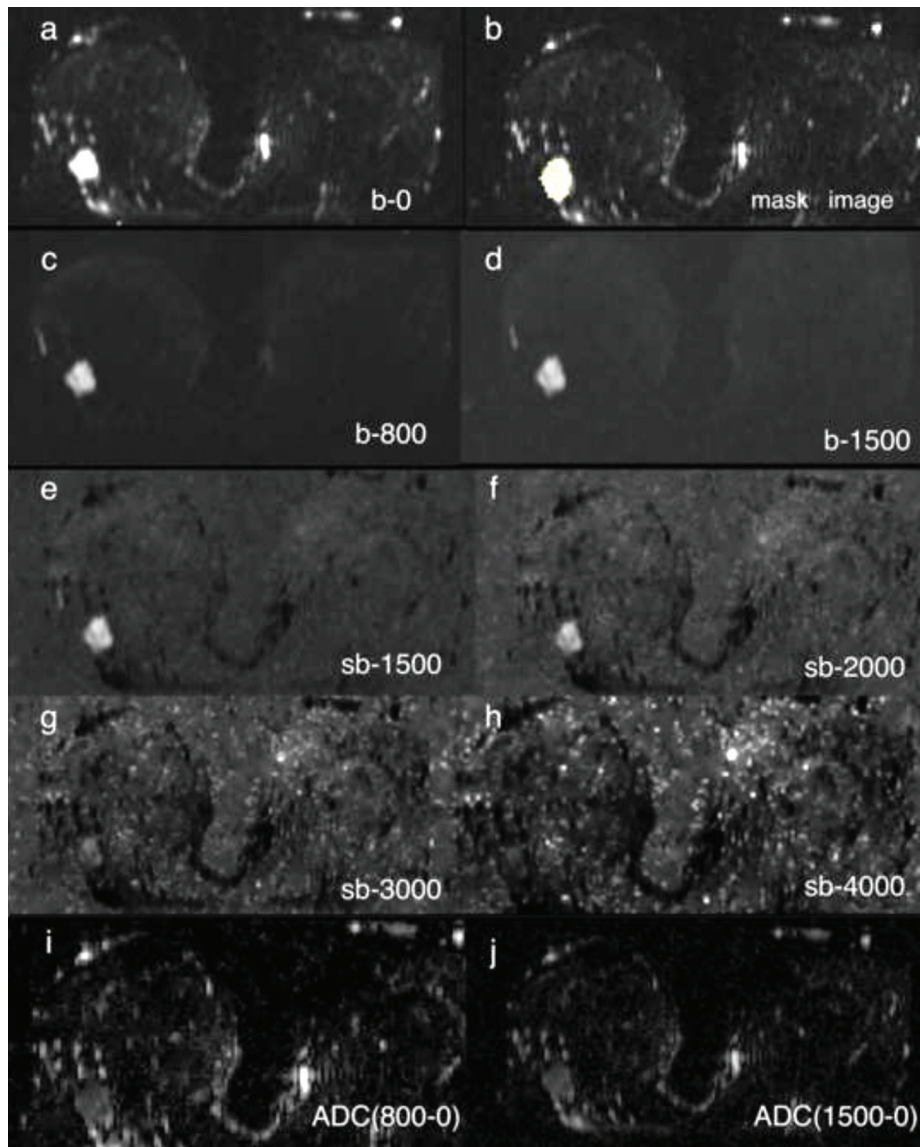


Figure 3. Conventional DWI (a, b, c, d) and synthetic DWI (e, f, g, h) images with different b-values and different ADC maps (i, j) of a patient with invasive NOS in the upper outer quadrant of the right breast are seen. The SNR, rSI, and lesion detectability decrease as the b-value gets very high (g, h). Low ADC signal was detected in ADC800 and ADC1500 images, as expected in malignant lesions. DWI, diffusion weighted imaging; ADC, apparent diffusion coefficient; SNR, signal-to-noise ratio; rSI, relative signal intensity.

Clinical significance

Implementing high-b-value sDWI into routine breast MRI protocols has the potential to enhance diagnostic accuracy, particularly for non-mass lesions without increasing scan time. By incorporating lesion-specific and patient-specific b-value optimization, radiologists can improve lesion characterization, potentially reducing unnecessary biopsies and improving clinical decision-making.

Footnotes

Conflict of interest disclosure

The authors declared no conflicts of interest.

References

1. Liberman L, Morris EA, Lee MJ, et al. Breast lesions detected on MR imaging: features and positive predictive value. *AJR Am J Roentgenol.* 2002;179(1):171-178. [\[Crossref\]](#)
2. Partridge SC, Nissan N, Rahbar H, Kitsch AE, Sigmund EE. Diffusion-weighted breast MRI: clinical applications and emerging techniques. *J Magn Reson Imaging.* 2017;45(2):337-355. [\[Crossref\]](#)
3. Pinker K, Moy L, Sutton EJ, et al. Diffusion-weighted imaging with apparent diffusion coefficient mapping for breast cancer detection as a stand-alone parameter: comparison with dynamic contrast-enhanced and multiparametric magnetic resonance imaging. *Invest Radiol.* 2018;53(10):587-595. [\[Crossref\]](#)
4. Spick C, Bickel H, Pinker K, et al. Diffusion-weighted MRI of breast lesions: a prospective clinical investigation of the quantitative imaging biomarker characteristics of reproducibility, repeatability, and diagnostic accuracy. *NMR Biomed.* 2016;29(10):1445-1453. [\[Crossref\]](#)
5. Ochi M, Kuroiwa T, Sunami S, et al. Diffusion-weighted imaging (b value = 1500 s/mm²) is useful to decrease false-positive breast cancer cases due to fibrocystic changes. *Breast Cancer.* 2013;20(2):137-144. [\[Crossref\]](#)
6. Baltzer P, Mann RM, Lima M, et al. Diffusion-weighted imaging of the breast-a consensus and mission statement from the EUSOBI International Breast Diffusion-Weighted Imaging working group. *Eur Radiol.* 2020;30(3):1436-1450. [\[Crossref\]](#)
7. Giannotti E, Waugh S, Pribal L, Davis Z, Crowe E, Vinnicombe S. Assessment and quantification of sources of variability in breast apparent diffusion coefficient (ADC) measurements at diffusion weighted imaging. *Eur J Radiol.* 2015;84(9):1729-1736. [\[Crossref\]](#)
8. Woodhams R, Inoue Y, Ramadan S, Hata H, Ozaki M. Diffusion-weighted imaging of the breast: comparison of b-values 1000 s/mm² and 1500 s/mm². *Magn Reson Med Sci.* 2013;12(3):229-234. [\[Crossref\]](#)
9. Choi BH, Baek HJ, Ha JY, et al. Feasibility study of synthetic diffusion-weighted MRI in patients with breast cancer in comparison with conventional diffusion-weighted MRI. *Korean J Radiol.* 2020;21(9):1036-1044. [\[Crossref\]](#)
10. Blackledge MD, Leach MO, Collins DJ, Koh DM. Computed diffusion-weighted MR imaging may improve tumor detection. *Radiology.* 2011;261(2):573-581. [\[Crossref\]](#)
11. Shukla-Dave A, Obuchowski NA, Chenevert TL, et al. Quantitative imaging biomarkers alliance (QIBA) recommendations for improved precision of DWI and DCE-MRI derived biomarkers in multicenter oncology trials. *J Magn Reson Imaging.* 2019;49(7):e101-e121. [\[Crossref\]](#)

12. O'Flynn EA, Blackledge M, Collins D, et al. Evaluating the diagnostic sensitivity of computed diffusion-weighted MR imaging in the detection of breast cancer. *J Magn Reson Imaging*. 2016;44(1):130-137. [\[Crossref\]](#)
13. Park JH, Yun B, Jang M, et al. Comparison of the diagnostic performance of synthetic versus acquired high b-value (1500 S/Mm²) diffusion-weighted MRI in women with breast cancers. *J Magn Reson Imaging*. 2019;49(3):857-863. [\[Crossref\]](#)
14. Bickel H, Polanec SH, Wengert G, et al. Diffusion-weighted MRI of breast cancer: improved lesion visibility and image quality using synthetic b-values. *J Magn Reson Imaging*. 2019;50(6):1754-1761. [\[Crossref\]](#)
15. Yilmaz E, Güldoğan N, Ulus S, et al. Diagnostic value of synthetic diffusion-weighted imaging on breast magnetic resonance imaging assessment: comparison with conventional diffusion-weighted imaging. *Diagn Interv Radiol*. 2024;30(2):91-98. [\[Crossref\]](#)
16. Kul S, Eyuboglu I, Cansu A, Alhan E. Diagnostic efficacy of the diffusion weighted imaging in the characterization of different types of breast lesions. *J Magn Reson Imaging*. 2014;40(5):1158-1164. [\[Crossref\]](#)
17. Avendano D, Marino MA, Leithner D, et al. Limited role of DWI with apparent diffusion coefficient mapping in breast lesions presenting as non-mass enhancement on dynamic contrast-enhanced MRI. *Breast Cancer Res*. 2019;21(1):136. [\[Crossref\]](#)
18. Jenkinson M, Beckmann CF, Behrens TE, Woolrich MW, Smith SM. FSL. *Neuroimage*. 2012;62(2):782-790. [\[Crossref\]](#)
19. Yushkevich PA, Piven J, Hazlett HC, et al. User-guided 3d active contour segmentation of anatomical structures: significantly improved efficiency and reliability. *Neuroimage*. 2006;31(3):1116-1128. [\[Crossref\]](#)
20. Ahn HS, Kim SH, Kim JY, Park CS, Grimm R, Son Y. Image quality and diagnostic value of diffusion-weighted breast magnetic resonance imaging: comparison of acquired and computed images. *PLoS One*. 2021;16(2):e0247379. [\[Crossref\]](#)
21. Daimiel Narango I, Lo Gullo R, Saccarelli C, et al. Diagnostic value of diffusion-weighted imaging with synthetic b-values in breast tumors: comparison with dynamic contrast-enhanced and multiparametric MRI. *Eur Radiol*. 2021;31(1):356-367. [\[Crossref\]](#)



Recent advances in vascular ultrasound imaging technology and their clinical implications

✉ Suna Özhan Oktar

✉ Mahi Nur Cerit

✉ Halit Nahit Şendur

✉ Atiye Cenay Karabörk Kılıç

Gazi University Faculty of Medicine, Department of Radiology, Ankara, Türkiye

ABSTRACT

A multiparametric ultrasound (US) approach, which is defined as the use of existing and new ultrasonographic technologies to enhance diagnostic accuracy, can be applied in vascular imaging. By incorporating techniques such as stiffness evaluation, elastography modalities, vector flow imaging, slow flow imaging, contrast-enhanced US, and three-dimensional imaging, this approach offers deeper insights into various vascular conditions, including vascular aging. Advancements in technology now make it possible to quickly obtain numerical values for various vessel properties on a screen or worksheet, simplifying and streamlining the multiparametric approach. Thus, recent advances in vascular US imaging technology allow for detailed investigation of many complex physiological and pathophysiological vascular phenomena.

KEYWORDS

Arterial, carotid artery, contrast agent, microvascular imaging, ultrasonography, vascular aging

Vascular ultrasound (US) has evolved as a cornerstone in the diagnosis and management of vascular diseases, offering a safe, non-invasive, and highly accessible imaging modality. It has traditionally been widely recognized as the first-line, and sometimes the only imaging modality for the screening, diagnosis, and monitoring of vascular diseases. The role of US is particularly important given the need for accurate and non-invasive methods for the early detection of vascular degenerative changes, which is crucial as cardiovascular disease remains the leading cause of mortality worldwide.¹⁻³ Doppler US, including color Doppler, spectral Doppler, and power Doppler modes, has been an essential component of vascular imaging for over 40 years, with its advantages and limitations extensively documented in the literature.⁴ However, several challenges persist in the US imaging of vascular conditions. For example, in patients with carotid artery disease, there is a need for improved methods to characterize atherosomatous plaques and enhance risk stratification, enabling more effective treatments.

Improvements in US image quality and the development of high-frequency transducers have enhanced the spatial resolution of images, enabling detailed visualization of small vessels and vascular pathologies, such as atherosclerotic plaques. In addition to improved B-mode tissue characterization, advancements in US technology and image analysis now enable the assessment of various physiological and pathophysiological conditions in vessels. The role of vascular US in diagnosing and managing vascular diseases has grown considerably, with recent innovative advances in US techniques enhancing its diagnostic capability, accuracy, and clinical utility.

This review covers recent and relatively new advancements in vascular US, with a focus on quantitative arterial stiffness for assessing vascular aging, microvascular US, tissue elastography, three-dimensional (3D) US and contrast-enhanced ultrasound (CEUS). The availability of these technologies facilitates the adoption of multiparametric US, integrating advanced imaging capabilities with existing techniques to deliver more comprehensive information and improve diagnostic accuracy in vascular imaging.

Corresponding author: Mahi Nur Cerit

E-mail: mahinur@yahoo.com

Received 09 May 2025; revision requested 16 June 2025;
accepted 27 July 2025



Epub: 27.08.2025

Publication date: 02.01.2026

DOI: 10.4274/dir.2025.253448

You may cite this article as: Özhan Oktar S, Cerit MN, Şendur HN, Karabörk Kılıç AC. Recent advances in vascular ultrasound imaging technology and their clinical implications. *Diagn Interv Radiol.* 2026;32(1):47-56.

Vascular aging and arterial stiffness

The notion that "A man is as old as his arteries," attributed to the English physician, Thomas Sydenham, in the 17th century, reflects the long-standing awareness of vascular aging. While this concept has been recognized for centuries, research into its underlying mechanisms has emerged only fairly recently.⁵ Vascular aging refers to the cumulative structural and functional changes that occur in the vasculature with normal aging, independent of other diseases, beginning as early as in utero. It is recognized as a substantial risk factor for the development of cardiovascular diseases.

With aging, arteries undergo notable structural and functional alterations, including vessel wall thickening caused by the proliferation and migration of vascular smooth muscle cells, fragmentation of elastin fibers, and increased collagen deposition, all contributing to vascular stiffness. These changes contribute to reduced arterial compliance and its capacity to resist stress. Endothelial cell dysfunction, chronic low-grade inflammation, oxidative stress, and traditional cardiovascular risk factors further exacerbate the progression. In more advanced stages—as in atherosclerosis—plaque accumulation, macrophage infiltration, and foam cell formation are observed.⁶⁻⁸

The hallmark of vascular aging is this increased "vascular stiffness," which broadly

refers to the reduced ability of the arteries to expand and recoil in response to changes in blood pressure with cardiac pulsations. Increased arterial stiffness by itself is a strong risk factor for a broad spectrum of cardiovascular diseases, including hypertension, heart failure, myocardial infarction, and stroke, independent of traditional risk factors. Vascular aging can be quantified by measuring vascular stiffness. Classical indirect methods for assessing arterial stiffness, such as arterial distensibility, compliance, elastic modulus, beta (β)-stiffness index, and pulse wave velocity (PWV) rely on the evaluation of changes in arterial diameter or volume during the cardiac cycle in response to corresponding changes in arterial pressure (Table 1). While these parameters are interrelated, each provides unique insights into the biomechanical properties of the vessel wall. These approaches remain central to understanding vascular biomechanics and age-related vascular changes. Among these, PWV is the most commonly used technique and is considered the gold standard for assessing arterial stiffness. The PWV increases with age due to reduced arterial elasticity, reflecting greater cardiovascular risk.⁹⁻¹¹

During each ventricular contraction, a "pulse wave" is generated, causing the aorta to expand and the pressure wave to propagate along the arterial tree. The speed of this pressure wave is proportional to the stiffness of the artery. In young individuals, the arteries are more elastic, causing the reflected wave to travel more slowly and return to the heart during diastole. This phenomenon enhances diastolic pressure, improving coronary perfusion, and dissipates part of the pulsatile energy in the central aorta, thereby protecting the microcirculation from damage. With vascular aging, arterial stiffness

increases, leading to a higher PWV (Figure 1). Given its strong association with vascular damage, PWV serves as a critical biomarker for evaluating cardiovascular risk and facilitates early detection of vascular dysfunction.^{8,6,12-15} Increased arterial stiffness has been shown to predict cardiovascular events even in asymptomatic individuals without overt cardiovascular disease.¹⁶

New sonographic techniques focus on detecting wave propagation. Several manufacturers have provided wall motion detection capability with different techniques. The radiofrequency data-based quantification technique used in arterial stiffness evaluation automatically identifies the intimal surface of the near- and far-field vessel walls under investigation, tracks movements over several cardiac cycles, and measures vessel diameter and displacement in micrometers. Vessel distensibility, an indicator of vascular stiffness, is calculated from the difference between systolic and diastolic measurements and is displayed on the screen (Figure 2). Ultrasonographic strain imaging using the speckle tracking method is another technique for assessing carotid stiffness. Using this technique, circumferential, longitudinal, and radial movements of the carotid artery can be analyzed, and displacement of the carotid wall can be represented graphically. Combined with diastolic and systolic blood pressure data, this technique allows for automatically calculating arterial stiffness parameters, such as elastic modulus, arterial distensibility, compliance, and β -stiffness index, via a special software program. Additionally, strain, strain rate, and peak circumferential and radial displacements can be measured (Figure 3). These techniques show promise as a valuable non-invasive tool for identifying early subclinical carotid artery disease.^{6,10,12,13}

Main points

- Increased arterial stiffness by itself is a strong risk factor for a broad spectrum of cardiovascular diseases, including hypertension, heart failure, myocardial infarction, and stroke, independent of traditional risk factors.
- The term "vulnerable plaque" refers to atherosclerotic plaques that are prone to rupture, potentially leading to thrombosis and embolism. The current challenge is to distinguish stable plaques from vulnerable ones, enabling identification of high-risk patients for acute cardiovascular and cerebrovascular events before clinical symptoms arise.
- Microvessel imaging also has potential for evaluating intraplaque neovascularization, a key factor in carotid plaque instability.
- Using microbubble-based contrast agents, contrast-enhanced ultrasound has significantly improved the ability to assess vascular perfusion and microvascular flow. This innovation has clinical implications for detecting tumor vascularity, characterizing plaques, and evaluating organ perfusion in both arterial and venous systems.

Table 1. Indirect methods for evaluating arterial stiffness

Parameter	Definition	Formula
Arterial compliance	Absolute change in vessel diameter for a given change in pressure	$[\text{diastolic diameter} - \text{systolic diameter} (\Delta D)] / [\text{systolic pressure} - \text{diastolic pressure} (\Delta P)]$
Arterial distensibility	The relative change in vessel diameter for a given change in pressure	$\Delta D / [\Delta P \times \text{vessel diameter in the diastolic phase} (D)] \text{ in mmHg}$
Elastic modulus index	Pressure change required for theoretical stretch from resting arterial diameter	$(\Delta P \times D) / \Delta D \text{ in mmHg}$
Beta-stiffness index	The ratio of the natural logarithm of systolic/diastolic pressure to relative change in diameter	$\log (\text{SBP}/\text{DBP}) / (\Delta D/D)$
Pulse wave velocity	The speed with which the pulse wave travels along the length of the artery	$\text{Stiffness index} \times \text{diastolic blood pressure} / (2 \times \text{blood density}) \text{ while assuming the blood density to be } 1.050 \text{ g/cm}^3$

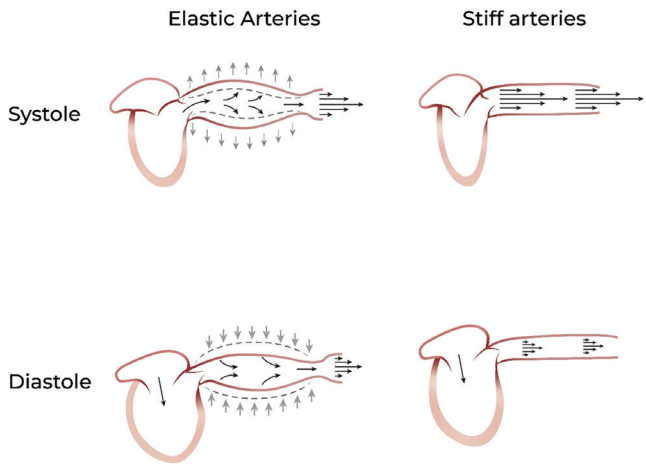


Figure 1. In a healthy artery, compliance allows the vessel to expand as blood is pumped from the heart and to recoil during diastole, propelling the accumulated blood forward into the peripheral tissues, providing continuous flow to the end organs. With vascular aging and increased arterial stiffness, the arterial walls become more rigid, reducing compliance and leading to higher pressure within the vessels, as demonstrated in the right column. In younger vessels, propagation velocity is slower than in aged vessels in which the walls move less.



Figure 2. Radiofrequency data-based quantification on arterial stiffness tracks movements of vessel walls during consecutive cardiac cycles, with automatic detection of both near- and far-field vessel walls. Vessel distensibility is calculated from the difference between systolic and diastolic diameter measurements and shown on the screen. The motion curve of the vessel wall is displayed under the image in real time.

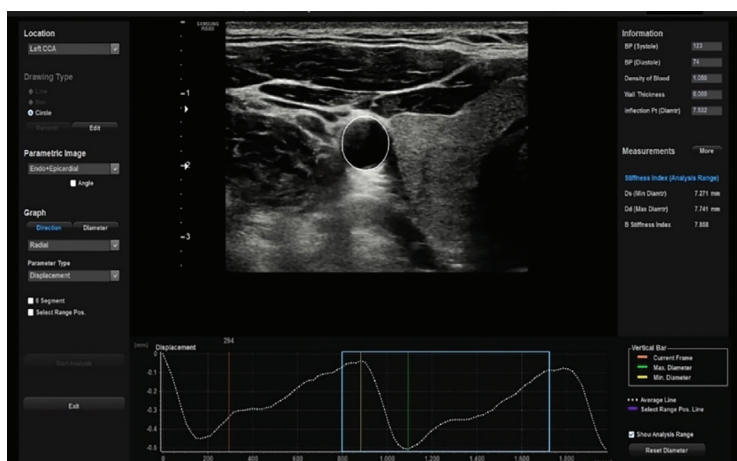


Figure 3. In the speckle tracking method, movements of the carotid artery can be analyzed and displacement of the carotid wall can be represented graphically.

Tissue elastography

US elastography is a method for assessing the elasticity of tissue, based on the cellular composition of the extracellular matrix. Several methods are available for elasticity evaluation, including real-time strain elastography or shear wave elastography (SWE), which have demonstrated efficacy in many clinical applications. The velocity of the shear wave created is directly linked to the elasticity of the arterial wall. Multiple factors influence arterial wall elasticity, such as personal factors (age, genetics, blood pressure, heart rate, different diseases), lifestyle factors (exercise, diet), and extrinsic factors (timing during cardiac cycle, acquisition characteristics, medical treatment). Unlike PWV, shear wave velocity is less dependent on other parameters, such as blood density and intra-arterial pressure. Local elasticity of the arterial wall or plaque can be calculated using SWE techniques.^{17,18}

In the evaluation of atherosclerotic plaques, the paradigm has shifted from solely focusing on the hemodynamic effects of luminal stenosis to a more comprehensive assessment of plaque structure and composition. The term "vulnerable plaque" refers to atherosclerotic plaques that are prone to rupture, potentially leading to thrombosis and embolism. The current challenge is to distinguish stable plaques from vulnerable ones, enabling identification of high-risk patients for acute cardiovascular and cerebrovascular events before clinical symptoms arise. Distinct morphological features of vulnerable plaques, including intraplaque hemorrhage, lipid-rich necrotic cores, thin fibrous caps, plaque ulceration, inflammation, and neovascularization, allow for their identification and characterization through a range of invasive and non-invasive imaging tools (Figure 4).¹⁹ The plaque elasticity quantification obtained via SWE is an indirect reflection of the major component of plaques, including dense fibrous tissue, calcifications, and lipid-rich necrotic core. Softer tissues such as lipid or hemorrhage, typically associated with vulnerable plaque, deform more easily and produce higher strains, whereas stiffer tissues such as those containing fibrous tissue deform less and result in lower strains (Figure 5). Preliminary investigations suggested that US elastography may be a clinically useful tool assessing plaque vulnerability. In some studies, it has been stated that SWE can identify statistically significant differences in elasticity and effectively distinguish different plaque types with good reproducibility in assessing rupture risk. Based on these results,

tissue elastography appears to be a promising method for risk stratification of carotid plaques. However, vascular elastography is challenging because of the relatively small heterogeneous tissue size, the dynamic environment resulting from pulsatile blood flow, thin vessel walls, anisotropy, and non-linear tissue elasticity. Therefore, in the European Federation of Societies for Ultrasound in Medicine and Biology guidelines and recommendations for the clinical practice of elastography, vascular US elastography has been considered as an area of active research, although it is currently not recommended for routine clinical decision-making.²⁰⁻²⁴ While US elastography shows promise in vascular applications, especially for the assessment of carotid plaque, larger, multicenter studies are needed to validate findings, define cutoff values, and optimize techniques.

Vector flow imaging

Doppler techniques are angle dependent, providing correct information only when the US beam is aligned parallel to the flow direction. A major limitation of this approach is that tortuous vessels or unusual anatomy can produce complex flow patterns, leading to a mixed or unclear color display. Vector flow

imaging (VFI) is an angle-independent technique that enables real-time visualization of complex blood flow patterns with extremely high frame rates. In conventional spectral Doppler imaging, the angle cursor must be manually aligned by the operator to estimate blood velocity based on the Doppler frequency, and only the velocity component along the direction of the beam is measured. In reality, a velocity vector representing blood flow consists of three components along the x, y, and z axes. The multibeam approach used in VFI enables the measurement of two or more velocity components. Using this technique, blood flow characteristics can be evaluated visually to assess the flow pattern. Each vector representing flow is displayed as a small color-coded arrow indicating the magnitude and the direction of a true velocity in real time at every point of the vessel (Figure 6).^{25,26}

Wall shear stress (WSS) measurement is another capability of VFI. There are two major types of hemodynamic forces that act on blood vessels: tensile pressure (ρ), the outward force that acts perpendicular to the arterial wall, which is greater in systole; and shear stress (τ), the tangential frictional force per unit area of the vessel wall that is exerted in the direction of blood flow (Figure 7). As a local mechanical force, WSS heavily affects

the biofunction of vascular endothelial and smooth muscle cells with diverse mechanisms.^{27,28} The VFI technique enables automated WSS measurements by aligning the reference line to coincide with the vascular wall (Figure 8).

Endothelial cells have the ability to sense and transduce the shear stress from blood flow into biochemical signals that cause initiation and progression of the atherosclerotic process depending on the type and the magnitude of shear stresses through specific mechanisms. In straight regions of arteries, flow has a normal laminar pattern and is always in the same direction. Endothelial cells in these areas exposed to sustained laminar flow and high WSS have an anti-inflammatory phenotype characterized by alignment in the direction of flow, downregulation of atherogenic genes, low levels of oxidative stress, cell turnover, and permeability, which help protect against atherosclerosis. However, in regions where arteries divide or curve sharply, such as carotid bifurcation, disturbed or "atherogenic" flow patterns are observed, including flow separation, gradients, flow reversal, and turbulence. Endothelial cells in regions of disturbed flow or low shear have an activated, pro-inflammatory phenotype characterized by poor alignment, oxidative stress, expression of inflammatory genes, and high turnover, which is associated with high susceptibility to atherosclerosis.

Briefly, disturbed and laminar flow patterns may induce different molecular responses in endothelial cells, leading to the preferential development of atherosclerotic lesions at arterial branches and curvatures while sparing the straight sections of the arterial tree. The VFI technique may be useful for evaluating turbulent or disturbed blood flow, such as in stenotic arteries or aneurysmal regions, while simultaneously enabling measurements of WSS (Figure 9).

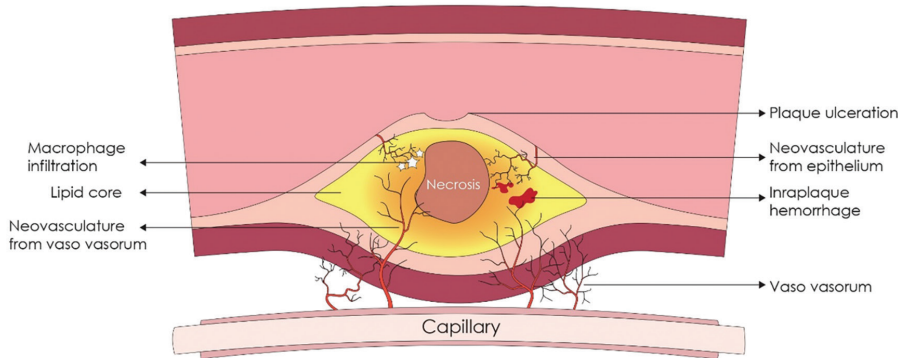


Figure 4. Schematic presentation of vulnerable plaque with remodeling.

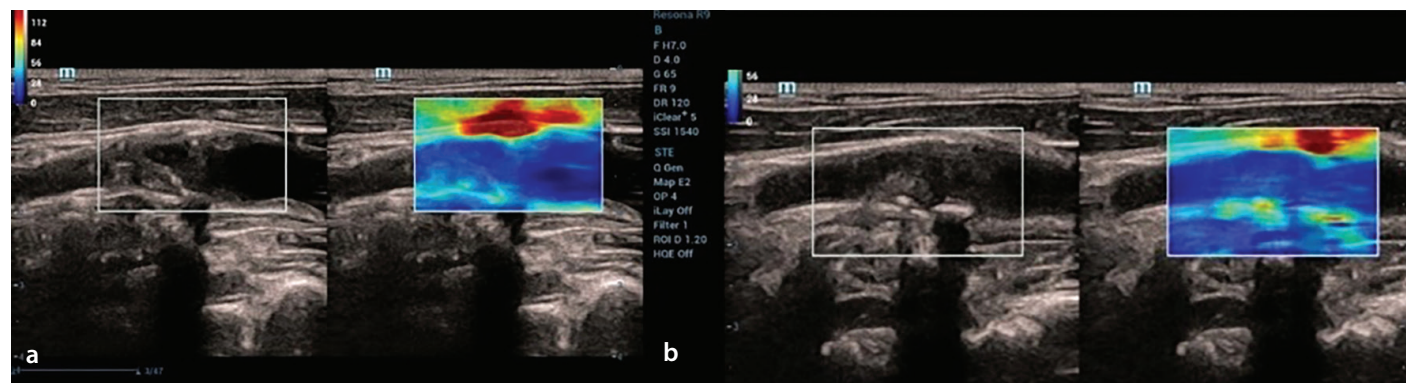


Figure 5. Shear wave elastography (SWE) imaging of plaques with different elastic properties: (a) SWE image displays a blue color at a hypoechoic plaque suggesting a soft texture; (b) B-mode image shows a mixed echogenicity of the plaque with hyperechoic areas suggesting calcifications. The SWE image shows a mixture of blue, red, and yellow colors, suggesting that the plaque contains stiff areas.

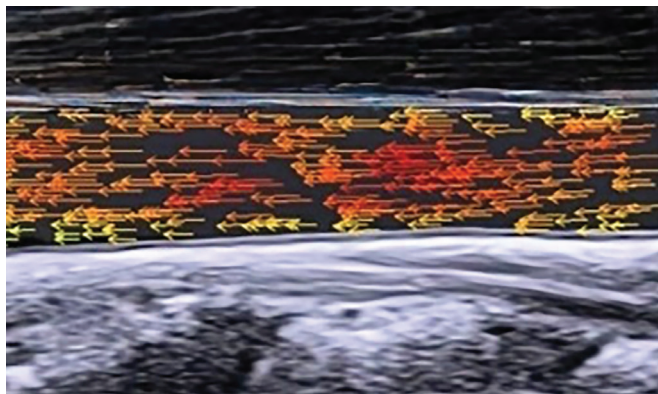


Figure 6. Vector flow imaging displays all velocity vectors in a selected region of interest. Each vector representing flow is shown as a small color-coded arrow indicating the magnitude and the direction of a true velocity in real time. The length and color of the arrows indicate the flow speed.

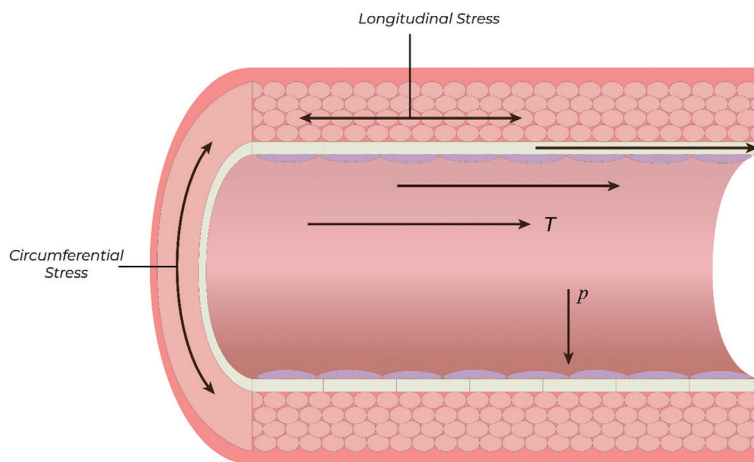


Figure 7. Schematic presentation of major hemodynamic forces that act on blood vessels. The tensile pressure (p) is the outward force acting perpendicular to the arterial wall, which is greater in systole. Shear stress (τ) is the tangential frictional force per unit area of the vessel wall, exerted in the direction of blood flow.

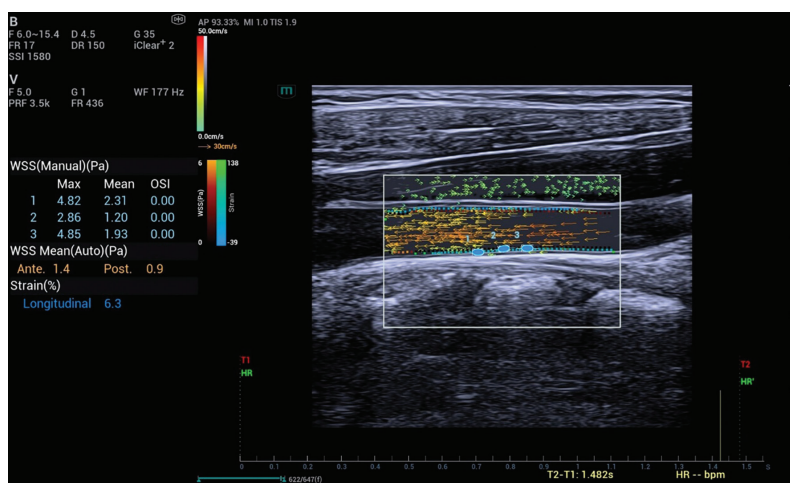


Figure 8. Wall shear stress measurements at a straight segment of a carotid artery by aligning the reference line to coincide with the vascular wall.

Non-physiological WSS also promotes plaque progression and the transformation of stable plaques into an unstable or vulnerable state.^{27,29,30} Obtaining the WSS value may be valuable in stratifying patients at risk and for further clinical decision-making in carotid stenosis.

The reference values for WSS have been established in previous studies, with the normal maximum WSS in arteries considered to range between 1 and 7 Pa. It is suggested that a local mean WSS below 0.4 Pa could change vessel wall morphology and contribute to the development of arteriosclerosis. Moreover,

other studies have indicated that excessively high WSS values in stenotic arteries may promote the rupture of high-risk plaques, with a rupture risk threshold identified as 7 Pa. It is suggested that high WSS values may lead to thinning of the fibrous plaque cap, increasing the risk of plaque rupture through elevated mechanical stress within the wall.³¹⁻³³

In brief, analyzing carotid flow patterns and measuring WSS via VFI can offer valuable insights into the development of atherosclerosis. However, due to the relative novelty of the technique, there remains a lack of strong clinical evidence regarding its use. Further research is required to explore the pathophysiological significance of various complex flow patterns, which may indicate plaque progression and thrombus formation.³¹

Microvessel imaging

Traditionally, color and power Doppler imaging have been the main tools for non-contrast microvascular flow visualization.³⁴ However, conventional Doppler techniques have limited sensitivity for the detection of slow vascular flow. Recently, a number of tools have been developed for assessing small-diameter vessels with low-velocity flow without the need for intravenous (IV) contrast agents, collectively referred to as microvascular flow imaging.

Doppler technologies employ single-dimensional wall filters for suppressing clutter artifacts resulting from vessel wall motion, which results in loss of slow flow signals from smaller vessels. Microvascular flow techniques, on the other hand, use multidimensional adaptive wall filters to selectively remove overlapping tissue movement artifacts, maintaining low flow signals otherwise lost in conventional Doppler imaging methods. This approach preserves slow flow signals originating from microvasculature, providing more sensitive and higher resolution blood flow evaluations with exquisite vascular details (Figure 10). Additionally, microflow imaging uses high-frequency sampling techniques and a high frame rate, enabling the display of high-resolution images. In certain cases, it can also rapidly confirm the presence or absence of blood flow without the need for IV contrast administration. Multiple vendors offer microvascular techniques on different ultrasonography devices, such as Superb Microvascular Imaging in Canon Medical Systems, ultra-micro angiography in Mindray Bio-Medical, Micro-vascular Imaging in GE Healthcare, Micro-vascular-flow in Samsung, Slow Flow in Siemens Healthineers, and MicroFlow Imaging in Philips systems. Display modes vary by manufacturer,

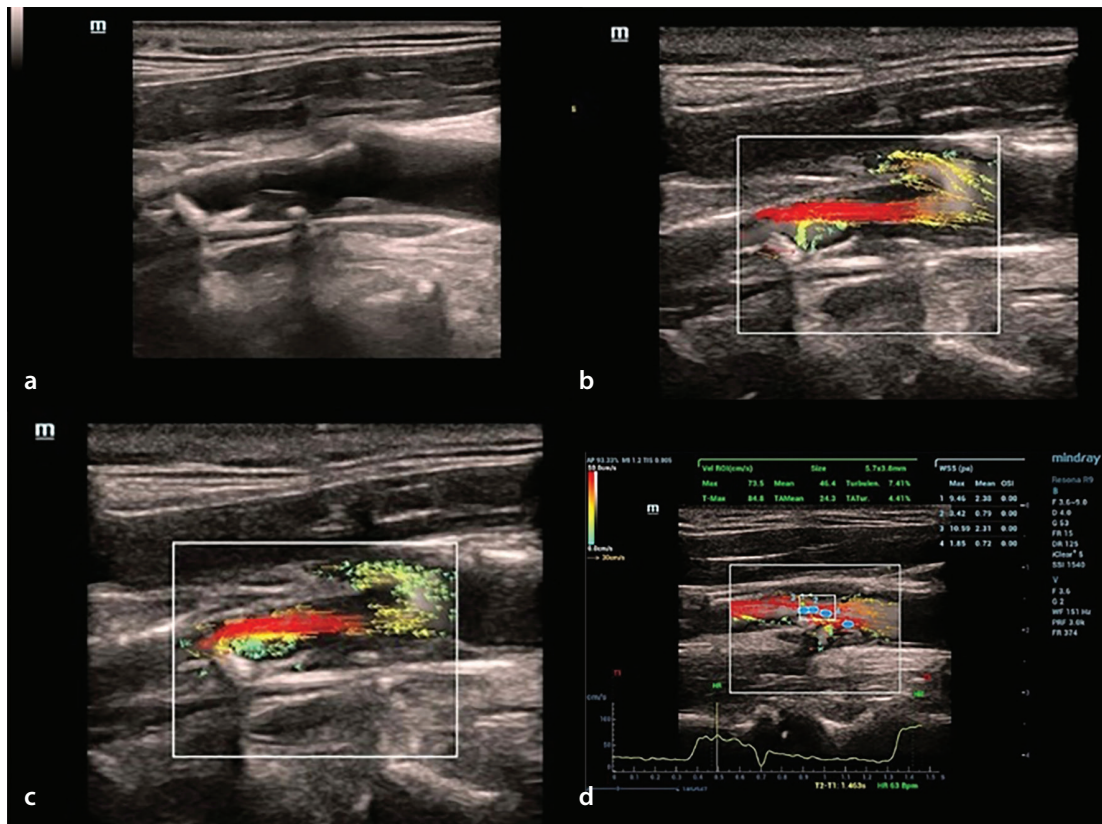


Figure 9. Vector flow imaging (VFI) of the carotid stenosis: **(a)** Grayscale image reveals calcified atherosclerotic plaque with irregular surface, causing severe stenosis of the right internal carotid artery; **(b, c)** VFI demonstrates complex flow patterns at different stages of cardiac cycle, with the vector arrows at the stenosis site becoming longer and the red color of the arrow indicating fast flow. Vortex flow is represented with short green or yellow vectors; **(d)** wall shear stress measurements at the level of stenosis.

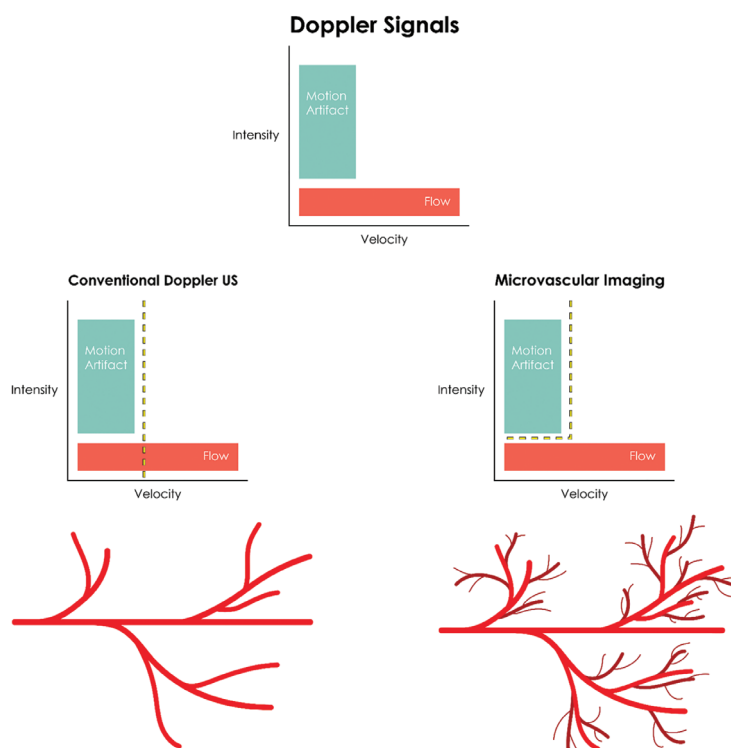


Figure 10. Imaging principles of microvascular ultrasound. The graph on the left shows that conventional Doppler techniques apply a single-dimensional wall filter (yellow dotted line) to remove clutter artifacts from wall motion, resulting in loss of signals from slow flow areas. In contrast, microvascular imaging techniques apply a multidimensional filter to remove only the clutter, preserving the slow flow signals, as shown on right. Exquisite detail of microvasculature can be detected via microvascular imaging.

but generally mimic the presentation of color or power Doppler modes, providing flow information overlaid on B-mode data using a variety of color hues.^{20,35-37}

Existing research suggests that microflow imaging enhances the diagnosis and monitoring of a range of medical conditions. Possible clinical applications include assessment of the vascularity of breast masses and thyroid nodules, characterization of focal and diffuse liver lesions, detection of increased vascularity in tendons, joint capsules, and peripheral nerves in musculoskeletal US, depiction of mass lesions, and pre- and post-transplant kidney evaluations. It has also potential neurosonological applications, including in the eye.^{35,38-41}

Microvessel imaging also has potential for evaluating intraplaque neovascularization, a key factor in carotid plaque instability, as illustrated schematically in Figure 4. The presence or progression of this neovascularization significantly affects the outcomes of vulnerable plaques, making its detection clinically important (Figure 11). The results of previous studies showed that blood flow detected by microvascular imaging frequently correlated with plaque enhancement signals

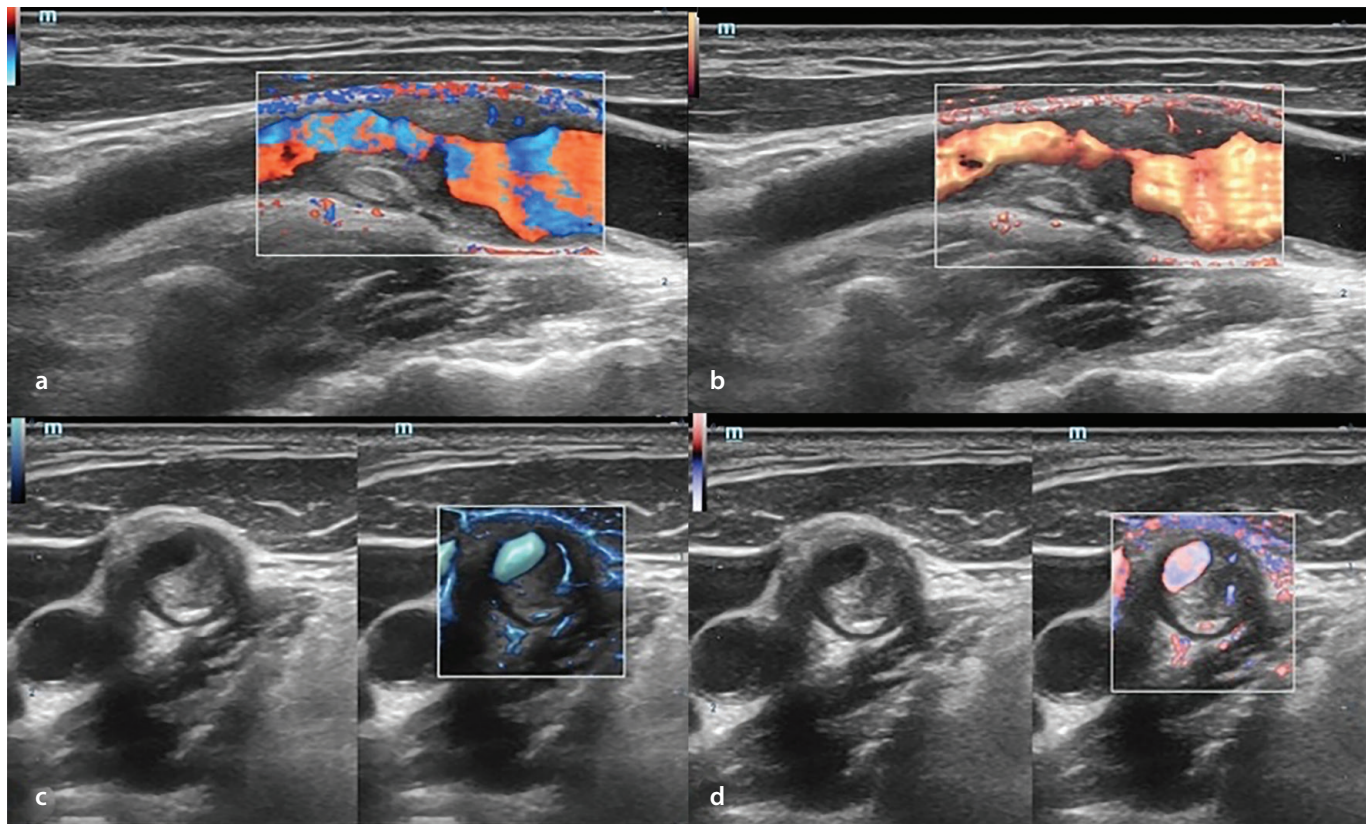


Figure 11. Microvascular ultrasound (US) imaging findings in complex plaques in the carotid bulb and proximal internal carotid artery causing high-grade carotid stenosis. Microvessel US imaging with different hues in longitudinal (a, b) and axial views (c, d) reveal tiny vessels at the anteriorly located plaque, representing neoangiogenesis.

observed in CEUS, demonstrating reliable consistency in assessing neovascularization in carotid plaques. The correlation between microvessel imaging and histology in detecting the neovascularization in atherosclerotic plaque has also been verified in corresponding studies.⁴²⁻⁴⁶ While microvessel imaging techniques are not as accurate as CEUS or computed tomography (CT) in detecting endoleaks following endovascular aneurysm repair (EVAR), they offer a valuable improvement over standard color Doppler imaging and can serve as a useful alternative in the follow-up period, especially for patients who are unsuitable for contrast-enhanced imaging modalities.⁴⁷

The development of increasingly sensitive microvascular flow imaging US techniques enhances the capability of non-contrast US to accurately diagnose or exclude pathologies, and may obviate the need for further contrast imaging methods, such as CEUS, CT, or magnetic resonance imaging, in selected cases. However, non-contrast US flow-detection methods have not achieved the same level of sensitivity as CEUS for detecting slow flow and perfusion. Additionally, they are unable to evaluate dynamic contrast kinetics. Moreover, microvascular US imaging has limited ability for deeper organs, making it

clinically challenging to decide whether the absence of flow detection is due to depth limitations or reduced perfusion. This technique is also susceptible to motion artifacts, especially those caused by breathing and cardiac pulsations.

Three-dimensional ultrasound

3D US imaging is gaining popularity because of its superiority over conventional two-dimensional (2D) US by providing more accurate and reproducible assessment for anatomical structures and disease entities. This technique combines a series of 2D US cross-sectional slices, collected in a computer and reconstructed into a 3D volume. 3D US imaging provides volumetric reconstructions and dynamic imaging of vessel anatomy and blood flow. One of the most widely accepted advantages of 3D US is the reduction of operator dependency compared with 2D US imaging. Moreover, its potential for shortening the examination time makes it cost effective, and it is safe for serial testing. Further advantages of 3D US over 2D versions include its higher accuracy in evaluating the relationship between anatomical structures, evaluating treatment effects, estimating quantitative volume, and providing access to an unlimited number of imaging planes.^{48,49}

The use of 3D US in obstetric imaging offers a new viewpoint on fetal anatomy, facilitates the identification of abnormalities, improves maternal–fetal bonding, and provides a better understanding of fetal abnormalities. In angiographic applications, viewing several 3D power Doppler US pictures in a fast cine loop has proven beneficial. Moreover, 3D US can help distinguish benign masses from malignant ones in breast imaging by exhibiting lesion borders and topography.⁵⁰⁻⁵²

There are three different methods for acquiring 3D US imaging. Mechanical 3D US consists of a motorized linear array transducer that moves within a housing to capture 2D image frames to be reconstructed into a 3D volume. Matrix 3D US has a larger imaging volume and acquires images more quickly compared with mechanical 3D US. However, the resolution of images decreases slightly. Lastly, in the freehand 3D US method, an external tracking system accompanies the transducer, and the operator can perform several maneuvers to avoid gas or artifacts.^{49,53}

These 3D US techniques are increasingly utilized in clinical practice. Atherosclerotic plaque burden may be helpful in predicting individual risk for cardiovascular diseases,

and 3D US can allow for more accurate estimation of plaque burden.⁵⁴ Furthermore, carotid artery plaque assessment can be performed reliably and effectively using 3D US. According to a study conducted by Landry et al.⁵⁵, the inter- and intra-observer reliability was 93.2% and 94%, respectively. This study also reported that the higher the amount of plaque volume is, the lower the variability of measurements. However, a recent study revealed that with the advancements in 3D US technology, a new commercially available 3D transducer may provide more accurate plaque volume measurements in carotid and femoral arteries independent of plaque size.⁵⁶ In addition, 3D US may be feasible for the assessment of the effects of statin treatment on carotid artery plaques.⁵⁷

The technique is also useful for preoperative planning and monitoring post-surgical outcomes, such as bypass grafts or endovascular repairs. Post-EVAR volume estimation of the aortic sac using 3D US can be both feasible and accurate. In a study conducted by Bredahl et al.⁵⁸, volume estimation in 93 consecutive patients undergoing EVAR was evaluated using 3D US, with CT angiography used as the reference standard. The authors reported that the mean difference between 3D US and CT angiography was 1 mm, and the limits of agreement ranged from -11% to 12%. Another study, which included 182 abdominal aortic aneurysms (AAAs) of patients under EVAR surveillance, reported no significant differences between 3D US and CT angiography in measuring the anteroposterior diameter of the residual sac, and underscored the potential benefit of 3D US in reducing the need for nephrotoxic contrast agents.⁵¹

Although 3D US has a promising role in clinical applications, a limited number of relevant studies are available. Therefore, future studies are required to better understand its clinical value.

Contrast-enhanced ultrasound

Using microbubble-based contrast agents, CEUS has notably improved the ability to assess vascular perfusion and microvascular flow. This innovation has clinical implications for detecting tumor vascularity, characterizing plaques, and evaluating organ perfusion in both arterial and venous systems. The method aims to address some of the drawbacks of traditional ultrasonography, such as the inability to clearly visualize slow flow, particularly in small vessels or in cases of substantial stenosis. US enables shell-encapsulated gas microbubbles, which

have sizes <10 µm, to expand and contract, resonating at common medical US frequencies.⁵⁹ The energy of the transmitted pulse is scattered at harmonic and subharmonic frequencies as a result of this interaction. While the covering shell is metabolized, primarily in the liver, the patient's lungs exhale the interior gas. The contrast agent SonoVue (Bracco, Milan, Italy), which is made up of sulfur hexafluoride bubbles enclosed in a phospholipid membrane shell, is widely used in Europe and the United States under the brand name LumaSon®. CEUS enables continuous real-time scanning and can detect microvasculature in vessels as small as 40 µm with extremely low velocities, a capability that is frequently lacking in color and power Doppler US, which can image vessels as small as 100 µm.^{49,60}

The CEUS method is used in the evaluation of extracranial carotid occlusive diseases. Regardless of the extent of stenosis, CEUS imaging can help determine whether a patient requires carotid endarterectomy by evaluating the shape and fragility of the plaque. The technique has a strong correlation with both conventional and magnetic resonance angiography, and it enables more precise evaluation of stenosis.⁶¹ Additionally, when compared with color Doppler US imaging, CEUS improves measurements of the length of stenosis by reducing the visibility of intrastenotic flow aberrations.⁶² Furthermore, abnormalities such as ulcers, hypoechoic plaques, and dissections that were previously missed by traditional US can be seen using CEUS imaging.⁶³ This imaging technique is a promising method for the diagnosis and treatment of pre-ruptured AAAs, ruptured AAAs, and endoleaks following EVAR, as well as the diagnosis of aortic dissections and peripheral arterial disease.⁶⁴ In summary, CEUS imaging is an important vascular imaging technology used to determine luminal perfusion, detect vascular irregularities, measure plaque vulnerability in various vascular pathologies, and measure neovascularization as a quantitative indicator of final muscle perfusion.

Footnotes

Conflict of interest disclosure

The authors declared no conflicts of interest.

References

- Rafailidis V, Sidhu PS. Vascular ultrasound, the potential of integration of multiparametric ultrasound into routine clinical practice. *Ultrasound*. 2018;26(3):136-144. [\[Crossref\]](#)
- Roth GA, Mensah GA, Johnson CO, et al. Global burden of cardiovascular diseases and risk factors, 1990-2019: update from the GBD 2019 study. *J Am Coll Cardiol*. 2020;76(25):2982-3021. [\[Crossref\]](#)
- Cheng Y, Wu A, Ying M, Chen X. The updated roles of new ultrasound imaging techniques in assessing carotid vulnerable plaques. *WFUMB Ultrasound Open*. 2023;1(2):100023. [\[Crossref\]](#)
- Bude RO, Rubin JM. Power Doppler sonography. *Radiology*. 1996;200(1):21-23. [\[Crossref\]](#)
- Brew BJ, McArthur JC. "A man is as old as his arteries" (attributed to Thomas Sydenham, the English Hippocrates). *AIDS*. 2020;34(4):637-639. [\[Crossref\]](#)
- Mikael LR, Paiva AMG, Gomes MM, et al. Vascular aging and arterial stiffness. *Arq Bras Cardiol*. 2017;109(3):253-258. [\[Crossref\]](#)
- Cefalu CA. Theories and mechanisms of aging. *Clinics in Geriatric Medicine*. 2011;27(4):491-506. [\[Crossref\]](#)
- Kim HL. Arterial stiffness and hypertension. *Clinical Hypertension*. 2023;29(1):31. [\[Crossref\]](#)
- Baradaran H, Gupta A. Carotid artery stiffness: imaging techniques and impact on cerebrovascular disease. *Front Cardiovasc Med*. 2022;9:852173. [\[Crossref\]](#)
- Fernández-Alvarez V, Linares Sánchez M, López Alvarez F, et al. Evaluation of intima-media thickness and arterial stiffness as early ultrasound biomarkers of carotid artery atherosclerosis. *Cardiol Ther*. 2022;11(2):231-247. [\[Crossref\]](#)
- van Sloten TT, Schram MT, van den Hurk K, et al. Local stiffness of the carotid and femoral artery is associated with incident cardiovascular events and all-cause mortality: the Hoorn study. *J Am Coll Cardiol*. 2014;63(17):1739-1747. [\[Crossref\]](#)
- Nichols WW, O'Rourke M, Edelman ER, Vlachopoulos C. *McDonald's Blood Flow in Arteries*. CRC Press; 2022. [\[Crossref\]](#)
- Safar ME, Levy BI, Struijker-Boudier H. Current perspectives on arterial stiffness and pulse pressure in hypertension and cardiovascular diseases. *Circulation*. 2003;107(22):2864-2869. [\[Crossref\]](#)
- Briet M, Boutouyrie P, Laurent S, London GM. Arterial stiffness and pulse pressure in CKD and ESRD. *Kidney Int*. 2012;82(4):388-400. [\[Crossref\]](#)
- Chang KC, Tseng YZ, Kuo TS, Chen HI. Impaired left ventricular relaxation and arterial stiffness in patients with essential hypertension. *Clin Sci (Lond)*. 1994;87(6):641-647. [\[Crossref\]](#)
- Bonarjee VVS. Arterial stiffness: a prognostic marker in coronary heart disease. Available methods and clinical application. *Front Cardiovasc Med*. 2018;5:64. [\[Crossref\]](#)

17. Messas E, Pernot M, Couade M. Arterial wall elasticity: state of the art and future prospects. *Diagn Interv Imaging*. 2013;94(5):561-569. [\[Crossref\]](#)

18. Pruijssen JT, de Korte CL, Voss I, Hansen HHG. Vascular shear wave elastography in atherosclerotic arteries: a systematic review. *Ultrasound Med Biol*. 2020;46(9):2145-2163. [\[Crossref\]](#)

19. Baun J. Contrast-enhanced ultrasound: identification of neovascularization permits characterization of vulnerable carotid plaques. *Journal of Diagnostic Medical Sonography*. 2020;36(5):471-477. [\[Crossref\]](#)

20. Yao Y, Zhang P. Novel ultrasound techniques in the identification of vulnerable plaques—an updated review of the literature. *Front Cardiovasc Med*. 2023;10:1069745. [\[Crossref\]](#)

21. Chen JW, Wasserman BA. Vulnerable plaque imaging. *Neuroimaging Clin N Am*. 2005;15(3):609-621. [\[Crossref\]](#)

22. Hafiane A. Vulnerable plaque, characteristics, detection, and potential therapies. *J Cardiovasc Dev Dis*. 2019;6(3):26. [\[Crossref\]](#)

23. Fedak A, Ciuk K, Urbanik A. Ultrasonography of vulnerable atherosclerotic plaque in the carotid arteries: B-mode imaging. *J Ultrasound*. 2020;20(81):e135-e145. [\[Crossref\]](#)

24. Säfoltu A, Gilja OH, Sidhu PS, et al. The EFSUMB guidelines and recommendations for the clinical practice of elastography in non-hepatic applications: update 2018. *Ultraschall Med*. 2019;40(4):425-453. [\[Crossref\]](#)

25. Dunmire B, Beach KW, Labs K, Plett M, Strandness DE Jr. Cross-beam vector Doppler ultrasound for angle-independent velocity measurements. *Ultrasound Med Biol*. 2000;26(8):1213-1235. [\[Crossref\]](#)

26. Hoskins PR, Kenwright DA. Recent developments in vascular ultrasound technology. *Ultrasound*. 2015;23(3):158-165. [\[Crossref\]](#)

27. Dhawan SS, Avati Nanjundappa RP, Branch JR, et al. Shear stress and plaque development. *Expert Rev Cardiovasc Ther*. 2010;8(4):545-556. [\[Crossref\]](#)

28. Zhou M, Yu Y, Chen R, et al. Wall shear stress and its role in atherosclerosis. *Front Cardiovasc Med*. 2023;10:1083547. [\[Crossref\]](#)

29. Mierke CT. Mechanosensory entities and functionality of endothelial cells. *Front Cell Dev Biol*. 2024;12:1446452. [\[Crossref\]](#)

30. Chiu JJ, Chien S. Effects of disturbed flow on vascular endothelium: pathophysiological basis and clinical perspectives. *Physiol Rev*. 2011;91(1):327-387. [\[Crossref\]](#)

31. Du Y, Goddi A, Bortolotto C, et al. Wall shear stress measurements based on ultrasound vector flow imaging: theoretical studies and clinical examples. *J Ultrasound Med*. 2020;39(8):1649-1664. [\[Crossref\]](#)

32. Malek AM. Hemodynamic shear stress and its role in atherosclerosis. *JAMA*. 1999;282(21):2035. [\[Crossref\]](#)

33. Dong Y, Gao W, Hong S, et al. Evaluation of turbulence index and flow pattern for atherosclerotic carotid stenosis: a high-frame-rate vector flow imaging study. *Ultrasound Med Biol*. 2024;50(4):549-556. [\[Crossref\]](#)

34. Szabo TL. *Diagnostic Ultrasound Imaging: Inside Out*. Elsevier/Academic Press; 2014.

35. Park AY, Seo BK. Up-to-date Doppler techniques for breast tumor vascularity: superb microvascular imaging and contrast-enhanced ultrasound. *Ultrasonography*. 2018;37(2):98-106. [\[Crossref\]](#)

36. Cannella R, Pilato G, Mazzola M, Tommaso Vincenzo Bartolotta. New microvascular ultrasound techniques: abdominal applications. *Radiol Med*. 2023;128(9):1023-1034. [\[Crossref\]](#)

37. Aziz MU, Eisenbrey JR, Deganello A, et al. Microvascular flow imaging: a state-of-the-art review of clinical use and promise. *Radiology*. 2022;305(2):250-264. [\[Crossref\]](#)

38. Xiao XY, Chen X, Guan XF, Wu H, Qin W, Luo BM. Superb microvascular imaging in diagnosis of breast lesions: a comparative study with contrast-enhanced ultrasonographic microvascular imaging. *Br J Radiol*. 2016;89(1066):20160546. [\[Crossref\]](#)

39. Cappelli C, Pirola I, Gandossi E, et al. Ultrasound microvascular blood flow evaluation: a new tool for the management of thyroid nodule? *Int J Endocrinol*. 2019;2019:7874890. [\[Crossref\]](#)

40. Lim AKP, Satchithananda K, Dick EA, Abraham S, Cosgrove DO. Microflow imaging: new Doppler technology to detect low-grade inflammation in patients with arthritis. *Eur Radiol*. 2018;28(3):1046-1053. [\[Crossref\]](#)

41. Brown AH, Riemann M, Ramasubramanian A. Microvascular flow imaging in anterior segment tumors. *Am J Ophthalmol*. 2024;261:e1-e2. [\[Crossref\]](#)

42. Wang Y, Yao M, Zou M, et al. Assessment of carotid intraplaque neovascularization using superb microvascular imaging in high risk of stroke individuals: results from a community-based study. *Front Neurol*. 2019;10:1146. [\[Crossref\]](#)

43. Oura K, Kato T, Ohba H, Terayama Y. Evaluation of intraplaque neovascularization using superb microvascular imaging and contrast-enhanced ultrasonography. *J Stroke Cerebrovasc Dis*. 2018;27(9):2348-2353. [\[Crossref\]](#)

44. Zhang H, Du J, Wang H, et al. Comparison of diagnostic values of ultrasound micro-flow imaging and contrast-enhanced ultrasound for neovascularization in carotid plaques. *Exp Ther Med*. 2017;14(1):680-688. [\[Crossref\]](#)

45. Meng Q, Xie X, Li L, et al. Assessment of neovascularization of carotid artery atherosclerotic plaques using superb microvascular imaging: a comparison with contrast-enhanced ultrasound imaging and histology. *Quant Imaging Med Surg*. 2021;11(5):1958-1969. [\[Crossref\]](#)

46. Chen X, Wang H, Jiang Y, et al. Neovascularization in carotid atherosclerotic plaques can be effectively evaluated by superb microvascular imaging (SMI): Initial experience. *Vasc Med*. 2020;25(4):328-333. [\[Crossref\]](#)

47. Cantisani V, David E, Ferrari D, et al. Color Doppler ultrasound with superb microvascular imaging compared to contrast-enhanced ultrasound and computed tomography angiography to identify and classify endoleaks in patients undergoing EVAR. *Ann Vasc Surg*. 2017;40:136-145. [\[Crossref\]](#)

48. Downey DB, Fenster A, Williams JC. Clinical utility of three-dimensional US. *Radiographics*. 2000;20(2):559-571. [\[Crossref\]](#)

49. Golemati S, Cokkinos DD. Recent advances in vascular ultrasound imaging technology and their clinical implications. *Ultrasonics*. 2022;119:106599. [\[Crossref\]](#)

50. Xu HX, Zhang QP, Lu MD, Xiao XT. Comparison of two-dimensional and three-dimensional sonography in evaluating fetal malformations. *J Clin Ultrasound*. 2002;30(9):515-525. [\[Crossref\]](#)

51. Ghulam Q, Bredahl K, Eiberg J, et al. Three-dimensional ultrasound is a reliable alternative in endovascular aortic repair surveillance. *J Vasc Surg*. 2021;74(3):979-987. [\[Crossref\]](#)

52. Sahiner B, Chan HP, Roubidoux MA, et al. Malignant and benign breast masses on 3D US volumetric images: effect of computer-aided diagnosis on radiologist accuracy. *Radiology*. 2007;242(3):716-724. [\[Crossref\]](#)

53. Lowe C, Ghulam Q, Bredahl K, et al. Three-dimensional ultrasound in the management of abdominal aortic aneurysms: a topical review. *Eur J Vasc Endovasc Surg*. 2016;52(4):466-474. [\[Crossref\]](#)

54. AlMuhandha K, Hossain MM, Zhao L, et al. Carotid plaque morphometric assessment with three-dimensional ultrasound imaging. *J Vasc Surg*. 2015;61(3):690-697. [\[Crossref\]](#)

55. Landry A, Spence JD, Fenster A. Measurement of carotid plaque volume by 3-dimensional ultrasound. *Stroke*. 2004;35(4):864-869. [\[Crossref\]](#)

56. López-Melgar B, Mass V, Nogales P, et al. New 3-dimensional volumetric ultrasound method for accurate quantification of atherosclerotic plaque volume. *JACC Cardiovasc Imaging*. 2022;15(6):1124-1135. [\[Crossref\]](#)

57. Chen Y, Xing H, Wen J, et al. Three-dimensional ultrasound imaging: an effective method to detect the effect of moderate intensity statin treatment in slowing carotid plaque progression. *J Clin Ultrasound*. 2021;49(7):731-740. [\[Crossref\]](#)

58. Bredahl K, Long A, Taudorf M, et al. Volume estimation of the aortic sac after EVAR using 3-D ultrasound - a novel, accurate and

promising technique. *Eur J Vasc Endovasc Surg.* 2013;45(5):450-455. [\[Crossref\]](#)

59. Helfield B. A review of phospholipid encapsulated ultrasound contrast agent microbubble physics. *Ultrasound in Medicine & Biology.* 2018;45(2):282-300. [\[Crossref\]](#)

60. Piscaglia F, Nolsøe C, Dietrich CF, et al. The EFSUMB Guidelines and Recommendations on the Clinical Practice of Contrast Enhanced Ultrasound (CEUS): update 2011 on non-hepatic applications. *Ultraschall Med.* 2012;33(1):33-59. [\[Crossref\]](#)

61. Kono Y, Pinnell SP, Sirlin CB, et al. Carotid arteries: contrast-enhanced US angiography—preliminary clinical experience. *Radiology.* 2004;230(2):561-568. [\[Crossref\]](#)

62. Clevert DA, Sommer WH, Helck A, Reiser M. Duplex and contrast enhanced ultrasound (CEUS) in evaluation of in-stent restenosis after carotid stenting. *Clin Hemorheol Microcirc.* 2011;48(1):199-208. [\[Crossref\]](#)

63. Feinstein SB. Contrast ultrasound imaging of the carotid artery vasa vasorum and atherosclerotic plaque neovascularization. *Journal of the American College of Cardiology.* 2006;48(2):236-243. [\[Crossref\]](#)

64. Mehta KS, Lee JJ, Taha AA, Avgerinos E, Chaer RA. Vascular applications of contrast-enhanced ultrasound imaging. *Journal of Vascular Surgery.* 2017;66(1):266-274. [\[Crossref\]](#)



Emergency radiology in displaced populations: imaging and practical challenges

✉ Vefa Çakmak¹
 ✉ Pınar Çakmak¹
 ✉ Duygu Herek¹
 ✉ Sonay Aydın²

¹Pamukkale University Faculty of Medicine,
Department of Radiology, Denizli, Türkiye

²Erzincan Binali Yıldırım University Faculty of
Medicine, Department of Radiology, Erzincan, Türkiye

ABSTRACT

Migrants and refugees tend to use emergency departments as their primary source of care, leading to a substantial increase in emergency radiological imaging. Migrants and refugees have risk factors, such as low vaccination rates, poor hygiene, malnutrition, and inadequate self-care, which increase their risk of contracting infectious diseases. For example, the prevalence of tuberculosis among refugee populations in host countries is increasing, and imaging findings related to tuberculosis are frequently observed by radiologists. Strengthening screening programs in host countries for tuberculosis and other infectious diseases among migrant populations can help mitigate the risk of transmission within migrant communities. Another condition, cystic echinococcosis, is more common among refugees and migrants from the Middle East and Afghanistan. For radiologists working in host countries, echinococcosis involving the liver and lungs should be considered in the differential diagnosis. Both intentional (e.g., violence, assault) and unintentional (e.g., workplace injuries, accidents) traumas are frequently encountered in emergency radiology, particularly among refugees and immigrants. Workplace injuries are four times more common among migrants and refugees than among the local population due to their work in high-risk industries, such as construction and heavy industry, and emergency radiology frequently encounters radiological findings of organ injuries due to falls from height. In addition, healthcare professionals in emergency radiology face various challenges when dealing with migrant and refugee patients, such as communication barriers, social security problems, and psychological distress.

KEYWORDS

Refugee, migrant, emergency radiology, tuberculosis, echinococcosis, firearm injury, computed tomography

Due to wars and economic hardships in the Middle East, Asia, and Africa, the number of migrants and refugees in developed countries, such as European Union (EU) countries and the United States (US), is high. Most frequently, it is the emergency departments of hospitals that migrants and refugees use to receive healthcare services. There is a rise in emergency imaging due to an increased workload in emergency departments, the higher incidence of infections not common in host countries, and the greater number of occupational injuries and forensic cases.¹ This increased workload, combined with incomplete patient histories, may result in delayed reporting by emergency radiologists, as well as inaccurate or incomplete interpretations. The aim of this study is to review the radiological findings of diseases whose incidence is expected to rise in host countries due to increased migration.

Notable data on migration

Word choice is important in migration-related contexts. Migration is the movement of people from one place to another, often across an international border, regardless of the reason. An immigrant is a person who comes to live permanently in another country to improve their material and social situation. Due to war in places such as Syria, Palestine, Afghanistan, Sudan, and Ukraine, the US and European countries have become target destinations for refugees, particularly in the last two decades. According to a United Nations High Commissioner for Refugees (UNHCR) report, 122.6 million people had been displaced worldwide as of 2024. The US has the highest number of asylum applications, followed by Germany, Türkiye, Germany, Iran, Colombia, and Uganda, which host approximately 32% of the world's people in need of international protection.²

Corresponding author: Vefa Çakmak

E-mail: vefacakm1408@gmail.com

Received 27 February 2025; revision requested 21 March 2025; last revision received 10 June 2025; accepted 21 July 2025.



Epub: 18.08.2025

Publication date: 02.01.2026

DOI: 10.4274/dir.2025.253297

You may cite this article as: Çakmak V, Çakmak P, Herek D, Aydın S. Emergency radiology in displaced populations: imaging and practical challenges. *Diagn Interv Radiol.* 2026;32(1):57-64.

Türkiye provides international and temporary protection for refugees and has implemented a temporary protection system for Syrian refugees. According to data provided by the Turkish Directorate of Migration Management, the number of Syrians under temporary protection in Türkiye was 3,088,863 as of October 2024.³ Although the gender distribution of this group is equal, three-quarters are under the age of 35. In the Mediterranean and Eastern Mediterranean regions, most asylum seekers and refugees are male, and 70% are under the age of 35.⁴ According to the Turkish Directorate of Migration Management, the most frequently apprehended irregular migrants in Türkiye were from Afghanistan and Syria, peaking in 2019 and 2022.³ According to European Commission data, the irregular migrants who were illegally in the EU in 2022 included Syrians (175,960), Afghans (119,520), and Moroccans (60,215). The EU countries where these people are mostly found are Hungary, Germany, and Italy, respectively.⁵

Increase in emergency service admissions and radiological imaging for migrants and refugees

The most important situation faced by countries of migration is the provision of healthcare to refugees and migrants.⁶ Although migrants, such as those in the Eastern Mediterranean, typically have better initial health status than that of the host population, this advantage tends to diminish over time due to various socioeconomic fac-

tors.⁷ A study conducted in Canada showed that the health of immigrants deteriorated 10 years after their arrival compared with before.⁸ It has been reported that common reasons why refugees and migrants do not attend healthcare appointments are language problems, transportation problems, and health insurance problems.⁹ In many countries, there exist barriers related to health insurance coverage and healthcare costs in the provision of health services. In Türkiye, however, the costs of health services for refugees under temporary protection are covered by the Disaster and Emergency Management Presidency of the Ministry of the Interior.

Migrants and refugees tend to use emergency departments as their primary source of healthcare.¹⁰ Compared with local people, their rate of emergency department admission is significantly higher, particularly for pediatric patients.¹¹⁻¹⁴ It has been reported that among migrants and refugees, emergency admissions are more common for men than for women and that musculoskeletal injuries and traumatic conditions are frequently found in young men.¹⁵ Accordingly, there is an increase in emergency radiological imaging of migrants and refugees in emergency departments.¹⁶ Access to emergency departments in Türkiye is free of charge for Syrians under temporary protection, and one-third of emergency department admissions have been reported to be inappropriate.¹⁷ Emergency departments in Türkiye are frequently preferred by Syrian immigrants because doctors' examinations, laboratory tests, and radiological imaging are free of charge.^{18,19}

Diseases with increased frequency detected upon emergency radiology in host countries

In emergency departments, where immigrants frequently seek healthcare, the utilization of radiological imaging is increasing (Figure 1).

Infections

Local people in host countries believe that refugees/migrants are at high risk of bringing infectious diseases.²⁰ Low vaccination rates, lack of hygiene, malnutrition, and low levels of self-care among migrants and refugees increase the incidence of infectious diseases.²¹ Beyond malnutrition, the intake of contaminated or low-hygiene food during migration can elevate the risk of gastrointestinal infections. Additionally, dietary restrictions stemming from cultural or religious beliefs may contribute to inadequate nutrition and di-

gestive issues in the host country. As a result, migrants and refugees are at increased risk of highly contagious bacterial and viral respiratory system infections, urinary infections, and gastrointestinal tract infections.²² In a study conducted in Türkiye, urinary tract infections were reported as the most common diagnosis in emergency department admissions of pediatric and adult female migrants.²³ During the coronavirus disease-2019 pandemic, the crowded living spaces of large groups of migrants/refugees, poor hygienic conditions, a lack of preventive measures, and difficulties in accessing vaccines increased the risk of contracting the disease.²⁴

Tuberculosis

Tuberculosis is the world's leading cause of death from a single infectious agent, with an incidence of 2.9 per 100,000 people.^{25,26} In 2015, 558 new cases were diagnosed among Syrian refugees.^{22,27} In 2010, approximately 25% of newly diagnosed patients with tuberculosis in the EU were migrants.²⁸ Due to the increase in Syrian and Ethiopian refugees coming to Lebanon, an increase in the frequency of tuberculosis has been observed in that country.²⁹ The World Health Organization (WHO), UNHCR, and the European Center for Disease Prevention and Control have recommended that countries of origin provide active tuberculosis screening.³⁰ Tuberculosis is transmitted by droplets among refugees and migrants with poor hygienic conditions and results in symptoms such as coughing, weight loss, and fever, with its frequency increasing among refugees/migrants in countries that accept migration.^{31,32}

In tuberculosis, the lungs are particularly affected, as seen with extrapulmonary tuberculosis with hematogenous spread. A person who is exposed to *Mycobacterium tuberculosis* for the first time (usually respiratory) develops signs of primary pulmonary tuberculosis. Although these people are often children in endemic areas, the disease can also be seen in adults in the countries of migration. Lymphadenopathy is a common finding, and computed tomography (CT) imaging typically shows peripheral contrast enhancement with central radiolucency in affected lymph nodes. Lobar or segmental consolidation may also be present in cases of primary pulmonary tuberculosis.^{33,34}

Post-primary tuberculosis, however, is typically seen in adults with reactivation of the bacillus. It is usually characterized by upper lobe involvement, cavitations, fibrosis, and tracheobronchial spread. Active

Main points

- According to the United Nations High Commissioner for Refugees, the country with the highest number of asylum applications is the United States, followed by Germany.
- Migrants and refugees tend to use emergency departments as their primary source of healthcare, and this has led to an increase in the use of radiologic imaging in emergency departments.
- The prevalence of tuberculosis is increasing among migrants and refugees in host countries, and host country radiologists should be familiar with tuberculosis radiology.
- Migrant workers are at higher risk of fatal accidents than local workers, and multiple organ injuries are frequently identified through imaging in emergency radiology.
- Radiology personnel in host countries may face challenges such as language barriers, cultural sensitivities, incomplete medical histories, and limited access to social security or imaging services among migrants.

tuberculosis should be considered in the differential diagnosis when lymphadenopathy, consolidation, centrilobular nodules, or peribronchial thickening are detected upon CT imaging of migrants with clinical findings, such as fever, night sweats, coughing, and chest pain. Miliary tuberculosis is defined by hematogenous spread of the infection and is characterized on CT by widespread centrilobular nodules, predominantly in the lung bases (Figure 2).³⁴

Echinococcus granulosus

Cystic echinococcosis is a parasitic (*Echinococcus granulosus*) disease that is transmitted from dogs to humans through intermediate hosts.³⁵ In Argentina, the Middle East, and China, the incidence of cystic echinococcosis is reportedly 5/10,000 people.³⁶ In Europe, it is more common in refugees/migrants of Middle Eastern and Afghan origin. Although liver and lung involvement are frequent, it can involve any part of the body.³⁷⁻³⁹ The liver is reportedly the most commonly affected organ, whereas the lungs are more frequently involved in children (Figure 3).⁴⁰⁻⁴²

The diagnosis of hepatic hydatid cysts is primarily based on ultrasonography, with the ultrasound classification system for hepatic cysts developed by the WHO used in such cases (Figure 4). In this classification, CE1 and CE2 group cysts are defined as active, CE3 group cysts as transitional, and CE4 and CE5 groups as inactive and important for treatment and follow-up.⁴³ Complications of cystic echinococcosis include cyst rupture or superinfection of the cyst, which may result in anaphylaxis.

Hepatitis

In a study conducted among 7,629 immigrants in GeoSentinel clinics, the prevalence of viral hepatitis was found to be 17%.⁴⁴ However, it has been reported that the frequency of hepatitis in immigrants is similar to the frequency in the countries of origin. Hepatitis B virus and hepatitis C virus infections have been reported to be more common in men than in women in countries with high immigration rates.^{45,46} Ultrasonography may reveal findings consistent with acute hepatitis, such as hepatomegaly, increased gallbladder wall thickness, decreased parenchymal echoge-

nicity, and increased periportal echogenicity.⁴⁷

Human immunodeficiency virus and opportunistic infections

It has been reported that there are no patients who are human immunodeficiency virus (HIV) infected among the refugees coming to the US from the Middle East, whereas HIV is detected in 3.3% of African refugees.⁴⁸ This virus has been found in 0.7% of Iraqi refugees entering the US and in 4% of immigrants/refugees in the United Kingdom.^{21,49} As a result, although the HIV rate among immigrants/refugees is lower than in local populations, infections due to factors such as *Toxoplasma gondii*, *Pneumocystis jirovecii*, *Cryptococcus neoformans*, *M. tuberculosis*, Cytomegalovirus, and herpes simplex virus can be identified upon emergency radiological imaging (Figure 5).⁵⁰

Trauma

Intentional trauma

In emergency radiology for migrants and refugees, trauma-related injuries are among the most common conditions requiring imaging after infections. Migrants and refugees often work in the construction and industrial sectors, and safety measures are often insufficient in host countries. Accordingly, injuries due to work accidents are frequently seen in migrants and refugees. It has been reported that refugees have workplace injuries four times more frequently than local people (Figure 6).^{51,52} In a study conducted in Saudi Arabia, 89% of the employees in the construction sector, 41% of whom reported workplace accidents, were migrant and refugee workers, and they suffer these traumatic injuries at a higher rate than the local population.⁵³ In addition, studies conducted in different countries have reported that migrant workers have a higher risk of fatal accidents than local workers.⁵⁴⁻⁵⁶

Unintentional trauma

It is believed that the rate of involvement in judicial incidents and crime among migrants and refugees is higher than among the local population in the host countries.⁵⁷ However, although it varies according to the country of migration and settlement, it has been reported that the rate of involvement of local people in judicial incidents is higher than that of migrants and refugees.⁵⁸ In a study by Yüzbaşıoğlu and Çırkıkcı İşık,⁵¹ it was reported that traffic accidents were the most

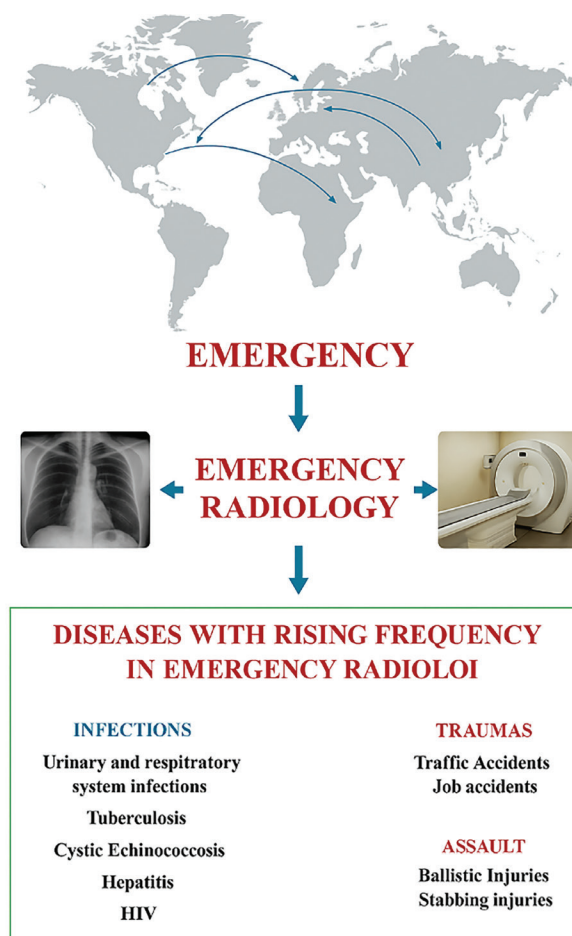


Figure 1. Flowchart of migrants and refugees in emergency radiology.

HIV, human immunodeficiency virus.

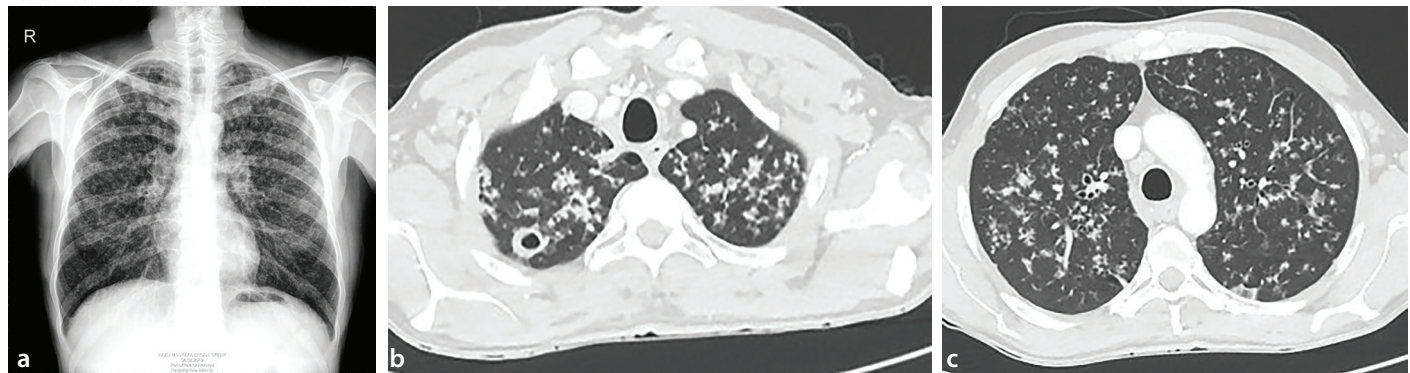


Figure 2. A 41-year-old Afghan man presented with cough and fever. (a) Chest X-ray revealed diffuse nodular radiopacities in the upper lung zones. (b, c) Computed tomography scans showed diffuse millimetric centrilobular nodules in the upper lobes and middle lobe, with cavitary nodules in the right upper lobe. Miliary tuberculosis was suspected, later confirmed by laboratory tests detecting *tuberculosis bacilli*.



Figure 3. A 38-year-old foreign man was diagnosed with a hydatid cyst in the posterior superior segment of the right hepatic lobe based on computed tomography imaging and laboratory confirmation.



Figure 4. In a 22-year-old foreign man, axial computed tomography imaging showed a cystic lesion in the right liver lobe with a detached membrane (arrow), confirming hydatid cyst.

common incidents (27.4%), with assaults the second most common incidents among migrants and refugees who presented at emergency departments for forensic reasons. In a study conducted in Switzerland, 14.6% of cases were related to assaults and 10.2% to traffic accidents, with the extremities being the most commonly affected sites.⁵⁹ A study

conducted in Lebanon found that local people and refugees were admitted to hospital at similar rates as a result of road traffic accidents.⁶⁰ According to a study by Duzkoylu et al.¹⁸, in a settlement area close to the Syrian border, trauma (36.8%) was the most common reason for the hospital admission of refugees/migrants; it was reported that this rate

was higher than that for the local population and that the assault rate (2.5%) was significantly lower than that for the local population. Regarding hospital admissions, the most common sites of injury were reported to be the extremities and the head and neck (Figure 7).^{18,60}

Firearm injuries are reportedly among the top five causes of death in the US.⁶¹ A Canadian study reported a lower risk of firearm injuries for immigrant children and adolescents than for non-immigrant locals. In addition, the study reported that the risk of assault-related firearm injuries was higher among long-term migrants than among non-immigrants (Figure 8).⁶² In Sweden, foreign-born adults reportedly have a higher risk of firearm-related death than locals.⁶³ In a study conducted in Lebanon, knife and gun injuries were found to be significantly higher among the refugee population than among the local population (Figure 9).⁶⁰ Metallic and non-metallic foreign bodies related to prior trauma, particularly in immigrants fleeing war, may be detected on radiological imaging, especially in the extremities. Sequelae of gunshot wounds, including retained bullets or fragments, are also commonly observed in emergency radiology.⁶⁴

Problems encountered in the evaluation of migrants and refugees in emergency radiology

Communication and language problems

Although there are interpreters in hospitals, migrants and refugees are often not able to communicate effectively. Incorrect or incomplete communication may result in improper patient positioning, failure to follow simple instructions such as breath holding, and difficulties in understanding the patient's clinical complaint or medical history. These issues can lead to artifacts in

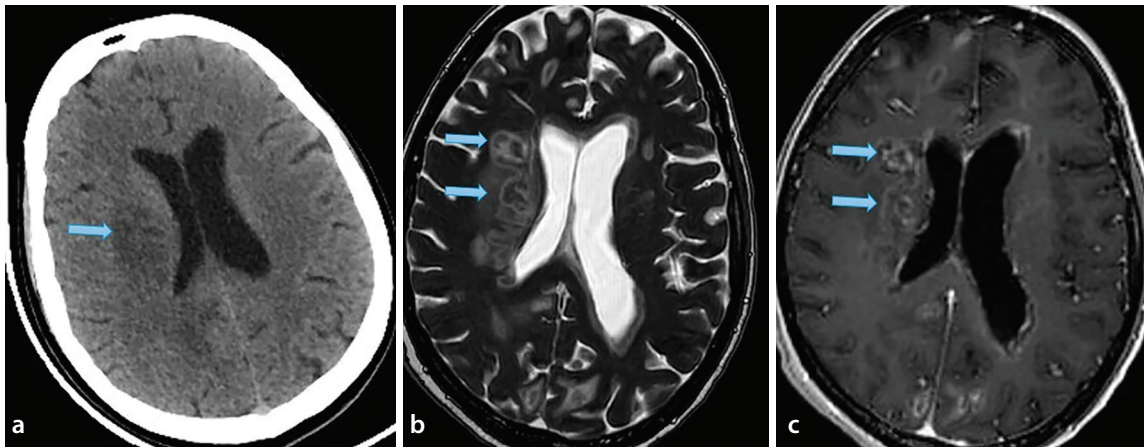


Figure 5. A 35-year-old woman who was HIV positive presented with severe headache and confusion. (a) Non-contrast brain computed tomography showed low-density lesions (arrows) in the right periventricular white matter. (b) Magnetic resonance imaging revealed peripheral hyperintense lesions with vasogenic edema (arrows) in T2-weighted images, with (c) peripheral contrast enhancement (arrows) on T1-weighted images, leading to a diagnosis of cerebral toxoplasmosis. HIV, human immunodeficiency virus.

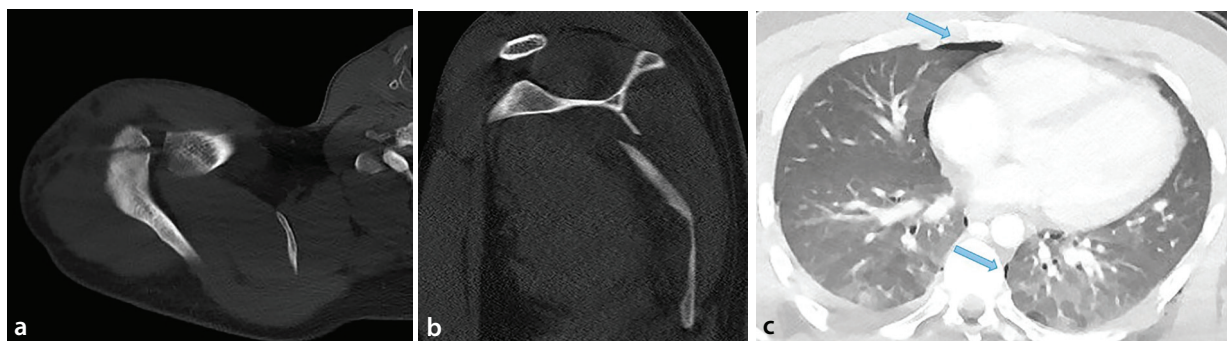


Figure 6. A 23-year-old Afghan man fell from construction scaffolding. (a, b) Computed tomography scans revealed right scapula and acromion fractures, along with (c) bilateral pneumothorax (arrow).

imaging, producing non-diagnostic images and increasing the risk of inaccurate or incomplete reporting. It has been reported that the length of emergency department stay increases for patients who use interpreters compared with those who do not.⁶⁵ This can be explained by a better understanding of patient complaints and the use of more appropriate communication methods.

Social security and insurance problems

It has been reported that the average cost of treatment for Syrian war victims is approximately US \$1,336.⁶⁶ In their study, Karakuş et al.¹ reported that the average cost per case of wounded war victims brought to the emergency department near the Syrian border was approximately US \$1,295. Other studies report that the possibility of not being able to afford hospital-related health expenses often results in refugees leaving the hospital.⁶⁷ In Lebanon, migrants/refugees have been found to be forced to receive health services in public hospitals and select health facilities, resulting in a high rate of non-communicable diseases and great pressure on health-care capacity.^{60,68} Diagnostic examinations

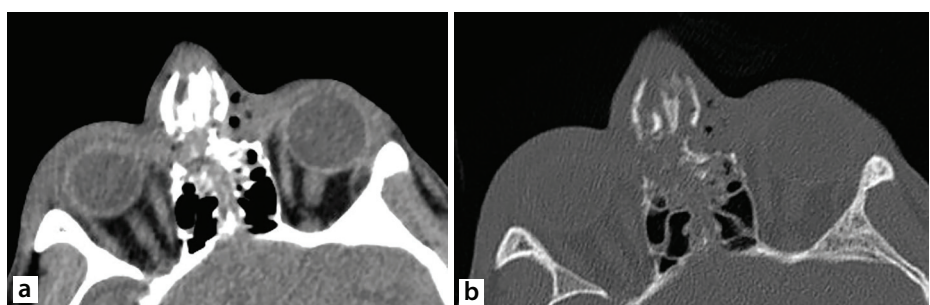


Figure 7. A 27-year-old Iranian man suffered blunt facial trauma due to an assault. (a, b) Computed tomography images showed perinasal and periorbital soft tissue swelling, with multiple displaced nasal bone fractures.

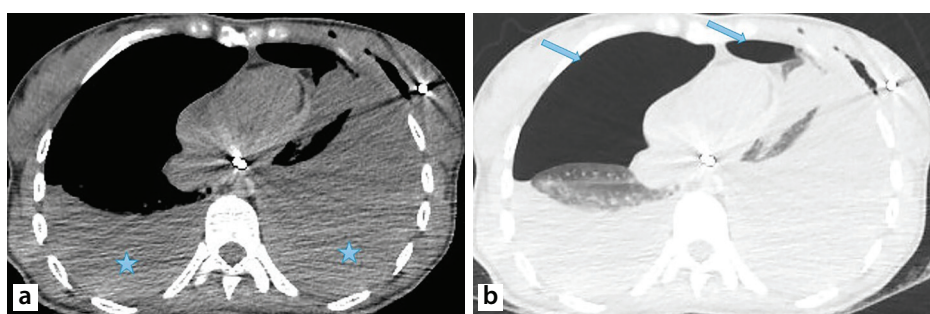


Figure 8. A 35-year-old Syrian woman with gunshot wounds was examined postmortem. (a, b) Computed tomography scans revealed metallic foreign bodies in the heart and left breast, bilateral hemothorax (stars), and bilateral pneumothorax (arrows), more severe on the right.

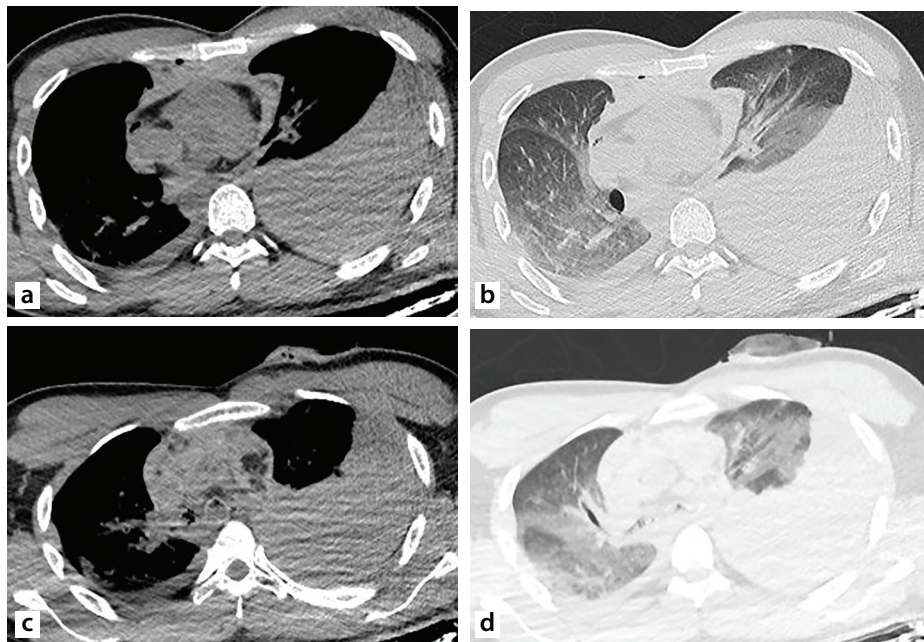


Figure 9. A 24-year-old Syrian man sustained a fatal stab wound to the anterior left chest wall. Computed tomography scans showed an anterior mediastinal hematoma (a), bilateral hemothorax, and a defect in the anterior chest wall (b). Retrosternal hematoma (c) and millimetric pneumothorax (d) were also noted.

may create financial difficulties, particularly among irregular migrants. These financial constraints may also indirectly affect radiological reporting, for example, by reducing the number of follow-up requests or leading to incomplete diagnostic workups.

Problems with migrant and refugee patients

Many behavioral problems can develop among migrants and refugees, especially those who leave their countries due to violence and war.⁶⁹ Problems faced by those working in emergency departments/emergency radiology relating to migrant and refugee patients frequently include psychological problems, cultural problems related to patient privacy, hygiene problems due to a lack of personal self-care, inconsistencies between the clinical histories of migrants and refugees and their past, and distrust of doctors/healthcare personnel and other authority figures. Some immigrants may refuse procedures such as removing clothing for radiological imaging or receiving intravenous contrast agents due to religious beliefs, especially when examined by a radiologist of the opposite sex. Additionally, non-compliance with instructions from radiology staff may occur in individuals with post-traumatic psychological disorders, particularly among those who have migrated from war zones.

Mass casualty incidents

In cases of mass casualty incidents, such as natural disasters or terrorist attacks in host countries, immigrants are often disproportionately affected due to poorer living conditions. A clear example of this occurred after the earthquake that struck Türkiye and Syria on February 6, 2023, when a shortage of regional radiologists led to emergency radiological reporting being performed via teleradiology.⁷⁰

In conclusion, As long as there are wars and economic hardship, there will be migration. Emergency departments will continue to be used by migrants as their primary source of healthcare in host countries, and the frequency of emergency radiological examinations will increase. Emergency radiologists may encounter privacy-related challenges when evaluating immigrant patients, as well as difficulties in imaging due to communication barriers. Imaging artifacts and incomplete reporting may also occur as a result of insufficient clinical history. It is important for radiology clinics in host countries to know the imaging characteristics of diseases whose frequency increases with migration to increase radiological diagnostic performance.

Footnotes

Conflict of interest disclosure

The authors declared no conflicts of interest.

References

1. Karakuş A, Yengil E, Akkükü S, Cevik C, Zeren C, Uruc V. The reflection of the Syrian civil war on the emergency department and assessment of hospital costs. *Ulus Travma Acil Cerrahi Derg.* 2013;19(5):429-433. [\[CrossRef\]](#)
2. United Nations High Commissioner for Refugees (UNHCR). Global trends report 2023. Accessed December 12, 2024. [\[CrossRef\]](#)
3. Syrians under temporary protection, Ministry of Interior of the Republic of Türkiye, Directorate of Migration Management. Accessed December 14, 2024. [\[CrossRef\]](#)
4. Scales SE, Park JW, Nixon R, Guha-Sapir D, Horney JA. A retrospective cross-sectional study of risk factors for communicable disease diagnoses among refugees in mainland Greek camps, 2016-2017. *Sci Rep.* 2024;14(1):15164. [\[CrossRef\]](#)
5. European Union Agency for Asylum (EUAA). Accessed December 14, 2024. [\[CrossRef\]](#)
6. Norredam M, Nielsen SS, Krasnik A. Migrants' utilization of somatic healthcare services in Europe—a systematic review. *Eur J Public Health.* 2010;20(5):555-563. [\[CrossRef\]](#)
7. Sandvik H, Hunskaar S, Diaz E. Immigrants' use of emergency primary health care in Norway: a registry-based observational study. *BMC Health Serv Res.* 2012;12:308. [\[CrossRef\]](#)
8. Ahmed S, Shommu NS, Rumana N, Barron GR, Wicklum S, Turin TC. Barriers to access of primary healthcare by immigrant populations in Canada: a literature review. *J Immigr Minor Health.* 2016;18:1522-1540. [\[CrossRef\]](#)
9. Zeidan AJ, Khatri UG, Munyikwa M, Barden A, Samuels-Kalow M. Barriers to accessing acute care for newly arrived refugees. *West J Emerg Med.* 2019;20(6):842-850. [\[CrossRef\]](#)

10. Silbermann M, Daher M, Kebudi R, Nimri O, Al-Jadiry M, Baider L. Middle eastern conflicts: implications for refugee health in the European Union and Middle Eastern host countries. *J Glob Oncol.* 2016;2(6):422-430. [\[CrossRef\]](#)

11. Oziri A, Schnapper M, Ovadia A, et al. Higher rates of hospitalizations among pediatric refugees than local population attending the emergency department and longer in-patient stay. *Isr Med Assoc J.* 2023;25(4):282-285. [\[CrossRef\]](#)

12. Ruth M C, Carmen M, Dawn B, et al. Use of emergency department for care access by refugees resettling in Kentucky, 2015: findings from the University of Louisville Global Health Center. *J Refug Glob Health.* 2017;1(1):24-28. [\[CrossRef\]](#)

13. Ballotari P, D'Angelo S, Bonvicini L, et al. Effects of immigrant status on emergency room (ER) utilisation by children under age one: a population-based study in the province of Reggio Emilia (Italy). *BMC Health Serv Res.* 2013;13:458. [\[CrossRef\]](#)

14. Yurtseven A, Özcan G, Saz EU. Comparison of between Syrian patients and Turkish patients who admitted to the pediatric emergency department: experience of Ege University. *J Pediatr Emerg Intensive Care Med.* 2015;2:133-136. [\[CrossRef\]](#)

15. Gulacti U, Lok U, Polat H. Emergency department visits of Syrian refugees and the cost of their healthcare. *Pathog Glob Health.* 2017;111(5):219-224. [\[CrossRef\]](#)

16. Ulintz A, Anderson K, Shah I, Khan M, Weinstein E, Peterson R. Pediatric emergency department use by Afghan refugees at a temporary housing facility. *J Am Coll Emerg Physicians Open.* 2023;4(2):12947. [\[CrossRef\]](#)

17. Oktay C, Cete Y, Eray O, Pekdemir M, Gunerli A. Appropriateness of emergency department visits in a Turkish university hospital. *Croat Med J.* 2003;44(5):585-591. [\[CrossRef\]](#)

18. Duzkoylu Y, Basceken SI, Kesilmez EC. Physical trauma among refugees: comparison between refugees and local population who were admitted to emergency department-experience of a state hospital in Syrian border district. *J Environ Public Health.* 2017;2017:8626275. [\[CrossRef\]](#)

19. Tunçyürek Ö, Onur MR, Ertekin E, Çalli C. Current practice of emergency radiology in Turkey and future expectations: a survey study. *Diagn Interv Radiol.* 2023;29(2):300-308. [\[CrossRef\]](#)

20. RKI. Überblick über epidemiologisch wichtige Infektionskrankheiten. *Dtsch Arztebl.* 2015;112(42):1717-1720. [\[CrossRef\]](#)

21. Clark RC, Mytton J. Estimating infectious disease in UK asylum seekers and refugees: a systematic review of prevalence studies. *Journal of Public Health.* 2007;29(4):420-428. [\[CrossRef\]](#)

22. Ozaras R, Leblebicioglu H, Sunbul M, et al. The Syrian conflict and infectious diseases. *Expert Rev Anti Infect Ther.* 2016;14(6):547-555. [\[CrossRef\]](#)

23. Sariaydin T, Erenler AK, Ay MO. Characteristics of refugee patients admitted to the emergency department. *Am J Emerg Med.* 2018;36(11):2109-2110. [\[CrossRef\]](#)

24. Hitch L, Masoud D, Moujabber M, Hobbs LA, Cravero K. COVID-19, migrants, and world large urban areas: a thematic policy brief. *J Public Health Policy.* 2024;45(4):757-770. [\[CrossRef\]](#)

25. World Health Organisation. Tuberculosis. Accessed December 21, 2024. [\[CrossRef\]](#)

26. U.S. Centers for disease control and prevention. National data about tuberculosis. Accessed December 21, 2024. [\[CrossRef\]](#)

27. Leblebicioglu H, Ozaras R. Syrian refugees and infectious disease challenges. *Travel Med Infect Dis.* 2015;13:443-444. [\[CrossRef\]](#)

28. Odone A, Tillmann T, Sandgren A, et al. Tuberculosis among migrant populations in the European Union and the European economic area. *Eur J Pub Health.* 2014;25:506-512. [\[CrossRef\]](#)

29. Araj GF, Saade A, Itani LY, Avedissian AZ. Tuberculosis burden in Lebanon: evolution and current status. *J Med Liban.* 2016;64(1):1-7. [\[CrossRef\]](#)

30. World Health Organization. Chest radiography in tuberculosis detection-summary of current WHO recommendations and guidance on programmatic approaches. Report No. WHO/HTM/TB/2016.20. Geneva, World Health Organization, 2016. [\[CrossRef\]](#)

31. Proença R, Mattos Souza F, Lisboa Bastos M, et al. Active and latent tuberculosis in refugees and asylum seekers: a systematic review and meta-analysis. *BMC Public Health.* 2020;20(1):838. [\[CrossRef\]](#)

32. Meaza A, Tola HH, Eshetu K, Mindaye T, Medhin G, Gumi B. Tuberculosis among refugees and migrant populations: systematic review. *PLoS One.* 2022;17(6):e0268696. [\[CrossRef\]](#)

33. Alshoabi SA, Almas KM, Aldofri SA, et al. The diagnostic deceiver: radiological pictorial review of tuberculosis. *Diagnostics (Basel).* 2022;12(2):306. [\[CrossRef\]](#)

34. Nachiappan AC, Rahbar K, Shi X, et al. Pulmonary tuberculosis: role of radiology in diagnosis and management. *Radiographics.* 2017;37(1):52-72. [\[CrossRef\]](#)

35. Aguadé Higuera NI, Brunetti E, McCloskey C. *Cystic echinococcosis.* *J Clin Microbiol.* 2016;54(3):518-523. [\[CrossRef\]](#)

36. Shrestha S, Ghimire SK, Shrestha M, Maharan S, Bishwakarma K. "Intraperitoneal ruptured hydatid cyst of liver with cystobiliary communication: A case report". *Int J Surg Case Rep.* 2025;127:111012. [\[CrossRef\]](#)

37. Brunetti E, Kern P, Vuitton DA; Writing Panel for the WHO-IWGE. Expert consensus for the diagnosis and treatment of cystic and alveolar echinococcosis in humans. *Acta Trop.* 2010;114(1):1-16. [\[CrossRef\]](#)

38. Richter J, Esmann L, Lindner AK, et al. Cystic echinococcosis in unaccompanied minor refugees from Afghanistan and the Middle East to Germany, July 2016 through June 2017. *Eur J Epidemiol.* 2019;34(6):611-612. [\[CrossRef\]](#)

39. Heendeniya A, Bogoch II. Multiple hepatic hydatid cysts in an Iraqi refugee. *Am J Trop Med Hyg.* 2018;99(5):1107. [\[CrossRef\]](#)

40. Yilmaz M, Akbulut S, Kahraman A, Yilmaz S. Liver hydatid cyst rupture into the peritoneal cavity after abdominal trauma: case report and literature review. *Int Surg.* 2012;97(3):239-244. [\[CrossRef\]](#)

41. Vázquez-Pérez Á, Santos-Pérez JL. Cystic echinococcosis in a Moroccan boy: a silent and neglected disease among refugee and migrant children. *BMJ Case Rep.* 2022;15(2):246399. [\[CrossRef\]](#)

42. Srinivas MR, Deepashri B, Lakshmeesha MT. Imaging spectrum of hydatid disease: usual and unusual locations. *Pol J Radiol.* 2016;81:190-205. [\[CrossRef\]](#)

43. Brunetti E, Tamarozzi F, Macpherson C, et al. Ultrasound and *Cystic echinococcosis*. *Ultrasound Int Open.* 2018;4(3):70-78. [\[CrossRef\]](#)

44. McCarthy AE, Weld LH, Barnett ED, et al. GeoSentinel Surveillance Network. Spectrum of illness in international migrants seen at GeoSentinel clinics in 1997-2009, part 2: migrants resettled internationally and evaluated for specific health concerns. *Clin Infect Dis.* 2013;56(7):925-933. [\[CrossRef\]](#)

45. Al Mahmasani L, Musharrafieh U, Bayram Z, Bizri AR. Hepatitis B and C: neglected infectious diseases among Syrian refugees in Lebanon. *Journal of Global Health Reports.* 2023;7:2023006. [\[CrossRef\]](#)

46. Gencer SK. Comparison of Hepatitis B and hepatitis C seropositivity of the Syrian immigrant and Turkish local people. *Viral Hepat J.* 2022;28(1):32-37. [\[CrossRef\]](#)

47. Heller MT, Tublin ME. The role of ultrasonography in the evaluation of diffuse liver disease. *Radiol Clin North Am.* 2014;52(6):1163-1175. [\[CrossRef\]](#)

48. Barnett ED, Weld LH, McCarthy AE, et al. GeoSentinel Surveillance Network. Spectrum of illness in international migrants seen at GeoSentinel clinics in 1997-2009. Part 1: US-bound migrants evaluated by comprehensive protocol-based health assessment. *Clin Infect Dis.* 2013;56(7):913-924. [\[CrossRef\]](#)

49. Centers for Disease Control and Prevention (CDC). Health of resettled Iraqi refugees – San Diego County, California, October 2007-September 2009. *MMWR Morb Mortal Wkly Rep.* 2010;59(49):1614-1618. [\[CrossRef\]](#)

50. Beckwith CG, DeLong AK, Desjardins SF, et al. HIV infection in refugees: a case-control analysis of refugees in Rhode Island. *Int J Infect Dis.* 2009;13(2):186-192. [\[CrossRef\]](#)

51. Yüzbaşıoğlu Y, Çıraklı İşık G. Retrospective analysis of forensic cases in refugees admitted to emergency department. *Am J Emerg Med.* 2019;37(9):1691-1693. [\[CrossRef\]](#)

52. Habib RR, Mikati D, Al-Barathie J, et al. Work-related injuries among Syrian refugee child workers in the Bekaa Valley of Lebanon: a gender-sensitive analysis. *PLoS One.* 2021;16(9):e0257330. [\[CrossRef\]](#)

53. Alruwaili M, Carrillo P, Soetanto R, Munir F. Occupational accidents, injuries, and associated factors among migrant and domestic construction workers in Saudi Arabia. *Buildings.* 2024; 14(9):2714. [\[CrossRef\]](#)

54. Ahonen EQ, Benavides FG. Risk of fatal and non-fatal occupational injury in foreign workers in Spain. *J Epidemiol Community Health.* 2006;60(5):424-426. [\[CrossRef\]](#)

55. Korkmaz S, Park DJ. Comparison of safety perception between foreign and local workers in the construction industry in Republic of Korea. *Saf Health Work.* 2018;9(1):53-58. [\[CrossRef\]](#)

56. Biering K, Lander F, Rasmussen K. Work injuries among migrant workers in Denmark. *Occup Environ Med.* 2017;74(4):235-242. [\[CrossRef\]](#)

57. Simon RJ, Sikich KW. Public attitudes toward immigrants and immigration policies across seven nations. *Int Migr Rev.* 2007;41(4):956-962. [\[CrossRef\]](#)

58. Çetin S, Gedikbaş M, Gedikbaş SS. Evaluation of foreign national cases applied to Tokat Gaziosmanpasa University Hospital Forensic Medicine Department, 2014-2022. *Int J Legal Med.* 2024;138(5):2015-2020. [\[CrossRef\]](#)

59. Jachmann A, Saffuri R, Eijer H, et al. Trauma consultations in a Swiss tertiary emergency department: Comparison of asylum seekers and the local population-Patient characteristics and patterns of injuries, a retrospective study. *PLoS One.* 2022;17(11):e0277418. [\[CrossRef\]](#)

60. Al-Hajj S, Chahrour MA, Nasrallah AA, Hamed L, Pike I. Physical trauma and injury: a multi-center study comparing local residents and refugees in Lebanon. *J Glob Health.* 2021;11:17001. [\[CrossRef\]](#)

61. Fowler KA, Dahlberg LL, Haileyesus T, Annest JL. Firearm injuries in the United States. *Prev Med.* 2015;79:5-14. [\[CrossRef\]](#)

62. Saunders NR, Lee H, Macpherson A, Guan J, Guttmann A. Risk of firearm injuries among children and youth of immigrant families. *CMAJ.* 2017;189(12):452-458. [\[CrossRef\]](#)

63. Ponzer S, Sundquist J, Johansson SE, Bergman B. Gender, marital status and ethnicity. A Swedish retrospective study of criminality, morbidity and mortality among victims of non-fatal firearm injuries. *Ethn Health.* 1998;3(4):275-282. [\[CrossRef\]](#)

64. Voss JO, Maier C, Wüster J, et al. Imaging foreign bodies in head and neck trauma: a pictorial review. *Insights Imaging.* 2021;12(1):20. [\[CrossRef\]](#)

65. Wallbrecht J, Hodes-Villamar L, Weiss SJ, Ernst AA. No difference in emergency department length of stay for patients with limited proficiency in English. *South Med J.* 2014;107(1):1-5. [\[CrossRef\]](#)

66. Duramaz A, Bilgili MG, Bayram B, Ziroğlu N, Bayrak A, Avkan MC. Orthopedic trauma surgery and hospital cost analysis in refugees; the effect of the Syrian Civil War. *Int Orthop.* 2017;41(5):877-884. [\[CrossRef\]](#)

67. Gornall J. Healthcare for Syrian refugees. *BMJ.* 2015;351:h4150. [\[CrossRef\]](#)

68. Blanchet K, Fouad FM, Pherali T. Syrian refugees in Lebanon: the search for universal health coverage. *Confl Health.* 2016;10:12. [\[CrossRef\]](#)

69. Cheung Chung M, AlQarni N, AlMazrouei M, et al. The impact of trauma exposure characteristics on post-traumatic stress disorder and psychiatric co-morbidity among Syrian refugees. *Psychiatry Res.* 2018;259:310-315. [\[CrossRef\]](#)

70. Aydin S, Kazci O, Ece B, Kantarci M. Earthquakes from a radiological perspective: what is demanded from the radiologists, and what can we do? A pictorial review. *Diagn Interv Radiol.* 2024;30(1):30-41. [\[CrossRef\]](#)



Radiologists' tendency to collaborate with referring physicians in managing contrast media-related risk factors

Burak Öztürk
Özgür Karabıyık²

¹Ünye State Hospital, Clinic of Radiology, Ordu, Türkiye

²Erciyes University Faculty of Medicine, Department of Radiology, Kayseri, Türkiye

PURPOSE

This study investigates radiologists' tendency to collaborate with referring physicians in managing risk factors associated with contrast media (CM) using a modified control preferences scale (CPS). This study is valuable, as it represents the first effort to capture radiologists' perspectives on this issue.

METHODS

The study was conducted through face-to-face interviews with 50 radiologists working at Kayseri City Hospital between June 2021 and April 2022. During the interviews, a modified CPS was used. Participants were presented with five different preference options, each written on a separate card. These preferences ranged from fully active involvement in managing CM-related risks to a completely passive role. At the end of the interview, the two most preferred roles of each participant were identified, categorized, and analyzed using descriptive statistics. All statistical analyses were conducted using the IBM SPSS statistical package.

RESULTS

Of the 50 interviews conducted, 44 were included in the analysis, as they met acceptable permutations. Among these, 6 interviewees (13.6%) preferred a completely active role and 19 (43.2%) preferred a completely passive role. Additionally, 19 radiologists (43.2%) chose one of the collaborative roles.

CONCLUSION

We believe that the preference for a passive role among the majority of radiologists (43.2%) is more closely related to the inadequacies of the existing medical service system and infrastructure rather than a lack of awareness or emotional/motivational inadequacy regarding team formation. These findings should not be interpreted as a negative indicator of teamwork but rather as data for healthcare managers and legal experts to make necessary organizational adjustments. A substantial proportion of radiologists who favor a collaborative role (43.2%) exhibit the emotional-motivational willingness and cognitive understanding needed to engage in team formation and teamwork.

CLINICAL SIGNIFICANCE

The preference for a passive role among radiologists appears to be driven more by the limitations of the current medical service system and infrastructure than by a lack of awareness or motivation for teamwork. Recognizing these systemic barriers is essential for healthcare managers and policymakers to implement necessary organizational improvements. Additionally, radiologists who prefer a collaborative role are likely aware of the benefits of teamwork, highlighting their potential to contribute to future research and improvements in CM-related risk management. Enhancing collaboration opportunities and addressing structural deficiencies may facilitate the greater involvement of radiologists in multidisciplinary teams, ultimately improving patient care and CM-related risk management.

KEYWORDS

Contrast agent, contrast medium, control preferences scale, organizational psychology, physician's role, team building

Corresponding author: Burak Öztürk

E-mail: dr.burak61@gmail.com

Received 28 December 2024; revision requested 06 January 2025; accepted 19 March 2025.



Epub: 11.04.2025

Publication date: 02.01.2026

DOI: 10.4274/dir.2025.243147

You may cite this article as: Öztürk B, Karabıyık Ö. Radiologists' tendency to collaborate with referring physicians in managing contrast media-related risk factors. *Diagn Interv Radiol.* 2026;32(1):65-70.

There are three fundamental principles for quality in healthcare management: patient focus, continuous improvement, and teamwork.¹ A team is defined by Salas et al.² as "interrelated individuals assigned to achieve a common goal". Four elements are necessary to build a team: goal setting, establishing interpersonal relationships, clarifying roles, and problem-solving.^{2,3} In radiology, one of the key challenges requiring effective teamwork is the management of risk factors associated with contrast media (CM).⁴

Like other drugs, CM can cause side effects. Although the severity and incidence of side effects from newer CM are lower than from earlier CM, the widespread use of imaging tools, increased imaging speed, and the preference for defensive medicine have increased public exposure to CM. This has led to an increase in unwanted side effects. Serious side effects can compromise the patient's health, hinder the progress of existing conditions, and necessitate changes in treatment. Consequently, hospital stays are prolonged, and treatment costs increase. Additionally, the patient's trust in the treatment and even in healthcare providers may be undermined, potentially leading to malpractice lawsuits against the clinician. Negative outcomes may eventually compel clinicians to adopt defensive medicine practices, resulting in unnecessary tests, time loss, increased work-

load for clinicians, and unnecessary costs for the national economy.

To mitigate these risks, it is recommended that, prior to any imaging procedure, the indication for contrast-enhanced imaging be clearly established, the benefits and risks carefully weighed, and alternative imaging modalities that can provide comparable or superior diagnostic quality considered.⁵ If contrast-enhanced imaging is deemed necessary, it must be ensured that the selected contrast agent is appropriate for both the patient and the specific indication. The benefits of the imaging study should be balanced against potential adverse reactions to ensure an effective and accurate diagnosis. Additionally, healthcare providers must be prepared to manage any potential adverse reactions promptly.^{5,6}

To manage the risk factors associated with CM, the team members should naturally include radiologists and physicians. Given the identified challenges, effective teamwork between radiologists and physicians is essential.

Many centers still face unresolved issues stemming from unclear role definitions, which hinder effective teamwork. A crucial question remains unanswered: How should the roles of radiologists and referring physicians be defined to establish effective teamwork in managing CM-related risk factors?

To address this, the American College of Radiology (ACR) provides pre-assessment criteria applicable to both radiologists and physicians during diagnostic processes. Adequate patient evaluation and effective communication between the radiologist and the referring physician are critical before administering CM.⁵ According to Bettman⁷, radiologists should first calculate creatinine clearance and assess whether a non-contrast imaging modality could achieve the same diagnostic goal. Furthermore, the Royal College of Radiologists (RCR) states that the ultimate responsibility for CM administration lies with the prescribing physician. Ideally, the patient's clinical history should be available at the time of the imaging request, and the radiology department must review this information before injection.⁸

The CM Safety Committee of the Japan Radiological Society conducted a questionnaire-based survey among radiologists on the use and safety of iodinated and gadolinium CM. The majority of respondents selected answers that indicated an active role in

CM safety. However, some participants chose the "others" option, which included responses such as "at the discretion of the referring physician" and "under the direct supervision of the referring physician".⁹

The European Society of Urogenital Radiology (ESUR) recommends that physicians complete standardized questionnaires when requesting contrast-enhanced examinations to inform radiologists about potential risk factors.⁶ This approach helps define the referring physician's role in the team by providing detailed pre-assessment information, enabling radiologists to prepare for acute reactions or take preventive measures for late-onset reactions. Although ESUR's recommendation promotes cognitive collaboration between team members, effective teamwork should also include motivational factors, such as a proactive willingness to engage in the process.^{10,11}

İmamoğlu et al.³ evaluated clinicians' motivation to collaborate with radiologists in managing CM side effects using the control preferences scale (CPS). A substantial proportion of referring physicians (70.5%) preferred a collaborative role in managing CM-related risk factors.

This study aimed to assess radiologists' tendency to collaborate with physicians in managing CM-related side effects using the CPS. The data obtained will help accurately determine radiologists' cognitive and/or motivational-emotional tendencies, facilitating effective role distribution in teams managing CM-related side effects.

Methods

This study was conducted between June 2021 and April 2022, following approval from the Ethics Committee at Erciyes University Medical Faculty Health Application and Research Center (date: 20.10.2021, decision/protocol no: 2021/701) and Kayseri City Hospital (date: 19.10.2021, decision/protocol no: 55). A total of 50 radiologists working in Kayseri were included. Written informed consent was obtained from each participant. Face-to-face interviews, lasting approximately 15 minutes each, were conducted by a single researcher in an isolated environment. Participants were informed of the study's purpose and scope before data on age, years of expertise, and gender were recorded. Subsequently, the modified CPS was administered.

Main points

- Effective teamwork in radiology is essential for managing risk factors associated with contrast media (CM).
- This study investigates radiologists' tendency to collaborate with referring physicians in managing CM-related risk factors using a modified control preferences scale.
- A substantial proportion of radiologists who favor a collaborative role (43.2%) are likely aware of the positive outcomes of teamwork and are inclined to contribute to future studies on CM-related risk management.
- The preference for passive roles (43.2%) among radiologists reflects the limitations of the current medical service system and infrastructure rather than a lack of awareness or emotional/motivational deficits related to team building.
- These findings should not be perceived as a negative factor in team building but should instead serve as data points for healthcare administrators and medical-legal professionals to implement necessary institutional regulations.

Control preferences scale

The CPS was developed by Degner et al.¹² to evaluate “the level of control an individual wishes to assume when decisions about their medical treatment are made”. Although originally designed for patients with life-threatening diseases, it is applicable to various decision-making processes related to treatment. The scale consists of five separate cards, each representing a different preference along a continuum from fully active (A) to fully passive (E). Each card displays a statement reflecting the level of control preference. Participants make pairwise comparisons between the cards to indicate their preference.

The results are presented as ordered permutations of the letters representing the five cards (e.g., CDBEA, ABCDE, or EDCBA). Only permutations that demonstrate the participant’s understanding of the desired level of control are considered valid. For example, although “ABCDE” is a valid permutation, “AEB-CD” is not, as it does not include two endpoints (A and E) among the most preferred roles. A list of acceptable CPS permutations is provided in Table 1.

The CPS used in this study was a modified version, with changes made to the introduction question and the statements describing control preferences. The introduction question was revised to the following: “What are your thoughts on sharing the responsibility of managing CM-related risk factors with referring physicians?” The control preference statements ranged from fully active (A) to fully passive (E) in managing risk factors. The statements and corresponding letters on the cards are provided in Table 2. The visual representations of the cards are shown in Figures 1-5.

Table 1. Acceptable permutations in the control preferences scale

ABCDE	BCDAE	CDBEA	DECBA
BACDE	CBDAE	CDEBA	EDCBA
BCADE	CDBAE	DCEBA	

Table 2. Statements defining control preferences and corresponding letters on the cards

Letter	Statement
A	I would like to make decisions regarding the prevention of contrast media (CM) reactions.
B	I would like to make decisions regarding the prevention of CM reactions but only after receiving the physician’s opinion.
C	I believe that both the physician and I should share equal responsibility in decisions regarding the prevention of CM reactions.
D	The physician should make the decisions regarding the prevention of CM reactions but only after receiving my opinion.
E	The physician should make all the decisions regarding the prevention of CM reactions.



Figure 1. (Card A) I would like to make decisions regarding the prevention of CM reactions. CM, contrast media.



Figure 3. (Card C) I believe that both the physician and I should share equal responsibility for decisions regarding the prevention of CM reactions. CM, contrast media.



Figure 2. (Card B) I would like to make decisions regarding the prevention of CM reactions but only after obtaining the physician’s views. CM, contrast media.



Figure 4. (Card D) The physician should make decisions regarding the prevention of CM reactions but only after obtaining my views. CM, contrast media.



Figure 5. (Card E) The physician should make decisions regarding the prevention of CM reactions. CM, contrast media.

Table 3. Results of the control preferences scale applied in our study

Role*	Count (n)	Percentage (%)
Active–Active (AB, BA)	6	13.6
Active–Collaborative (BC)	6	13.6
Collaborative–Active (CB)	2	4.5
Collaborative–Passive (CD)	8	18.2
Passive–Collaborative (DC)	3	6.8
Passive–Passive (DE, ED)	19	43.2
Total	44	100

*The meanings of the abbreviations and the definitions of the roles can be found in the “definition of preferences” subsection under the “materials and methods” section.

Definition of preferences

When classifying the results, the first two letters of the acceptable permutations were considered. Accordingly, preferences were classified as follows:

- AB or BA: “Active–Active role”
- BC: “Active–Collaborative role”
- CB: “Collaborative–Active role”
- CD: “Collaborative–Passive role”
- DC: “Passive–Collaborative role”
- DE or ED: “Passive–Passive role”

Statistical analysis

All statistical analyses were conducted using the SPSS software version 30.0 (IBM, Armonk, NY, USA). Descriptive statistics were performed on the role distribution obtained from the CPS classification. The Shapiro–Wilk test was used to assess the assumption of normal distribution. The Mann–Whitney U test was applied to compare control preferences across genders, with a significance level of $P < 0.05$. The Spearman or Kendall correlation test was performed to assess the relationship between age and preferred roles. A significance level of $P < 0.05$ was considered statistically significant.

Results

A total of 50 radiologists were interviewed (18 women, 32 men; age range 30–61 years). However, only 44 interviews were included in the analysis, as they met acceptable permutation criteria. Six interviews were excluded because they did not achieve valid combinations despite repeated attempts.

The results from the 44 interviews are summarized as follows (Table 3):

- Active–active role: 6 radiologists (13.6%)
- Collaborative role: 19 radiologists (43.2% total)

Among those inclined toward collaboration, six (13.6%) preferred an active–collaborative role, two (4.5%) preferred a collaborative–active role, eight (18.2%) preferred a collaborative–passive role, and three (6.8%) preferred a passive–collaborative role.

- Nineteen radiologists (43.2%) preferred a passive–passive role.
- In total, 25 radiologists (56.8%) preferred non-collaborative roles (either active–active or passive–passive).
- Among those who adopted a collaborative role, the most preferred role was collaborative–passive (18.2%). When considering both collaborative and non-collaborative roles, the most preferred role overall was passive–passive (43.2%).

The analysis indicated that men and women had similar preferences, with no statistically significant differences between genders regarding role preferences ($z = -0.433, P = 0.665$). Additionally, there was no statistically significant relationship between age and preferred roles ($P = 0.614$).

Discussion

With advancements in modern medicine, diagnostic methods have become increasingly diverse. Imaging techniques, driven by technological progress, have taken a leading role in this field. Despite improvements in diagnostic quality, the necessity for CM, a fundamental component of these techniques, has not diminished accordingly.

Like other drugs, CM is associated with side effects. Although the severity and frequency of side effects related to newer contrast agents are lower than those of earlier agents, the widespread use of imaging tools, the accelerated pace of imaging procedures, and the preference for defensive medicine have substantially increased public exposure

to CM. Consequently, adverse effects have become more common. Serious side effects can compromise patient health, overshadow the primary illness, and necessitate changes in treatment. This leads to prolonged hospital stays, increased treatment costs, and diminished patient trust in both the treatment itself and healthcare professionals.

From a physician-focused perspective, the global increase in malpractice lawsuits is a well-documented phenomenon. Such potential negative scenarios may inevitably prompt physicians to practice defensive medicine, resulting in unnecessary investigations, time loss, increased workloads, and avoidable economic burdens on national healthcare systems.

To mitigate these risks, it is recommended that, prior to any imaging procedure, the indication for contrast-enhanced imaging be clearly established, the benefits and risks carefully weighed, and alternative imaging modalities that can provide comparable or superior diagnostic quality considered.⁵ If contrast-enhanced imaging is deemed necessary, it must be ensured that the selected contrast agent is suitable for both the patient and the specific indication. The benefits of the imaging study should be balanced against potential adverse reactions to ensure an effective and accurate diagnosis. Additionally, healthcare providers must be prepared to manage any potential adverse reactions promptly.^{5,6}

To address these issues, effective teamwork between radiologists and physicians is essential from a healthcare management perspective. As mentioned earlier, Kelly¹ emphasized that quality in healthcare is built on three principles: patient centeredness, continuous improvement, and teamwork. Salas et al.² define a “team” as “interdependent individuals assigned to accomplish a shared goal”. Key elements of effective teamwork include goal setting, interpersonal communication, clear role differentiation, and problem-solving.^{2,3} Kozlowski and Ilgen¹⁰ classify the psychological processes necessary for achieving these goals into three categories: cognitive, emotional–motivational, and behavioral. Team members are expected to cognitively understand the team’s tasks, be willing to emotionally and motivationally respond to these tasks, and exhibit the necessary behavioral changes.

If the goal is defined as the effective management of risk factors related to CM, the natural team members would include the

radiologist, physician, and patient. However, for the team to function effectively, active interpersonal communication and clearly defined roles are essential.

To facilitate this, the ACR provides pre-assessment criteria applicable to both radiologists and physicians during any diagnostic process. Adequate patient evaluation and effective communication between the radiologist and the referring physician are critical before administering CM.⁵ According to Bettman⁷, radiologists should calculate creatinine clearance and determine whether the diagnosis can be established using an alternative imaging method that does not require CM. The RCR states that the ultimate responsibility for CM administration lies with the prescribing physician. However, the injection itself may be delegated to a practitioner in accordance with local rules and protocols. Additionally, a patient's clinical history should ideally be available at the time of the imaging request, and the radiology department must verify this information before administering contrast agents.⁸

The CM Safety Committee of the Japan Radiological Society conducted a questionnaire-based survey among radiologists on the use and safety of iodinated and gadolinium CM. The majority of respondents selected answers that indicated an active role in CM safety. However, some participants chose the "others" option, which included responses such as "at the discretion of the referring physician" or "under the direct supervision of the referring physician." The percentage of responses falling under the "others" category varied between 10.6% and 19.8%, depending on the survey questions.⁹ The primary aim of this study was to support practitioners in clinical practice. Therefore, it can be inferred that the survey responses reflect the participants' level of knowledge and practical approach rather than their role preferences.

In this context, the ESUR recommends that physicians requesting contrast-enhanced examinations complete standardized questionnaires to inform radiologists about potential risk factors.⁶ According to this recommendation, the role of physicians in the team is to identify risk factors and communicate them to radiologists. This approach enables radiologists to prepare for acute reactions during imaging procedures or take preventive measures against delayed reactions.

However, it is important to recognize that effective teamwork consists not only of cog-

nitive collaboration but also of emotional and motivational engagement.¹⁰ This raises a critical question: Is the cognitive communication between physicians and radiologists adequately supported by emotional and motivational factors?

In this study, the inclination of radiologists in Kayseri to collaborate with physicians in managing CM side effects was investigated. The researcher conducting the interviews did not provide explanations to physicians regarding problem-solving strategies or role definitions. Thus, the adoption of a collaborative role may suggest that radiologists are willing to respond to team-building objectives not only cognitively but also emotionally and motivationally.

The proportion of radiologists who preferred one of the active roles in this study was 31.7%. Several questions arise if radiologists were to assume a more active role:

- Would a separate patient examination room be established for radiologists?
- What methods would be used to identify risk factors? Are there internal guidelines for sharing risk factors with physicians? What is the potential for physician collaboration in creating these guidelines?
- Although acute reactions might be considered the radiologist's responsibility, how would physicians handle unpredictable subacute and chronic reactions?
- Legally, who is responsible for failing to identify risk factors?
- Currently, there are no definitive answers to these questions. In another study using the same method but focusing on physicians, 56.8% preferred one of the active roles.³

In general, considering the collaborative attitude without distinguishing subcategories, the percentage of radiologists adopting a collaborative stance was 43.2%. Among those who preferred a collaborative role, the proportion of passive-collaborative radiologists (those prioritizing passivity over collaboration) was 1.5–2 times lower than that of collaborative-passive radiologists (those prioritizing collaboration over passivity). This finding suggests an inherent inclination toward collaboration. On the other hand, İمامoğlu et al.³ reported that 70.5% of physicians adopted a collaborative attitude.

We infer that radiologists and physicians who favor a collaborative role exhibit both emotional-motivational willingness and cognitive understanding to engage in team

formation and teamwork. This group is likely aware of the positive outcomes of teamwork and is inclined to support future studies that could drive advancements in this field.

In this study, a tendency toward adopting a passive attitude among radiologists was observed (68.2%). Notably, a substantial proportion of radiologists (43.2%) preferred to take a completely passive role (as seen in the last row of the table, the passive-passive role). In a previous study, physicians showed a tendency toward adopting a passive attitude at a rate of 43%, with 15.6% preferring to take a completely passive role.³ Comparing the findings, it is evident that radiologists tend to adopt a passive attitude more frequently than physicians (68.2% vs. 43%).

The predominance of the passive role among radiologists in this study could have several explanations, including the following:

- **Lack of direct patient interaction:** Radiologists do not interact directly with patients, which may lead to limited awareness of clinical and laboratory parameters unless physicians provide this information. As a result, there may be insufficient knowledge of the risk factors needed for managing CM.
- **Excessive workload:** The high volume of daily imaging reports in many healthcare centers makes direct patient interaction challenging.
- **Physical separation of reporting and imaging rooms:** In many healthcare facilities, imaging rooms are located far from reporting rooms, making it difficult to respond promptly to acute reactions.
- **Increasing malpractice cases:** The rising number of malpractice lawsuits has a demotivating effect on radiologists, reducing their willingness to assume additional responsibilities.

Therefore, we believe the preference for passive roles among radiologists is less about a lack of team-building awareness or emotional/motivational deficits and more about the limitations of the current medical service system and infrastructure.

This study has several limitations. It is single-centered, conducted solely among radiologists working in our region, and has a relatively small sample size. Broader, multi-centered studies are necessary to gain a more comprehensive understanding of preferences that align with national or international approaches.

In conclusion, a considerable number of radiologists who favor a collaborative role are likely aware of the positive outcomes of teamwork and demonstrate a willingness to contribute to future studies that could guide this domain. This group exhibits emotional-motivational willingness and cognitive understanding to engage in team formation and teamwork. Radiologists tend to adopt a more passive role than physicians in managing CM reactions. The preference for passive roles among radiologists appears to be driven less by a lack of team-building awareness or emotional/motivational deficits and more by the limitations of the current medical service system and infrastructure. These findings should not be perceived as a negative factor in team building but rather as data points for healthcare administrators and medical-legal professionals to implement necessary institutional regulations. This is particularly important because practices for managing CM reactions are not yet fully institutionalized worldwide. We hope that data obtained from future studies using reliable methodologies—such as the CPS employed in this study—will provide a foundation for

developing standardized practices in this field.

Footnotes

Conflict of interest disclosure

The authors declared no conflicts of interest.

References

1. Kelly DL. Applying quality management in healthcare: a systems approach. 2nd ed. *Health Administration Press*; 2007. [\[Crossref\]](#)
2. Salas E, DiazGranados D, Weaver SJ, King H. Does team training work? Principles for health care. *Acad Emerg Med*. 2008;15(11):1002-1009. [\[Crossref\]](#)
3. İmamoğlu H, Doğan S, Erdoğan N. Referring physicians' tendency to collaborate with radiologists in managing contrast media-related risk factors. *J Am Coll Radiol*. 2018;15(2):296-300. [\[Crossref\]](#)
4. Beckett KR, Moriarity AK, Langer JM. Safe use of contrast media: what the radiologist needs to know. *Radiographics*. 2015;35(6):1738-1750. [\[Crossref\]](#)
5. ACR manual on contrast media. 2024. Last Accessed Date: 24.03.2025. [\[Crossref\]](#)
6. ESUR guidelines on contrast agents 10.0.2018. Last Accessed Date: 24.03.2025. [\[Crossref\]](#)
7. Bettmann MA. Frequently asked questions: iodinated contrast agents. *Radiographics*. 2004;24 (Suppl 1):S3-10. [\[Crossref\]](#)
8. The Royal College of Radiologists. Standards for intravascular contrast agent administration to adult patients. *R Coll Radiol*. 2010; (second edition):6-7. [\[Crossref\]](#)
9. Japan Radiological Society. Guideline. Last Accessed Date: 24.03.2025. [\[Crossref\]](#)
10. Kozlowski SWJ, Ilgen DR. Enhancing the effectiveness of work groups and teams. *Psychol Sci Public*. 2006;7(3):77-124. [\[Crossref\]](#)
11. West MA. The Human Team: Basic Motivations and Innovations. In: *Handbook of Industrial, Work & Organizational Psychology - Volume 2: Organizational Psychology*. SAGE Publications Ltd; 2001:270-288. [\[Crossref\]](#)
12. Degner LF, Sloan JA, Venkatesh P. The control preferences scale. *Can J Nurs Res*. 1997;29(3):21-43. [\[Crossref\]](#)



Bibliometric analysis of radiology residency theses in Türkiye: publication metrics and trends

Ali Salbas

Ali Murat Koc

Izmir Katip Çelebi University, Atatürk Training and Research Hospital, Department of Radiology, İzmir, Türkiye

PURPOSE

This study aimed to conduct the first comprehensive bibliometric analysis of radiology residency theses in Türkiye, evaluating publication rates, indexing characteristics, citation performance, and key factors associated with successful thesis-to-publication conversion.

METHODS

This retrospective study included 3,136 radiology residency theses completed between 1971 and December 2024, retrieved from the National Thesis Center. Data were collected on the thesis topic, advisor title, institution type, and study design. Publication status was assessed through searches using author and advisor names and keywords across Google, Google Scholar, PubMed, Web of Science, TR Index, and DergiPark. For published articles, the journal name, indexing category, impact factor quartile, citation count, and time to publication were recorded. Statistical analyses included descriptive statistics, the chi-squared, Mann-Whitney U, and Kruskal-Wallis tests, and regression models (a P value of <0.05 was considered significant).

RESULTS

Most theses were from university hospitals (83.1%) and supervised by professors (45.8%). A total of 1,165 theses (37.1%) were published as journal articles, of which 651 (20.8% of all theses) appeared in Science Citation Index Expanded (SCIE)-indexed journals. Among the SCIE publications, 39.2% were in Q3 or Q4 journals. The most frequent thesis topics were neuroradiology (16.0%) and abdominal radiology (13.3%), whereas imaging physics and radiation safety was least represented (1.6%). Publication rates significantly increased over time ($P = 0.045$), and time to publication decreased ($P < 0.001$), with a median of 1,300 days. Theses supervised by assistant professors had the highest publication rate (43.0%, $P = 0.013$). University-based theses received more citations than those from training and research hospitals ($P < 0.001$). Residency students were first authors in 76.4% of publications. Articles with the advisor or another researcher as the first author were more frequently published in SCIE journals ($P < 0.001$), received more citations ($P < 0.001$), and had shorter time to publication ($P < 0.001$).

CONCLUSION

Approximately one-third of radiology theses in Türkiye are published, with a notable share in SCIE-indexed journals. Thesis publication performance has improved significantly over time.

CLINICAL SIGNIFICANCE

This study highlights the publication potential of radiology residency theses and reveals key factors associated with research visibility. Recognizing these trends may help guide institutional policies, promote academic mentorship, and encourage residents to pursue higher-impact publications. Residency theses should be regarded as integral components of scholarly activity, rather than solely as graduation requirements.

KEYWORDS

Bibliometrics, radiology, residency training, thesis publication, journal impact factor

Corresponding author: Ali Salbas

E-mail: dralisaalbas@gmail.com

Received 20 June 2025; revision requested 23 July 2025;
accepted 30 July 2025.



Epub: 15.09.2025

Publication date: 02.01.2026

DOI: 10.4274/dir.2025.253525

You may cite this article as: Salbas A, Koc AM. Bibliometric analysis of radiology residency theses in Türkiye: publication metrics and trends. *Diagn Interv Radiol.* 2026;32(1):71-80.

Bibliometrics, defined in 1969, is a method that enables the statistical analysis of academic documents.¹ Such studies reveal research trends and the development of the literature, thereby guiding future investigations. In Türkiye, medical residency students are required to prepare an original thesis in their field of specialization to qualify for the specialty examination. This requirement is explicitly stated in the "Regulation on Medical Specialization Training".² Similar practices also exist in some European countries.³ The thesis process is a fundamental component of medical education, providing physicians with scientific research skills while contributing to the academic literature. Moreover, residency theses carry significant potential to enrich the medical literature. Thesis data serve as valuable resources for evaluating research trends, knowledge gaps, and academic productivity; their bibliometric analysis is therefore critical for scientific guidance.⁴

In recent years, bibliometric analyses of residency theses in various medical specialties have been conducted in Türkiye.⁴⁻⁸ However, as of February 2025—when this study was initiated—no such study specific to the field of radiology had been identified. In this regard, our study represents the first bibliometric analysis of radiology residency theses in Türkiye.

Methods

This retrospective and descriptive study examined the bibliometric characteristics of radiology residency theses in Türkiye, as well as their publication rates in peer-reviewed journals. Theses were retrieved from the online database of the National Thesis Center of the Council of Higher Education of Türkiye.⁹ During the search process, "medical residency thesis" was selected as the thesis type, and both "Radiology" and "Radiodiagnostics" were selected separately as the department fields. Records from all available years were included without

Main points

- Approximately 37% of radiology residency theses in Türkiye have been published in peer-reviewed journals, with 20.8% appearing in Science Citation Index Expanded (SCIE)-indexed journals.
- More than half of these SCIE publications were in lower-quartile (Q3–Q4) journals.
- Publication performance has significantly improved over time, with higher publication rates and shorter time to publication.

applying a date restriction. Theses with incomplete data or access restrictions, as well as those belonging to other specialties but erroneously categorized under radiology due to user error, were excluded from the study. Additionally, based on the assumption that the conversion of a thesis into a publication generally requires a minimum of 6 months, theses dated January 2025 and later were excluded. As a result, a total of 3,136 theses were included in the final analysis (Figure 1).

For each thesis, variables such as the title, gender of the author, gender and academic title of the advisor, number of pages, year of publication, name and type of institution, number of advisors, study type, and sample size were recorded. In cases of dual supervision, the advisor with the higher academic title was considered the primary advisor.

Thesis topics were categorized into 14 subgroups based on the subject areas defined with reference to the Education and Scientific Research Groups of the Turkish Society of Radiology (TSR):¹⁰ Neuroradiology, Head and Neck Radiology, Musculoskeletal Radiology, Breast Radiology, Thoracic Radiology, Abdominal Radiology, Genitourinary Radiology, Interventional Radiology, Cardiovascular Radiology, Imaging Physics and Radiation Safety, Obstetric Radiology, Emergency Radiology, Pediatric Radiology, and Other (for theses not falling into the aforementioned 13 groups). The classification of the theses into subgroups was performed

by a team of two radiology consultants, and consensus was achieved in all evaluations.

For each thesis, its status of publication as an original research article was investigated. Conference presentations and abstracts were excluded due to systematic accessibility limitations and lack of alignment with the study's objectives. Searches were conducted using the names of the thesis author and advisor, along with relevant keywords, across multiple databases and platforms: Google, Google Scholar, PubMed, Web of Science (WoS), and TR Index (a national citation index for Turkish academic journals).¹¹⁻¹⁵ Additionally, Dergipark, an academic publication platform based in Türkiye, was included in the screening process.¹⁶ When a corresponding article was identified, the following data were recorded: article title, name of the journal, country of publication, year of publication, identity of the first author (i.e., whether the thesis author), number of citations (according to Google Scholar and PubMed), and the indexing status. The indexing status was determined based on how the journal was indexed at the time of article publication. Furthermore, the number of days between the thesis completion date and the article publication date was calculated to determine the time to publication.

Publications were classified into the following five categories based on the indexing status of the journals:

1. Journals indexed in the Science Citation Index Expanded (SCIE)

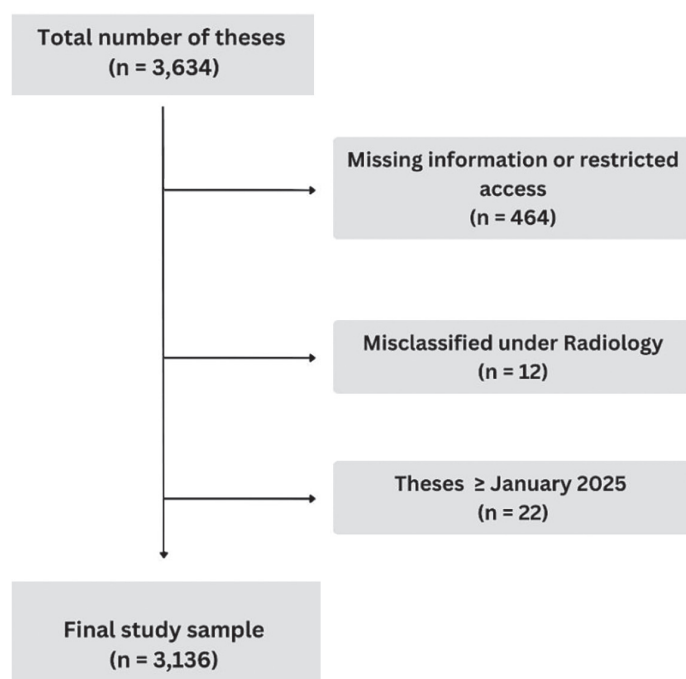


Figure 1. Flowchart illustrating the selection process of radiology residency theses included in the study.

2. Journals indexed in the Emerging Sources Citation Index (ESCI)
3. Other internationally indexed journals not listed in WoS
4. National peer-reviewed journals indexed in TR Index
5. Other national peer-reviewed journals not indexed in TR Index

Note: Currently, the WoS platform includes only the SCIE category. Journals previously categorized under the Science Citation Index are now considered part of the SCIE.

If a journal was indexed in more than one database, it was classified only under the highest-ranking category according to the predefined hierarchy. Accordingly, journals indexed in both TR Index and ESCI were classified under ESCI only, while those indexed in both TR Index and SCIE were classified under SCIE only.

For publications in the SCIE category, the Journal Impact Factor quartile ranking (Q1–Q4) was determined using the Journal Citation Reports database provided by Clarivate's WoS.¹⁷ These rankings were recorded based on the year in which the article was published.

Ethical approval for the study was obtained from the İzmir Katip Çelebi University Ethics Committee (date: January 16, 2025; decision no: 0014). This study did not involve any patient data or human participants; therefore, informed consent was not required.

Statistical analysis

Statistical analyses were performed using IBM SPSS Statistics version 25.0 (IBM Corp., Armonk, NY, USA). Descriptive statistics were reported as mean, median, standard deviation, and minimum–maximum values for continuous variables, and as frequencies and percentages for categorical variables. The Shapiro–Wilk test was used to assess the distribution characteristics of continuous variables. For data that did not show a normal distribution, non-parametric tests were applied. The chi-squared test was used to evaluate associations between categorical variables. For comparisons between two independent groups with non-normally distributed continuous data, the Mann–Whitney U test was used; for comparisons among three or more groups, the Kruskal–Wallis H test was employed. In cases where the Kruskal–Wallis test indicated statistical significance, Bonferroni-corrected post-hoc Mann–Whitney U tests were con-

ducted to determine pairwise differences. The Z-test for proportions was used for pairwise comparison of proportions and to identify which groups differed in chi-squared analyses with significant results. The annual number of theses was analyzed using Poisson regression, and the probability of publication according to thesis year was assessed using binary logistic regression. A *P* value of <0.05 was considered statistically significant in all tests.

Results

The majority of the 3,136 radiology residency theses were conducted at university hospitals (83.1%) and under the supervision of professors (45.8%). A total of 84 theses were supervised by two advisors. Additional descriptive characteristics are presented in Table 1.

A statistically significant increase in the number of radiology residency theses was observed after the year 2000 ($P < 0.001$), with the highest number recorded in 2010 ($n = 198$) (Figure 2). Among thesis topics, neuroradiology (16.0%), abdominal radiology (13.3%), and interventional radiology (12.4%) were the most frequently selected fields, whereas imaging physics and radiation safety (1.6%) was the least preferred (Figure 3). The distribution of topics by year is detailed in Figure 4.

Out of the 3,136 radiology residency theses, 1,165 (37.1%) were found to have been published as scientific articles in national or

international peer-reviewed journals. Among all theses, the publication rate in journals indexed in the SCIE was 20.8% ($n = 651$). However, when considering only the published articles, more than half (55.9%) appeared in SCIE-indexed journals, and 39.2% of these were published in journals classified under the Q3 and Q4 quartiles (Table 2).

The most frequently published-in journals were *Diagnostic and Interventional Radiology* (7.0%) and the *European Journal of Radiology* (4.2%), and the detailed distribution of journals is provided in Supplementary Table 1. The time from thesis completion to publication ranged from 151 to 11,680 days, with a median of 1,300 days [interquartile range (IQR): 826–2,106]. The mean time was $1,662.6 \pm 1,270.2$ days. The number of citations per publication ranged from 0 to 416, with a median of 3 (IQR: 0–17). The mean number of citations was 14.7 ± 30.2 . In the vast majority of published articles (76.4%, $n = 890$), the first author was the residency student; in contrast, thesis advisors and other researchers were listed as first authors in 12.9% ($n = 150$) and 10.7% ($n = 125$) of publications, respectively.

The rate at which theses were converted into publications showed an upward trend, particularly after the year 2000, with a statistically significant increase in the probability of publication over time ($P = 0.045$) (Figure 5). Similarly, the time to publication significantly decreased over the years ($P < 0.001$) (Figure 6). The publication rates of theses varied across different radiology subspe-

Table 1. Descriptive characteristics of radiology residency theses ($n = 3,136$)

	Category	n (%)
Resident gender	Male	1,977 (63.1%)
	Female	1,159 (36.9%)
Supervisor gender	Male	2,187 (69.8%)
	Female	949 (30.2%)
Academic titles of supervisors	Professor	1,437 (45.8%)
	Associate professor	1,047 (33.4%)
	Assistant professor	498 (15.9%)
	Consultant	154 (4.9%)
Institution	University hospital	2,605 (83.1%)
	Training and research hospital	531 (16.9%)
Study design	Retrospective	2,718 (86.7%)
	Prospective	409 (13.0%)
	Other (e.g., experimental)	9 (0.3%)
Page count	Mean \pm SD (min–max)	77.4 \pm 22.9 (28–226)
	1–50 patients	1,129 (36.1%)
Number of patients per thesis	51–100 patients	791 (25.3%)
	≥ 101 patients	1,208 (38.6%)

SD, standard deviation; min, minimum; max, maximum.

cialties. The highest publication rate was observed in the field of imaging physics and radiation safety (51.0%), followed by abdominal radiology (40.4%) and musculoskeletal radiology (40.3%). In contrast, the lowest publication rates were recorded in breast radiology (32.6%), thoracic radiology (33.2%), and obstetric radiology (34.0%) (Table 3).

No statistically significant relationship was found between thesis topic and publication rate, number of citations, or time to publication ($P = 0.296$, $P = 0.842$, and $P = 0.280$, respectively) (Table 3). Since the overall group differences were not statistically significant, no post hoc comparisons were performed for these analyses.

There were no significant differences in publication rate ($P = 0.537$) or citation count ($P = 0.089$) based on the gender of the residency student. However, the time to publication was significantly longer for theses authored by female residents than by their male counterparts ($P < 0.001$).

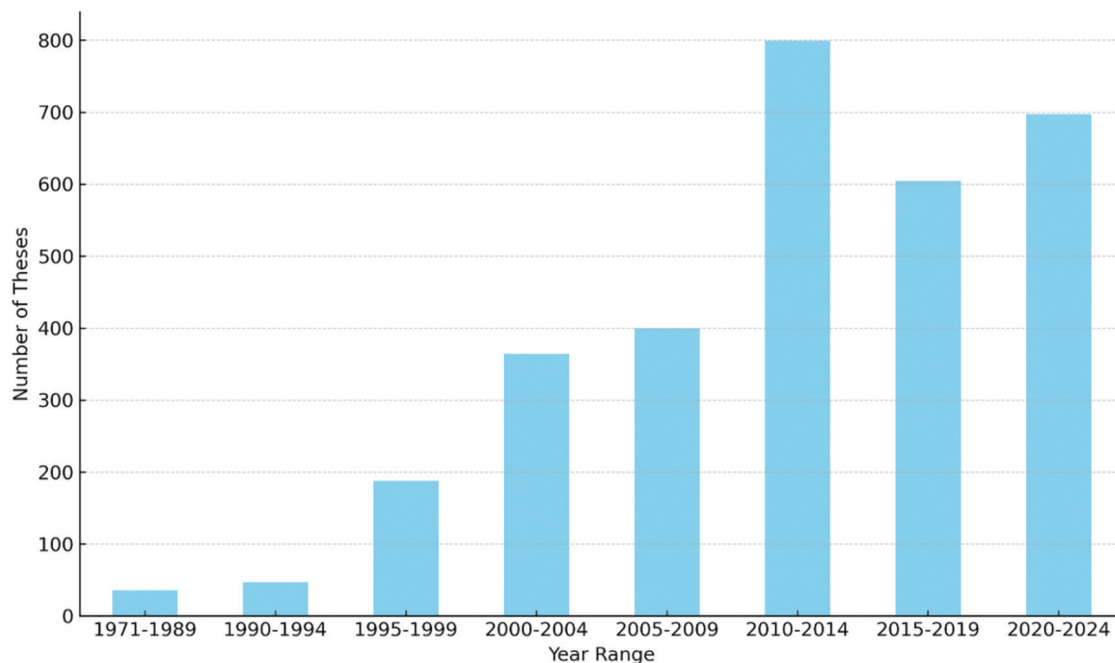


Figure 2. Distribution of radiology residency theses by year range. The number of theses shows a marked increase starting from the 2000s, with the highest number of theses observed during the 2010–2014 period.

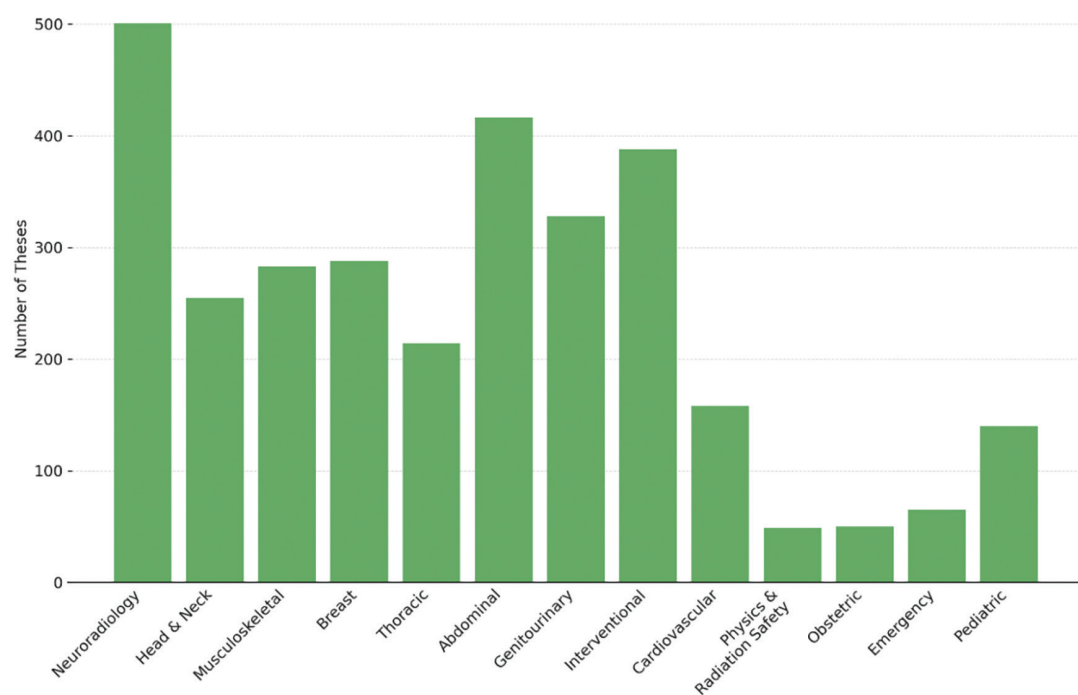


Figure 3. Distribution of radiology residency theses by subspecialty area. One thesis categorized as "Other" was excluded for visual clarity. The data cover the entire period of 1971–2024.

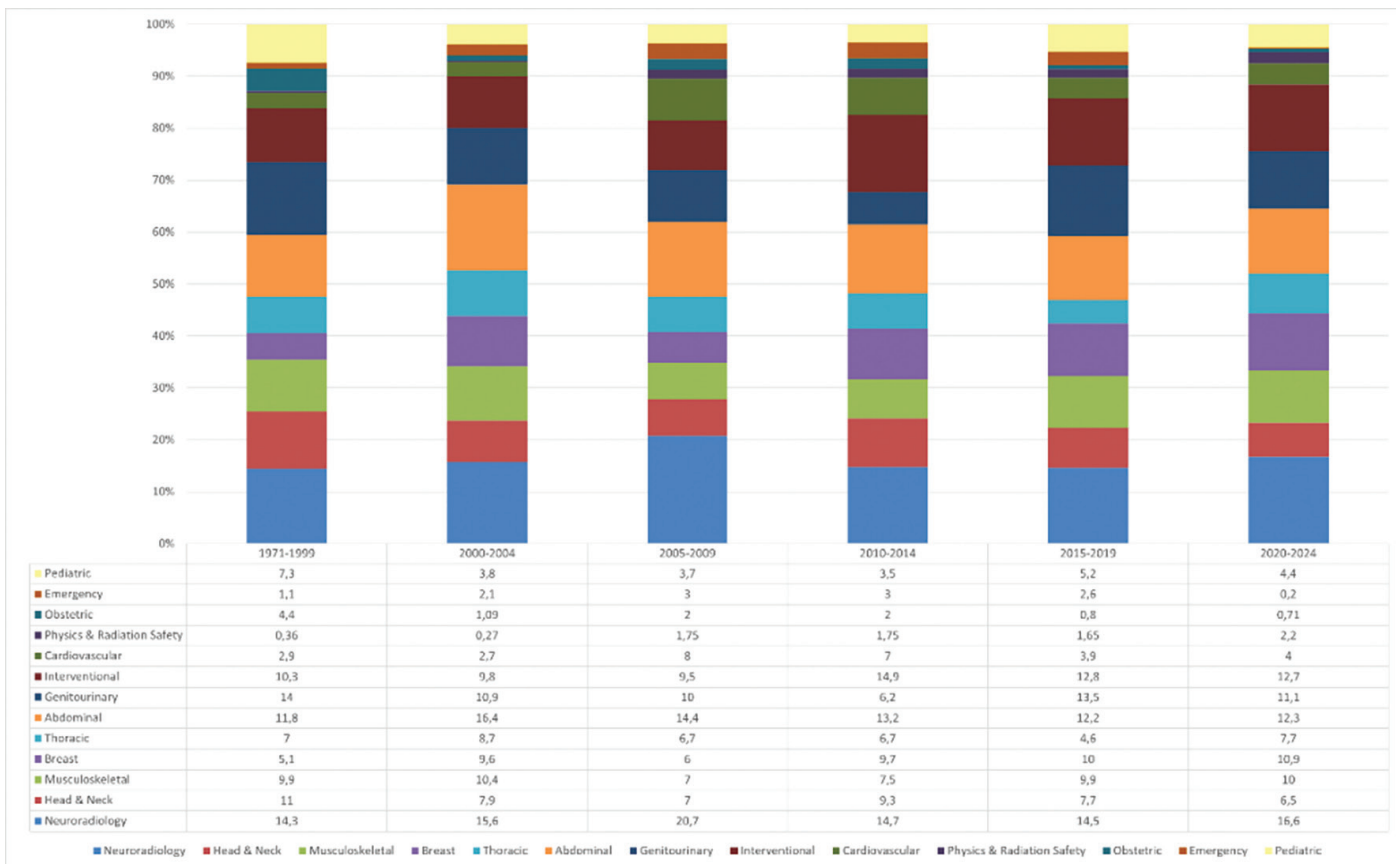


Figure 4. Temporal distribution of radiology residency thesis topics by 5-year intervals. The chart illustrates the proportional representation (%) of each subspecialty area between 1971 and 2024. Neuroradiology and abdominal radiology have consistently remained among the most frequently studied fields, whereas topics such as imaging physics and radiation safety, emergency radiology, and obstetric radiology have maintained relatively low proportions across all periods.

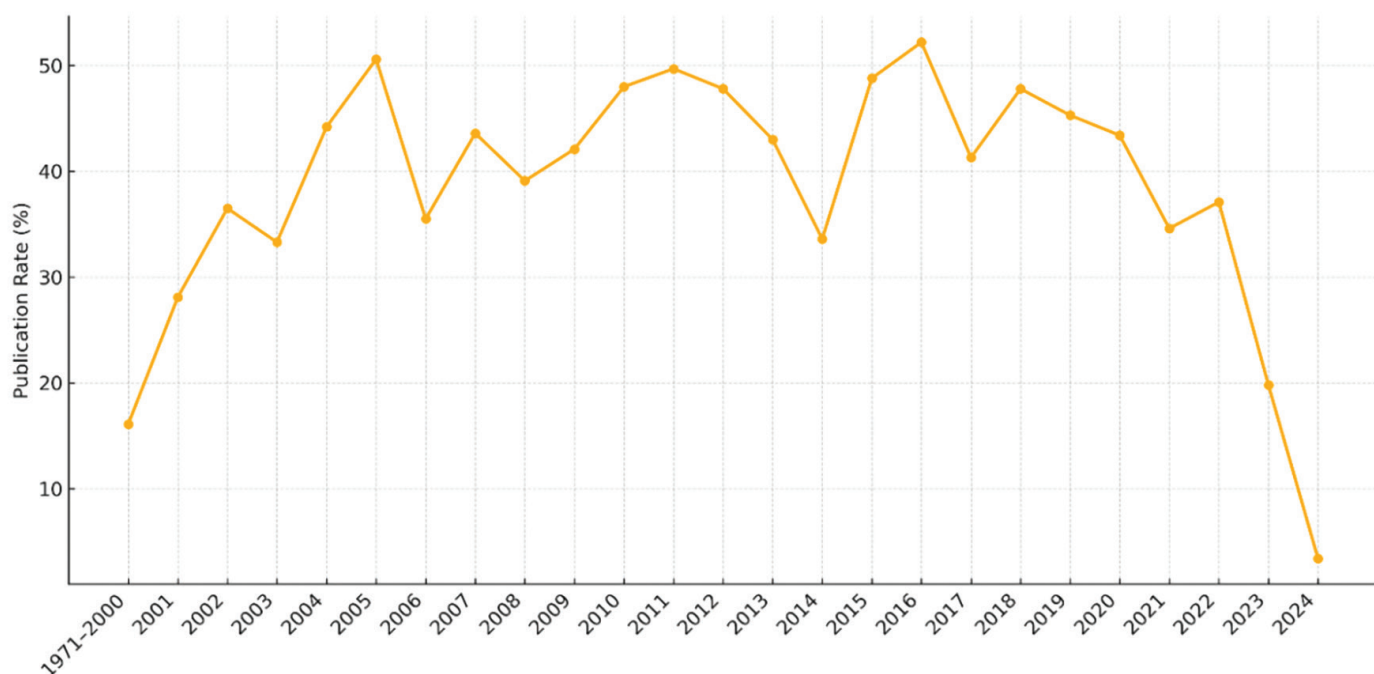


Figure 5. Article publication rates of radiology residency theses by year (1971–2024). Years indicate the thesis completion year. Percentages represent the proportion of theses that were published as journal articles.

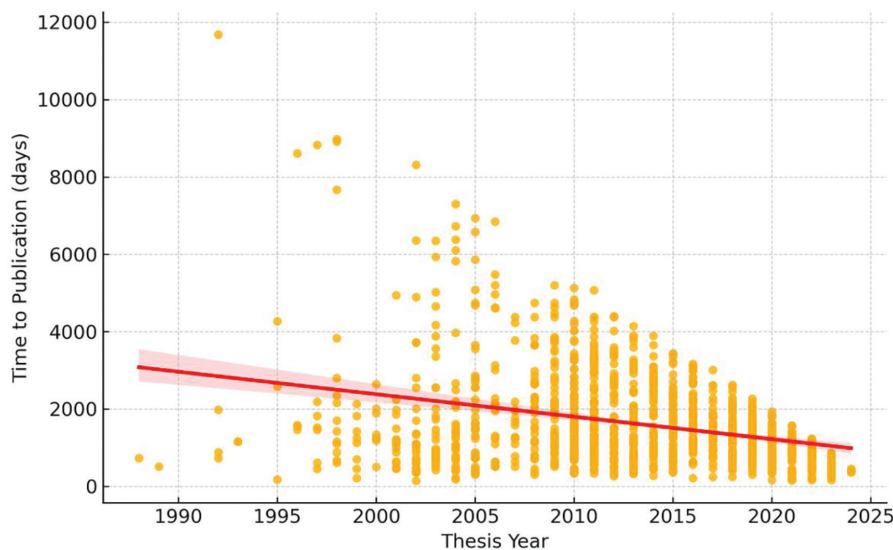


Figure 6. Time to conversion into a published article by thesis year. Each dot represents a thesis that was eventually published as a journal article. The red regression line indicates a statistically significant decrease in time to publication over the years ($\beta = -58.1$; $P < 0.001$).

Table 2. Journal index and quartile distribution of published theses

Journal index	n	%
SCIE	651	55.9%
Q1	53	4.6%
Q2	141	12.1%
Q3	222	19.1%
Q4	234	20.1%
ESCI	135	11.6%
TR Index	235	20.2%
Other international	31	2.7%
Other national	113	9.7%
Total	1,165	100%

SCIE, Science Citation Index Expanded; ESCI, Emerging Sources Citation Index; TR Index, a national database of scholarly journals published in Türkiye, maintained by ULAKBİM (Turkish Academic Network and Information Center), and often referred to as TR Dizin; Other international, International peer-reviewed journals that are not indexed in Web of Science Core Collection (i.e., not included in SCIE or ESCI); Other national, peer-reviewed Turkish journals that are not indexed in TR Index; Q1–Q4, Journal Impact Factor-based quartile rankings within SCIE-indexed journals, as defined by Web of Science.

Note: One SCIE-indexed article published in 1996 was not assigned a quartile rank, as journal quartile data were introduced by Web of Science starting in 1997.

No significant differences were observed in publication rate, citation count, or time to publication based on the gender of the thesis advisor (Table 3). Similarly, there were no statistically significant differences in citation count ($P = 0.322$) or time to publication ($P = 0.057$) according to the academic title of the advisor. However, a statistically significant difference was found in publication rates based on the advisor's academic title ($P = 0.013$). The highest publication rate (43.0%) was observed in theses supervised by advisors with the title of assistant professor, which was significantly higher than those supervised by professors ($P = 0.001$) and associate professors ($P = 0.041$). No significant

differences were observed between assistant professors and consultants ($P = 0.243$), or among the other group pairs, including professor versus associate professor ($P = 0.160$), professor versus consultant ($P = 0.479$), or associate professor versus consultant ($P = 0.976$).

No statistically significant differences were found in publication rate ($P = 0.539$) or time to publication ($P = 0.659$) based on the type of institution. However, when citation counts were compared, publications originating from universities had significantly higher citation numbers than those from training and research hospitals ($P < 0.001$) (Table 3).

Among the theses that were converted into publications, the rate of publication in SCIE-indexed journals was 50.8% when the residency student was the first author, whereas this rate was higher for publications where the advisor (74.7%) or another researcher (69.6%) was the first author. A statistically significant difference was found between groups when comparing SCIE publication rates according to first authorship status ($P < 0.001$). Articles with the advisor or another researcher as the first author were significantly more likely to be published in SCIE-indexed journals than those authored by the residency student ($P < 0.001$ for both comparisons). No significant difference was found between publications with the advisor versus another researcher as first author ($P = 0.349$).

Articles with the advisor or another researcher as the first author received significantly more citations than those authored by the residency student ($P < 0.001$ for both comparisons), with no significant difference between the advisor and other researcher groups ($P = 1.000$).

Time to publication also differed significantly among the groups ($P < 0.001$); publications first-authored by the residency student had a longer time to publication than those authored by the advisor ($P < 0.001$) or another researcher ($P < 0.001$). No significant difference was observed between the advisor and other researcher groups ($P = 0.101$).

Discussion

This bibliometric analysis is the first comprehensive study to evaluate the publication rates and academic characteristics of medical residency theses in the field of radiology in Türkiye. By examining all radiology theses available in the National Thesis Center database, the study systematically identified the factors influencing the publication process.

The finding that the majority of theses were conducted in university hospitals (83.1%) and primarily under the supervision of professors (45.8%) and associate professors (33.4%) is consistent with trends observed in other medical specialties.^{4,7,18} This distribution may be related to the number of residency students in these institutions and the academic experience of the advisors.

A marked increase in the number of radiology residency theses has been observed, particularly since the 2000s, which is associated with the expansion of radiology residency quotas in Türkiye (e.g., from 38 positions in 2008 to 105 in 2018).¹⁹ Considering

Table 3. Publication rate, citation count, and time to publication by demographic and institutional variables

Variable	Category	Publication rate (%)	Citations median (IQR)	Time to publication (days); median (IQR)
Resident gender	Male	37.6 (743/1,977)	3 (0–15)	1,247 (777–1,984)
	Female	36.4 (422/1,159)	4 (0–20)	1,461 (933–2,329)
	P	P = 0.537	P = 0.089	P < 0.001
Supervisor gender	Male	37.0 (810/2,187)	4 (0–18)	1,289 (791–2,029)
	Female	37.4 (355/949)	3 (0–14)	1,339 (872–2,274)
	P	P = 0.875	P = 0.224	P = 0.159
Titles of supervisors	Professor	34.8 (500/1,437)	4 (0–17)	1,308 (837–2,099)
	Assoc. Prof.	37.5 (393/1,047)	3 (0–19)	1,316 (832–2,176)
	Asst. Prof.	43.0 (214/498)	2 (0–14)	1,166 (787–1,836)
	Consultant	37.7 (58/154)	2.5 (0.25–18)	1,547 (900–2,822)
	P	P = 0.013*	P = 0.322	P = 0.057
Institution type	University	36.9 (961/2,605)	4 (0–18)	1,294 (838–2,071)
	TRH	38.4 (204/531)	1 (0–9)	1,309 (792–2,218)
	P	P = 0.539	P < 0.001	P = 0.659
Thesis topic	Neuroradiology	34.7 (174/501)	4 (0–15.5)	1,416 (794–2,192)
	Head and neck	37.6 (96/255)	4 (0–18)	1,304 (767–2,146)
	Musculoskeletal	40.3 (114/283)	2.5 (0–15.75)	1,299 (901–2,249)
	Breast	32.6 (94/288)	3.5 (0–15.75)	1,254 (930–2,034)
	Thoracic	33.2 (71/214)	2 (0–10)	1,322 (835–2,069)
	Abdominal	40.4 (168/416)	4 (0–14.25)	1,249 (814–2,004)
	Genitourinary	34.8 (114/328)	5 (0–24.75)	1,220 (732–1,639)
	Interventional	38.9 (151/388)	3 (0–19)	1,461 (974–2,512)
	Cardiovascular	39.9 (63/158)	3 (0–14)	1,236 (790–2,267)
	Physics and radiation safety	51.0 (25/49)	3 (0–11)	974 (780–1,978)
	Obstetric	34.0 (17/50)	2 (0–5)	1,698 (1,034–2,192)
	Emergency	40.0 (26/65)	5 (0.25–20)	1,488 (1,113–1,697)
	Pediatric	37.1 (52/140)	4 (0–21.25)	1,200 (716–1,910)
	P	P = 0.296	P = 0.842	P = 0.280
First author identity	Resident	-	2 (0–11)	1,430 (882–2,300)
	Supervisor	-	17 (3–35)	916 (638–1,393)
	Other researcher	-	12 (3–40)	1,072 (700–1,734)
P			P < 0.001*	P < 0.001*

Note: *Post-hoc pairwise tests were conducted for these variables (see Results section for details). The "Publication rate (%)" column includes all theses, while the "Citations" and "Time to publication" columns reflect data derived exclusively from published theses. Assoc. Prof., Associate professor; Asst. Prof., Assistant professor; TRH, training and research hospital; IQR, interquartile range.

that residency training lasts 5 years, the sevenfold increase in quotas after 2022 is also expected to be reflected in the number of theses in the coming years.

In our study, the most frequently selected fields for radiology residency theses were neuroradiology (16.0%), abdominal radiology (13.3%), and interventional radiology (12.4%). This trend largely aligns with the academic and clinical areas of interest reported in the literature. Among the most highly cited radiology articles, neuroradiology has been identified as the most commonly represented subspecialty.²⁰ A similar distribution has been observed in resident preferences in

the United Kingdom and in Oral Presentations at National Radiology Congresses in Türkiye.^{21,22} According to the residency training curriculum of the Qualification Board of the TSR, these three subspecialties collectively account for 15 months of training duration.²³ The broad patient population, diversity of imaging techniques, and extended allocated training time may explain the high preference rates for these fields.

In contrast, subspecialties such as imaging physics and radiation safety and obstetric radiology were represented in only 1.6% of the theses. The low number of theses in the field of imaging physics and radiation safe-

ty in Türkiye is concerning, especially given the reported deficiencies in radiation safety knowledge among radiology personnel and the fundamental importance of physics for image quality.^{24,25} This limited representation may be attributed to residents' tendency to focus on clinically oriented fields and the relatively low level of academic interest in these topics. Considering the existing knowledge gaps and shortcomings in radiation safety practices in Türkiye, promoting more thesis work in this area is crucial for both optimizing clinical practice and enhancing the quality of training.

The low proportion of theses in obstetric radiology may be attributed to several factors previously described in the literature, including insufficient training duration, limited theoretical content, and a lack of hands-on experience in this field.^{26,27} In addition, obstetric imaging in Türkiye is predominantly performed by obstetricians, which may reduce radiology residents' exposure to this subspecialty and, consequently, their motivation to pursue thesis work in this area. Improving the educational and clinical infrastructure in obstetric radiology could help enhance both care quality and academic engagement in the field.

In our study, 37.1% of radiology residency theses were found to have been published in national or international peer-reviewed journals, and 20.8% of all theses were published in journals indexed in the SCIE. When compared with studies conducted in other medical specialties in Türkiye, these rates are higher than those reported in fields such as anesthesiology,⁷ general surgery,²⁸ public health,²⁹ family medicine,³⁰ physical medicine and rehabilitation,³¹ and emergency medicine,³² however, they are lower than those in thoracic surgery,³³ child and adolescent psychiatry,³⁴ and endocrinology.³⁵ In neurosurgery, reported publication rates have ranged between 26.8% and 37.9%.^{36,37} Such variation, observed both across different specialties and within the same specialty, may be attributed to differences in study periods, indexing criteria, and overall methodological designs. A similar pattern is also observed across medical specialties in terms of SCIE publication rates (Table 4).^{7,28-38} These findings suggest that, in terms of publication output, radiology

theses in Türkiye occupy an upper-intermediate position among medical specialties. However, the majority of radiology theses published in SCIE-indexed journals (456 out of 651) appeared in journals ranked in the lower quartiles, specifically Q3 and Q4, in terms of impact factor. The literature emphasizes that experimental and prospective studies not only tend to have higher publication rates but are also more likely to be published in higher-impact and more prestigious journals.^{28,39} In this context, the fact that 86.7% of theses had a retrospective design highlights the need to encourage prospective and methodologically stronger studies. Nevertheless, well-designed retrospective studies can also make significant contributions, particularly in data-rich fields, such as radiology. To improve publication quality, not only the study design but also methodological rigor is a key determinant.

The publication process in high-impact journals is shaped not only by scientific content but also by structural and economic factors. It has been reported that Turkish researchers place importance on journal prestige, yet high article processing charges pose a significant challenge.⁴⁰ This financial barrier may lead some authors to prefer journals with lower impact factors.

The study demonstrated a statistically significant increase over time in the rate of thesis-to-article conversion, alongside a significant decrease in the time interval between thesis completion and article publication. In the study by Ozgen et al.,⁴¹ which covered the period 1980–2005, the publication rate of radiology theses in SCIE-indexed journals was reported as 6.3%, whereas in our study (covering 1971–2024), this rate increased to

20.8%. This finding indicates a substantial improvement in the publication potential of radiology theses over time.

Similarly, Akpinar and Karcaaltincaba⁴² reported an increase in Turkish radiology publications after the year 2000 in their study covering the period 1945–2008. This trend may be associated with the updated academic promotion criteria established by the Council of Higher Education.^{38,43} In particular, the increased academic credit awarded for publications in internationally indexed journals, such as those in the SCIE, has become a motivating factor for both advisors and residency students to publish their theses. However, the contribution of alternative indexing platforms should also be acknowledged. In our study, TR Index was the second most common indexing source among published theses, accounting for 20.2% of all publications. Additionally, 11.6% of the publications appeared in journals indexed in the ESCI, a component of the WoS that includes newer or regionally focused journals. These results suggest that both national (TR Index) and secondary international platforms (ESCI) can provide useful publication avenues, particularly for researchers in the early stages of their academic careers or working with limited resources.

In our study, the highest publication rate was observed in the field of imaging physics and radiation safety (51.0%), whereas lower rates were noted in breast radiology (32.6%), thoracic radiology (33.2%), and neuroradiology (34.7%). Although neuroradiology was the most frequently selected thesis topic, its publication rate remained relatively limited. In contrast, a study investigating the publication outcomes of presentations from the

Table 4. Publication rates and Science Citation Index Expanded (SCIE)-indexed publication rates of residency theses in various medical specialties in Türkiye

Study	Specialty	Years evaluated	Publication rate (%)	SCIE-indexed publication rate (%)
Ferhatoğlu et al. ²⁸	General surgery	1998–2018	20.5	14.4
Güç et al. ⁷	Anesthesiology	1970–2016	25.7	11.3
Bahadır and Başar ³⁶	Neurosurgery	2015–2019	26.8	-
Bahadır and Lüleci ²⁹	Public health	1973–2022	29.2	<9
Karakullukçu and Ardiç ³⁰	Family medicine	2000–2020	28.1	5.6
Yılmaz et al. ³¹	Physical medicine and rehabilitation	2010–2020	34.3	24.5
Özturan and Sarbay ³²	Emergency medicine	1998–2021	35.5	18
Current study	Radiology	1971–2024	37.1	20.8
Sarıca and Aksu Sayman ³⁷	Neurosurgery	2000–2017	37.9	36.2
Sarbay ³³	Thoracic surgery	2001–2019	38.5	20.7
Sipahi et al. ³⁸	Microbiology & infectious diseases	1997–2007	-	11.4
Usta and Şahin ³⁴	Child and adolescent psychiatry	1997–2017	50.6	40.7
Tura Bahadır and Yılmaz ³⁵	Endocrinology	1980–2023	51.3	38.6

European Congress of Radiology reported higher publication rates for breast radiology (50%) and thoracic radiology (58%) than for radiologic physics (30%).⁴⁴ This discrepancy may stem from differences in study methodology, time periods covered, and research types. Although congress presentations typically originate from more recent and shorter-term projects, theses usually involve longer research timelines, and their conversion into publications may vary depending on individual and institutional factors.

In our study, no statistically significant differences were found between the gender of the residency student and publication rate or citation count. However, the time to publication was significantly longer for female authors than for their male counterparts. Similarly, studies conducted in the fields of psychiatry and ophthalmology have also reported that female researchers face greater challenges in the publication process.^{45,46}

The highest publication rate (43.0%) was observed in theses supervised by assistant professors, whereas the lowest rate (34.8%) was found in those supervised by professors. Additionally, the shortest time to publication was noted in theses conducted under the supervision of assistant professors. This finding contrasts with the common assumption that professors, due to their greater academic experience, tend to produce more publications. Although a study conducted in the field of neurosurgery reported no significant difference in publication rates based on advisor academic title, similar findings to ours have been documented in other specialties, such as anesthesiology, otorhinolaryngology, and plastic surgery, where theses supervised by assistant professors were more frequently published and converted into articles in a shorter time frame.^{7,36,39} This may be related to the increased contribution of faculty members who are in the process of academic advancement and are therefore more engaged in the publication process.

In our study, no statistically significant differences were found between institution type and either publication rate or time to publication. However, publications originating from universities received significantly more citations than those from training and research hospitals.

The literature indicates that this relationship varies by specialty; in some fields, universities (e.g., emergency medicine) demonstrate greater publication success, whereas in others, training and research hospitals (e.g., endocrinology, cardiovascular surgery)

perform better.^{32,33,35} These findings indicate that, although publication rates were similar, the higher citation impact of university-based theses is particularly noteworthy. This highlights the need for strategies that aim not only to increase the number of publications but also to enhance their scientific impact. To achieve this, it is essential for institutions to develop policies that strengthen research infrastructure and improve academic visibility.

In our study, the identity of the first author was found to influence publication success in the thesis-to-article conversion process. Publications in which the first author was someone other than the thesis student—either another researcher or the advisor—were more frequently published in higher-impact journals, received more citations, and were published in a shorter time. This may be attributed to the academic writing experience, knowledge of journal selection, and process management skills of these individuals. In our study, the thesis student was the first author in 76.4% of the published articles, a rate that is comparable with those reported in other medical specialties.^{7,47} This finding suggests that radiology residents are actively involved in the publication process. However, the extended time to publication indicates that students may require greater support from their advisors, particularly in areas such as academic writing, journal selection, and publication management.

This study has several limitations. Since the thesis-to-publication status was investigated solely through online databases, some articles, particularly those published in local or low-visibility journals, may have been missed. Although multiple platforms were used for the screening process (e.g., Google Scholar, PubMed, and WOS), certain major databases, such as Scopus, were not separately queried. Although there is substantial overlap between Scopus and the databases already utilized, publications indexed exclusively in Scopus and not visible in the other sources may have been inadvertently overlooked. The thesis-article linkage was based on name and content similarity, as direct verification was not feasible, which may have led to occasional mismatches. Conference abstracts, proceedings, and book chapters were excluded. Due to the time-dependent nature of citation counts, the data—especially for recently published articles—represent only a snapshot and may underestimate long-term citation impact. Both our findings and previous studies indicate that the process of converting a thesis into a journal ar-

icle typically takes >2 years. Therefore, some of the theses completed in 2023 and 2024 may not yet have been published. This may have led to an underestimation of recent publication rates and should be considered an important limitation of our study. Finally, the study included only theses available in the National Thesis Center of the Council of Higher Education; inaccessible or externally archived theses were not evaluated. Despite these limitations, this study represents the first comprehensive bibliometric analysis to evaluate systematically the publication outcomes of radiology residency theses in Türkiye and offers valuable academic insights into the field.

In conclusion, certain subspecialty areas were more frequently chosen as thesis topics, whereas others remained underrepresented. Approximately one-third of the theses were published in peer-reviewed journals, with a substantial proportion appearing in journals indexed by the SCIE. The increasing publication rates and the decreasing time to publication over the years highlight a growing trend of academic productivity during residency training. To sustain this progress, it is essential to promote effective mentorship practices, provide structured training on the publication process for early-career researchers, and strengthen institutional research infrastructure. Ultimately, a holistic approach should be adopted in which residency theses are regarded not merely as a graduation requirement but as an integral part of academic research.

Footnotes

Conflict of interest disclosure

The authors declared no conflicts of interest.

Supplementary: <https://d2v96fxpocvxx.cloudfront.net/51ec7646-9122-48c7-a1d9-90e9cb16981b/content-images/c556808b-69d4-4990-ad21-0b7d5c15fd1d.pdf>

References

1. Pritchard A. Statistical bibliography or bibliometrics. *Journal of Documentation*. 1969;25(4):348-349. [\[Crossref\]](#)
2. Republic of Türkiye Ministry of Health. Regulation on Specialty Training in Medicine and Dentistry. Official Gazette. September 3, 2022. Accessed May 12, 2025. [\[Crossref\]](#)
3. Brunod I, Rességuier N, Fabre A. Medical thesis publication and academic productivity of pediatric residents at the Medical University of Marseille: associated factors and evolution over 20 years. *Archives de Pédiatrie*. 2020;27(8):408-415. [\[Crossref\]](#)

4. Baysan C, Yapar D, Ali Tokgöz M, Yapar A, Kul Baysan E, Tulinay T. Bibliometric analysis of orthopedic theses in Turkey. *Jt Dis Relat Surg.* 2021;32(3):752-758. [\[Crossref\]](#)

5. Erim BR, Petekkaya S. Retrospective analysis of psychiatry specialization theses made between 1981-2018 in Turkey. *Turk Psikiyatri Derg.* 2020;31(1):1-8. [\[Crossref\]](#)

6. Öğrenci A, Ekşi MŞ, Özcan-Ekşi EE, Koban O. From idea to publication: publication rates of theses in neurosurgery from Turkey. *Neurochir Pol.* 2016;50(1):45-47. [\[Crossref\]](#)

7. Güç Z, Hancı V, Özbilgin S. Thesis studies of universities in anaesthesiology and reanimation between 1970 and 2016: retrospective evaluation of work areas, publishing rates and evidence levels. *Turk J Anaesthesiol Reanim.* 2021;49(5):379-388. [\[Crossref\]](#)

8. Uzun SU, Baysan C, Bekar T. Bibliometric analysis of specialization thesis in medicine, master's and doctoral theses on public health in the last 11 years in Turkey. 2021;26(3):124-129. [\[Crossref\]](#)

9. Council of Higher Education of Turkey. National Thesis Center. 2025. Accessed March 12, 2025.

10. Turkish Society of Radiology. Education and Scientific Research Groups. 2025. Accessed February 10, 2025. [\[Crossref\]](#)

11. TÜBİTAK ULAKBİM. TR Dizin. Accessed May 20, 2025. [\[Crossref\]](#)

12. U.S. National Library of Medicine. PubMed. National Center for Biotechnology Information. Accessed May 20, 2025. [\[Crossref\]](#)

13. Google. Accessed May 20, 2025. [\[Crossref\]](#)

14. Google Scholar. Accessed May 20, 2025. [\[Crossref\]](#)

15. Clarivate. Web of Science. Accessed May 20, 2025. [\[Crossref\]](#)

16. DergiPark. Accessed May 20, 2025. [\[Crossref\]](#)

17. Journal Citation Reports. Clarivate. Accessed May 20, 2025. [\[Crossref\]](#)

18. Koca K, Ekinci S, Akpancar S, Gemci MH, Erşen Ö, Akyıldız F. An analysis of orthopaedic theses in Turkey: evidence levels and publication rates. *Acta Orthop Traumatol Turc.* 2016;50(5):562-566. [\[Crossref\]](#)

19. ÖSYM. Student Selection and Placement Center (ÖSYM) – Official Website. Student Selection and Placement Center of Turkey. Accessed May 25, 2025. [\[Crossref\]](#)

20. McKay Parry N, Rich J, Erian M, Lloyd T. A bibliometric analysis of the highest cited and highest category normalised articles in radiological literature from 2009-2019. Published online November 17, 2020. [\[Crossref\]](#)

21. Parvizi N, Bhuva S. A national UK survey of radiology trainees special interest choices: what and why? *Br J Radiol.* 2017;90(1079):20170338. [\[Crossref\]](#)

22. Seçil M, Uçar G, Sentürk C, Karasu S, Dicle O. Publication rates of scientific presentations in Turkish national radiology congresses. *Diagn Interv Radiol.* 2005;11(2):69-73. [\[Crossref\]](#)

23. Turkish Society of Radiology. Radiology Residency Training Curriculum – Turkish Society of Radiology. 2025. Accessed May 25, 2025. [\[Crossref\]](#)

24. Ozkan S, Aba G, Tekinsoy B. The importance of radiation safety in terms of hospital administration and research on the awareness stage of radiology technicians. *JAREM.* 2016;6(3):162-169. [\[Crossref\]](#)

25. Hendee WR. Teaching physics to radiology residents. *AJR Am J Roentgenol.* 2009;192(4):855-858. [\[Crossref\]](#)

26. Kasales CJ, Coulson CC, Mauger D, Chertoff JD, Matthews A. Training in obstetric sonography for radiology residents and fellows in the United States. *AJR Am J Roentgenol.* 2001;177(4):763-767. [\[Crossref\]](#)

27. Emekli E, Coşkun Ö, Budakoğlu İl, Cerit MN. Obstetric ultrasonography in postgraduate radiology training. *Ultrasound Q.* 2022;38(4):297-303. [\[Crossref\]](#)

28. Ferhatoğlu MF, Kivilcim T, Kartal A, Filiz Al, Kebudi A. An analysis of general surgery theses set up between years 1998-2018 in Turkey: evidence levels and publication rates of 1996 theses. *Turk J Surg.* 2020;36(1):9-14. [\[Crossref\]](#)

29. Bahadır H, Lüleci D. Bibliometric analysis and publication status of public health specialization theses in Turkey. *BAUN Health Sci J.* 2025;14(1):40-47. [\[Crossref\]](#)

30. Karakullukçu A, Ardiç C. Bibliometric analysis of medical speciality dissertation studies in family medicine departments and clinics between 2000-2020. *Ankara Med J.* 2023;23(3):295-311. [\[Crossref\]](#)

31. Yılmaz B, Mutlu Ari P, Büşra Aycıçek H, Yardımcı G. Comprehensive analysis of publication of physical medicine and rehabilitation theses in Türkiye between years 2010 and 2020: academic productivity and related factors. *Turk J Phys Med Rehabil.* 2024;70(2):233-240. [\[Crossref\]](#)

32. Özturan İU, Sarbay İ. Scholarly impact of the dissertation requirement for postgraduate medical education and factors affecting transformation into publication. *Turk J Emerg Med.* 2023;23(4):219-224. [\[Crossref\]](#)

33. Sarbay İ. A bibliometric analysis of 25 years and 1273 dissertations in thoracic and cardiovascular surgery. *Cerrahpaşa Med J.* 2024;48(3):243-247. [\[Crossref\]](#)

34. Usta MB, Şahin İ. Child and adolescent psychiatry thesis in specialty training: analysis of the last 20 years in Turkey. *Turk J Child Adolesc Ment Health.* 2021;28(1):25-30. [\[Crossref\]](#)

35. Tura Bahadir C, Yılmaz M. Factors affecting the publication rate of adult endocrinology theses in Turkey: a comprehensive bibliometric analysis. *Med Bull Haseki.* 2024;62(2):65-74. [\[Crossref\]](#)

36. Bahadır S, Başar İ. A study on neurosurgery specialty theses and their publication status in international journals. *Med J Bakırköy.* 2023;19(1):97-103. [\[Crossref\]](#)

37. Sarıca C, Aksu Sayman O. Analysis of research productivity of neurosurgical residents in turkey and publication rates of theses. *Turk Neurosurg.* 2020;30(5):673-678. [\[Crossref\]](#)

38. Sipahi OR, Caglayan Serin D, Pullukcu H, et al. Publication rates of Turkish medical specialty and doctorate theses on medical microbiology, clinical microbiology and infectious diseases disciplines in international journals. *Mikrobiyol Bul.* 2014;48(2):341-345. [\[Crossref\]](#)

39. Guvey A. Affecting factors on the publication rate of surgical theses from different departments in Turkey. *J Exp Clin Med.* 2021;38(4):533-537. [\[Crossref\]](#)

40. Tazegul G, Etçioğlu E, Emre E, Özlü C. Factors affecting the journal choice for manuscript submission: a qualitative study on Turkish medical researchers. *J Inf Sci.* 2024;50(3):625-634. [\[Crossref\]](#)

41. Ozgen Ü, Egri M, Aktas M, et al. Publication pattern of Turkish medical theses: analysis of 22,625 medical theses completed in years 1980-2005. *Türkiye Klinikleri J Med Sci.* 2011;31(5):1122-1131. [\[Crossref\]](#)

42. Akpinar E, Karcaaltincaba M. Analysis of scientific papers in the field of radiology and medical imaging included in science citation index expanded published by Turkish authors. *Diagn Interv Radiol.* 2010;16(3):175-178. [\[Crossref\]](#)

43. Interuniversity Board of the Council of Higher Education (ÜAK - YÖK). Archive of Regulations (2015–2020: Associate Professorship Application and Academic Promotion Requirements). [\[Crossref\]](#)

44. Loughborough W, Dale H, Youssef AH, Wareham JH, Rodrigues MA, Rodrigues JCL. Scientific papers presented orally at radiology meetings—trends in subspecialty publication rates and adaptations associated with the highest impact factor journal publications. *Quant Imaging Med Surg.* 2016;6(4):462-465. [\[Crossref\]](#)

45. Er A. A retrospective overview of the scientific researches of Turkish female ophthalmologist scholars: is there any gender discrimination? *Eur Eye Res.* 2024;4(1):37-41. [\[Crossref\]](#)

46. Yılmaz Karaman İG, Gündüz T, Yastıbaş C. Is Women's Place Beyond the Glass Ceiling? The gender Gap in academic psychiatry publications in Turkey. *Noro Psikiyatr Ars.* 2022;59(4):290-295. [\[Crossref\]](#)

47. Yüksel M, İpekçi T, Tunçkiran A. Publication rates of dissertations written in medical faculties of Turkey in the field of urology between the years 2008, and 2011, and citation analysis: a cross-sectional study. *Turk J Urol.* 2018;44(4):341-345. [\[Crossref\]](#)

Supplementary Table 1. Most common journals publishing radiology residency theses

Journal name	Number of articles	Percentage (%)	JIF	Index	Country
<i>Diagnostic and Interventional Radiology</i>	81	7.0	1.4	SCIE	Türkiye
<i>European Journal of Radiology</i>	49	4.2	3.2	SCIE	Ireland
<i>Acta Radiologica</i>	25	2.1	1.1	SCIE	England
<i>Journal of Ultrasound in Medicine</i>	23	2.0	2.1	SCIE	USA
<i>Polish Journal of Radiology</i>	23	2.0	0.9	ESCI	Poland
<i>Clinical Imaging</i>	21	1.8	1.8	SCIE	USA
<i>Cukurova Medical Journal</i>	16	1.4	0.3	ESCI	Türkiye
<i>Neuroradiology</i>	15	1.3	2.4	SCIE	Germany
<i>American Journal of Neuroradiology</i>	15	1.3	3.1	SCIE	USA
<i>Turkish Journal of Medical Sciences</i>	14	1.2	1.2	SCIE	Türkiye
<i>Journal of Clinical Ultrasound</i>	13	1.1	1.2	SCIE	USA
<i>European Radiology</i>	13	1.1	4.7	SCIE	Germany
<i>Dicle Medical Journal</i>	13	1.1	-	TR Index	Türkiye
<i>Ultrasound Quarterly</i>	13	1.1	0.9	SCIE	USA
<i>Journal of Computer Assisted Tomography</i>	13	1.1	1.0	SCIE	USA
<i>Abdominal Radiology</i>	12	1.0	2.3	SCIE	USA
<i>American Journal of Roentgenology</i>	12	1.0	4.7	SCIE	USA
<i>Surgical and Radiologic Anatomy</i>	10	0.9	1.2	SCIE	France
<i>Japanese Journal of Radiology</i>	10	0.9	2.9	SCIE	Japan
<i>Journal of Harran University Medical Faculty</i>	10	0.9	-	TR Index	Türkiye
<i>Iranian Journal of Radiology</i>	10	0.9	0.2	SCIE	Iran
<i>Ortadoğu Medical Journal</i>	10	0.9	-	TR Index	Türkiye
<i>JBR-BTR, Journal of the Belgian Society of Radiology*</i>	10	0.9	1.0	SCIE	Belgium
<i>European Review for Medical and Pharmacological Sciences</i>	9	0.8	3.3	SCIE	Italy
<i>Balkan Medical Journal</i>	9	0.8	1.9	SCIE	Türkiye
<i>Medical Bulletin of Sisli Etfal Hospital</i>	9	0.8	1.0	ESCI	Türkiye
Others (<9)	698	59.8	-	-	-
Total	1,165	100	-	-	-

JIF, Journal Impact Factor; SCIE, Science Citation Index Expanded; ESCI, Emerging Sources Citation Index; TR Index, a national database of scholarly journals published in Türkiye, maintained by ULAKBİM (Turkish Academic Network and Information Center), and often referred to as TR Dizin.

*JBR-BTR changed its name to *Journal of the Belgian Society of Radiology* in 2016. Data for both titles were combined as they represent the same journal continuum.

Note: Journal indexes presented in this table reflect their most current status. The Journal Impact Factor values listed here are for descriptive purposes only and correspond to the year 2023. For the primary bibliometric analysis, both indexing status and JIF quartile rankings (Q1–Q4) were based on the journal's classification in the year of article publication, as detailed in the Methods section.



Normal physiological variants and benign conditions in pelvic oncologic fluorodeoxyglucose positron emission tomography/magnetic resonance imaging

Ayşe Erden¹

Diğdem Kuru Öz¹

Nuriye Özlem Küçük²

¹Ankara University Faculty of Medicine, Department of Radiology, Ankara, Türkiye

²Ankara University Faculty of Medicine, Department of Nuclear Medicine, Ankara, Türkiye

ABSTRACT

Fluorodeoxyglucose (FDG) positron emission tomography (PET)/magnetic resonance imaging (MRI) is an advanced hybrid imaging modality that holds substantial promise in oncologic imaging. FDG PET, a well-established molecular imaging technique, enables assessment of tumor glucose metabolism and is widely utilized for diagnosing and monitoring a range of malignancies; MRI offers superior soft tissue contrast, facilitating precise anatomical localization of PET findings. This pictorial essay presents a series of physiological FDG uptake variants observed in the uterus, fallopian tubes, ovaries, colon, internal anal sphincter, pelvic musculature, and bone marrow. Additionally, it highlights benign conditions such as uterine tumors, vaginal condyloma acuminatum, and infected Bartholin cysts that may exhibit FDG uptake and potentially mimic malignancy. The essay also illustrates FDG-avid post-treatment changes and various infectious and inflammatory lesions such as osteitis pubis, perianal fistulas, and pelvic abscesses that may complicate oncologic interpretation.

KEYWORDS

Benign, bone marrow, bowel, fallopian tube, false positive results, inflammation, magnetic resonance imaging, ovary, positron emission tomography, radiation therapy, uterus

Positron emission tomography (PET) combined with magnetic resonance imaging (MRI) using fluorodeoxyglucose (FDG) is a promising hybrid imaging tool for evaluating gynecologic and genitourinary malignancies. It has a potential pivotal role in staging, treatment planning, recurrence detection, and prognosis assessment. However, interpreting pelvic PET/MRI is often challenging due to physiological uptake patterns and benign mimickers that may resemble pathology. In this pictorial essay, we aim to illustrate incidental FDG uptake in various pelvic structures encountered during routine oncologic PET/MRI examinations.

Normal Physiological Variants

Physiological uptake of FDG in the uterus, fallopian tubes, and ovaries is a common finding on FDG PET/computed tomography (CT), particularly in premenopausal women, and may mimic pathological processes if not carefully interpreted.

Physiological endometrial uptake

FDG uptake in the uterus varies with hormonal changes during the menstrual cycle, especially in premenopausal women. Increased endometrial FDG activity is commonly observed during the menstrual (Figure 1) and ovulatory phases and is considered physiological.¹ This uptake likely reflects the peristaltic activity of the subendometrial myometrium, which facilitates menstrual blood expulsion.²

Corresponding author: Ayşe Erden

E-mail: ayse.erden@medicine.ankara.edu.tr

Received 10 April 2025; revision requested 15 May 2025; last revision received 16 July 2025; accepted 27 July 2025.



Epub: 06.10.2025

Publication date: 02.01.2026

DOI: [10.4274/dir.2025.253390](https://doi.org/10.4274/dir.2025.253390)

You may cite this article as: Erden A, Kuru Öz D, Küçük NÖ. Normal physiological variants and benign conditions in pelvic oncologic fluorodeoxyglucose positron emission tomography/magnetic resonance imaging. *Diagn Interv Radiol.* 2026;32(1):81-90.

In postmenopausal women, endometrial FDG uptake is typically low. Any focal or intense uptake in this age group should prompt further investigation.¹

Physiological uptake in fallopian tubes

Studies performed with PET/CT demonstrate that the fallopian tubes may exhibit physiological FDG uptake, particularly in premenopausal women. In a study by Yun et al.,³ bilateral tubal FDG activity was observed in 8.8% of women aged <53 years, most commonly during the mid-menstrual cycle. The uptake appears as tubular, comma-, or tadpole-shaped foci adjacent to the ovaries, corresponding to fallopian tube anatomy.

MRI coregistration and analysis of morphologic features and symmetry can aid differentiation (Figure 2). In the absence of corresponding structural abnormalities or clinical suspicion, further investigations are usually unnecessary. Misinterpretation of tubal uptake as peritoneal implants, enlarged lymph nodes, or adnexal malignancy may lead to unwarranted procedures.

Physiological ovarian uptake

Ovarian FDG uptake fluctuates with the menstrual cycle. A common physiological variant is FDG accumulation in the corpus luteum during the luteal phase. The corpus lu-

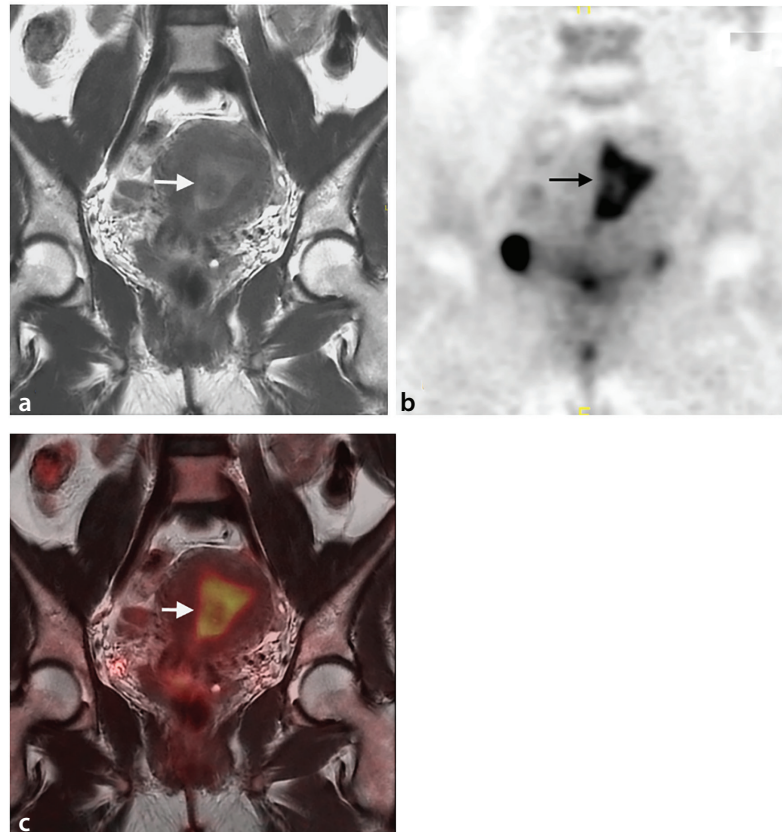


Figure 1. Menstrual endometrial uptake. The coronal T2-weighted image (a) shows the endometrial cavity containing hypointense blood products (arrow). The coronal maximum intensity projection fluorodeoxyglucose (FDG) positron emission tomography (PET) (b) and coronal fused PET/magnetic resonance (c) images demonstrate increased FDG uptake in the endometrium (arrows), consistent with menstruation-related physiological activity in a 41-year-old premenopausal woman.

Main points

- Physiological fluorodeoxyglucose (FDG) uptake is frequently observed, particularly in the uterine cavity, fallopian tubes, corpus luteum, colon, and the distal internal anal sphincter.
- Benign processes and post-treatment changes with FDG uptake can result in false-positive interpretations during positron emission tomography/magnetic resonance imaging for oncologic evaluation.
- Increased FDG uptake can be seen in conditions such as perianal fistulas, vaginal condyloma acuminatum, infected Bartholin cysts, osteitis pubis, and inflammatory bowel disease.
- Diffuse or asymmetrical FDG uptake may be present in pelvic muscles following insulin administration or strenuous physical activity.
- Physiological FDG accumulation in the sigmoid colon and rectum varies among individuals and may be increased in patients on metformin therapy, potentially complicating colorectal cancer assessment.

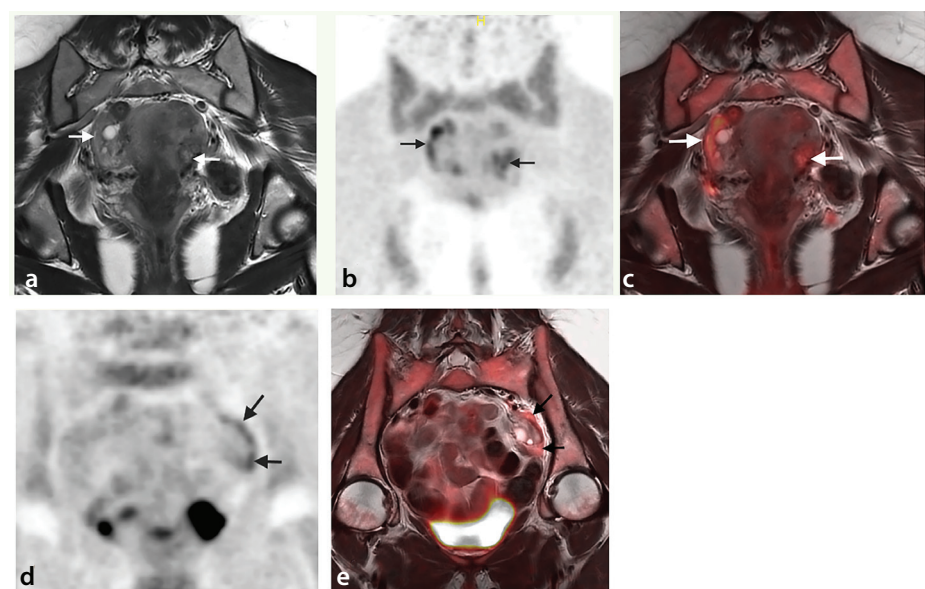


Figure 2. Physiological fluorodeoxyglucose (FDG) uptake in fallopian tubes. The coronal T2-weighted image (a) shows bilateral fallopian tubes (arrows). The coronal positron emission tomography (PET) (b) and coronal fused PET/magnetic resonance images (MRI) (c) show increased comma- or tadpole-shaped FDG uptake in both fallopian tubes (arrows). The arrow on the left indicates to intramural (interstitial) part of the left tube. The coronal PET (d) and coronal fused PET/MRI (e) show increased FDG uptake in the ampullar part of the left fallopian tube (arrows) that forms a curve over and around the ovary.

teum, a transient endocrine structure formed post-ovulation, produces progesterone and may demonstrate moderate FDG avidity.^{1,3-5}

This uptake typically appears as a unilateral, focal, rounded lesion (Figure 3). Although it may mimic malignancy, it is transient and usually resolves in subsequent cycle phases. Correlation with MRI can clarify the nature of the lesion, as corpus luteum cysts appear as unilocular structures (1–3 cm) with thick, crenulated enhancing walls. Presence of blood products may cause signal heterogeneity in the corpus luteum.^{1,3-5}

Physiological bowel activity on fluorodeoxyglucose positron emission tomography/magnetic resonance imaging

FDG accumulation is frequently observed in the colon and rectum, typically in a diffuse, linear pattern (Figure 4).⁶ However, focal or segmental uptake may also be present. Rectal FDG activity can pose diagnostic challenges, and correlation with clinical data and MRI is essential.

Effect of metformin on intestinal fluorodeoxyglucose uptake

Metformin, a widely used oral antidiabetic, is known to increase FDG uptake in the intestines, especially in the sigmoid colon and rectum (Figure 5). Although the mechanism is not fully understood,⁶ this effect may mimic pathological lesions and result in false-positive findings during oncologic evaluation.⁷

If focal colonic uptake is identified, colonoscopy may be required for further evaluation to rule out neoplasia. Despite this effect of metformin on intestinal FDG uptake, the European Association of Nuclear Medicine guideline (v2.0) recommends continuing this drug unless there are other clinical concerns.⁸

Anal uptake from internal anal sphincter activity

The internal anal sphincter (IAS) is a smooth muscle structure that maintains resting anal tone and is responsible for >70% of baseline anal pressure.^{9,10} Physiological FDG uptake in the IAS is a well-recognized finding on pelvic PET/MRI (Figure 6), typically seen at its distal end. This uptake is attributed to the basal tone and metabolic activity of the sphincter muscle, even in the absence of anal disease, such as hemorrhoids or fissures.

Muscular fluorodeoxyglucose uptake

Increased FDG uptake in skeletal muscles can result from voluntary or involuntary con-

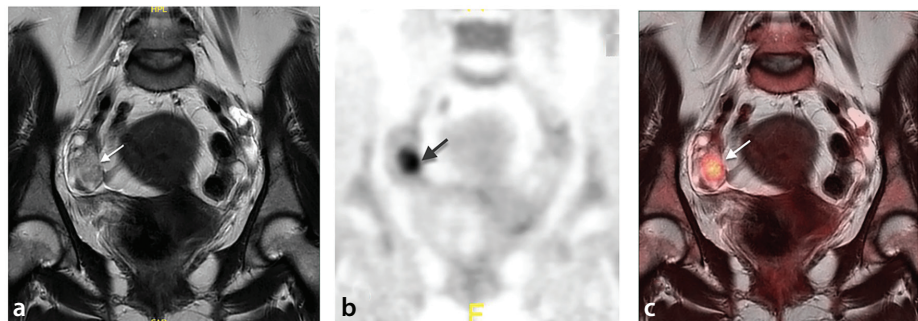


Figure 3. Corpus luteum. The coronal T2-weighted magnetic resonance image (MRI) (a) shows normal corpus luteum in the right ovary (arrow) along with ovarian follicles. The coronal positron emission tomography (PET) (b) and coronal fused PET/MRI (c) display focal fluorodeoxyglucose uptake in the corpus luteum (arrow), reflecting its metabolic activity.

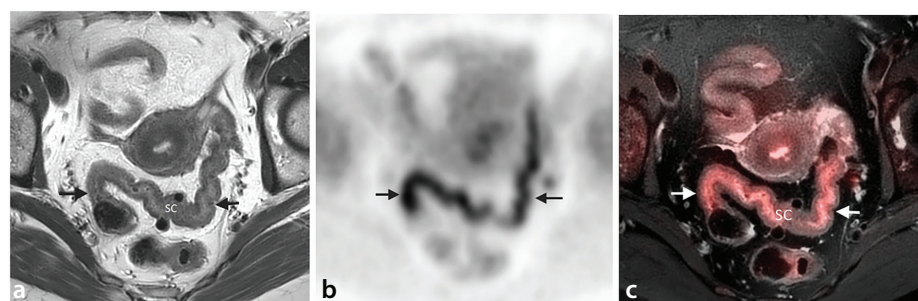


Figure 4. Physiological colonic uptake. The axial T2-weighted image of the pelvis (a) reveals a normal sigmoid colon (SC) (arrows) with incidental diverticula. The axial positron emission tomography (PET) (b) and fused PET/magnetic resonance (c) images show mild physiological fluorodeoxyglucose uptake exhibiting the diffuse and linear pattern in a normal SC (arrows).

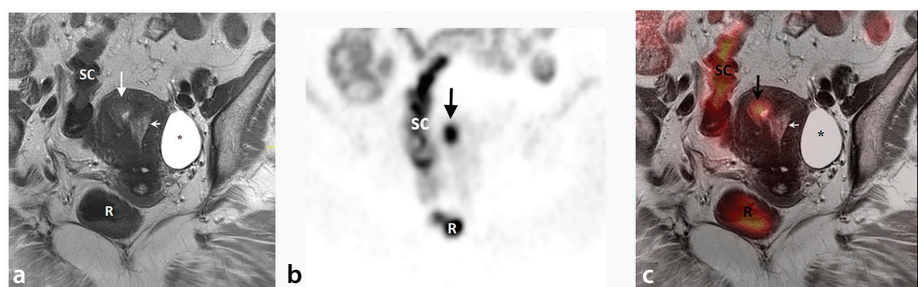


Figure 5. High fluorodeoxyglucose (FDG) bowel uptake in a patient with diabetes treated with metformin. The coronal oblique T2-weighted image of the pelvis (a) shows a normal-appearing sigmoid colon (SC) and rectum (R). Note, the long white arrow points to a *uterine serous carcinoma* arising in an endometrial *polyp* (short arrow). The maximum intensity projection coronal oblique FDG positron emission tomography (PET) (b) and coronal oblique fused PET/magnetic resonance images (MRI) (c) show intense physiological activity accumulation in the rectum and SC due to metformine use. Coregistration with MRI and attention to morphologic features and distribution patterns can aid differentiation from pathologic conditions. Furthermore, note the pathological FDG accumulation in the uterine cavity, compatible with endometrial cancer (black arrow). No FDG uptake is seen in the left portion of the endometrial cavity that corresponds to the polyp (short arrow). An incidental left ovarian serous cystadenoma is marked with an asterisk in (a) and (c). Diagnoses were made by histopathological evaluation of a total abdominal hysterectomy and bilateral salpingo-oophorectomy specimens.

tractions. Normally, pelvic muscle uptake is either absent or very mild and homogeneous. Intense uptake may occur due to the following:¹¹

- Recent insulin administration,
- Strenuous physical activity within 6 hours of imaging,

- Inadequate fasting (minimum 4 hours required before FDG injection).⁸

Uptake typically appears linear and symmetric (Figure 7), but may sometimes be focal or asymmetric (Figure 8), potentially complicating interpretation.

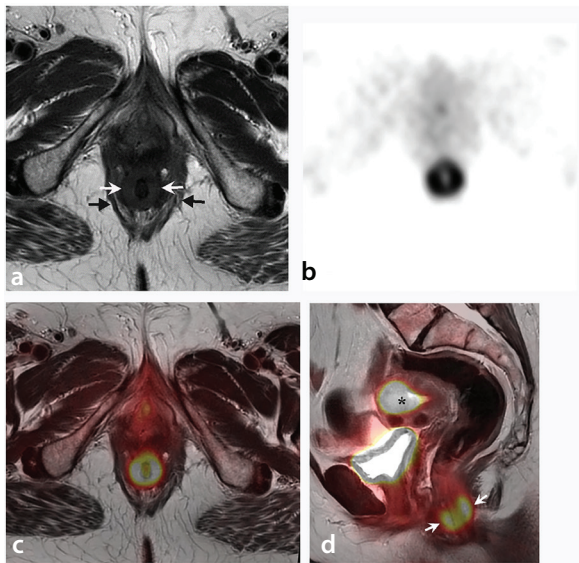


Figure 6. Physiological fluorodeoxyglucose (FDG) uptake in the internal anal sphincter (IAS). The axial T2-weighted image (a) shows the normal IAS with slightly higher signal intensity (white arrows) than the external anal sphincter (black arrows). The axial positron emission tomography (PET) (b) and axial fused PET/magnetic resonance images (MRI) (c) show physiological uptake in the normal IAS. High FDG uptake may indicate high *metabolic* activity in the IAS due to its basal tone, which is fundamental for anal continence. The sagittal fused PET/MRI (d) shows intense physiological FDG accumulation in the distal IAS. An asterisk indicates concurrent endometrial cancer.

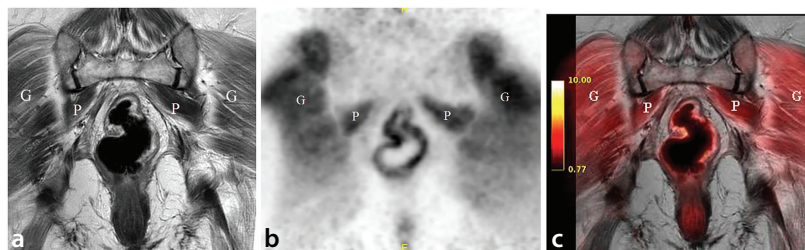


Figure 7. Symmetrical muscular fluorodeoxyglucose (FDG) uptake. Variable FDG uptake within the muscles throughout the body may be observed in individuals who have recently received an insulin injection, engaged in intense physical activity, or consumed a meal. In this patient, who had a history of external radiotherapy and brachytherapy due to endometrial cancer, the muscles in the pelvic region appear normal on the coronal T2-weighted image (a). The maximum intensity projection coronal positron emission tomography (PET) (b) and coronal fused PET/magnetic resonance images (MRI) (c) show diffuse and intense bilateral FDG uptake in the gluteal and piriform muscles, while body PET/CT imaging obtained approximately 30 minutes earlier than the PET/MRI showed no muscular uptake elsewhere in the body.

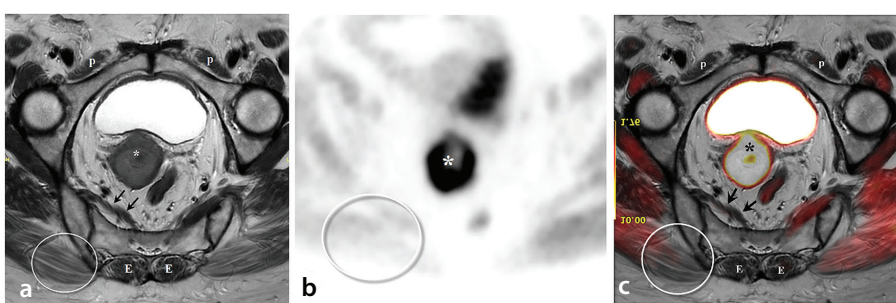


Figure 8. Asymmetrical muscular fluorodeoxyglucose (FDG) uptake. The axial oblique T2-weighted magnetic resonance image (MRI) (a) shows no abnormality in the striated pattern of pelvic muscle architecture except for the right piriform muscle (arrows), which exhibits atrophy and fat replacement in a patient with endometrial cancer invading the cervical stroma (asterisk). The axial positron emission tomography (PET) (b) and axial oblique fused PET/MRI (c) show uneven and asymmetrical FDG uptake in the pelvic muscles. Uptake is not observed in the right piriformis muscle (arrows), the medial portion of the right gluteus maximus muscle (circle), the pectenous muscles (p), or the erector spinae (E) muscles. Since the patient was using insulin, the FDG accumulation in the pelvic muscles could be attributed to a recent insulin injection.

Bone marrow fluorodeoxyglucose uptake

Although there is no physiological FDG uptake in the cortical bone, uptake may be observed in the bone marrow, which may vary depending on patient factors and hematopoietic activity (Figure 9). Conditions such as anemia, infection, inflammation, or use of hematopoietic stimulants [e.g., granulocyte colony-stimulating factor (G-CSF), erythropoietin] may lead to diffuse bone marrow hypermetabolism.^{8,12,13}

Following administration of pegylated G-CSF, a minimum interval of 3 weeks is recommended before performing PET imaging to avoid false-positive marrow uptake.¹²

Benign Gynecologic Lesions

Endometritis refers to inflammation or infection of the endometrial lining. On MRI, it may present as endometrial thickening with heterogeneous signal intensity, which is non-specific. The differential diagnosis includes endometrial carcinoma, intrauterine hematoma, and endometrial polyps.¹⁴

FDG PET/MRI typically shows faint FDG uptake in endometritis (Figure 10), helping to distinguish it from endometrial cancer. Minimal metabolic activity supports a benign etiology.

Adenomyosis is a benign condition characterized by ectopic endometrial glands within the myometrium. In premenopausal women, adenomyosis often demonstrates mild FDG uptake (Figure 11), which may increase during menstruation or ovulation.^{2,15}

In patients with gynecologic malignancies, FDG-avid adenomyosis may mimic or obscure intrauterine metastases.¹⁶ The MRI component of PET/MR is highly valuable, typically revealing a globally enlarged uterus with a thickened junctional zone containing tiny hyperintense foci on T2-weighted imaging (Figure 11).

Endometrial hyperplasia is defined by an increased gland-to-stroma ratio due to abnormal glandular proliferation. On T2-weighted MRI, it appears as a diffusely thickened endometrium, with low or intermediate signal intensity, though imaging features are non-specific.¹⁴

FDG uptake in endometrial hyperplasia is typically mild [mean standardized uptake value (SUV) ~2], significantly lower than in endometrial carcinoma (mean SUV ~9.3).¹⁷ It often occurs in peri- or postmenopausal women (Figure 12).

Endometrial polyps are benign overgrowths of endometrial glands and stroma that protrude into the uterine cavity. Although usually indolent, they may carry a risk of malignant transformation.^{14,18}

On FDG PET, polyps generally exhibit faint or no uptake. However, hypermetabolic activity has been reported, similar to carcinomas.¹⁹ In this study, cases of histopathologically confirmed polyps did not show significant FDG avidity (Figure 5). In contrast, in a case of serous carcinoma arising within a polyp, the fusion PET/MR image clearly demonstrated marked FDG uptake in the cancerous portion while the polyp itself remained photopenic (Figure 5).

Leiomyomas (fibroids) are the most common benign gynecologic tumors. FDG uptake is uncommon, reported in approximately 10.4% of premenopausal and 1.2% of postmenopausal women.²⁰ Uptake, when present, is typically mild (Figure 13), although rare cases with high FDG avidity exist, particularly during the proliferative phase of the menstrual cycle.^{15,21}

Uptake variability may be influenced by cellularity, vascularity, hormonal status, or degenerative changes.²¹ MRI remains essential for characterization and differentiation from malignancy (Figure 14). Importantly, new FDG avidity in a known leiomyoma does not necessarily indicate malignant transformation.²⁰

Smooth muscle tumors of uncertain malignant potential lesions exhibit histologic features that overlap with leiomyosarcoma, but with much less aggressive behavior. These rare tumors can demonstrate intense FDG uptake²² and may coexist with benign leiomyomas (Figure 14).

Vaginal condyloma acuminata (genital warts) is a common sexually transmitted infection caused by low-risk types of human papillomavirus. In patients undergoing PET/MRI for gynecologic malignancies, vaginal FDG uptake due to condylomas may raise suspicion for metastasis (Figure 15).²³ Awareness of this entity is crucial to avoid false-positive interpretations.

Bartholin gland cysts result from ductal obstruction and are typically seen in women of reproductive age. Uninfected cysts do not show FDG uptake.²⁴ However, when infected or forming an abscess, they may become FDG-avid (Figure 16), often appearing as a small focus in the distal vagina.

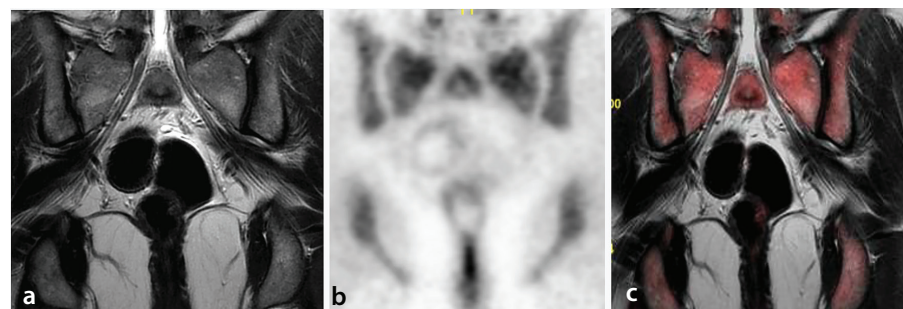


Figure 9. Bone marrow fluorodeoxyglucose (FDG) uptake. Pelvic bone marrow signal intensity is seen to be normal on a coronal T2-weighted magnetic resonance image (MRI) (a). The maximum intensity projection coronal positron emission tomography (PET) (b) and coronal fused PET/MRI (c) show mild diffuse uptake in the pelvic bone marrow. Mild FDG accumulation in bone marrow tends to occur as a result of benign conditions. This patient with endometrial cancer also had severe anemia and a chronic urinary tract infection.

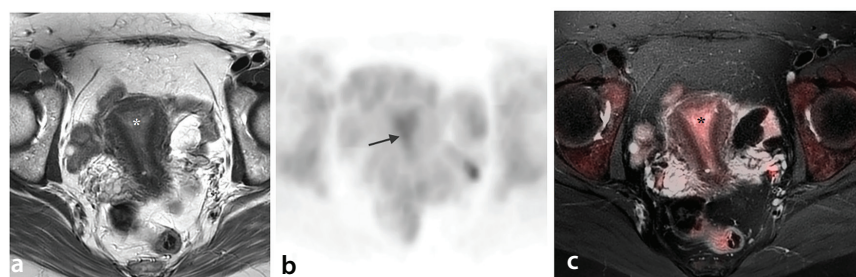


Figure 10. Endometritis. The axial oblique T2-weighted magnetic resonance images (MRI) (a) shows a thickened endometrium with heterogeneous signal intensity (asterisk) in a patient with histopathologically proven endometritis. The maximum intensity projection axial oblique positron emission tomography (PET) (b) and axial oblique fused PET/MRI (c) show faint fluorodeoxyglucose uptake in the endometrium, consistent with a benign process (arrow in b; asterisk in c).

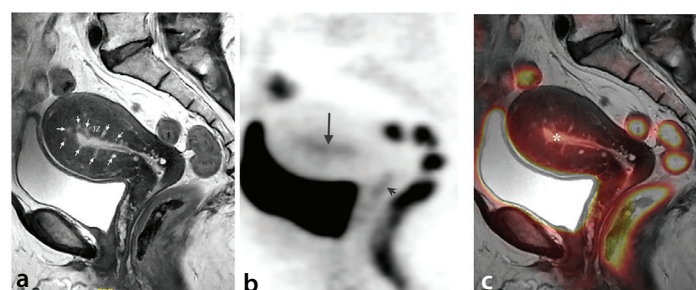


Figure 11. Adenomyosis. The sagittal T2-weighted magnetic resonance image (MRI) (a) shows hyperintense tiny foci (arrows) in the enlarged junctional zone (JZ), consistent with diffuse adenomyosis. The maximum intensity projection sagittal positron emission tomography (PET) (b) and sagittal fused PET/MRI (c) show mild FDG uptake in the endometrium in some places and in the JZs (inner myometrium) (long arrow in b; asterisk in c). Note also the mild FDG accumulation in the cervical canal (small arrow in b). A histopathological evaluation revealed active severe cervicitis characterized by erosion. FDG, fluorodeoxyglucose.

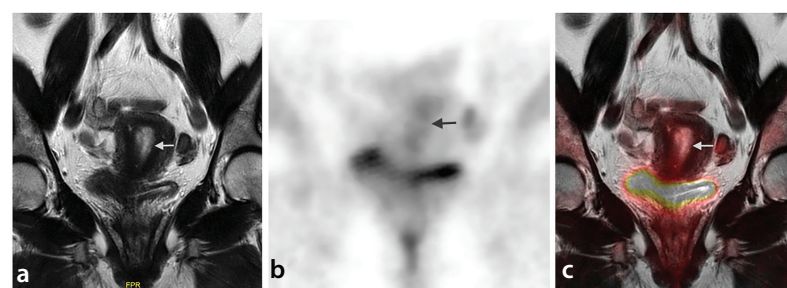


Figure 12. Endometrial hyperplasia in a postmenopausal woman. The coronal T2-weighted MRI (a) shows thickened endometrium (arrow). The coronal positron emission tomography (PET) (b) and coronal fused PET/MRI (c) reveal faint FDG uptake, consistent with histologically confirmed atypical hyperplasia. MRI, magnetic resonance imaging; FDG, fluorodeoxyglucose.

Posttreatment Changes in Pelvic Tissues

FDG uptake in the presacral region following rectal cancer surgery may raise concern for local recurrence. However, benign postoperative complications, such as anastomotic leakage, can result in inflammatory changes, abscesses, or sinuses, which may also exhibit FDG avidity.

Studies have reported a positive predictive value of only 58% for FDG-avid presacral lesions in identifying true local recurrence.²⁵ The high soft-tissue contrast of the MRI component of PET/MRI helps differentiate between recurrent tumor and postoperative fibrosis. In such cases, diffusion-weighted imaging (DWI) is reported to be helpful for further characterization.²⁶ However, it can sometimes be difficult to comment on the nature of lesions that are of intermediate intensity on T2-weighted images and FDG-avid on PET (Figure 17).

Radiation-induced proctitis, inflammation of the rectal mucosa, is a complication of pelvic radiotherapy, particularly in patients with cervical, rectal, and prostate cancer. Early imaging findings on MRI include submucosal edema and high signal intensity of the rectal wall on T2-weighted images, along with prominent mucosal enhancement. Progressive damage leads to wall thickening and elevated signal in the muscularis layer.^{27,28}

Mild FDG uptake can be observed in the irradiated rectum on PET/MRI (Figure 18). Although this generally does not interfere with post-treatment response assessment in patients with rectal cancer,²⁷ it may complicate interpretation in cases with only partial metabolic response, as simultaneous inflammatory activity cannot be fully excluded.²⁸

Fat necrosis is a benign process that typically occurs after surgery, trauma, or infection. In this entity, a fibrous connective tissue capsule covers necrotic and degenerated fatty tissue. On imaging, it can mimic tumor recurrence by appearing as a mass-like lesion.²⁹ Features in MRI often include a well-circumscribed lesion with a hyperintense fatty center and a hypointense fibrous capsule—the so-called “doughnut sign.”

Increased FDG uptake may be observed along the periphery of fat necrosis lesions (Figure 19), and this uptake can persist for up to 12 months postoperatively. Importantly, serial imaging typically shows no change in lesion size or metabolic activity, supporting a benign etiology.²⁹

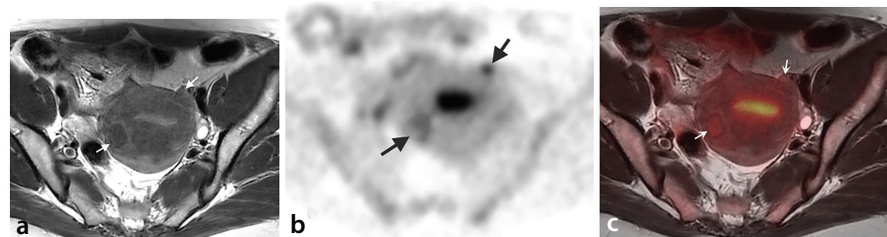


Figure 13. Uterine leiomyomas. The axial T2-weighted magnetic resonance image (MRI) (a) shows two leiomyomas with typical low signal intensity (arrows). The axial positron emission tomography (PET) (b) and axial fused PET/MRI (c) show mild FDG uptake in the leiomyomas, better distinguishable in the PET image [black arrows in (b)]. FDG uptake in leiomyomas may vary during the menstrual cycle and may be higher in the proliferative phase. The high activity in the uterine cavity in this patient is physiological and is related to menstruation. FDG, fluorodeoxyglucose.

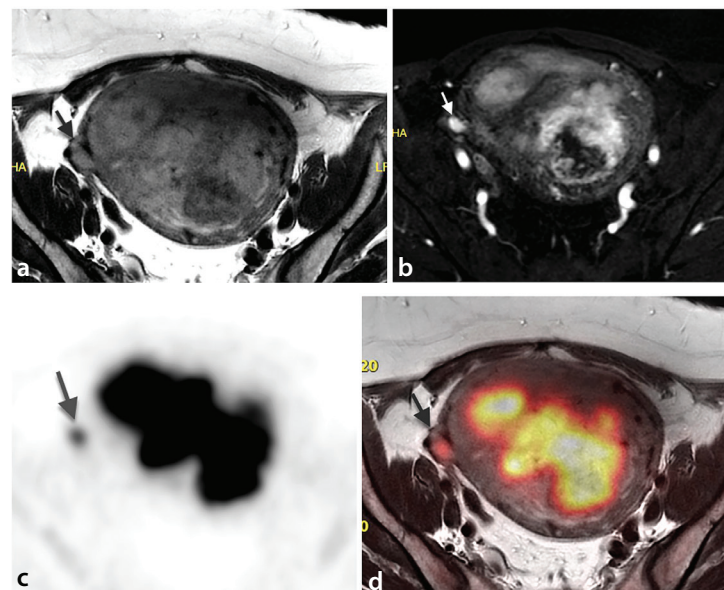


Figure 14. Fluorodeoxyglucose (FDG)-avid leiomyoma in a patient with large smooth muscle tumors of uncertain malignant potential (STUMP). The axial T2-weighted MRI (a) shows a high-signal subserosal leiomyoma (arrow). The axial early postcontrast T1-weighted fat-saturated MRI (b) shows intense enhancement in leiomyoma (arrow). The axial positron emission tomography (PET) (c) and axial fused PET/MRI (d) demonstrate high FDG activity in leiomyoma. Leiomyomas showing high signal intensity on T2-weighted MRI tend to show higher FDG uptake than that of the hypointense leiomyomas. A histopathological diagnosis of the total abdominal hysterectomy and bilateral salpingo-oophorectomy specimen in this patient revealed STUMP and multiple leiomyoma nodules without dysplasia or malignancy. MRI, magnetic resonance imaging.

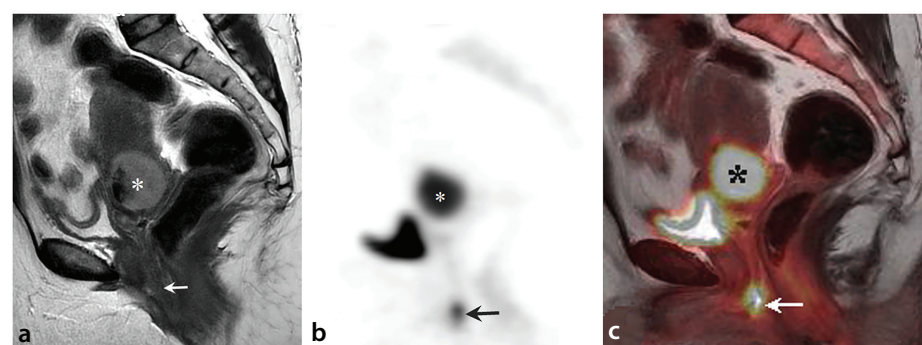


Figure 15. Vaginal condyloma acuminatum. The sagittal T2-weighted magnetic resonance image (MRI) (a) shows no visible vaginal abnormality (arrow) in a patient with endometrial cancer invading cervical stroma (asterisk). The sagittal positron emission tomography (PET) (b) and sagittal fused PET/MRI (c) show FDG uptake in the vagina (arrow), mimicking metastasis. However, the hospital records indicate the presence of vaginal condyloma acuminatum, which are known to exhibit FDG uptake. FDG, fluorodeoxyglucose.

Radiation-induced changes in the sacral bone marrow are a common consequence of pelvic radiotherapy. These include radiation osteitis, insufficiency fractures, and, less commonly, osteoradionecrosis. These changes may present with sacral FDG uptake on PET imaging (Figure 20).

Differentiating between benign post-radiation effects and metastatic bone lesions is essential for accurate interpretation. The MRI component of the PET/MRI study can be useful in localizing and characterizing foci of increased FDG accumulation within the bone. MRI can reveal these changes bilaterally or unilaterally, with findings more prominent adjacent to the sacroiliac joints.³⁰

Various Infectious and Inflammatory Lesions

General mechanism of fluorodeoxyglucose uptake in inflammation and infection

FDG uptake in infection and inflammation is mediated by activated inflammatory cells, particularly neutrophils and cells of the monocyte/macrophage lineage. These cells demonstrate upregulated glucose transporter (GLUT) expression (mainly GLUT 1 and GLUT3) and enhanced hexokinase activity, leading to increased glucose metabolism. Both acute and chronic inflammation can produce intense FDG uptake.³¹

Inflammatory bowel disease includes Crohn's disease and ulcerative colitis, each with distinct imaging patterns. PET/MRI offers a non-invasive method for assessing disease extent and activity. Increased FDG uptake may appear as focal or linear enhancement along affected bowel segments (Figure 21).³² Additionally, PET imaging may be helpful in therapy monitoring and in distinguishing between fibrotic and active inflammatory strictures.^{31,32}

Perianal fistula is an infected tract that develops between the anal canal and the perianal skin, often resulting from prior or ongoing abscess formation. FDG uptake in perianal fistulas may be encountered incidentally in PET/MRIs obtained for oncological purposes (Figure 22).

Osteitis pubis is a non-infectious inflammatory condition affecting the pubic symphysis and surrounding structures. It has been associated with pelvic surgery, childbirth, trauma, urological interventions, and repetitive mechanical stress.

MRI may demonstrate parasympyseal bone marrow edema, diffusion restriction

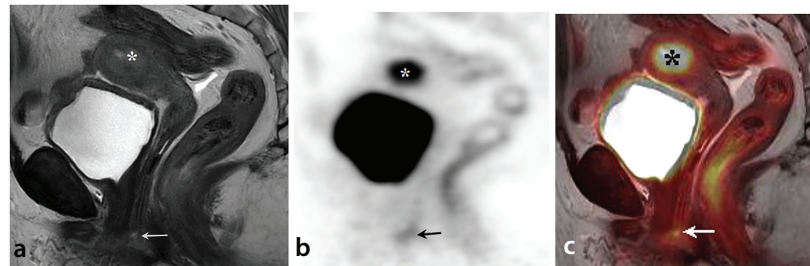


Figure 16. Infected Bartholin gland cyst. The sagittal T2-weighted magnetic resonance image (MRI) (a) shows a hyperintense small rounded lesion (arrow) compatible with a Bartholin cyst lying at the distal end of the vagina in a patient with endometrial cancer (asterisk). Its location below the level of the pubic symphysis is typical. The sagittal positron emission tomography (PET) (b) and sagittal fused PET/MRI (c) show a tiny focus with fluorodeoxyglucose (FDG) uptake (arrows) in the distal vagina, suggesting that it is infected. Asterisks in (b) and (c) indicate intense FDG accumulation in endometrial cancer.

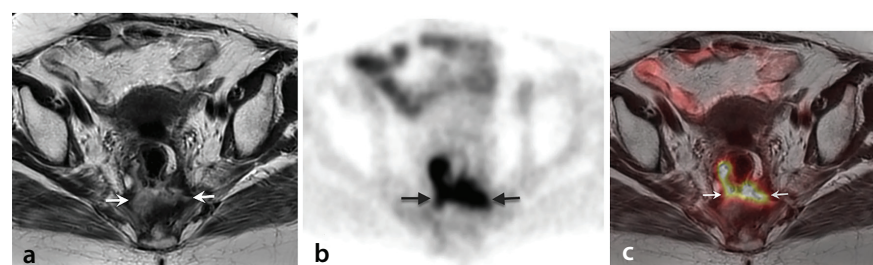


Figure 17. Fluorodeoxyglucose (FDG) uptake in presacral soft tissue after rectal cancer surgery. The axial T2-weighted magnetic resonance image (MRI) (a) reveals a lesion of intermediate signal intensity with presacral extension (arrows). The lesion showed diffusion restriction on diffusion-weighted images (not shown). The axial positron emission tomography (PET) (b) and axial fused PET/MRI (c) exhibit high FDG activity (arrows) in the lesion. Pathological FDG accumulation in PET (b) was evaluated in favor of recurrence. A computed tomography-guided fine needle aspiration biopsy confirmed highly hypocellular fibrocollagenous mesenchymal tissue without malignancy.

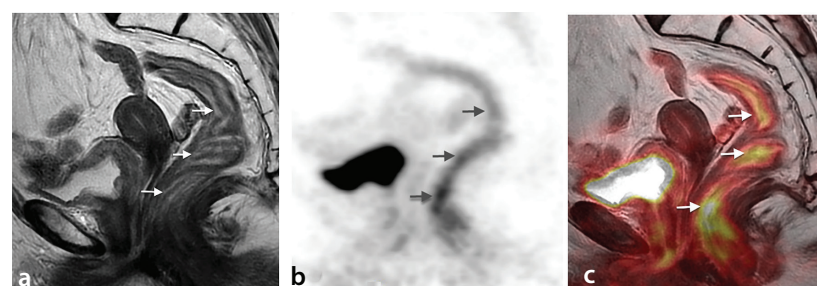


Figure 18. Radiation-induced proctitis in a patient with cervical cancer. The sagittal T2-weighted magnetic resonance image (MRI) (a) shows rectal wall thickening and submucosal edema (arrows) in a patient who underwent radiation therapy. The sagittal positron emission tomography (PET) (b) and sagittal fused PET/MRI (c) demonstrate increased uptake consistent with post-radiation inflammation.

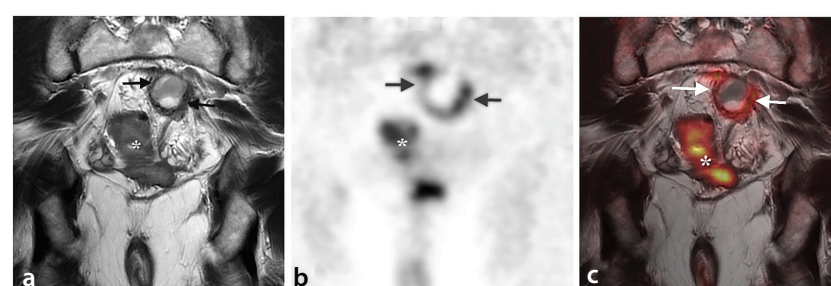


Figure 19. Post-surgical fat necrosis in a patient with operated rectal cancer arising from ulcerative colitis. The coronal T2-weighted magnetic resonance image (MRI) (a) shows a presacral lesion with central hyperintensity and a hypointense fibrous capsule (arrows) (the "doughnut sign"). The coronal positron emission tomography (PET) (b) and coronal fused PET/MRI (c) reveal peripheral fluorodeoxyglucose (FDG) uptake. There was no progression on follow-up. Note also that the asterisks in images (a-c) mark FDG-avid bowel segments with ulcerative colitis.

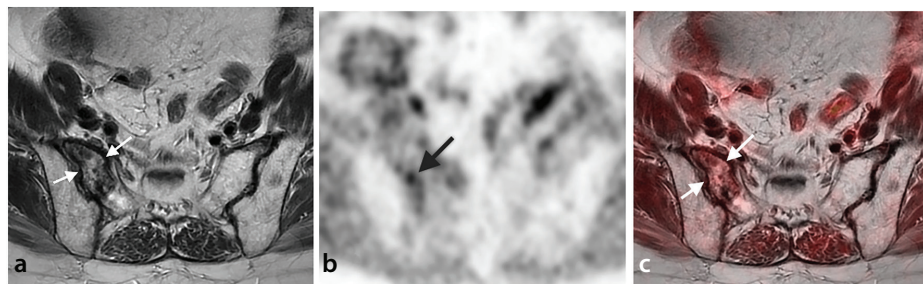


Figure 20. Sacral osteonecrosis following radiation therapy in a patient with cervical cancer. The axial T2-weighted magnetic resonance image (MRI) (a) shows a heterogeneous lesion of intermediate signal intensity in the sacral side of the right sacroiliac joint (arrows). The lesion is newly developed after radiation therapy. The axial positron emission tomography (PET) (b) and axial fused PET/MRI (c) show moderate fluorodeoxyglucose activity (arrows) in the osseous lesion.

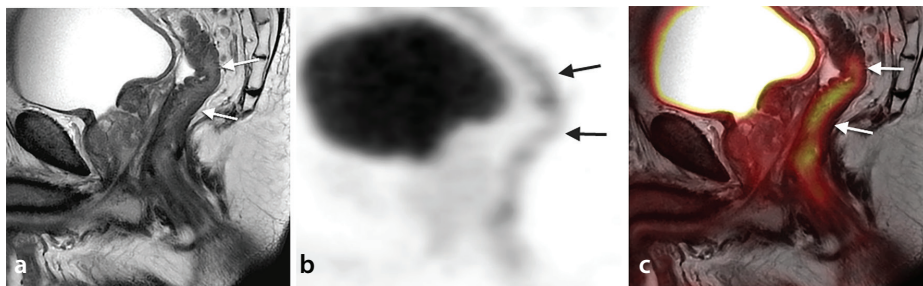


Figure 21. Ulcerative colitis. In the patient who underwent rectal excision, the sagittal T2-weighted magnetic resonance image (MRI) (a) shows subtle wall thickening and loss of haustration of the colon segment (arrows) that is pulled into the pelvis for coloanal anastomosis. The sagittal positron emission tomography (PET) (b) and sagittal fused PET/MRI (c) demonstrate diffuse, linear fluorodeoxyglucose uptake in the affected bowel segment (arrows).

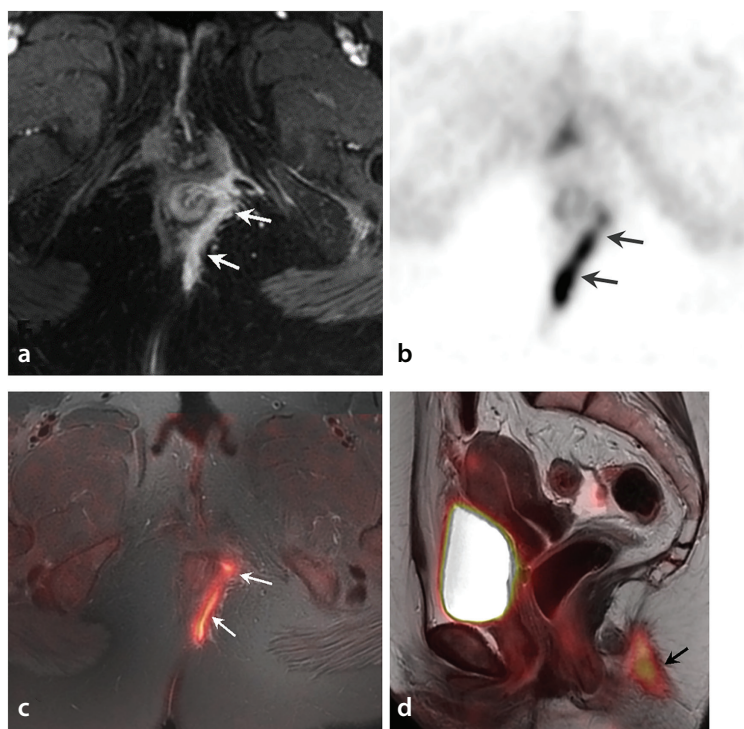


Figure 22. Transsphincteric perianal fistula. The axial contrast-enhanced fat-suppressed T1-weighted image (a) shows a fistula tract (arrows), which begins at the 1 o'clock position and curves posteriorly, penetrating the external anal sphincter. The axial positron emission tomography (PET) (b) and axial fused PET/magnetic resonance images (MRI) (c) reveal intense fluorodeoxyglucose accumulation along the tract (arrows). The sagittal fused PET/MRI (d) shows pathological uptake posterior to the external anal sphincter (arrow).

(Figure 23), and surrounding soft-tissue inflammation. On PET/MRI, moderate to intense unilateral or bilateral FDG uptake near the symphysis pubis is observed (Figure 23).³³

Pelvic abscess formation may result from surgical complications or underlying inflammatory conditions, such as pelvic inflammatory disease, diverticulitis, or inflammatory bowel disease. Imaging reveals complex cystic masses with heterogeneous contents, thick enhancing walls, and perilesional fat stranding. Typically, FDG PET shows intense peripheral uptake with a centrally photopenic (non-avid) core, which is characteristic of abscesses (Figure 24).²⁴

In conclusion, PET/MRI is a powerful imaging modality that integrates the functional capabilities of FDG PET with the superior anatomical detail and tissue characterization provided by MRI. A comprehensive understanding of physiological FDG uptake patterns—in the uterus, fallopian tubes, ovaries, bowel, muscles, and bone marrow—is essential to avoid misinterpretation. Moreover, recognizing benign conditions and posttreatment changes that may mimic malignancy helps reduce false-positive findings and unnecessary interventions.

The MRI component of PET/MRI adds significant value by offering high-resolution anatomical information, functional insights (by DWI), lesion characterization, and reduced radiation exposure compared with PET/CT. These advantages make PET/MRI a highly valuable tool in oncologic imaging, particularly in complex cases involving the pelvis.

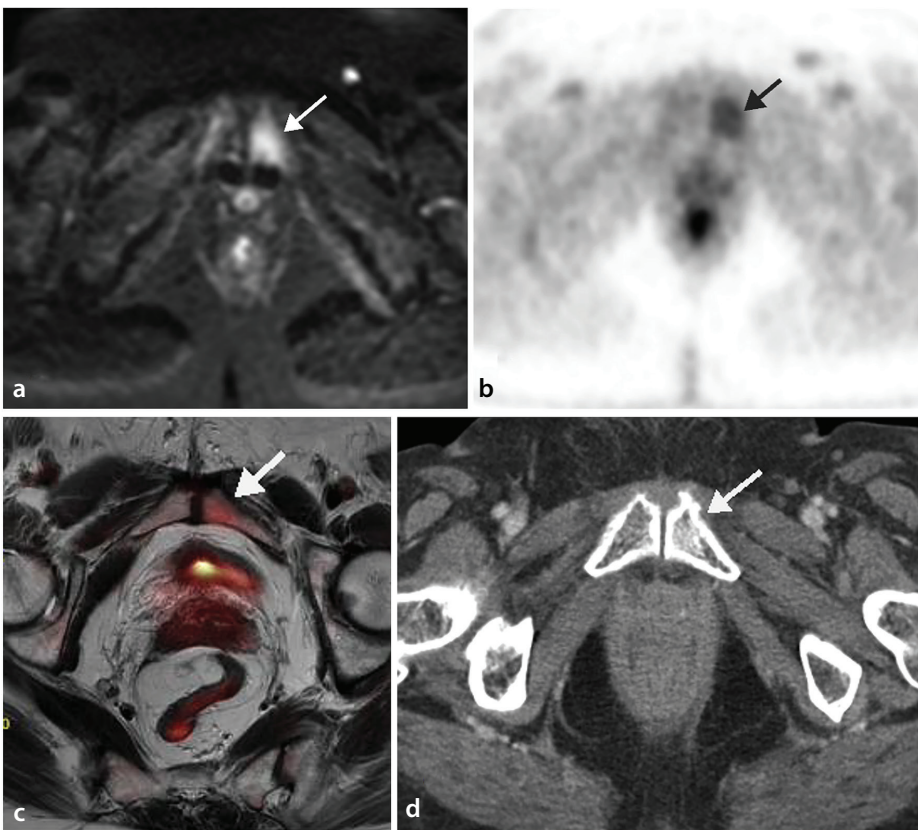


Figure 23. Osteitis pubis. The axial diffusion-weighted magnetic resonance image (MRI) (a) shows diffusion restriction (arrow) at the left side of the pubic symphysis. The axial positron emission tomography (PET) (b) and axial fused PET/MRI (c) show moderate unilateral fluorodeoxyglucose uptake (arrows) adjacent to the pubic symphysis. On the computed tomography (d) image, mild subchondral sclerosis associated with cortical irregularity (arrow) supports the diagnosis.

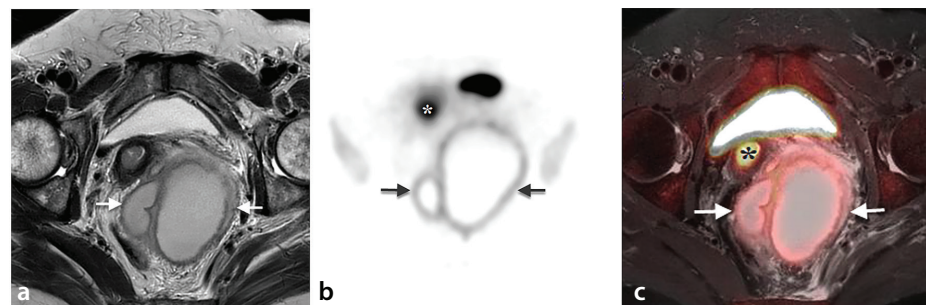


Figure 24. Pelvic abscess. The axial T2-weighted magnetic resonance image (MRI) (a) shows a walled-off biloculated fluid-filled collection (arrows) displaying moderately high signal intensity content in keeping with pus. The axial positron emission tomography (PET) (b) and axial fused PET/MRI (c) show intense peripheral fluorodeoxyglucose (FDG) uptake (arrows) and central photopenia, consistent with abscess. Surgical pathology revealed fibrous tissue with mixed inflammation and abscess formation. The uterine lesion seen as an FDG-avid focus [asterisks in (b) and (c)] on the right anterior aspect of the abscess was diagnosed as serous endometrial cancer invading the cervix uteri.

Footnotes

Conflict of interest disclosure

The authors declared no conflicts of interest.

References

1. Lerman H, Metser U, Grisaru D, Fishman A, Lievshitz G, Even-Sapir E. Normal and abnormal 18F-FDG endometrial and ovarian uptake in pre- and postmenopausal patients: assessment by PET/CT. *J Nucl Med*. 2004;45(2):266-271. [\[CrossRef\]](#)
2. Yu JL, Huh SJ, Kim YI, Kim TJ, Park BK. Variable uterine uptake of FDG in adenomyosis during concurrent chemoradiation therapy for cervical cancer. *Radiat Oncol J*. 2011;29(3):214-217. [\[CrossRef\]](#)
3. Yun M, Cho A, Lee JH, Choi YJ, Lee JD, Kim CK. Physiologic 18F-FDG uptake in the fallopian tubes at mid cycle on PET/CT. *J Nucl Med*. 2010;51(5):682-685. [\[CrossRef\]](#)
4. Bonde AA, Korngold EK, Foster BR, et al. Radiological appearances of corpus luteum cysts and their imaging mimics. *Abdom Radiol (NY)*. 2016;41(11):2270-2282. [\[CrossRef\]](#)
5. Ames J, Blodgett T, Meltzer C. 18F-FDG uptake in an ovary containing a hemorrhagic corpus luteal cyst: false-positive PET/CT in a patient with cervical carcinoma. *AJR Am J Roentgenol*. 2005;185(4):1057-1059. [\[CrossRef\]](#)
6. Lakhani A, Khan SR, Bharwani N, et al. FDG PET/CT Pitfalls in gynecologic and genitourinary oncologic imaging. *Radiographics*. 2017;37(2):577-594. [\[CrossRef\]](#)
7. Gontier E, Fourme E, Wartski M, et al. High and typical 18F-FDG bowel uptake in patients treated with metformin. *Eur J Nucl Med Mol Imaging*. 2008;35(1):95-99. [\[CrossRef\]](#)
8. Boellaard R, Delgado-Bolton R, Oyen WJ, et al. FDG PET/CT: EANM procedure guidelines for tumour imaging: version 2.0. *Eur J Nucl Med Mol Imaging*. 2015;42(2):328-354. [\[CrossRef\]](#)
9. Keef KD, Cobine CA. Control of motility in the internal anal sphincter. *J Neurogastroenterol Motil*. 2019;25(2):189-204. [\[CrossRef\]](#)
10. Kumar L, Emmanuel A. Internal anal sphincter: clinical perspective. *Surgeon*. 2017;15(4):211-226. [\[CrossRef\]](#)
11. Parida GK, Roy SG, Kumar R. FDG-PET/CT in skeletal muscle: pitfalls and pathologies. *Semin Nucl Med*. 2017;47(4):362-372. [\[CrossRef\]](#)
12. Minamimoto R, Baratto L, Iagaru A. Association between time since administration of pegylated G-CSF (Pegfilgrastim) and bone marrow uptake on FDG PET/CT: determination of a minimum interval. *AJR Am J Roentgenol*. 2022;218(2):351-358. [\[CrossRef\]](#)
13. Blodgett TM, Ames JT, Torko FS, McCook BM, Meltzer CC. Diffuse bone marrow uptake on whole-body F-18 fluorodeoxyglucose positron emission tomography in a patient taking recombinant erythropoietin. *Clin Nucl Med*. 2004;29(3):161-163. [\[CrossRef\]](#)
14. Pintcan R, Bura V, Zerunian M, et al. MRI of the endometrium - from normal appearances to rare pathology. *Br J Radiol*. 2021;94(1125):20201347. [\[CrossRef\]](#)
15. Kitajima K, Murakami K, Kaji Y, Sugimura K. Spectrum of FDG PET/CT findings of uterine tumors. *AJR Am J Roentgenol*. 2010;195(3):737-743. [\[CrossRef\]](#)
16. Sebastian J, Rodriguez C, Samuels ZV, Pepin K, Zeglis BM. Molecular Imaging in Gynecology: Beyond Cancer. *J Nucl Med*. 2024;65(7):998-1003. [\[CrossRef\]](#)
17. Tsujikawa T, Okazawa H, Yoshida Y, et al. Distinctive FDG and FES accumulation pattern of two tamoxifen-treated patients

with endometrial hyperplasia. *Ann Nucl Med*. 2008;22(1):73-77. [\[CrossRef\]](#)

18. Kawaguchi M, Kato H, Suzui N, et al. MR imaging findings differentiating uterine submucosal polypoid adenomyomas from endometrial polyps. *Br J Radiol*. 2019;92(1095):20180430. [\[CrossRef\]](#)
19. Salem AE, Fine GC, Covington MF, et al. PET-CT in Clinical Adult Oncology-IV. Gynecologic and Genitourinary Malignancies. *Cancers (Basel)*. 2022;14(12):3000. [\[CrossRef\]](#)
20. Nishizawa S, Inubushi M, Kido A, et al. Incidence and characteristics of uterine leiomyomas with FDG uptake. *Ann Nucl Med*. 2008;22(9):803-810. [\[CrossRef\]](#)
21. Kitajima K, Murakami K, Yamasaki E, Kaji Y, Sugimura K. Standardized uptake values of uterine leiomyoma with 18F-FDG PET/CT: variation with age, size, degeneration, and contrast enhancement on MRI. *Ann Nucl Med*. 2008;22(6):505-512. [\[CrossRef\]](#)
22. Zhang R, Tian X, Qin L, Lu D, Shen J. High 18F-FDG uptake for uterine smooth muscle tumor of uncertain malignant potential. *Clin Nucl Med*. 2015;40(4):349-351. [\[CrossRef\]](#)
23. Kishimoto T, Mabuchi S, Kato H, Kimura T. Condyloma acuminata induces focal intense FDG uptake mimicking vaginal stump recurrence from uterine cervical cancer: a case report. *Eur J Gynaecol Oncol*. 2013;34(1):99-100. [\[CrossRef\]](#)
24. Dejanovic D, Hansen NL, Loft A. PET/CT Variants and pitfalls in gynecological cancers. *Semin Nucl Med*. 2021;51(6):593-610. [\[CrossRef\]](#)
25. Pennings JP, de Haas RJ, de Jong KP, Dierckx RAJO, Kwee TC. Beware of false-positive FDG PET/CT interpretations for presacral recurrent rectal cancer. *Clin Nucl Med*. 2019;44(5):e342-e344. [\[CrossRef\]](#)
26. Pennings JP, de Haas RJ, Murshid KJA, de Jong KP, Dierckx RAJO, Kwee TC. FDG-avid presacral soft tissue mass in previously treated rectal cancer: diagnostic outcome and additional value of MRI, including diffusion-weighted imaging. *Eur J Surg Oncol*. 2019;45(4):606-612. [\[CrossRef\]](#)
27. Kalff V, Ware R, Heriot A, Chao M, Drummond E, Hicks RJ. Radiation changes do not interfere with postchemoradiation restaging of patients with rectal cancer by FDG PET/CT before curative surgical therapy. *Int J Radiat Oncol Biol Phys*. 2009;74(1):60-66. [\[CrossRef\]](#)
28. Kalff V, Duong C, Drummond EG, Matthews JP, Hicks RJ. Findings on 18F-FDG PET scans after neoadjuvant chemoradiation provides prognostic stratification in patients with locally advanced rectal carcinoma subsequently treated by radical surgery. *J Nucl Med*. 2006;47(1):14-22. [\[CrossRef\]](#)
29. Davidson T, Lotan E, Klang E, et al. Fat necrosis after abdominal surgery: a pitfall in interpretation of FDG-PET/CT. *Eur Radiol*. 2018;28(6):2264-2272. [\[CrossRef\]](#)
30. Meixel AJ, Hauswald H, Delorme S, Jobke B. From radiation osteitis to osteoradionecrosis: incidence and MR morphology of radiation-induced sacral pathologies following pelvic radiotherapy. *Eur Radiol*. 2018;28(8):3550-3559. [\[CrossRef\]](#)
31. Abikhzer G, Treglia G, Pelletier-Galarneau M, et al. EANM/SNMMI guideline/procedure standard for [18F]FDG hybrid PET use in infection and inflammation in adults v2.0. *Eur J Nucl Med Mol Imaging*. 2025;52(2):510-538. [\[CrossRef\]](#)
32. Lovinfosse P, Hustinx R. The role of PET imaging in inflammatory bowel diseases: state-of-the-art review. *Q J Nucl Med Mol Imaging*. 2022;66(3):206-217. [\[CrossRef\]](#)
33. Broos WAM, van der Zant FM, Knol RJ. Athletic osteitis pubis detected on 18 F-FDG PET/CT. *Clin Nucl Med*. 2022;47(9):822-823. [\[CrossRef\]](#)



Possible use of digital variance angiography in uterine fibroid embolization: a retrospective observational study

✉ **Viktor Bérczi**
Szuzina Fazekas¹
István Góó³
Marcell Gyánó²
Ambrus Tóth¹
Ákos Bérczi²
Osama Habeeballah⁴
Krzysztof Pyra⁵
Zoltán Harmat⁶
Dat Tin Nguyen²

¹Semmelweis University, Medical Imaging Center, Department of Radiology, Budapest, Hungary

²Semmelweis University, Heart and Vascular Center, Department of Interventional Radiology, Budapest, Hungary

³Semmelweis University, Heart and Vascular Center, Department of Vascular and Endovascular Surgery, Budapest, Hungary

⁴University Hospital Augsburg, University of Augsburg, Department of Diagnostic and Interventional Radiology, Augsburg, Germany

⁵Medical University of Lublin, Department of Interventional Radiology and Neuroradiology, Lublin, Poland

⁶Premier Med Healthcare, Training and Research Institute, Budapest, Hungary

Corresponding author: Viktor Bérczi

E-mail: berczi.viktor@semmelweis.hu

Received 17 October 2024; revision requested 18 November 2024; accepted 25 January 2025.



Epub: 02.05.2025

Publication date: 02.01.2026

DOI: 10.4274/dir.2025.243042

PURPOSE

Digital variance angiography (DVA), a recently developed image processing technology, provides a higher contrast-to-noise ratio (CNR) and better image quality during lower limb interventions than digital subtraction angiography (DSA). Our aim was to investigate whether the quality reserve of DVA can also be observed in uterine fibroid embolization (UFE).

METHODS

In this retrospective observational study, the CNR and image quality of DSA and DVA images from 56 patients (mean \pm standard deviation age: 44.2 ± 5.3 years) who underwent UFE at our institution were assessed. For the visual evaluation of the same image pairs, the visibility of large vessels, small vessels, tissue blush, and background noise was compared by three experienced readers using a four-grade Likert scale. Data were analyzed using the Wilcoxon signed-rank test or the one-sample Wilcoxon test.

RESULTS

DVA provided significantly higher CNR than DSA (the median $\text{CNR}_{\text{DVA}}/\text{CNR}_{\text{DSA}}$ was 1.96). In the visual comparison of DVA and DSA images, Likert scores did not significantly differ from zero (equal quality level) in any evaluated categories. The median (interquartile range) values were 0.00 (1.00) for large vessels, -0.33 (1.33) for small vessels, 0.00 (0.67) for tissue blush, and 0.00 (0.75) for background noise.

CONCLUSION

Although the visual image quality of DSA and DVA was identical, DVA provided a twofold CNR in UFE, indicating a significant quality advantage for this technology.

CLINICAL SIGNIFICANCE

The observed quality reserve may allow for dose management (reduction of applied radiation dose and/or contrast media), enhancing the safety of UFE for both patients and personnel.

KEYWORDS

Angiography, contrast-to-noise, digital, uterine, uterine fibroid embolization

Digital variance angiography (DVA) is a recently developed image processing alternative to digital subtraction angiography (DSA). The technology is based on the principles of kinetic imaging.¹ Although DVA uses the same unsubtracted acquisition as DSA, it does not use a mask but instead calculates the standard deviation (SD) of pixel intensities. This algorithm enhances the contrast media signal and suppresses background noise, thereby providing a higher contrast-to-noise ratio (CNR) and better image quality than DSA. The quality reserve of DVA has already been validated in lower limb angiography,²⁻⁵ liver transarterial chemoembolization,⁶ prostatic artery embolization,⁷ and carotid angiography.⁸ As the quality advantage of DVA can be effectively used for dose management,⁸⁻¹⁰ the aim of this study was to investigate whether DVA can improve the image quality of angiograms in transcatheter

uterine fibroid embolization (UFE), which could serve as a basis for radiation dose management in this endovascular intervention.

Over the last 29 years, as stated in the 2015 CIRSE guideline, numerous publications have demonstrated that UFE is a viable alternative to hysterectomy for women who wish to preserve their uterus (level 1 evidence).¹¹⁻¹⁴ The 2021 ACOG guideline confirms these findings, stating that "uterine artery embolization (UAE) is recommended as an interventional procedure for the treatment of uterine leiomyomas in patients who desire uterine preservation and are counseled about the limited available data on reproductive outcomes".¹⁵ In addition to fibroids, UAE has also been proposed as a minimally invasive alternative to hysterectomy for patients with symptomatic adenomyosis.^{16,17}

UAE is much less invasive and a non-surgical alternative to myomectomy or hysterectomy; however, ionizing radiation is used to identify and access the uterine artery for the embolization procedure. The literature shows that radiation exposure doses remain below the threshold for any deterministic radiation risks. Despite these data, implementing the ALARA principle and minimizing the radiation dose as much as possible is of utmost importance in every interventional radiological procedure, especially in UAE, as many patients are women of child-bearing age. Many papers have discussed different dose reduction techniques, such as adjusting collimation, minimizing DSA runs, reducing frame rates, using PA projections, and em-

ploying dose optimization software.^{18,19} The use of DVA has not yet been tested in UFE.

Methods

In this single-center retrospective observational study, 56 patients (mean \pm SD age: 44.2 \pm 5.3 years) were included who had previously undergone UFE at the Medical Imaging Center, Semmelweis University, Budapest, Hungary, between February 2021 and June 2022. All procedures were conducted in accordance with the 1964 Helsinki Declaration and its later amendments. The study was approved by the Regional Institutional Scientific and Research Ethics Committee, Semmelweis University, Budapest, Hungary (SE RKEB), approval no. 186/2022 on September 26, 2022. Due to the retrospective nature of the study, informed consent was waived.

Study Design

One pre-embolization posteroanterior (PA) pelvic acquisition was included from each patient. Pre-embolization acquisition was preferred as it depicts small arteries and tissue blush of the fibroid, thereby providing a better basis for performance comparison. DSA and DVA images were generated retrospectively from the same unsubtracted acquisition using the GE Advantage Workstation (GE Healthcare, Chicago, Ill., U.S.A.) and the Kinepict Medical Imaging Tool software (Kinepict Ltd., Budapest), respectively. Absolute CNR values and ratios were calculated for each image pair, and visual image quality was assessed by readers in a blinded and randomized manner using a 4-grade Likert scale.

Image acquisition

All procedures followed institutional protocols. UFE was performed on a GE Innova IGS 5 angiography system by an experienced interventional radiologist with over 20 years of experience. A 4F UF (Cordis, Miami Lakes, FL, U.S.A.) catheter was introduced via right femoral access. Aortography was performed to assess arterial filling of the fibroids. A Medrad Avanta (Bayer AG, Leverkusen, Germany) automated injector was used to inject 20 mL of iodinated contrast media (Ultravist 370, Bayer) at a flow rate of 10 mL/s. A 4F Cobra 1 Glidecath (Terumo, Leuven, Belgium) was positioned in the left uterine artery, followed by the right uterine artery. Hand injections of contrast media (3–6 mL) were performed for the selective angiograms into the uterine arteries. Standard PA pelvic acquisitions (2 fps)

were obtained on both sides before and after embolization. DSA runs were saved on the GE workstation, and the unsubtracted files were later used to generate stacked DSA and DVA images as described above.

Contrast-to-noise ratio analysis

Regions of interest (ROIs) were defined on vessels and background regions using ImageJ (v.2.0.0-rc-68/1.52e, Creative Commons License, NIH). As adjacent regions of blood vessels often contained signals from small arteries or tumor blush, background ROIs were placed outside the fibroid area. Vascular and background ROIs were paired accordingly.

The CNR values were calculated for all ROI pairs individually using the following formula [21], where $Mean_v$ and $Mean_b$ represent the mean pixel intensity values of the vascular and background ROIs, respectively, and Std_b is the background SD:

$$CNR = \frac{|Mean_v - Mean_b|}{Std_b}$$

CNRDVA/CNRDSA ratios (R) were also calculated for each corresponding DVA and DSA ROI.

Visual evaluation

Evaluations were conducted by three interventional radiologists with at least 5 years of experience in UFE. The readers were not involved in the treatment of enrolled patients.

A randomized, paired evaluation was performed with corresponding DSA and DVA image pairs. The readers were blinded to the imaging modality. The diagnostic value of the acquisitions was compared based on the visibility of large vessels, small vessels, tissue blush (if visible), and the extent of background noise (Figure 1).

Diagnostic value was graded using the following 4-grade bidirectional Likert scale:

0. Identical
1. Slightly better/less noise
2. Clear-cut advantage/less noise, no interference with structures
3. Better in every aspect/less noise, no interference, background clear

Each image pair was evaluated only once during the survey, and scores were automatically collected in a database for later processing.

Main points

- Use of digital variance angiography (DVA) in uterine fibroid embolization (UFE): the study evaluates DVA as an alternative to traditional digital subtraction angiography (DSA) in UFE.
- Enhanced contrast-to-noise ratio (CNR): findings demonstrate that DVA offers a two-fold higher CNR compared with DSA, indicating a substantial quality reserve.
- Potential for dose management: with the higher CNR provided by DVA, there is potential to reduce radiation exposure without compromising image quality, which is particularly advantageous for women of child-bearing age.
- Implications for future clinical trials: the study suggests that future prospective clinical trials should focus on validating the dose management capabilities of DVA in endovascular treatments, with the potential to reduce radiation exposure for both patients and personnel.

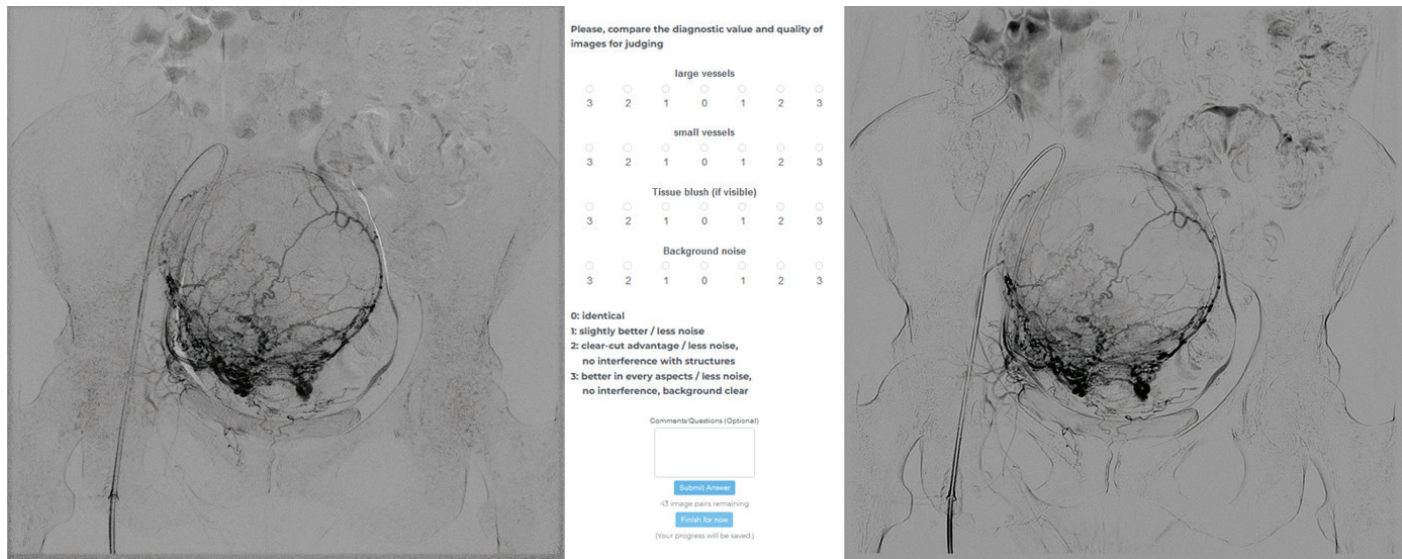


Figure 1. Survey template for the visual evaluation of DSA and DVA image sets. The modality of images was not disclosed to the readers. The web-based survey allowed for the automatic collection of scores into a database for later processing. DSA, digital subtraction angiography; DVA, digital variance angiography.

Table 1. Contrast-to-noise ratio (CNR) analysis

	CNR		R	Wilcoxon signed-rank test
	DSA	DVA		
Mean \pm SEM	19.2 \pm 0.55	33.4 \pm 0.73	2.01 \pm 0.04	$P < 0.001$
Median (IQR)	16.2 (13.24)	29.6 (24.96)	1.96 (0.88)	

Data are expressed as mean \pm standard error of the mean (SEM) and median and interquartile range (IQR). The Wilcoxon signed-rank test was used for statistical comparison, with a significance level set at $P < 0.05$. DVA, digital variance angiography; DSA, digital subtraction angiography.

Radiation dose and total fluoroscopy time measurements Results

Radiation dose (total dose-area product - DAP) and total fluoroscopy time were gathered from the radiation dose information provided for each patient in the "X-ray Radiation Dose Report" of the GE Innova IGS 5 angiography system. Data are presented as median (interquartile range).

Statistical analysis

Calculations of CNR and R medians, along with interquartile ranges (IQR), were performed using Excel 2016 (Microsoft, Redmond, WA). CNR values were compared using the Wilcoxon signed-rank test (Prism 8.4.2, GraphPad).

For visual evaluation scores, the mean and standard error of the mean were calculated. Due to the non-Gaussian distribution of the data, the median and IQR were also determined. To assess potential differences between modalities, image pair scores were compared with 0 (equal quality level) using the one-sample Wilcoxon test. Interrater agreement was characterized by Kendall's W value. The level of significance was set at $P < 0.05$ for all tests.

Patients

Patients ($n = 56$, mean \pm SD age: 44.2 ± 5.3 years) with previously diagnosed uterine fibroids received UFE treatment between February 2021 and June 2022 at the Medical Imaging Center, Semmelweis University, Budapest, and were retrospectively enrolled for image analysis in a consecutive manner.

Contrast-to-noise ratio results

A total of 695 ROI pairs were analyzed from 56 pre-embolization image pairs. The results of the CNR measurements are summarized in Table 1. The median CNR of DVA images was significantly higher than that of DSA images [29.55 (IQR: 24.96) vs. 16.23 (IQR: 13.24), Wilcoxon signed-rank test, $P < 0.001$]. The R ($\text{CNR}_{\text{DVA}}/\text{CNR}_{\text{DSA}}$) value was 1.96 (IQR: 0.88) (Figure 2).

Visual evaluation results

Readers evaluated 56 DSA-DVA image pairs using the 4-grade bidirectional Likert scale, where 0 represented identical image quality. According to the score settings, negative values indicated an advantage for DSA, whereas positive values indicated an ad-

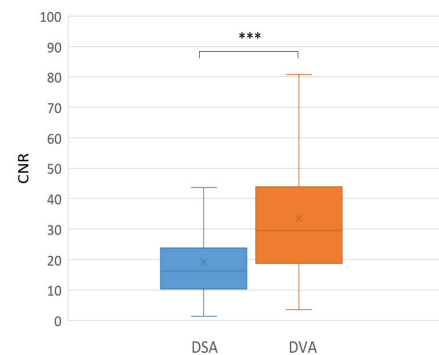


Figure 2. The CNR results. The box-and-whisker plots show the median (line), mean (x), IQR (box), and internal fences (whiskers) of CNR values in each group. Data sets were analyzed using the Wilcoxon signed-rank test ($*P < 0.001$). CNR, contrast-to-noise ratio; IQR, interquartile range; DSA, digital subtraction angiography; DVA, digital variance angiography.

vantage for DVA (Table 2). The median (IQR) Likert scores were 0.00 (1.00) for large vessels, -0.33 (1.33) for small vessels, 0.00 (0.67) for tissue blush, and 0.00 (0.75) for background noise (Figure 3). None of these values were significantly different from zero (one-sample Wilcoxon test).

Table 2. Visual comparison scores. Readers compared the visibility of large vessels, small vessels, tissue blush, and the level of background noise in a blinded, randomized manner, expressing their image preference using a 4-grade Likert scale

	Large vessels	Small vessels	Tissue blush	Background noise
Mean \pm SEM	0.11 \pm 0.11	-0.24 \pm 0.14	0.10 \pm 0.07	0.01 \pm 0.10
Median (IQR)	0.00 (1.00)	-0.33 (1.33)	0.00 (0.67)	0.00 (0.75)
One-sample Wilcoxon test	$P = 0.355$	$P = 0.054$	$P = 0.151$	$P = 0.98$

Data are expressed as mean \pm SEM and median and IQR. Deviation from zero (equal quality level) was analyzed using the one-sample Wilcoxon test. None of the scores differed significantly from zero. SEM, standard error of the mean; IQR, interquartile range.

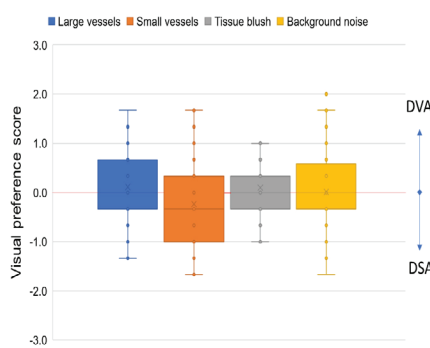


Figure 3. Paired comparison of DSA and DVA images. Readers compared the visibility of large vessels, small vessels, tissue blush, and background noise in a blinded, randomized manner, expressing their preference using a 4-grade Likert scale. The box-and-whisker plot displays the mean (x), median (line), interquartile range (box), and internal fences (whiskers) of the complete image set. The 0 line represents the theoretical equal quality level. Data were analyzed using the one-sample Wilcoxon test. None of the scores differed significantly from zero. DSA, digital subtraction angiography; DVA, digital variance angiography.

Despite moderate interrater agreement levels, ratings were significantly associated with large vessels ($W = 0.568, P < 0.001$) and small vessels ($W = 0.502, P < 0.01$). However, agreement was only slight and not significant for tissue blush ($W = 0.285, P = 0.766$) and background noise ($W = 0.349, P = 0.378$).

Radiation dose and total fluoroscopy time

Total DAP was 57.0 (21–284) Gy·cm², and total fluoroscopy time was 736 (360–1570) sec.

Discussion

Our aim was to investigate whether the previously described advantages of DVA can also be observed in UFE intervention. Therefore, we compared the CNR and visual performance of DSA and DVA images in this retrospective observational study. Our results show that DVA provides a significantly higher (about twofold) CNR than DSA, but there is no difference in the visibility of large vessels, small vessels, tissue blush, and back-

ground noise. The poor interrater agreement in the latter two categories might reflect that the judgment of tissue blush and background noise is even more subjective. These findings are partly inconsistent with previous observations, as earlier studies demonstrated that DVA was always superior to DSA in both parameters.^{2–10} However, in the present study, angiography conditions were different, as the catheter was in the uterine artery, very close to the target area, ensuring a highly selective injection of contrast media, and the acquisition was performed at a standard radiation level. Under these conditions, DSA provides excellent visual representation, which cannot be outperformed (ceiling effect). Nevertheless, the improved CNR value clearly indicates the quality reserve of DVA.

Previous studies have demonstrated that the quality reserve of DVA can be effectively utilized for dose management. A reduction of dose/frame value by 70% provided non-inferior or superior image quality in lower limb interventions compared with full-dose DSA acquisitions.²⁰ A subsequent randomized controlled trial showed that applying a similar low-dose protocol reduced total DSA-related DAP by 63% and total procedural DAP by 46% without compromising image quality or the diagnostic value of angiograms.²¹ The quality reserve of DVA can also be used to reduce contrast media, as DVA provided non-inferior image quality in carotid angiography compared with full-dose DSA when only 50% of the contrast media amount was used.⁸ Our preliminary unpublished observation suggests that an 80% reduction in contrast media achieved through dilution still provides excellent image quality in UFE using DVA images, whereas the concomitant DSA images under the same conditions appear poor.

Our finding may have important clinical implications if further studies prove the relevance of the increased CNR and increased quality reserve. UFE is a good alternative for the treatment of uterine fibroids, as it presents less burden and less risk for patients than surgical solutions. Nevertheless, this endovascular intervention requires several

X-ray angiography acquisitions and repeated injections of iodinated contrast media. These steps carry their own risks, including possible acute and long-term side effects of radiation and potential impairment of kidney function. Obviously, the dose management capabilities, especially the radiation dose reduction ability of DVA, could be very beneficial in UFE, as patients are often of reproductive age. In addition, lower radiation exposure would reduce the risk of radiation-induced occupational hazards for medical staff. The reduction of contrast media usage could also be advantageous by lowering the risk of contrast-induced nephropathy.

Our results reveal the potential of DVA for dose management in UFE; nevertheless, further clinical studies are required to validate these claims. Such a study has already been initiated at our center. The radiation dose from our center serves as a baseline for such a study; our data fall well within the range of recent literature [DAP (Gy·cm²; median, range): Nocum et al.²²: 113.1 (21.9–792); Lacayo et al.²³: 74.8 (0.32–795); our data: 57 (21–284); total fluoroscopy time (minutes, median, range): Nocum et al.²²: 11.1 (6.2–33.6); Lacayo et al.²³: 13.5 (5.7–104); our data: 12.2 (6.0–26.2)].

Our study has some limitations. Due to its retrospective observational nature, the acquisition protocol was predefined and optimized for DSA; therefore, we could not detect any differences in the visual performance of DSA and DVA images. The full validation of DVA in UFE requires prospective clinical trials in which the protocol is appropriately modified to achieve dose management and DVA images are available for the interventional radiologist in real-time in the operating room.²⁴

In conclusion, our data show that DVA has a substantial quality reserve in uterine artery angiography compared with the traditionally used DSA technology. Although a visual advantage was not observed in the current clinical setting, the twofold CNR of DVA images provides a solid basis for prospective clinical trials, where the dose management

capabilities of DVA can be validated in the endovascular treatment of fibroids and adenomyosis. These trials aim to achieve a 70% reduction in dose/frame value while maintaining non-inferior or superior image quality, as already demonstrated in lower limb interventions. Thus, our study indicates that DVA has the potential to reduce the applied radiation dose during UFE for both patients and personnel.

Footnotes

Conflict of Interest

The authors declared no conflicts of interest.

References

1. Szigeti K, Máté D, Osváth S. Motion based X-ray imaging modality. *IEEE Trans Med Imaging*. 2014;33:2031-2038. [\[CrossRef\]](#)
2. Gyánó M, Góó I, Óriás VI, et al. Kinetic Imaging in lower extremity arteriography: comparison to digital subtraction angiography. *Radiology*. 2019;290(1):246-253. [\[CrossRef\]](#)
3. Óriás VI, Gyánó M, Góó I, et al. Digital variance angiography as a paradigm shift in carbon dioxide angiography. *Invest Radiol*. 2019;54(7):428-436. [\[CrossRef\]](#)
4. Bastian MB, König AM, Viniol S, et al. Digital variance angiography in lower-limb angiography with metal implants. *Cardiovasc Interv Radiol*. 2021;44(3):452-459. [\[CrossRef\]](#)
5. Thomas RP, Bastian MB, Viniol S, et al. Digital variance angiography in selective lower limb interventions. *J Vasc Interv Radiol*. 2022;33(2):104-112. [\[CrossRef\]](#)
6. Lucatelli P, Rocco B, Ciaglia S, et al. Possible use of digital variance angiography in liver transarterial chemoembolization: a retrospective observational study. *Cardiovasc*
7. Alizadeh LS, Gyánó M, Góó I, et al. Initial experience using digital variance angiography in context of prostatic artery embolization in comparison with digital subtraction angiography. *Acad Radiol*. 2023;30(4):689-697. [\[CrossRef\]](#)
8. Óriás VI, Szöllősi D, Gyánó M, et al. Initial evidence of a 50% reduction of contrast media using digital variance angiography in endovascular carotid interventions. *Eur J Radiol Open*. 2020;7:100288. [\[CrossRef\]](#)
9. Gyánó M, Berczeli M, Csobay-Novák C, et al. Digital variance angiography allows about 70% decrease of DSA-related radiation exposure in lower limb X-ray angiography. *Sci Rep*. 2021;11(1):21790. [\[CrossRef\]](#)
10. Sótónyi P, Berczeli M, Gyánó M, et al. Radiation exposure reduction by digital variance angiography in lower limb angiography: a randomized controlled trial. *J Cardiovasc Dev Dis*. 2023;10(5):198. [\[CrossRef\]](#)
11. Ravina JH, Herbreteau D, Ciraru-Vigneron N, et al. Arterial embolisation to treat uterine myomata. *Lancet*. 1995;346(8976):671-672. [\[CrossRef\]](#)
12. Hehenkamp WJ, Volkers NA, Birnie E, Reekers JA, Ankum WM. Symptomatic uterine fibroids: treatment with uterine artery embolization or hysterectomy—results from the randomized clinical Embolisation versus Hysterectomy (EMMY) trial. *Radiology*. 2008;246(3):823-832. [\[CrossRef\]](#)
13. Edwards RD, Moss JG, Lumsden MA, et al. Uterine-artery embolization versus surgery for symptomatic uterine fibroids. *N Engl J Med*. 2007;356(4):360-370. [\[CrossRef\]](#)
14. van Overhagen H, Reekers JA. Uterine artery embolization for symptomatic leiomyomata. *Cardiovasc Interv Radiol*. 2015;38(3):536-542. [\[CrossRef\]](#)
15. Management of symptomatic uterine leiomyomas: ACOG practice bulletin, number
228. *Obstet Gynecol*. 2021;137(6):e100-e115. [\[CrossRef\]](#)
16. de Brujin AM, Smink M, Lohle PNM, et al. Uterine artery embolization for the treatment of adenomyosis: a systematic review and meta-analysis. *J Vasc Interv Radiol*. 2017;28(12):1629-1642.e1. [\[CrossRef\]](#)
17. Dason ES, Maxim M, Sanders A, et al. Guideline no. 437: diagnosis and management of adenomyosis. *J Obstet Gynaecol Can*. 2023;45(6):417-429.e1. [\[CrossRef\]](#)
18. Nocum DJ, Robinson J, Liang E, Thompson N, Reed W. The factors contributing to the total radiation exposure of patients during uterine artery embolisation. *J Med Radiat Sci*. 2019;66(3):200-211. [\[CrossRef\]](#)
19. Cina A, Steri L, Barbieri P, et al. Optimizing the angiography protocol to reduce radiation dose in uterine artery embolization: the impact of digital subtraction angiographies on radiation exposure. *Cardiovasc Interv Radiol*. 2022;45(2):249-254. [\[CrossRef\]](#)
20. Sugawara H, Suzuki S, Katada Y, et al. Comparison of full-iodine conventional CT and half-iodine virtual monochromatic imaging: advantages and disadvantages. *Eur Radiol*. 2019;29(3):1400-1407. [\[CrossRef\]](#)
21. Rose A. Quantum and noise limitations of the visual process. *J Opt Soc Am*. 1953;43:715-716. [\[CrossRef\]](#)
22. Nocum DJ, Robinson J, Halaki M, et al. Identifying predictors of patient radiation dose during uterine artery embolisation. *J Med Radiat Sci*. 2021;68(2):131-138. [\[CrossRef\]](#)
23. Lacayo EA, Khera SS, Spies JB. Impact of patient and procedure-related factors on radiation exposure from uterine artery embolization. *Cardiovasc Interv Radiol*. 2020;43(1):120-126. [\[CrossRef\]](#)
24. Gyánó M, Csobay-Novák C, Berczeli M, et al. Initial operating room experience with digital variance angiography in carbon dioxide-assisted lower limb interventions: a pilot study. *Cardiovasc Interv Radiol*. 2020;43(8):1226-1231. [\[CrossRef\]](#)



Combined therapy with microwave ablation and conventional transarterial chemoembolization for hepatocellular carcinoma tumors larger than five centimetres: a prospective study

Hui Liu^{1*}
 Zhuoyang Fan^{2*}
 Ranying Zhang¹
 Xingwei Zhang¹
 Jianhua Wang²

¹Fudan University Zhongshan Hospital, Department of Radiology, Shanghai, China

²Fudan University Zhongshan Hospital, Department of Interventional Radiology, Shanghai, China

PURPOSE

This study aimed to compare the safety and efficacy of a combined therapy involving microwave ablation (MWA) and transarterial chemoembolization (TACE) versus only TACE for the treatment of hepatocellular carcinoma (HCC) tumors ≥ 5 cm.

METHODS

This prospective study enrolled 186 patients with HCC tumors ≥ 5 cm. Patients were divided into a test group (TACE + MWA) and a control group (TACE only). The average tumor size was 9.2 ± 3.7 cm, ranging from 5 to 19 cm. Forty-five patients (27.4%) had Barcelona Clinic Liver Cancer class A disease, and 119 (72.6%) had class B disease. The viable tumor volume was quantified utilizing ITK-SNAP, a free and open-source software package for medical image segmentation and visualization, along with contrast-enhanced magnetic resonance imaging. The tumor response was assessed according to the modified response evaluation criteria in solid tumors rules. Serum alpha-fetoprotein (AFP) levels were monitored, and the tumor necrosis ratio and AFP variation rate were calculated.

RESULTS

The final analysis of 164 patients (median age 57 years, range 26–80 years; 19 women, 145 men) showed that the test group exhibited a significantly higher tumor necrosis ratio than the control group (87.5% vs. 76.1%, $P = 0.002$). The serum AFP levels were markedly reduced in the test group relative to the control group 30 days after surgery ($P = 0.001$). The AFP variation rate in the test group (79.5%) was significantly greater than that observed in the control group (47.5%) ($P < 0.001$). A significant positive correlation existed between the tumor necrosis ratio and AFP variation rate ($P < 0.001$). Compared with the control group, the test group demonstrated a significantly higher partial response rate (68.6% vs. 51.3%, $P < 0.05$), a lower rate of progressive disease (17.4% vs. 35.9%, $P < 0.05$), an increased overall response rate (70.9% vs. 55.1%, $P = 0.036$), and an enhanced disease control rate (82.6% vs. 64.1%, $P = 0.007$). Post-MWA, 3 patients experienced hemorrhage and 2 developed arteriovenous fistulae, all of which were treated with embolization.

CONCLUSION

The combination of TACE and MWA demonstrated safety, good tolerability, and greater efficacy compared with TACE alone for HCC tumors ≥ 5 cm.

CLINICAL SIGNIFICANCE

The combination of TACE and MWA offers new possibilities for improving tumor necrosis rates, reducing AFP levels, and enhancing short-term prognosis. These findings not only provide new treatment options for clinical doctors but also promote the application of three-dimensional quantitative assessment technology and provide important references for future research and clinical practice.

KEYWORDS

Hepatocellular carcinoma, microwave ablation, therapeutic evaluation, three-dimensional, transarterial chemoembolization

*Joint first authors

Corresponding author: Jianhua Wang

E-mail: wjh1953a@163.com

Received 21 February 2025; revision requested 13 April 2025; last revision received 12 May 2025; accepted 18 May 2025



Epub: 07.07.2025

Publication date: 02.01.2026

DOI: 10.4274/dir.2025.253308

You may cite this article as: Liu H, Fan Z, Zhang R, Zhang X, Wang J. Combined therapy with microwave ablation and conventional transarterial chemoembolization for hepatocellular carcinoma tumors larger than five centimetres: a prospective study. *Diagn Interv Radiol.* 2026;32(1):96-103.

Primary liver cancer is the sixth most frequently occurring cancer worldwide and is the third most common cause of death related to cancer.¹ Hepatocellular carcinoma (HCC) is the predominant form of liver cancer. More than 70% of patients received a diagnosis during the intermediate to advanced stages and were limited to non-invasive treatment options.² For patients with intermediate to advanced HCC, transarterial chemoembolization (TACE) is the initial treatment choice.³ However, the effectiveness of TACE is restricted for large HCC lesions, often leading to TACE-refractoriness and deteriorating liver function with repeated treatments.^{4,5}

Recent studies indicate that combining TACE with ablative methods is increasingly recognized for improving tumor response and patient survival.⁶⁻⁹ However, the majority of these studies have concentrated on sequential combination therapy. Only a small number of studies have dealt with TACE plus concurrent ablation.^{7,10} A retrospective study found that microwave ablation (MWA) immediately followed by TACE was a reliable and efficient therapy for large HCC tumors.¹¹ However, prospective studies on the topic have not been reported.

Therapeutic response in HCC was mainly assessed by measuring the target lesion's diameter through contrast-enhanced imaging.¹² Indeed, most large HCC tumors exhibit irregular morphology and significant internal heterogeneity pre-and post-treatment. Numerous studies have found that three-dimensional (3D) quantitative assessment is more precise than diameter-based measurements.¹³⁻¹⁵ Precise delineation and quantitative assessment of the complete tumor active lesion are essential for an accurate

evaluation of therapeutic efficacy. Few studies have evaluated the treatment efficacy on large HCC tumors by measuring viable tumor volumes using contrast-enhanced magnetic resonance imaging (MRI). Furthermore, although dynamic changes in serum alpha-fetoprotein (AFP) levels have been shown to correlate with treatment efficacy and patient outcomes,^{16,17} the relationship between viable tumor volume and AFP dynamics remains unexplored.

Therefore, we performed a prospective study to assess changes in viable tumor volume and AFP levels before and after treatment, aiming to precisely analyze short-term efficacy differences between TACE alone and TACE combined with MWA in treating large HCC tumors.

Methods

Study design

A prospective, randomized controlled trial was performed at a single center for this research. The study was registered on ClinicalTrials.gov (NCT04721470). Before being enrolled, all patients gave their written informed consent. The study protocol received approval from all relevant institutional review boards, adhering to the Declaration of Helsinki and local regulations. The study was approved by the Ethics Committee of Zhongshan Hospital Affiliated to Fudan University (protocol number: B2018-146R, date: 17.11.2018). Participants were randomly assigned to either the TACE-only group or the TACE plus MWA group between December 2018 and December 2021. Demographic and clinical data, such as age, gender, tumor diameter, Child-Pugh class, hepatitis B virus (HBV) infection status, and serum AFP levels, for patients with HCC were obtained from medical records.

The main inclusion criteria were as follows: (1) age ≥ 18 years; (2) nodular and hypervascular HCC diagnosis was established using either non-invasive methods or pathological examination; (3) large (≥ 5 cm) HCC lesions confined to the liver as determined by contrast-enhanced MRI before treatment; (4) Barcelona Clinic Liver Cancer (BCLC) stage A or B; and (5) eastern cooperative oncology group performance status score of ≤ 2 . Participants were excluded if they satisfied any of the following conditions: (1) having more than three HCC lesions (3 patients); (2) were involved in other clinical research treatments simultaneously (5 patients); (3) showed extrahepatic me-

tastasis or significant vascular invasion (11 patients); (4) did not undergo MRI enhancement assessment 30 days after treatment (3 patients); or (5) had a platelet concentration $< 3 \times 10^9/L$ and prothrombin activity $< 40\%$, which excluded 22 patients. Randomization occurred within 1 week following the verification of eligibility, with treatment protocols commencing in the subsequent week. Figure 1 depicts the study population inclusion process flowchart. Three interventional radiologists, each with > 10 years of experience, conducted all treatment procedures at the study's onset.

Transarterial chemoembolization group

Angiography of the hepatic artery was conducted through the right common femoral access with a 5-F catheter (RH; Terumo, Tokyo, Japan) to evaluate the tumor's burden, localization, and blood supply. A 2.7-F microcatheter (Progreat; Terumo) was precisely manipulated to access the tumor's supplying arteries. A mixture of 5–20 mL iodized oil (lipiodol) and 50 mg epirubicin (Farmorubicin; Pfizer, Wuxi, China) was used for chemoembolization. The tumor's vascular characteristics, size, and number primarily dictated the dosage of ethiodized oil. The tumor's blood supply was cut off by fully embolizing all its arterial branches for optimal devascularization. Embolization was performed using a lipiodol emulsion mixed with gelatin sponge particles (350–560 mm; Alikang Medicine Co., Ltd.).

Transarterial chemoembolization plus microwave ablation group

A right common femoral approach was used for hepatic artery angiography to assess tumor burden, localization, and blood supply. Ultrasound-guided percutaneous MWA (IPC-1530; Aloka, Tokyo, Japan) was performed, followed immediately by chemoembolization.

The MWA utilized a water-cooled microwave system (ECO-100C; Nanjing, Jiangsu, China) featuring a 2.45 GHz generator with adjustable power of 0–100 W. The antenna placement, power, and emission duration were customized according to the tumor's characteristics. Power was set between 60–100 W for 5–15 minutes per session, as per guidelines. Multiple overlapping ablations were monitored via real-time ultrasound. A 14-gauge antenna—or two if necessary—was placed into the target tumor to cover the tumor's margin. The session was ended if the deep region of the

Main points

- The transarterial chemoembolization (TACE) + microwave ablation (MWA) group exhibited a significantly higher viable tumor necrosis ratio than the TACE group.
- Post-treatment serum alpha-fetoprotein (AFP) levels were significantly lower in the TACE + MWA group than in the TACE group. The AFP variation rate was significantly higher in the TACE + MWA group than in the TACE group.
- A positive correlation was found between tumor necrosis ratio and AFP variation rate.
- The TACE + MWA group demonstrated superior partial response, overall response rate, and disease control rate relative to the TACE group.

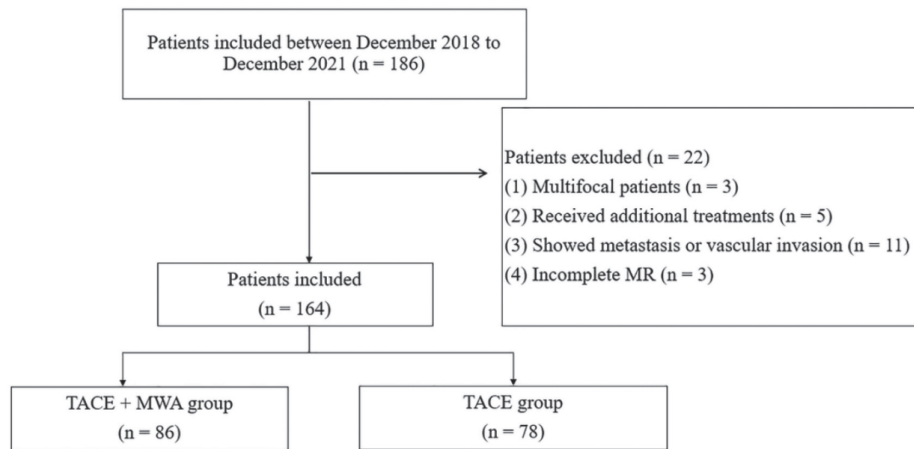


Figure 1. Flowchart of the study. TACE, transarterial chemoembolization; MWA, microwave ablation; MR, magnetic resonance.

lesion was covered by hyperechoic regions on ultrasound. Subsequently, the antenna was withdrawn gradually, and microwave emission was restarted. The end of the procedure was signaled when the entire tumor was hyperechoic on ultrasound. Post-ablation, needle pathway coagulation was performed to reduce bleeding or the spread of the tumor.

After MWA, hepatic angiography was quickly performed to evaluate ablation results, check for remaining tumor vascularity, and detect complications, such as arteriovenous fistula or bleeding. A mixture of 2–20 mL iodized oil (lipiodol) and 20–50 mg epirubicin (Farmorubicin; Pfizer, Wuxi, China) was used for chemoembolization until the tumor's blood supply was saturated. Gelatin sponge particles, sized 350–510 µm (Ailikang Medicine, Hangzhou, China) and combined with a contrast medium, were then injected to reduce any remaining blood flow. In cases of arteriovenous fistula or hemorrhage, arterial embolization was performed utilizing gelatin sponge particles or a Tornado embolization coil (Cook, Bloomington, Indiana). Patients were monitored with an electrocardiograph for 24 hours afterward.

Magnetic resonance imaging protocol

All participants underwent contrast-enhanced MRI using a 1.5 T scanner (Magnetom Aera, Siemens Healthcare, Germany). Liver protocols included T1-weighted imaging in-phase and opposed-phase, T2-weighted imaging, diffusion-weighted imaging with *b* values of 0, 50, and 500 s/mm², and dynamic contrast-enhanced imaging. The MR units automatically calculated the apparent diffusion coefficient. Gadopentetate dimeglu-

mine was administered at 2 mL/s with a 0.1 mmol/kg dose, followed by a saline flush. Images for arterial, portal, and delayed phases were captured at 20–25, 70–90, and 150–180 seconds, respectively.

Viable tumor volume segmentation

The MRI were processed using open-source software (ITK-SNAP, version 3.8.0, www.itksnap.org) for segmentation and quantification by a radiologist with 12 years of experience. The free ITK-SNAP package provides the capabilities of semi-automatic segmentation as well as image navigation. Regions of interest were placed on arterial phase images to measure viable tumor volume (Figure 2), unless no lesion enhancement was detected, indicating inactivity (Figure 3). Another radiologist with 15 years of experience verified all segmented images.

Definition and evaluation of data

The viable tumor necrosis ratio was calculated as follows:

$$\text{Tumor necrosis ratio} = \frac{\text{VOLUME pretherapy} - \text{VOLUME posttherapy}}{\text{VOLUME pretherapy}} \times 100\%$$

Patients underwent contrast-enhanced MR examinations 7 days before and 30 days after the surgery. The volume of the viable tumor was calculated using ITK-SNAP. Patients were then followed up with contrast-enhanced MRI or computed tomography (CT). Routine laboratory tests, including AFP level evaluations, were conducted within 30 days post-treatment and subsequently every 6–8 weeks. Six months after initial treatment, local tumor response was assessed using the modified response evaluation criteria in solid tumors rules, categorizing outcomes as complete response (CR), partial response (PR),

stable disease, or progressive disease (PD).¹² The disease control rate (DCR) and objective response rate (ORR) were also evaluated. The approach was evaluated by two radiologists with >10 years of specialization in abdominal imaging. The AFP variation rate was calculated 30 days after treatment as follows:

$$\text{AFP variation rate} = \frac{\text{AFP}_{\text{pretherapy}} - \text{AFP}_{\text{posttherapy}}}{\text{AFP}_{\text{pretherapy}}} \times 100\%$$

Possible complications during treatment include contrast agent extravasation (indicating bleeding) or arteriovenous fistula. The most common short-term complication was postembolization syndrome, including mild to moderate pain, fever, nausea, and vomiting.

Statistical analysis

Statistical analysis was performed using GraphPad Prism 9.0 (GraphPad Software, San Diego, CA, USA) and SPSS Version 24 (IBM Corporation, Armonk, NY, USA). Continuous variables with a normal distribution were presented as mean \pm standard deviation and analyzed using either the Student's *t*-test or the Mann-Whitney *U* test, based on their distribution. Spearman tests assessed correlations between pre-therapy viable tumor volume and post-therapy necrosis rate, as well as post-therapy viable tumor volume necrosis rate and AFP decline rate. Chi-squared tests were used for categorical variables, with significance set at *P* < 0.05.

Results

The study included 164 patients (median age 57 years, range 26–80 years; 19 women, 145 men), divided into TACE (*n* = 78) and TACE + MWA (*n* = 86) groups. The primary HCC lesions had a median size of 8.6 cm (range 5–17 cm), with 62.2% of patients having elevated AFP levels (≥ 20 ng/mL) and 62.8% having HBV infection. Table 1 shows there were no notable differences in clinical characteristics or laboratory results between the treatment groups.

Table 2 shows there were no significant differences in viable tumor volume between the two groups, both pre- and post-treatment. The MRI 30 days post-treatment indicated a significantly higher tumor necrosis ratio in the TACE + MWA group (87.5%) than in the TACE group (76.1%) (Figure 4).

Before treatment, both groups exhibited comparable elevated AFP levels, with no significant difference (*P* = 0.137). The AFP levels declined in all patients (Table 3), with the TACE + MWA group showing significantly lower levels (46.7 vs. 601.3, *P* < 0.001) than

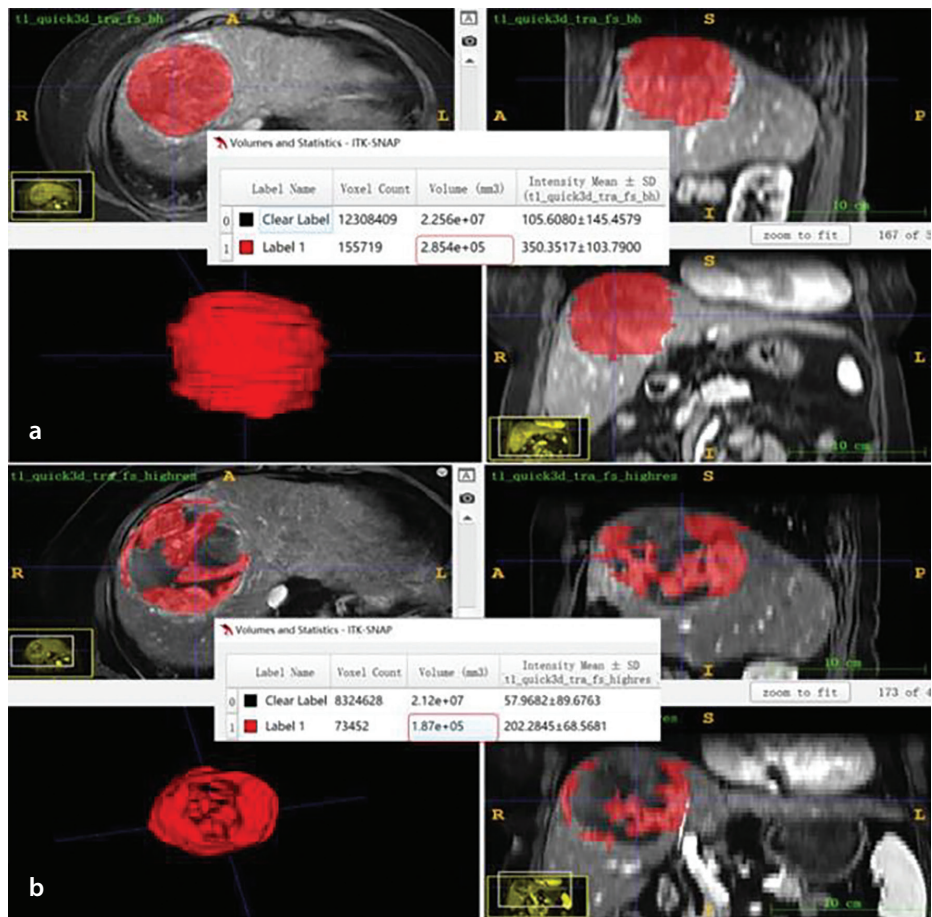


Figure 2. Images of a 76-year-old female patient with hepatocellular carcinoma. Arterial phase contrast-enhanced T1-weighted imaging before transarterial chemoembolization (TACE) revealed a tumor with a volume of 285,400 mm³ in the right liver lobe (a). Contrast-enhanced T1-weighted imaging in the arterial phase revealed heterogeneous enhancement 30 days after TACE. The volume of tumor enhancement (viable tissue) was 187,000 mm³ (b).

Table 1. Clinical characteristics of patients (n = 164)

Characteristic	TACE + MWA (n = 86)	TACE (n = 78)	P value
Age (y)			
≥60	38 (44.2%)	36 (46.2%)	0.8
<60	48 (55.8%)	42 (53.8%)	
Sex			
Male	78 (90.7%)	67 (85.9%)	0.34
Female	8 (9.3%)	11 (14.1%)	
Tumor diameter (cm)			
5-10	51 (59.3%)	52 (66.7%)	0.33
>10	35 (40.7%)	26 (33.3%)	
Child-Pugh class			
A	67 (77.9%)	61 (78.2%)	0.96
B	19 (22.1%)	17 (21.8%)	
Hepatitis B virus infection			
Yes	52 (60.5%)	51 (65.4%)	0.52
No	34 (39.5%)	27 (34.6%)	
AFP level (ng/mL)			
>20	52 (60.5%)	50 (64.1%)	0.63
≤20	34 (39.5%)	28 (35.9%)	

TACE, transarterial chemoembolization; MWA, microwave ablation; AFP, alpha-fetoprotein.

those in the TACE group after treatment (Figure 5). The AFP variation rate in the TACE + MWA group was significantly higher than that in the TACE group (Figure 6) ($P < 0.001$). Furthermore, a positive correlation was identified between tumor necrosis ratio and AFP variation rate ($r = 0.46$, $P < 0.001$) (Figure 7).

In the TACE + MWA group, the CR, PR, SD, and PD rates were 2.3%, 68.6%, 11.6%, and 17.4%, respectively, whereas in the TACE group, they were 3.8%, 51.3%, 8.9%, and 35.9%, respectively. Both PR and PD significantly differed between the groups ($P < 0.05$). The TACE + MWA group had a DCR of 82.6% and an ORR of 70.9%, both significantly higher than the TACE group's DCR of 64.1% ($P = 0.007$) and ORR of 55.1% ($P = 0.036$) (Table 4).

The treatment was well-tolerated, with no major complications or procedure-related fatalities. Post-MWA, 3 patients experienced hemorrhage and 2 developed arteriovenous fistulae, all of which were treated with embolization. Post-embolization syndrome was the most frequent short-term complication, treated with medication and supportive care. Alanine aminotransferase (150.3 ± 82.8 U/L) and aspartate aminotransferase (135.2 ± 25.6 U/L) levels were transiently increased on the third day after treatment compared with baseline levels (42.3 ± 7.6 U/L and 67.3 ± 6.3 U/L, respectively). The respective aminotransferase levels decreased to 39.8 ± 9.9 U/L and 60.1 ± 4.7 U/L at 1 month after treatment.

Discussion

This study assessed the effectiveness of combining TACE with MWA versus TACE alone for treating HCC tumors ≥ 5 cm. The results indicated that the combination treatment led to better short-term outcomes, including greater tumor volume reduction and lower serum AFP levels. The combined therapy showed promise in controlling tumor progression and improving patient outcomes for large HCC tumors.

For patients with BCLC stage A and B tumors ≥ 5 cm who are ineligible for surgical resection, TACE is generally preferred. However, complete tumor necrosis is difficult to achieve. TACE with drug-eluting beads achieves precise delivery and sustained release of drugs through drug-loaded microspheres, which may reduce systemic toxicity and improve local efficacy. In contrast, conventional TACE relies on iodized oil as a chemotherapy carrier, which is suitable for a wider range of clinical scenarios. Recent studies indicated that combining TACE with ablation was more effective for liver cancer

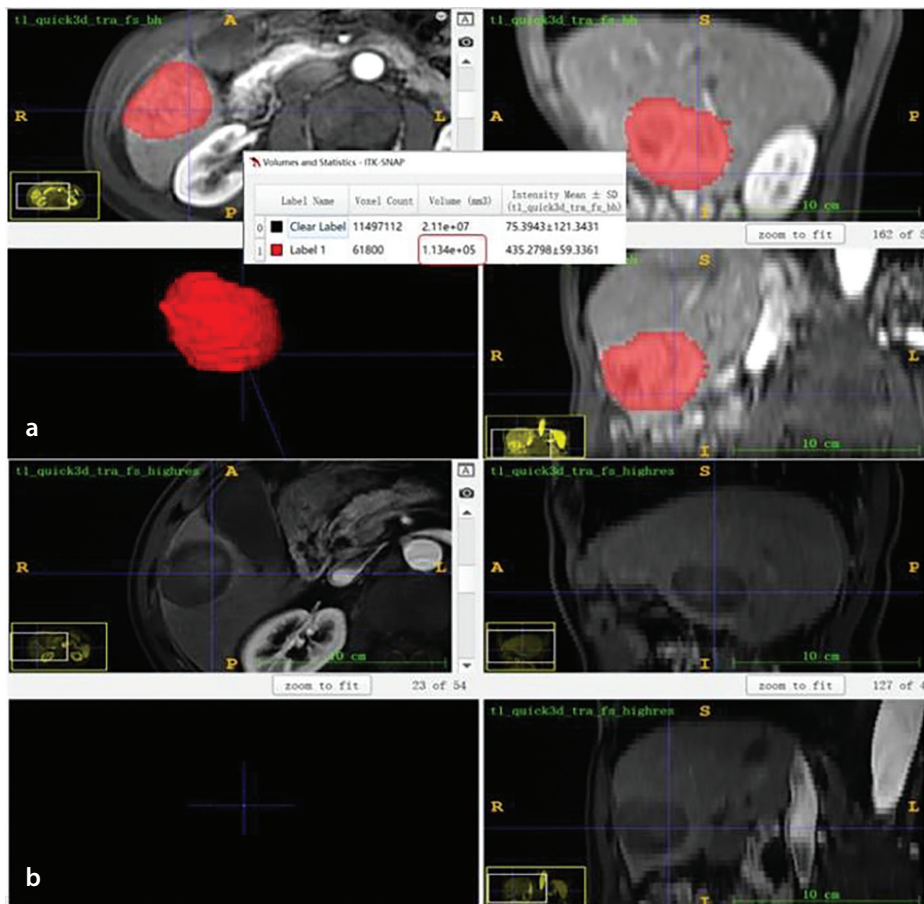


Figure 3. Images of a 62-year-old male patient with hepatocellular carcinoma. An arterial phase contrast-enhanced T1-weighted image revealed a tumor with a volume of $113,400 \text{ mm}^3$ in the right liver lobe before treatment (a). No enhancement was observed in the tumor (complete necrosis) 30 days after transarterial chemoembolization + microwave ablation (b).

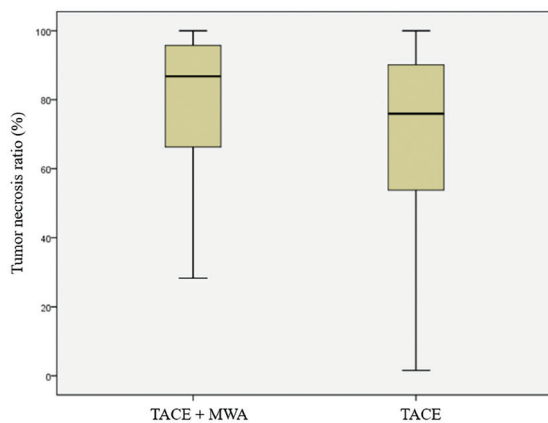


Figure 4. Boxplot of tumor necrosis ratio. TACE, transarterial chemoembolization; MWA, microwave ablation.

treatment than TACE alone.^{7,18,19} The meta-analysis evaluated TACE combined with MWA versus TACE alone for BCLC stage A or B patients with HCC tumors $\geq 5 \text{ cm}$. The findings indicated notable enhancements in CR, PR, and ORR with the combined TACE and MWA treatment.⁸ Another study demonstrated that combined therapy significantly improved ORR and DCR compared with TACE alone.²⁰ These findings are similar to our

study. Our prospective study revealed that combined therapy significantly improved PR, ORR, and DCR compared with TACE alone. These findings may be attributed to the direct ablative effect of MWA on the lesion core, whereas TACE demonstrates a more pronounced therapeutic impact on the hypervascularized peripheral regions of the lesion. However, those investigations presented results for combination treatments

on tumors exhibiting heterogeneous size ranges, stages, and tumor burden. This study focused mainly on tumors $\geq 5 \text{ cm}$.

Traditional liver cancer treatment evaluation relied on measuring the target lesion's diameter during arterial phase enhancement.¹² However, this method may not accurately reflect the true condition of the tumor, as it only considers changes in a single dimension and overlooks variations in volume and shape. Recent research suggested that 3D quantitative analysis offered a more comprehensive assessment of tumor response.²¹⁻²⁴ Pandey et al.²¹ found that it can more precisely assess the tumor response and patient prognosis after treatment by accurately measuring tumor volume. Fleckenstein et al.²² found that 3D quantitative analysis can be used to evaluate early responses in patients with liver cancer following local therapy, which is crucial for the timely adjustment of treatment plans. These findings support our study. The TACE + MWA cohort showed a greater necrosis ratio than the TACE cohort ($P < 0.05$), suggesting greater efficacy of the combined treatment. Additionally, another study pointed out that changes in tumor volume enhanced by 3D imaging significantly correlated with overall patient survival.^{23,24} However, this aspect was not addressed in our study.

CT can evaluate the morphological and hemodynamic changes of tumors, but it is not as effective as MRI in displaying viable lesions. For patients with renal insufficiency or allergies to CT/MRI contrast agents, contrast-enhanced ultrasound can be used as a useful complementary technique.²⁵ The ITK-SNAP interactive software package allows manual and semi-automatic 3D medical image segmentation on computers.²⁶ Compared with traditional methods that require specific workstations, ITK-SNAP is more flexible and suitable for various clinical and research environments. The use of ITK-SNAP is not limited to image "omics" research but is also widely applied in clinical practice for precise tumor volume measurement. In clinical applications, the semi-automatic segmentation function of ITK-SNAP has been proven to reduce the time required for manual segmentation significantly while maintaining high accuracy.²⁶

In patients with HCC, AFP levels were often used as a biomarker for diagnosis and prognosis assessment. Studies have shown that the dynamic changes in AFP levels can reflect the effectiveness of treatment and patient outcomes.^{16,27,28} Previous studies have

shown that a notable reduction in AFP levels may suggest increased tumor necrosis and improved treatment outcomes.^{16,17,28} Guo et al.²⁰ found that AFP levels significantly decreased in both groups after treatment, with the test group showing a greater reduction than the control group. This is in agreement with our results. Additionally, there was a significant positive correlation between the ne-

rosis ratio and AFP variation rate after treatment in the present study, indicating that treatment has led to the death of tumor cells, thereby reducing AFP production. In addition, the decline in AFP levels can help identify patients who respond well to treatment, guiding subsequent treatment decisions.²⁸

To date, numerous investigations have

explored the application of transcutaneous thermal ablation in conjunction with TACE for the management of HCC. Nevertheless, the majority of existing reports on combination therapy described sequential treatment regimens with diverse temporal intervals (from 1–42 days).^{6,29–31} Recent studies have validated the safety and efficacy of TACE combined with thermal ablation, showing no significant impairment of liver function.^{9–11,17} In this prospective study, MWA combined with simultaneous TACE was a safe treatment for HCC tumors ≥ 5 cm without increasing the risk of major complications. These findings were consistent with previous studies.¹¹ Immediate TACE after MWA was considered to increase tumor necrosis by exposing sublethal heat-damaged tumor tissues to high drug concentration, potentially reducing the dosage of iodinated oil and chemotherapy drugs in subsequent TACE. Severe complications related to MWA, including arteriovenous fistula and hemorrhage, can be promptly identified and treated.^{9,11} In addition, immediate TACE after MWA can reduce hospitalizations and costs. Hence, this method has a high potential for popularization in clinical applications. In studies on performing TACE prior to MWA, the accuracy of needle punctures into lesions is improved, and the “thermal settling effect” during the ablation process is reduced. Previous studies have not compared the two operation sequences, nor have they indicated a clear optimal sequence.

Our study had several limitations. First, some HCC tumors were diagnosed using clinical criteria, including contrast-enhanced MRI findings and AFP level, rather than histopathological confirmation. Second, this investigation assessed the effectiveness of the treatment over a short period and did not include an analysis of long-term efficacy, which is inadequate to establish conclusively

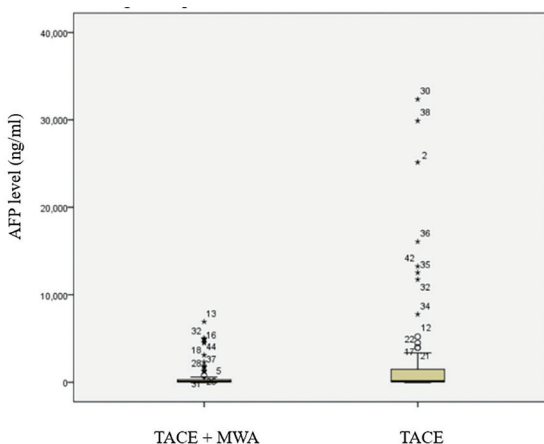


Figure 5. Boxplot of alpha-fetoprotein level after treatment. TACE, transarterial chemoembolization; MWA, microwave ablation; AFP, alpha-fetoprotein.

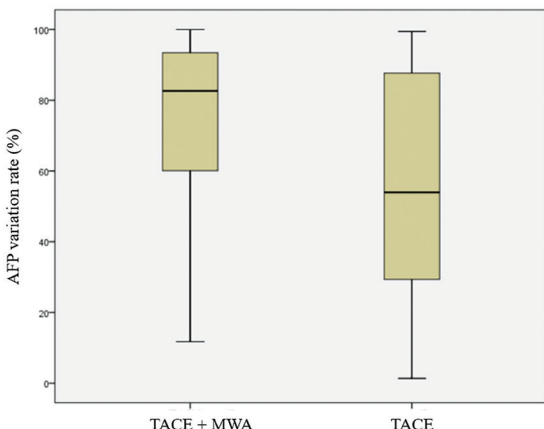


Figure 6. Boxplot of alpha-fetoprotein variation rate. TACE, transarterial chemoembolization; MWA, microwave ablation; AFP, alpha-fetoprotein.

Table 2. Measurements of viable tumor before and after treatment (n = 164)

Characteristic	TACE + MWA (n = 86)	TACE (n = 78)	P value
Pretherapy viable tumor volume	275,700 mm ³	250,000 mm ³	0.683
Posttherapy viable tumor volume	32,245 mm ³	54,995 mm ³	0.085
Tumor necrosis ratio	87.5%	76.1%	0.002*

*Data are statistically significant results. TACE, transarterial chemoembolization; MWA, microwave ablation.

Table 3. Alpha-fetoprotein level before and after treatment (n = 102)

	TACE + MWA (n = 52)	TACE (n = 50)	P value
AFP level before treatment (ng/mL)	978.7	2,178.5	0.137
AFP level after treatment (ng/mL)	46.7	601.3	0.001*
AFP variation rate	79.5%	47.5%	<0.001*

*Data are statistically significant results. TACE, transarterial chemoembolization; MWA, microwave ablation; AFP, alpha-fetoprotein.

Table 4. Assessment of target lesion response according to the modified response evaluation criteria in solid tumors rules (n = 164)

TACE + MWA (n = 86)	TACE (n = 78)	P value
CR	2 (2.3%)	3 (3.8%)
PR	59 (68.6%)	40 (51.3%)
SD	10 (11.6%)	7 (8.9%)
PD	15 (17.4%)	28 (35.9%)
ORR	61 (70.9%)	43 (55.1%)
DCR	71 (82.6%)	50 (64.1%)

*Data are statistically significant results. CR, complete response; PR, partial response; SD, stable disease; PD, progressive disease; ORR, objective response rate; DCR, disease control rate; TACE, transarterial chemoembolization; MWA, microwave ablation.

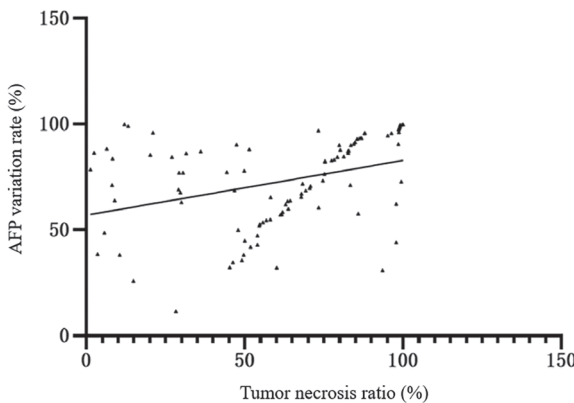


Figure 7. Scatter plot of the correlation between the tumor necrosis ratio and the alpha-fetoprotein variation rate. AFP, alpha-fetoprotein.

the superiority of combination therapy. Finally, as a single-center study, it was limited by a small sample size and a unique patient setting. Therefore, larger sample sizes in multicenter studies are necessary to further validate the treatment protocol's efficacy and safety.

In conclusion, TACE combined with MWA was more effective for treating HCC tumors ≥ 5 cm than TACE alone, as it significantly reduced AFP levels and enhanced tumor necrosis. This suggested that the combined therapy could be a viable treatment option for larger HCC tumors. However, larger multicenter studies are needed to confirm these benefits.

Footnotes

Conflict of interest disclosure

The authors declared no conflicts of interest.

References

- Bray F, Laversanne M, Sung H, et al. Global cancer statistics 2022: GLOBOCAN estimates of incidence and mortality worldwide for 36 cancers in 185 countries. *CA Cancer J Clin.* 2024;74(3):229-263. [\[Crossref\]](#)
- Siegel RL, Miller KD, Jemal A. Cancer statistics, 2015. *CA Cancer J Clin.* 2015;65(1):5-29. [\[Crossref\]](#)
- Raoul JL, Forner A, Bolondi L, Cheung TT, Kloeckner R, de Baere T. Updated use of TACE for hepatocellular carcinoma treatment: how and when to use it based on clinical evidence. *Cancer Treat Rev.* 2019;72:28-36. [\[Crossref\]](#)
- Lencioni R, de Baere T, Soulen MC, Rilling WS, Geschwind JF. Lipiodol transarterial chemoembolization for hepatocellular carcinoma: a systematic review of efficacy and safety data. *Hepatology.* 2016;64(1):106-116. [\[Crossref\]](#)
- Hiraoka A, Kumada T, Kudo M, et al. Hepatic function during repeated TACE procedures and prognosis after introducing sorafenib in patients with unresectable hepatocellular carcinoma: multicenter analysis. *Dig Dis.* 2017;35(6):602-610. [\[Crossref\]](#)
- Li HZ, Tan J, Tang T, An TZ, Li JX, Xiao YD. Chemoembolization plus microwave ablation vs chemoembolization alone in unresectable hepatocellular carcinoma beyond the Milan criteria: a propensity scoring matching study. *J Hepatocell Carcinoma.* 2021;8:1311-1322. [\[Crossref\]](#)
- Özen Ö, Boyvat F, Zeydanlı T, Kesim Ç, Karakaya E, Haberal M. Transarterial chemoembolization combined with simultaneous thermal ablation for solitary hepatocellular carcinomas in regions with a high risk of recurrence. *Exp Clin Transplant.* 2023;21(6):512-519. [\[Crossref\]](#)
- Liu C, Li T, He JT, Shao H. TACE combined with microwave ablation therapy vs. TACE alone for treatment of early- and intermediate-stage hepatocellular carcinomas larger than 5 cm: a meta-analysis. *Diagn Interv Radiol.* 2020;26(6):575-583. [\[Crossref\]](#)
- Floridi C, Cacioppa LM, Rossini N, et al. Microwave ablation followed by cTACE in 5-cm HCC lesions: does a single-session approach affect liver function? *Radiol Med.* 2024;129(8):1252-1264. [\[Crossref\]](#)
- Wu M, Gao S, Song H, et al. Percutaneous thermal ablation combined with simultaneous transarterial chemoembolization for hepatocellular carcinoma ≤ 5 cm. *J Cancer Res Ther.* 2019;15(4):766-772. [\[Crossref\]](#)
- Si ZM, Wang GZ, Qian S, et al. Combination therapies in the management of large (≥ 5 cm) hepatocellular carcinoma: microwave ablation immediately followed by transarterial chemoembolization. *J Vasc Interv Radiol.* 2016;27(10):1577-1583. [\[Crossref\]](#)
- Lencioni R, Llovet JM. Modified RECIST (mRECIST) assessment for hepatocellular carcinoma. *Semin Liver Dis.* 2010;30(1):52-60. [\[Crossref\]](#)
- Bonekamp S, Li Z, Geschwind JF, et al. Unresectable hepatocellular carcinoma: MR imaging after intraarterial therapy. Part I. Identification and validation of volumetric functional response criteria. *Radiology.* 2013;268(2):420-430. [\[Crossref\]](#)
- Chapiro J, Wood LD, Lin M, et al. Radiologic-pathologic analysis of contrast-enhanced and diffusion-weighted MR imaging in patients with HCC after TACE: diagnostic accuracy of 3D quantitative image analysis. *Radiology.* 2014;273(3):746-758. [\[Crossref\]](#)
- Tacher V, Lin M, Duran R, et al. Comparison of existing response criteria in patients with hepatocellular carcinoma treated with transarterial chemoembolization using a 3D quantitative approach. *Radiology.* 2016;278(1):275-284. [\[Crossref\]](#)
- Masior Ł, Krasnodębski M, Kuncewicz M, et al. Alpha-fetoprotein response after first transarterial chemoembolization (TACE) and complete pathologic response in patients with hepatocellular cancer. *Cancers (Basel).* 2023;15(15):3962. [\[Crossref\]](#)
- Zaitoun MMA, Elsayed SB, Zaitoun NA, et al. Combined therapy with conventional transarterial chemoembolization (cTACE) and microwave ablation (MWA) for hepatocellular carcinoma $>3-5$ cm. *Int J Hyperthermia.* 2021;38(1):248-256. [\[Crossref\]](#)
- Yan L, Ren Y, Qian K, et al. Sequential transarterial chemoembolization and early radiofrequency ablation improves clinical outcomes for early-intermediate hepatocellular carcinoma in a 10-year single-

center comparative study. *BMC Gastroenterol.* 2021;21(1):182. [\[Crossref\]](#)

19. Zhu ZY, Yuan M, Yang PP, et al. Single medium-sized hepatocellular carcinoma treated with sequential conventional transarterial chemoembolization (cTACE) and microwave ablation at 4 weeks versus cTACE alone: a propensity score. *World J Surg Oncol.* 2022;20(1):192. [\[Crossref\]](#)

20. Guo JY, Zhao LL, Cai HJ, Zeng H, Mei WD. Radiofrequency ablation combined with transcatheter arterial chemoembolization for recurrent liver cancer. *World J Gastrointest Surg.* 2024;16(6):1756-1764. [\[Crossref\]](#)

21. Pandey A, Pandey P, Aliyari Ghasabeh M, et al. Unresectable intrahepatic cholangiocarcinoma: multiparametric MR imaging to predict patient survival. *Radiology.* 2018;288(1):109-117. [\[Crossref\]](#)

22. Fleckenstein FN, Schernthaler RE, Duran R, et al. Renal cell carcinoma metastatic to the liver: early response assessment after intraarterial therapy using 3D quantitative tumor enhancement analysis. *Transl Oncol.* 2016;9(5):377-383. [\[Crossref\]](#)

23. Hajkova M, Andrasina T, Ovesna P, et al. Volumetric analysis of hepatocellular carcinoma after transarterial chemoembolization and its impact on overall survival. *In Vivo.* 2022;36(5):2332-2341. [\[Crossref\]](#)

24. Onur İD, Akdur PÖ, Çamöz ES, Çiledağ N, Yıldız F. Evaluation of the prognostic effectiveness of liver metastasis volume by volumetric measurement in colorectal cancer. *Future Oncol.* 2024;20(38):3133-3140. [\[Crossref\]](#)

25. Moschouris H, Malagari K, Papadaki MG, et al. mRECIST criteria and contrast-enhanced US for the assessment of the response of hepatocellular carcinoma to transarterial chemoembolization. *Diagn Interv Radiol.* 2014;20(2):136-142. [\[Crossref\]](#)

26. Yushkevich PA, Pashchinskiy A, Oguz I, et al. User-guided segmentation of multimodality medical imaging datasets with ITK-SNAP. *Neuroinformatics.* 2019;17(1):83-102. [\[Crossref\]](#)

27. Paul SB, Sahu P, Sreenivas V, et al. Prognostic role of serial alpha-fetoprotein levels in hepatocellular carcinoma treated with locoregional therapy. *Scand J Gastroenterol.* 2019;54(9):1132-1137. [\[Crossref\]](#)

28. Chen IH, Hsu CC, Yong CC, et al. AFP response to locoregional therapy can stratify the risk of tumor recurrence in HCC patients after living donor liver transplantation. *Cancers (Basel).* 2023;15(5):1551. [\[Crossref\]](#)

29. Zhang TQ, Huang ZM, Shen JX, et al. Safety and effectiveness of multi-antenna microwave ablation-oriented combined therapy for large hepatocellular carcinoma. *Therap Adv Gastroenterol.* 2019;12:1756284819862966. [\[Crossref\]](#)

30. Smolock AR, Cristescu MM, Hinshaw A, et al. Combination transarterial chemoembolization and microwave ablation improves local tumor control for 3- to 5-cm hepatocellular carcinoma when compared with transarterial chemoembolization alone. *Abdom Radiol (NY).* 2018;43(9):2497-2504. [\[Crossref\]](#)

31. Zhu ZY, Qian Z, Qin ZQ, et al. Effectiveness and safety of sequential transarterial chemoembolization and microwave ablation for subphrenic hepatocellular carcinoma: a comprehensive evaluation. *World J Gastrointest Oncol.* 2024;16(7):2941-2951. [\[Crossref\]](#)



Factors influencing diagnostic yield and complication risk in computed tomography fluoroscopy-guided lung biopsies: a 10-year single-center study

✉ Nabeel Mansour¹
 ✉ Hannah Gildein¹
 ✉ Frederik F. Strobl²
 ✉ Osman Öcal^{1,3}
 ✉ Tobias Geith⁴
 ✉ Daniel Puhr-Westerheide¹
 ✉ Matthias Stechele¹
 ✉ Sinan Deniz¹
 ✉ Muzaffer R. Ümütlu¹
 ✉ Nicola Fink¹
 ✉ Dirk Mehren¹
 ✉ Moritz Wildgruber¹
 ✉ Max Seidensticker¹
 ✉ Maximilian F. Reiser¹
 ✉ Jens Ricke¹
 ✉ Philipp M. Paprottka^{4#}
 ✉ Matthias P. Fabritius^{1#}

¹LMU University Hospital, LMU Munich, Department of Radiology, Munich, Germany

²DIE RADIOLOGIE, Munich, Germany

³Heidelberg University Hospital, Department of Diagnostic and Interventional Radiology, Heidelberg, Germany

⁴University Hospital Klinikum Rechts Der Isar TUM, School of Medicine, Technical University of Munich, Department of Interventional Radiology, Munich, Germany

#Contributed equally

Corresponding author: Nabeel Mansour

E-mail: Nabeel.Mansour@med.uni-muenchen.de

Received 04 June 2025; revision requested 12 July 2025; accepted 28 July 2025.



Epub: 11.09.2025

Publication date: 02.01.2026

DOI: 10.4274/dir.2025.253496

PURPOSE

Computed tomography fluoroscopy (CTF)-guided biopsy is an established technique for sampling pulmonary lesions, particularly with the growing prevalence of lung nodule screening programs. This study investigated procedural and lesion-related factors affecting success and complication rates in routine CTF-guided lung core-needle biopsies at a tertiary center.

METHODS

Consecutive patients undergoing percutaneous CTF-guided lung biopsies over a 10-year period (2007–2016) were retrospectively analyzed. Data collected included lesion characteristics, procedural details, and outcomes, including technical and clinical success and complications. Multivariable logistic regressions were used to identify predictors of complications and biopsy failure.

RESULTS

Among 641 patients (43% female; median age 67 years) with a median lesion size of 3.1 cm, technical and clinical success rates were 99% and 93%, respectively. Clinical success was associated with multiple pulmonary lesions and longer specimen length, with multivariable analysis identifying multiple lesions as the sole independent predictor [odds ratio (OR): 2.4]. Major complications (n = 70, 11%), primarily pneumothorax (n = 62, 90%), were associated with a longer intrapulmonary needle tract, greater pleura-to-lesion distance, smaller lesion size, fissure crossing, and the presence of emphysema or subpleural air cysts. Multivariable analysis identified smaller lesion size (OR: 0.8) and greater pleura-to-lesion distance (OR: 1.5) as independent risk factors.

CONCLUSION

CTF-guided lung biopsy is a safe and effective method for tissue sampling with high diagnostic success rates. Although multiple samples do not increase the risk of major complications, factors such as small lesion size, greater pleura-to-lesion distance, and emphysema-related changes are associated with a higher incidence of pneumothorax, emphasizing the need for risk-aware procedural planning.

CLINICAL SIGNIFICANCE

CTF-guided lung biopsy demonstrates high diagnostic performance in routine practice. Understanding how specific anatomical features influence complication risk can guide radiologists in selecting safer biopsy approaches, especially in patients undergoing evaluation through lung cancer screening programs. Integrating these risk factors into procedural planning supports more informed, patient-centered decision-making in routine clinical practice.

KEYWORDS

Biopsy, computed tomography, fluoroscopy, interventional, lung

You may cite this article as: Mansour N, Gildein H, Strobl FF, et al. Factors influencing diagnostic yield and complication risk in computed tomography fluoroscopy-guided lung biopsies: a 10-year single-center study. *Diagn Interv Radiol.* 2026;32(1):104-114.

Lung cancer remains the leading cause of cancer-related deaths worldwide, accounting for the highest mortality among both men and women.¹ Low-dose computed tomography (CT) screening has been shown to reduce mortality significantly in high-risk populations, as demonstrated by the National Lung Screening Trial and confirmed by European randomized trials.²⁻¹⁰ The widespread adoption of CT imaging, both for screening and routine diagnostics, has led to a marked increase in the detection of pulmonary nodules, including incidental findings in asymptomatic patients.¹¹⁻¹⁴

Recent advancements in imaging technology and artificial intelligence have improved the detection and characterization of these nodules. However, accurate diagnosis and timely intervention remain essential, particularly as early and minimally invasive approaches are increasingly favored.¹⁵⁻¹⁷ At the same time, the rise of precision oncology and molecular profiling has shifted clinical focus toward targeted therapies based on tumor genetics.¹⁸ This shift has increased demand for larger and repeated biopsy samples to assess histologic transformation, tumor heterogeneity, and resistance mutations.¹⁸⁻²² Evidence suggests that obtaining at least three core samples optimizes diagnostic yield, and four or more enhances the accuracy of next-generation sequencing.²³

Percutaneous transthoracic needle biopsy (PTNB) is widely used for evaluating pulmonary nodules that are inaccessible via a transbronchial route. Both CT and CT fluoroscopy (CTF) guidance are common techniques, especially for small or deep lesions.^{24,25} Among

these, CTF offers real-time imaging with continuous needle visualization, improving targeting accuracy and reducing procedure time compared with conventional stepwise CT guidance.²⁶⁻²⁸ These advantages are further supported by the radiologist's presence during the procedure, allowing immediate adjustments as needed. However, the benefits of CTF must be balanced against increased radiation exposure to both patients and operators, as well as the need for specialized training and equipment.

Despite its established safety and diagnostic performance, there remains a limited understanding of how clinical and procedural variables influence outcomes and complication rates in routine CTF-guided lung biopsies. This study aims to address this gap by evaluating a heterogeneous patient cohort, encompassing a range of needle sizes, procedural techniques, and lesion characteristics.

Methods

Patients

A retrospective analysis was conducted on all patients who underwent routine CTF-guided core-needle lung biopsies at the LMU University Hospital between 2007 and 2016. Each case had been previously reviewed by a multidisciplinary team comprising oncologists, radiation oncologists, surgeons, and interventional radiologists to assess the clinical indications in accordance with the guidelines for radiologically guided lung biopsies.²⁹ Pre-biopsy imaging, including CT, positron emission tomography/CT, or magnetic resonance imaging, was assessed to evaluate the feasibility of the transthoracic biopsy procedure. In some cases, patients had undergone previous unsuccessful histological sampling via transbronchial needle aspiration. Patients undergoing lung biopsy were initially identified retrospectively through hospital procedural scheduling and billing systems, which captured all planned and completed CTF-guided lung biopsies during the study period. Excluded cases were identified during the data curation process and were removed due to incomplete or missing key data elements, including biopsy outcome, complication documentation, or procedural imaging. These exclusions were not based on cancelled or declined biopsies but rather on documentation gaps that precluded reliable inclusion in the analysis. Informed consent was obtained at least 24 hours before the procedure, following a comprehensive explanation of the procedure and its potential complications. Pre-procedural

evaluations included serum creatinine level, platelet count, and coagulation parameters. Anticoagulation medications were discontinued before the biopsy, following the Society of Interventional Radiology (SIR) Guidelines.³⁰ All procedures in this study were conducted in accordance with the institutional ethics board of the Ludwig Maximilian University of Munich (protocol number: IRB 17-410, date: 28.06.2017) according to the Declaration of Helsinki.

Data collection

Data extracted from medical records and images included information on patient positioning, access point, the use of a coaxial technique or direct puncture, needle size, the size and location of the targeted lesion, various needle tract measurements, the presence of solitary or multiple lesions, and biopsy outcomes, including the number and length of the obtained specimens. Additionally, lung parenchymal changes, such as emphysema, air cysts, or fibrotic alterations, were retrospectively assessed on pre-procedural CT images and categorized as absent, emphysema/air cyst, or fibrosis. The density of the planned biopsy tract was also measured in Hounsfield units (HU) by averaging the attenuation at the midpoint of the needle path on non-contrast CT.

The number of pleural passes, however, was not systematically recorded and could not be reliably extracted from procedural documentation. Although the specimen count was used as a surrogate in some analyses, it does not always reflect the actual number of pleural entries. In direct puncture cases, multiple specimens may be obtained through a single pass, whereas in coaxial procedures, additional entries may occur despite a typically single-access approach. To assess procedure-associated complications, an experienced interventional radiologist with >8 years of expertise reviewed all CT images obtained during the procedures. Additionally, patient records were reviewed to document complications occurring during the procedure that were not identifiable on imaging alone or within the 30-day post-procedural period.

Biopsy procedures

All procedures were performed on multi-detector CT scanners with fluoroscopy mode, including primarily 128-slice systems (Definition Edge, Definition AS, and Flash, Siemens Healthineers, Erlangen, Germany; Optima CT660 and Discovery, GE Healthcare,

Main points

- Computed tomography fluoroscopy-guided lung biopsy is a highly effective technique, achieving a clinical success rate of 93% and technical success rate of 99% in a large, real-world cohort.
- The procedure is safe, with major complications occurring in only 11% of cases—most commonly treatable pneumothorax requiring chest tube placement.
- Small lesion size and greater pleura-to-lesion distance are the strongest predictors of complications and should be considered when planning biopsies.
- Taking multiple tissue samples does not increase complication rates.
- The presence of multiple pulmonary lesions significantly improves diagnostic success, offering flexibility in selecting the most accessible or safest target.

Waukesha, USA), which together accounted for 619 procedures. Additionally, two 16-slice systems (Sensation 16 and Emotion/Aura, Siemens Healthineers) were used in 22 procedures. Scanning parameters typically included 10–20 mAs and 120 kV. The procedures were performed by a board-certified interventional radiologist with ≥ 6 years of experience or a radiology resident in years 3–5 under the supervision of a board-certified radiologist. Operator experience was categorized based on this documentation—either as procedures performed by certified specialists or supervised residents—and used for subgroup analysis. For planning and monitoring, an online dose modulation system (CareDOSE 4D, Siemens Medical Solutions, Forchheim, Germany) was used, adjusting tube current to patient anatomy within ranges of 80–120 kV and 100–200 mAs. A non-contrast-enhanced planning CT determined the lesion's size and optimal approach. The true-cut biopsy system's diameter and length were selected based on individual lesion characteristics (13–18 gauge). These included lesion depth from the pleural surface, overall puncture length, and suspected lesion composition, such as necrosis or firmness indicative of fibrosis or malignancy, as assessed on prior imaging. A semi-automatic spring-loaded cutting needle system was used for all procedures. Patient positioning (supine, prone, or lateral) was adjusted according to the planned access trajectory. Key considerations for the needle approach included avoiding fissures, selecting the shortest path from the visceral pleura to the lesion, steering clear of vessels and bronchi, and positioning the lesion dependently. Following skin disinfection, sterile draping, and the administration of local anesthesia (2% Scandicain, AstraZeneca, London, UK), a small skin incision was made. Under CTF guidance, the coaxial needle (for coaxial approaches) or the biopsy needle (for direct punctures) was intermittently advanced toward the lesion until proper positioning was achieved. Between one and five true-cut samples were collected, fixed in formalin, and sent to the pathology department for histological analysis. A post-procedure unenhanced CT was obtained to check for complications. Each needle pass through the lung parenchyma was documented with fluoroscopic images saved to the picture archiving and communication system. Patients with small, asymptomatic pneumothorax or intrapulmonary hemorrhage received conservative treatment (case example: see Figure 1). If no pneumothorax was detected on CT, patients were observed clinically for 2 hours, with radiography performed only if symptoms developed.

Technical and histopathological results

Procedures were considered technically successful if at least one histological sample of the target was obtained. Cases where tissue type, tumor grade in case of malignancy, and a definitive histopathological diagnosis of the lesion could be established were classified as clinically successful. Samples containing insufficient tissue for histologic diagnosis were documented and classified as technically successful but clinically unsuccessful.

Complications

Peri-procedural complications were classified as major or minor based on the SIR Guidelines.^{31,32} Minor complications were defined as events with no lasting sequelae, requiring minimal therapy or brief hospital observation, such as pneumothorax not requiring intervention, localized pulmonary hemorrhage (ground-glass opacity), or short episodes of hemoptysis. Major complications included events leading to hospitalization (for outpatients), unplanned escalation of care, prolonged hospitalization, permanent sequelae, or death.

Effective patient dose

For each procedure, the effective patient radiation dose was calculated. The effective dose was determined by summing the doses from the pre-procedural planning CT, all intra-procedural CT fluoroscopic acquisitions, and the post-procedural CT, as recorded in the CT examination protocol. Effective doses for the planning CT scan and post-procedural control CT scan were calculated using the formula ($E = DLP \times t$), where E is the effective dose, DLP is the dose length product, and t is the tissue weighting factor. The tissue weighting factor for the chest region was defined as $t = 0.0147$.³³ The effective dose for the sum of all CTF acquisitions was calculated using the adjusted formula for CTF ($E = DLP \times k$), with $k = 0.018 \text{ mSv} / (\text{mGy.cm})$ for chest imaging radiation. As over 95% of procedures were performed on 128-slice CT systems, dose calculations were mainly based on these systems, and data from 16-slice systems were not analyzed.

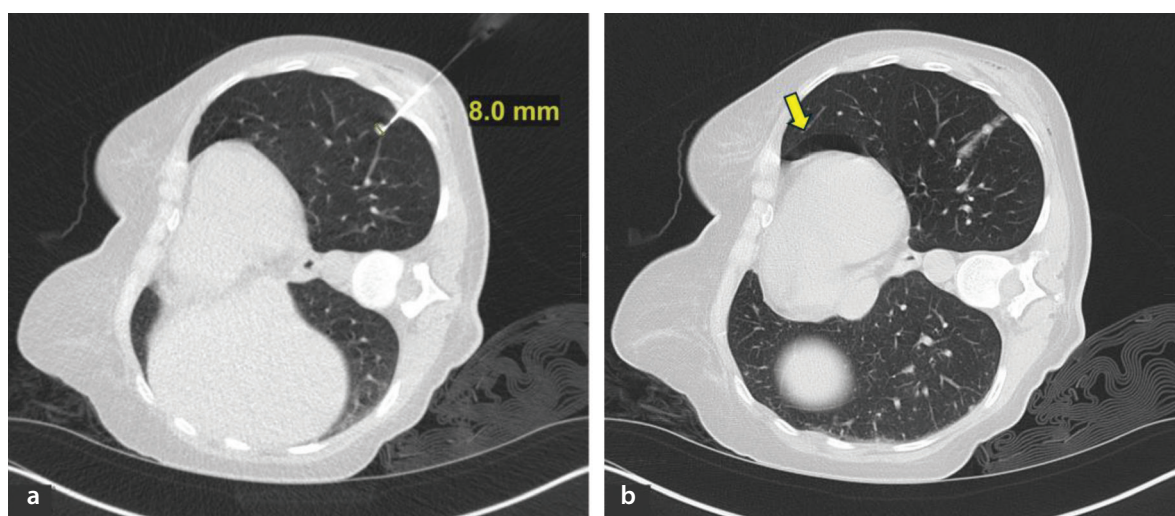


Figure 1. Computed tomography (CT) fluoroscopy-guided lung biopsy of an 8 mm nodule in the left lower lobe in a female patient with suspected recurrence of ovarian carcinoma. (a) Fluoroscopic image during the procedure, performed with the patient in the right lateral decubitus position using an 18G semi-automatic spring-loaded cutting needle system. (b) Post-procedural CT scan showing minor hemorrhage at the puncture site and a small ventral pneumothorax (yellow arrow), both of which were successfully managed conservatively.

separately due to their minimal representation.

Statistical analysis

Data analysis was performed using R software (version 4.4.1). Descriptive statistics, including medians with interquartile ranges (IQRs) and means with standard deviations, were calculated to summarize the data. The Mann-Whitney U test was applied to compare medians between two independent groups. Univariable and multivariable regression analyses were conducted to identify factors associated with clinical outcomes. Multivariable binary logistic regressions were performed, including baseline covariates with $P < 0.05$ in univariate analysis, as well as sex, age, and occasionally other variables of clinical interest, even if they did not reach statistical significance in univariate analysis. Variables not meeting these criteria (e.g., needle size for clinical success or major complication) were excluded from the respective multivariable models. In cases of collinearity, only one of the correlated variables was included in the multivariable model to ensure robustness. A P value of <0.05 was considered statistically significant.

Results

Patient characteristics

A total of 641 patients were included in the study (Table 1). Of these, 365 (57%) were male and 276 (43%) were female, with a median age of 67 years (IQR: 59–73 years). Emphysematous or cystic lung changes were present in 363 cases (56.7%), representing the predominant pattern among patients with parenchymal abnormalities, whereas fibrotic changes were observed in only 10

cases (1.6%). Patients had solitary lesions in 52.3% of cases and multiple lesions in 47.7%.

Procedural characteristics

Technical success was achieved in 638 out of 641 procedures (99%), with only three instances of technical failure. Clinical biopsy success was achieved in 593 (93%) cases. The median fluoroscopy time was 7 minutes (IQR: 4–11 minutes). General anesthesia was required in 2% of cases, and the remainder were conducted under local anesthesia. Procedures were almost evenly performed by the two groups of radiologists (53% by an attending and 47% by a resident radiologist). A total of 575 (90%) biopsies were performed using direct puncture and 66 (10%) using the coaxial technique. The overall needle tract from skin to the lesion was 7.7 cm (IQR: 6.2–9.5 cm), with a corresponding intrapulmonary needle tract length of 3.3 cm (IQR: 2.3–4.6 cm). The median shortest pleura-to-lesion distance was 0.8 cm (IQR: 0–2.1 cm). The maximal lesion diameter was 3.1 cm (IQR: 1.9–5.3 cm) and did not differ significantly between clinically successful and failed biopsies (3.22 vs. 2.57 cm, $P = 0.11$). The smallest successfully biopsied lesion measured 0.5 cm, and the largest reached 17.8 cm. Juxtapleural lesions were present in 47% of cases. The median number of specimens acquired during a procedure was 2 (range: 1–5), and the median specimen length was 14 mm (IQR: 8–24 mm). Needle size was documented in 605 procedures, with an 18G needle being the most used (491 cases, 81%), followed by a 16G needle (107 cases, 18%) and larger needles (13–14G) in a small subset (6 cases, 1%). The median total effective dose was 7.5 mSv (IQR: 5.6–10.1 mSv), with a median fluoroscopy-specific dose of 0.7 mSv (IQR: 0.4–1.2 mSv).

Pathology analysis

Histological analysis of the 593 clinically successful biopsies confirmed malignancy in 468 cases (79%). In the remaining 125 cases (21%), malignancy was excluded. Among the malignant cases, adenocarcinoma was identified in 207 cases (35%), squamous cell carcinoma in 84 cases (14%), and other tumor entities in 177 cases (30%). Technical failure occurred in 3 cases (0.5%) due to the absence of material.

Parameters influencing clinical biopsy success

The univariable analysis identified several factors significantly associated with clinical success (Table 2), including the use of coaxial technique (11% vs. 2.1%, $P = 0.049$), the presence of multiple pulmonary lesions (47% vs. 27%, $P = 0.007$), a longer specimen length (14 mm vs. 9 mm, $P = 0.013$), and a narrower angle of entry observed in the failure cohort (57° vs. 68°, $P = 0.034$). Although the acquisition of at least three specimens showed a numerical difference (27% vs. 19%), the association was not statistically significant ($P = 0.2$). In multivariable analysis, only the presence of multiple pulmonary lesions remained significantly associated with clinical biopsy success [odds ratio (OR): 2.4, 95% confidence interval (CI): 1.1–5.1, $P = 0.020$]. Lung parenchymal changes (emphysema, air cysts, or fibrosis) were not significantly associated with clinical biopsy success ($P = 0.52$, chi-squared test). Similarly, attenuation values along the puncture tract showed no significant difference between clinically successful and failed procedures (median –857.0 vs. –855.5 HU, $P = 0.77$, Wilcoxon rank-sum test).

Complications

The most common complication was pneumothorax, occurring in 227 (35%) patients, followed by superficial puncture site bleeding ($n = 46$; 7%) and mild hemothorax ($n = 7$; 1%). Less frequent complications included systemic effects of local anesthetic ($n = 1$), transient unconsciousness ($n = 1$), and pleural effusion ($n = 1$). There were no instances of air embolism in the cohort. When stratified by complication grade, 379 patients (59%) had no complications (Grade 0), whereas 192 patients (30%) experienced minor complications (Grade 1), collectively representing 571 cases (89%) with no major complications. Major complications requiring direct intervention or prolonged hospital stay (Grade 2) occurred in 70 cases (11%). The most common was pneumothorax, affecting

Table 1. Patient characteristics

Parameter	Frequency n (%)	Median (interquartile range)
Patients	641 (100%)	
Sex		
Male	365 (57%)	
Female	276 (43%)	
Age (years)		67 (59, 73)
Clinical biopsy success	593 (93%)	
Targeted lesion size (cm)		3.1 (1.9, 5.3)
Entity		
Malignant	468 (79%)	
Non-malignant	125 (21%)	
Total effective radiation dose (mSv)		7.5 (5.6, 10.1)
Effective radiation dose from fluoroscopy (mSv)		0.7 (0.4, 1.2)

Table 2. Univariable and multivariable analyses for clinical success

Parameter	Univariate analysis			Multivariate analysis	
	Failure n = 45 ¹	Success n = 593 ¹	P value ²	P value ³	Odds ratio (95% CI)
Sex					
Male	23 (48%)	342 (58%)	0.2	0.454	0.8 (0.4–1.5)
Female	25 (52%)	251 (42%)			
Age (years)	64 (59, 69)	67 (59, 74)	0.017*	0.252	1.0 (1.0–1.0)
Targeted lesion size (cm)	2.6 (1.7, 4.7)	3.2 (1.9, 5.5)	0.11		
Number of pulmonary lesions					
Solitary	35 (73%)	313 (53%)	0.007*	0.020*	2.4 (1.1–5.1)
Multiple	13 (27%)	280 (47%)			
Lung changes					
No changes	15 (34%)	249 (42%)			
Emphysema/air cysts	28 (64%)	336 (57%)	0.087		
Fibrosis	2 (2%)	8 (1%)			
Targeted lesion location					
Apical	22 (46%)	225 (38%)			
Mid	13 (27%)	250 (42%)	0.12		
Basal	13 (27%)	118 (20%)			
Juxtapleural lesion location	23 (48%)	280 (47%)	>0.9		
Hounsfield units of puncture tract	–856 (–883, –830)	–857 (–889, –817)	0.43		
Patient positioning					
Prone	25 (52%)	284 (48%)			
Supine	15 (31%)	207 (35%)	0.8		
Side	8 (17%)	102 (17%)			
Access point					
Ventral	4 (8.3%)	90 (15%)			
Dorsal	27 (56%)	327 (55%)	0.4		
Lateral	17 (35%)	176 (30%)			
Coaxial technique	1 (2.1%)	65 (11%)	0.049		
Overall needle tract (cm)	8.4 (5.9, 9.6)	7.6 (6.2, 9.5)	>0.9		
Intrapulmonary needle tract (cm)	2.9 (1.8, 4.1)	3.3 (2.4, 4.6)	0.032*	0.523	1.1 (0.9–1.3)
Shortest pleura-to-lesion distance (cm)	1.1 (0.0, 2.3)	0.8 (0.0, 2.1)	0.5		
Angle pleura/needle (degrees)	57 (41, 78)	68 (52, 80)	0.034*	0.237	1.0 (1.0–1.0)
Fissure crossing	0 (0%)	33 (5.6%)	0.2		
Length of procedure (fluoroscopy time in minutes)	9.0 (5.5, 12.0)	7.0 (4.0, 11.0)	0.058		
Needle size (gauge)					
13	0 (0%)	3 (0.5%)			
14	0 (0%)	3 (0.5%)			
16	6 (13%)	101 (18%)	0.7		
17	0 (0%)	1 (0.2%)			
18	42 (88%)	449 (81%)			
Not documented	36	0			
Intervening radiologist					
Attending	25 (52%)	274 (47%)			
Resident	23 (48%)	308 (53%)	0.5		
Not documented	0	11			
Number of specimens					
<3	39 (81%)	432 (73%)	0.2		
≥3	9 (19%)	161 (27%)			
Overall length of biopsy specimen (mm)	9 (4, 20)	14 (8, 25)	0.013*	0.103	1.0 (1.0–1.1)
Not documented	11	89			

¹Median (interquartile range); n (%).²Wilcoxon rank sum test; Pearson's chi-squared test.³Multivariable logistic regression model.

*Indicates a P value < 0.05; CI, confidence interval.

63 (90%) patients, all of whom required chest tube placement. Two patients with bleeding into the thoracic cavity and 3 patients with parenchymal hemorrhage required a prolonged hospital stay with close monitoring but no surgical or angiographic intervention. Systemic effects of the local anesthetic were observed in 1 patient. Notably, 1 patient experienced active arterial bleeding from a peripheral left pulmonary artery, which was successfully managed with angiographic coil embolization. The resulting hemothorax was drained with two large chest tubes, which were removed after 8 days. The patient was discharged 29 days after the embolization procedure. Importantly, there were no instances of periprocedural mortality among the patients. Complication rates were compared between the two biopsy techniques; major complications occurred in 11.6% of direct puncture cases and 4.5% of coaxial cases, though this difference was not statistically significant ($P = 0.122$, chi-squared test). This analysis is limited by the substantial imbalance in group sizes, with coaxial cases comprising only approximately 10% of the cohort. Additionally, patients with emphysema or air cysts were significantly more likely to develop pneumothorax than those without lung parenchymal changes (46% vs. 20%, $P < 0.0001$, chi-squared test). The presence of fibrotic changes was infrequent and did not show a significant association with pneumothorax. Furthermore, the HU values of the biopsy tract were significantly lower in patients who developed pneumothorax than in those who did not (median -876 HU vs. -846 HU, $P < 0.0001$, Wilcoxon rank-sum test), suggesting that a less dense parenchymal trajectory may contribute to increased vulnerability to post-procedural air leaks.

Parameters associated with major complications

The analysis identified several factors significantly associated with major complications (Table 3). Univariable analysis revealed procedural factors, such as a longer intrapulmonary needle tract (3.9 cm vs. 3.2 cm, $P = 0.004$) and fissure crossing (11% vs. 4.4%, $P = 0.02$). Anatomical contributors included a greater pleura-to-lesion distance (1.8 cm vs. 0.6 cm, $P < 0.001$) and smaller lesion size (2.4 cm vs. 3.3 cm, $P < 0.001$). Multivariable analysis identified independent predictors of major complications; male sex (OR: 0.4, 95% CI: 0.2–0.7, $p = 0.002$) and smaller lesion size (OR: 0.8, 95% CI: 0.6–0.9, $P = 0.002$) were significantly associated with an elevated risk, whereas a greater pleura-to-lesion distance

further increased the likelihood of complications (OR: 1.5, 95% CI: 1.1–2.2, $P = 0.016$). Other variables, including access points and overall specimen length, were not significantly associated with major complications. Further multivariable regression analysis identified distinct risk factors for pneumothorax occurrence (Table 4): a longer intrapulmonary needle tract was significantly associated with a higher likelihood of pneumothorax (OR: 1.5, 95% CI: 1.1–1.9, $P = 0.003$), as well as biopsies involving fissure crossing (OR: 4.4, 95% CI: 1.2–16.3, $P = 0.021$). Additionally, smaller lesion size significantly increased the risk of pneumothorax, with each 1 cm increase in lesion size reducing the odds (OR: 0.7, 95% CI: 0.6–0.8, $P < 0.0001$).

Discussion

In this retrospective study of 641 patients who underwent CTF-guided lung core-needle biopsies, the complication rates were consistent with previously reported findings, with pneumothorax being the most common complication (35%).^{34–36} Most complications (89%) were minor, necessitating no additional treatment and causing no extended hospital stays. Importantly, major complications, though infrequent, were promptly managed without serious adverse outcomes, highlighting the safety of this diagnostic approach in routine clinical practice.

Prior studies have demonstrated that small lesion size is an independent risk factor for pneumothorax, with up to an 11-fold increased risk for lesions ≤ 2 cm in diameter.^{37–39} Consistent with these findings, lesion size was also a significant determinant of major complications in this study (OR: 0.8). Smaller lesions were linked to a higher incidence of complications requiring therapeutic intervention, primarily pneumothorax necessitating chest tube placement. Furthermore, several well-established risk factors for pneumothorax were confirmed in this analysis.³⁴ These include a greater pleura-to-lesion distance (OR: 1.5), a longer intrapulmonary needle tract (OR: 1.5), and fissure crossing (OR: 4.4). Pleura-to-lesion distance and intrapulmonary needle tract length are strongly interrelated, as a deeper lesion naturally results in a longer tract. Their individual statistical associations likely reflect a compounded effect of target depth on complication risk, rather than fully independent predictors. Interestingly, male sex (OR: 0.4) also emerged as a risk factor for pneumothorax in our cohort. Although the underlying reason is not entirely clear, this association may reflect underlying confounding factors. Emphysema

and subpleural air cysts—both associated with increased pneumothorax risk—are more prevalent among older male patients, likely due to higher historical smoking rates. In line with this, we found a significant correlation between parenchymal fragility (i.e., emphysema/air cysts) and pneumothorax occurrence. Thus, the observed sex-based difference may reflect a greater burden of structural lung changes rather than a direct effect of sex alone. Procedural variables, such as patient positioning, access point, and pleura-to-needle angle, were analyzed. Although often constrained by anatomical feasibility, they define the procedural geometry and may indirectly influence complication risk. In our cohort, dorsal and lateral approaches were most common, reflecting a preference for minimizing tract length and avoiding fissures or major vessels. Although not always modifiable, understanding their associations with outcomes remains relevant for procedural planning. Notably, pleura-to-lesion distance and intrapulmonary needle tract length, though related, are distinct; the former represents the shortest linear distance, whereas the latter reflects the actual needle trajectory chosen by the operator. This path may be angled or extended to avoid ribs or vascular structures, even in superficially located lesions.

A strength of this study is the inclusion of a large, unselected real-world cohort encompassing all lung lesions requiring biopsy, not just those with a high suspicion of a specific malignancy. This broad inclusion enhances generalizability and reflects clinical practice more accurately than studies limited to specific entities. Notably, the use of larger biopsy needles (13–18 gauge) and the acquisition of multiple samples (≥ 3) achieved high diagnostic success rates without increasing procedural complications, demonstrating the safety and effectiveness of this approach. However, it is important to note that only three procedures each were performed using 13G and 14G needles. Upon review, these cases involved large, mainly necrotic and pleura-adjacent lesions where a higher tissue yield was clinically justified. Given the small number of cases, no statistically meaningful conclusions can be drawn regarding the safety of these large-gauge needles, and these findings should be interpreted with caution. Additionally, longer biopsy specimens significantly improved diagnostic success without elevating the risk of major complications, consistent with findings from recent studies.^{40,41} A recent large cohort study by Kim et al.⁴² ex-

Table 3. Univariable and multivariable analyses for major complications

Parameter	Univariate analysis			Multivariate analysis	
	No n = 571 ¹	Yes n = 70 ¹	P value ²	P value ³	Odds ratio (95% CI)
Sex			0.002*	0.002*	0.4 (0.2–0.7)
Male	313 (55%)	52 (74%)			
Female	258 (45%)	18 (26%)			
Age (years)	67 (59, 74)	68 (60, 73)	0.7	0.316	1.0 (1.0–1.0)
Targeted lesion size (cm)	3.3 (2.0, 5.5)	2.4 (1.6, 3.1)	<0.001*	0.002*	0.8 (0.6–0.9)
Number of pulmonary lesions			0.4	0.273	0.7 (0.4–1.3)
Solitary	307 (54%)	41 (59%)			
Multiple	264 (46%)	29 (41%)			
Targeted lesion location			0.6		
Apical	221 (39%)	26 (37%)			
Mid	231 (40%)	32 (46%)			
Basal	119 (21%)	12 (17%)			
Juxtapleural lesion location	292 (51%)	11 (16%)	<0.001*		
Patient positioning			0.14		
Prone	283 (50%)	26 (37%)			
Supine	193 (34%)	29 (41%)			
Side	95 (17%)	15 (21%)			
Access point			0.011		
Ventral	86 (15%)	8 (11%)			
Dorsal	324 (57%)	30 (43%)			
Lateral	161 (28%)	32 (46%)			
Coaxial technique	63 (11%)	3 (4.3%)	0.08	0.225	0.4 (0.1–1.7)
Overall needle tract (cm)	7.6 (6.2, 9.4)	8.4 (6.4, 10.0)	0.12		
Intrapulmonary needle tract (cm)	3.2 (2.3, 4.5)	3.9 (3.1, 5.4)	0.004	0.53	0.9 (0.7–1.2)
Shortest pleura-to-lesion distance (cm)	0.6 (0.0, 1.9)	1.8 (1.10, 3.0)	<0.001*	0.016*	1.5 (1.1–2.2)
Angle pleura/needle (degrees)	67 (51, 80)	62 (49, 79)	0.3		
Fissure crossing	25 (4.4%)	8 (11%)	0.02	0.064	2.9 (0.9–8.8)
Length of procedure (fluoroscopy time in minutes)	7.0 (4.0, 11.0)	7.0 (3.0, 12.0)	>0.9		
Needle size (gauge)			0.4		
13	3 (0.6%)	0 (0%)			
14	3 (0.6%)	0 (0%)			
16	100 (19%)	7 (10%)			
17	1 (0.2%)	0 (0%)			
18	428 (80%)	63 (90%)			
Not documented	36	0			
Intervening radiologist			0.8		
Attending	267 (48%)	32 (46%)			
Resident	294 (52%)	37 (54%)			
Not documented	10	1			
Number of specimens			0.3		
<3	416 (73%)	55 (79%)			
≥3	155 (27%)	15 (21%)			
Overall length of biopsy specimen (mm)	14 (8, 25)	10 (6, 17)	<0.001*	0.388	1.0 (1.0–1.0)
Not documented	94	6			

¹Median (interquartile range); n (%).²Wilcoxon rank sum test; Pearson's chi-squared test.³Multivariable logistic regression model.

*Indicates a P value < 0.05; CI, confidence interval.

Table 4. Univariable and multivariable analyses for pneumothorax

Parameter	Univariate analysis		Multivariate analysis	
	No n = 414 ¹	Yes n = 227 ¹	P value ²	P value ³
Sex			0.3	0.156
Male	230 (56%)	135 (59%)		0.7 (0.4–1.2)
Female	184 (44%)	92 (41%)		
Age (years)	66 (59, 73)	68 (60, 74)	0.022*	0.207
Targeted lesion size (cm)	3.8 (2.3, 6.1)	2.5 (1.6, 3.8)	<0.001*	<0.001*
Number of pulmonary lesions			0.9	0.7 (0.6–0.8)
Singular	224 (54%)	124 (55%)		
Multiple	190 (46%)	103 (41%)		
Lung changes			<0.001*	
No changes	214 (52%)	54 (24%)		
Emphysema/air cysts	194 (47%)	169 (74%)		
Fibrosis	6 (1%)	4 (2%)		
Targeted lesion location			0.02*	
Apical	176 (43%)	71 (31%)		
Mid	158 (38%)	105 (46%)		
Basal	80 (19%)	51 (22%)		
Juxtapleural lesion location	256 (62%)	47 (21%)	<0.001*	
Hounsfield units of puncture tract	–846 (–880, –806)	–876 (–897, –847)	<0.001*	
Patient positioning			0.8	
Prone	201 (49%)	108 (48%)		
Supine	234 (57%)	120 (53%)		
Side	114 (28%)	79 (35%)		
Access point			0.12	
Ventral	66 (16%)	28 (12%)		
Dorsal	234 (57%)	120 (53%)		
Lateral	114 (28%)	79 (35%)		
Coaxial technique	41 (9.9%)	25 (11%)	0.7	
Overall needle tract (cm)	7.6 (6.2, 9.3)	7.9 (6.4, 9.9)	0.06	
Intrapulmonary needle tract (cm)	3.0 (2.0, 4.2)	3.8 (2.9, 5.3)	<0.001*	0.004*
Shortest pleura-to-lesion distance (cm)	0.0 (0.0, 1.5)	1.6 (0.7, 3.0)	<0.001*	0.153
Angle pleura/needle (degrees)	67 (51, 81)	67 (52, 80)	0.8	
Fissure crossing	9 (2.2%)	24 (11%)	<0.001	0.021*
Length of procedure (fluoroscopy time in minutes)	7.0 (4.0, 10.0)	7.0 (4.0, 11.0)	>0.9	4.4 (1.2–16.3)
Needle size (gauge)			0.005*	0.823
13	3 (0.8%)	0 (0%)		1.1 (0.5–2.2)
14	1 (0.3%)	2 (0.9%)		
16	82 (21%)	25 (12%)		
17	1 (0.3%)	0 (0%)		
18	304 (78%)	187 (87%)		
Not documented	23	13		
Intervening radiologist			0.5	
Attending	196 (48%)	103 (46%)		
Resident	209 (52%)	122 (54%)		
Not documented	9	2		
Number of specimens			0.09	
<3	295 (71%)	176 (78%)		
≥3	119 (29%)	51 (22%)		
Overall length of biopsy specimen (mm)	16 (8, 25)	12 (7, 20)	0.004*	0.17
Not documented	69	39		1.0 (1.0–1.0)

¹Median (interquartile range); n (%)²Wilcoxon rank sum test; Pearson's chi-squared test³Multivariable logistic regression model

*Indicates a P value < 0.05; CI, confidence interval.

amined the feasibility of CTF-guided coaxial lung biopsies, focusing on the number of cores acquired. Their findings aligned with ours, contradicting earlier research that suggested an association between the number of coaxial cores and the risk of complications.⁴³ However, a limitation of the study by Kim et al.⁴² is the restriction of inclusion criteria to patients suspected of primary lung cancer, limiting the generalizability of findings. In contrast, our analysis evaluated multiple lesion- and procedure-related variables—including lesion multiplicity, depth, and needle trajectory—providing deeper insight into predictors of success and complications across a wide clinical spectrum.

Interestingly, the presence of multiple pulmonary lesions (OR: 2.4) was the only significant factor associated with clinical success in this study. This finding is reasonable, as the availability of multiple lesions provides the operator with the flexibility to select the most promising target, such as one that is more accessible, larger in size, or located in a safer anatomical position. This strategic choice increases the likelihood of obtaining sufficient tissue for histopathological evaluation, ultimately improving the clinical success rate of the procedure.^{44,45} Remarkably, lesion size itself had no impact on the clinical success rate of biopsies, with even lesions as small as 5 mm successfully targeted and yielding sufficient tissue for histopathological analysis. Additionally, this study provides practical data on the safety of obtaining multiple core samples and employing different needle calibers in routine clinical settings—an area that remains underreported in the current literature.

Equally noteworthy is that the experience level of the performing radiologist did not influence the complication or success rates. This finding suggests that the technique is well-standardized and relatively easy to learn, making it feasible for implementation even in smaller centers with fewer annual procedures.⁴⁶ Nonetheless, maintaining high-quality standards remains crucial to ensure optimal patient outcomes and procedural safety. Radiation exposure to both patients and operators remains a notable drawback of CTF-guided procedures compared with conventional CT-guided approaches.⁴⁷ Nevertheless, fluoroscopy accounted for <10% of the total effective radiation dose during the procedures in this study. Scanner configuration (16-slice vs. 128-slice systems) may influence dose values; given the small proportion of 16-slice cases in this study (<5%), dose calculations are mainly based on the 128-slice systems. This limitation

must be taken into account when interpreting the data. Moreover, advancements in imaging technology are likely to further decrease radiation levels in the future, particularly for procedures in anatomically high-contrast areas, such as the lungs.⁴⁸

A limitation of this analysis is its retrospective, single-center design, which is subject to inherent biases, such as selection bias, and potential inaccuracies in data extraction from medical records. Notably, hemoptysis was not documented in any of the medical records in this cohort. This likely reflects the absence of higher-grade hemoptysis events that could have influenced clinical outcomes but also underscores the limitations of retrospective data collection, where less severe complications may go underreported unless explicitly documented. Similarly, other minor complications that lacked clinical consequences may not have been captured, potentially leading to an underestimation of the overall complication rate. However, major complications requiring intervention were systematically documented through imaging and clinical records, supporting the reliability of safety outcomes. Although hemoptysis is a recognized complication, its clinical relevance appears to be limited, as demonstrated by (among others) a recent study by Kim et al.⁴² (Radiology 2024), where it occurred in 2.4% of patients (20 out of 827) without major events. In addition, the number of pleural penetrations, an intra-procedural factor known to correlate with pneumothorax risk, especially in non-coaxial techniques, was not consistently documented in procedure reports or imaging archives. This reflects another inherent limitation of retrospective data collection, particularly in earlier cases. Although specimen count was used as a surrogate in some analyses, it may not reliably reflect the number of pleural entries. Despite these limitations, this study offers valuable insights into a real-world cohort, providing practical data that enhance and complement the existing literature on CTF-guided lung biopsies.

In conclusion, this study demonstrates that CTF-guided biopsy is a reliable, effective, and safe method for diagnosing pulmonary lesions. Incorporating factors associated with major complications can improve patient selection, procedure planning, and peri-procedural monitoring, thereby enhancing patient safety. These findings are particularly relevant in the era of advanced molecular diagnostics, where obtaining multiple tissue samples is essential for guiding treatment and prognosis. Prospective studies with

standardized procedural annotation could further refine risk prediction and validate these findings in varied practice settings.

Footnotes

Conflict of interest disclosure

The authors declared no conflicts of interest.

References

1. Siegel RL, Miller KD, Wagle NS, Jemal A. Cancer statistics, 2023. *CA Cancer J Clin.* 2023;73(1):17-48. [\[CrossRef\]](#)
2. Adams SJ, Stone E, Baldwin DR, Vliegenthart R, Lee P, Fintelmann FJ. Lung cancer screening. *Lancet.* 2023;401(10374):390-408. [\[CrossRef\]](#)
3. National Lung Screening Trial Research Team; Aberle DR, Adams AM, et al. Reduced lung-cancer mortality with low-dose computed tomographic screening. *N Engl J Med.* 2011;365(5):395-409. [\[CrossRef\]](#)
4. Pinsky PF, Church TR, Izmirlian G, Kramer BS. The National Lung Screening Trial: results stratified by demographics, smoking history, and lung cancer histology. *Cancer.* 2013;119(22):3976-3983. [\[CrossRef\]](#)
5. Horeweg N, van Rosmalen J, Heuvelmans MA, et al. Lung cancer probability in patients with CT-detected pulmonary nodules: a prespecified analysis of data from the NELSON trial of low-dose CT screening. *Lancet Oncol.* 2014;15(12):1332-1341. [\[CrossRef\]](#)
6. Wille MM, Dirksen A, Ashraf H, et al. Results of the randomized Danish lung cancer screening trial with focus on high-risk profiling. *Am J Respir Crit Care Med.* 2016;193(5):542-551. [\[CrossRef\]](#)
7. Paci E, Puliti D, Pegna AL, et al. Mortality, survival and incidence rates in the ITALUNG randomised lung cancer screening trial. *Thorax.* 2017;72(9):825-831. [\[CrossRef\]](#)
8. Pastorino U, Silva M, Sestini S, et al. Prolonged lung cancer screening reduced 10-year mortality in the MILD trial: new confirmation of lung cancer screening efficacy. *Ann Oncol.* 2019;30(7):1162-1169. Erratum in: *Ann Oncol.* 2019;30(10):1672. [\[CrossRef\]](#)
9. Becker N, Motsch E, Trotter A, et al. Lung cancer mortality reduction by LDCT screening—results from the randomized German LUSI trial. *Int J Cancer.* 2020;146(6):1503-1513. [\[CrossRef\]](#)
10. de Koning HJ, van der Aalst CM, de Jong PA, et al. Reduced lung-cancer mortality with volume CT screening in a randomized trial. *N Engl J Med.* 2020;382(6):503-513. [\[CrossRef\]](#)
11. Morgan L, Choi H, Reid M, Khawaja A, Mazzone PJ. Frequency of incidental findings and subsequent evaluation in low-dose computed tomographic scans for lung cancer screening. *Ann Am Thorac Soc.* 2017;14(9):1450-1456. [\[CrossRef\]](#)

12. Jacobs PC, Mali WP, Grobbee DE, van der Graaf Y. Prevalence of incidental findings in computed tomographic screening of the chest: a systematic review. *J Comput Assist Tomogr.* 2008;32(2):214-221. [\[CrossRef\]](#)

13. Tsai EB, Chiles C, Carter BW, et al. Incidental findings on lung cancer screening: significance and management. *Semin Ultrasound CT MR.* 2018;39(3):273-281. [\[CrossRef\]](#)

14. Bach PB, Mirkin JN, Oliver TK, et al. Benefits and harms of CT screening for lung cancer: a systematic review. *JAMA.* 2012;307(22):2418-2429. [\[CrossRef\]](#)

15. Chamberlin J, Kocher MR, Waltz J, et al. Automated detection of lung nodules and coronary artery calcium using artificial intelligence on low-dose CT scans for lung cancer screening: accuracy and prognostic value. *BMC Med.* 2021;19:55. [\[CrossRef\]](#)

16. Cellina M, Cacioppa LM, Cè M, et al. Artificial intelligence in lung cancer screening: the future is now. *Cancers (Basel).* 2023;15(17):4344. [\[CrossRef\]](#)

17. Schreuder A, Scholten ET, van Ginneken B, Jacobs C. Artificial intelligence for detection and characterization of pulmonary nodules in lung cancer CT screening: ready for practice? *Transl Lung Cancer Res.* 2021;10(5):2378-2388. [\[CrossRef\]](#)

18. Folch E, Costa DB, Wright J, VanderLaan PA. Lung cancer diagnosis and staging in the minimally invasive age with increasing demands for tissue analysis. *Transl Lung Cancer Res.* 2015;4(4):392-403. [\[CrossRef\]](#)

19. Piotrowska Z, Isozaki H, Lennerz JK, et al. Landscape of acquired resistance to osimertinib in EGFR-mutant NSCLC and clinical validation of combined EGFR and RET inhibition with osimertinib and BLU-667 for acquired RETfusion. *Cancer discovery.* 2018;8(12):1529-1539. [\[CrossRef\]](#)

20. Gainor JF, Dardaei L, Yoda S, et al. Molecular mechanisms of resistance to first-and second-generation ALK inhibitors in ALK-rearranged lung cancer. *Cancer Discov.* 2016;6(10):1118-1133. [\[CrossRef\]](#)

21. Silk MT, Mikkilineni N, Silk TC, et al. Prospective evaluation of unprocessed core needle biopsy DNA and RNA yield from lung, liver, and kidney tumors: implications for cancer genomics. *Anal Cell Pathol (Amst).* 2018;2018(1):2898962. [\[CrossRef\]](#)

22. Haragan A, Field JK, Davies MPA, Escriu C, Gruver A, Gosney JR. Heterogeneity of PD-L1 expression in non-small cell lung cancer: Implications for specimen sampling in predicting treatment response. *Lung Cancer.* 2019;134:79-84. [\[CrossRef\]](#)

23. Uchimura K, Yanase K, Imabayashi T, et al. The impact of core tissues on successful next-generation sequencing analysis of specimens obtained through endobronchial ultrasound-guided transbronchial needle aspiration. *Cancers (Basel).* 2021;13(23):5879. [\[CrossRef\]](#)

24. Hiraki T, Mimura H, Gobara H, et al. CT fluoroscopy-guided biopsy of 1,000 pulmonary lesions performed with 20-gauge coaxial cutting needles: diagnostic yield and risk factors for diagnostic failure. *Chest.* 2009;136(6):1612-1617. [\[CrossRef\]](#)

25. Nakamura K, Matsumoto K, Inoue C, Matsusue E, Fujii S. Computed tomography-guided lung biopsy: a review of techniques for reducing the incidence of complications. *Interv Radiol (Higashimatsuyama).* 2021;6(3):83-92. [\[CrossRef\]](#)

26. Gianfelice D, Lepanto L, Perreault P, Chartrand-Lefebvre C, Milette PC. Value of CT fluoroscopy for percutaneous biopsy procedures. *J Vasc Interv Radiol.* 2000;11(7):879-884. [\[CrossRef\]](#)

27. Froelich JJ, Ishaque N, Regn J, Saar B, Walther EM, Klose KJ. Guidance of percutaneous pulmonary biopsies with real-time CT fluoroscopy. *Eur J Radiol.* 2002;42(1):74-79. [\[CrossRef\]](#)

28. Kim GR, Hur J, Lee SM, et al. CT fluoroscopy-guided lung biopsy versus conventional CT-guided lung biopsy: a prospective controlled study to assess radiation doses and diagnostic performance. *Eur Radiol.* 2011;21(2):232-239. [\[CrossRef\]](#)

29. Manhire A, Charig M, Clelland C, et al. Guidelines for radiologically guided lung biopsy. *Thorax.* 2003;58(11):920-936. [\[CrossRef\]](#)

30. Patel IJ, Rahim S, Davidson JC, Hanks SE, Tam AL, Walker TG, Wilkins LR, Sarode R, Weinberg I. Society of Interventional Radiology Consensus Guidelines for the Periprocedural Management of Thrombotic and Bleeding Risk in Patients Undergoing Percutaneous Image-Guided Interventions-Part II: Recommendations: Endorsed by the Canadian Association for Interventional Radiology and the Cardiovascular and Interventional Radiological Society of Europe. *J Vasc Interv Radiol.* 2019;30(8):1168-1184. [\[CrossRef\]](#)

31. Gupta S, Wallace MJ, Cardella JF, Kundu S, Miller DL, Rose SC; Society of Interventional Radiology Standards of Practice Committee. Quality improvement guidelines for percutaneous needle biopsy. *J Vasc Interv Radiol.* 2010;21(7):969-975. [\[CrossRef\]](#)

32. Sacks D, McClellan TE, Cardella JF, Lewis CA. Society of Interventional Radiology clinical practice guidelines. *J Vasc Interv Radiol.* 2003;14(9 Pt 2):199-202. [\[CrossRef\]](#)

33. Deak PD, Smal Y, Kalender WA. Multisection CT protocols: sex-and age-specific conversion factors used to determine effective dose from dose-length product. *Radiology.* 2010;257(1):158-166. [\[CrossRef\]](#)

34. Heerink WJ, de Bock GH, de Jonge GJ, Groen HJ, Vliegenthart R, Oudkerk M. Complication rates of CT-guided transthoracic lung biopsy: meta-analysis. *Eur Radiol.* 2017;27(1):138-148. [\[CrossRef\]](#)

35. Ren Q, Zhou Y, Yan M, Zheng C, Zhou G, Xia X. Imaging-guided percutaneous transthoracic needle biopsy of nodules in the lung base: fluoroscopy CT versus cone-beam CT. *Clin Radiol.* 2022;77(5):e394-e399. [\[CrossRef\]](#)

36. Ruud EA, Stavem K, Geitun JT, Borthne A, Søyseth V, Ashraf H. Predictors of pneumothorax and chest drainage after percutaneous CT-guided lung biopsy: a prospective study. *Eur Radiol.* 2021;31(6):4243-4252. [\[CrossRef\]](#)

37. Gohari A, Haramati LB. Complications of CT scan-guided lung biopsy: lesion size and depth matter. *Chest.* 2004;126(3):666-668. [\[CrossRef\]](#)

38. Yeow KM, Tsay PK, Cheung YC, Lui KW, Pan KT, Chou AS. Factors affecting diagnostic accuracy of CT-guided coaxial cutting needle lung biopsy: retrospective analysis of 631 procedures. *J Vasc Interv Radiol.* 2003;14(5):581-588. [\[CrossRef\]](#)

39. Ozturk K, Soylu E, Gokalp G, Topal U. Risk factors of pneumothorax and chest tube placement after computed tomography-guided core needle biopsy of lung lesions: a single-centre experience with 822 biopsies. *Pol J Radiol.* 2018;83:e407-e414. [\[CrossRef\]](#)

40. Huang MD, Weng HH, Hsu SL, et al. Accuracy and complications of CT-guided pulmonary core biopsy in small nodules: a single-center experience. *Cancer Imaging.* 2019;19(1):51. [\[CrossRef\]](#)

41. Tian P, Wang Y, Li L, Zhou Y, Luo W, Li W. CT-guided transthoracic core needle biopsy for small pulmonary lesions: diagnostic performance and adequacy for molecular testing. *J Thorac Dis.* 2017;9(2):333-343. [\[CrossRef\]](#)

42. Kim CR, Sari MA, Grimaldi E, VanderLaan PA, Brook A, Brook OR. CT-guided coaxial lung biopsy: number of cores and association with complications. *Radiology.* 2024;313(2):e232168. [\[CrossRef\]](#)

43. Beck KS, Kim TJ, Lee KY, Kim YK, Kang JH, Han DH. CT-guided coaxial biopsy of malignant lung lesions: are cores from 20-gauge needle adequate for histologic diagnosis and molecular analysis? *J Thorac Dis.* 2019;11(3):753-765. [\[CrossRef\]](#)

44. Saggiante L, Biondetti P, Lanza C, et al. Computed-tomography-guided lung biopsy: a practice-oriented document on techniques and principles and a review of the literature. *Diagnostics (Basel).* 2024;14(11):1089. [\[CrossRef\]](#)

45. Borelli C, Vergara D, Simeone A, et al. CT-guided transthoracic biopsy of pulmonary lesions: diagnostic versus nondiagnostic results. *Diagnostics (Basel).* 2022;12(2):359. [\[CrossRef\]](#)

46. Schmanke KE, Zackula RE, Unruh ZA, Burdick WA, Trent JJ, Ali KM. Resident experience associated with lung biopsy outcomes: a cross-sectional study of diagnostic radiology residents. Does the Level of Training Matter? *Kans J Med.* 2020;13:235-241. [\[CrossRef\]](#)

47. Kim GR, Hur J, Lee SM, et al. CT fluoroscopy-guided lung biopsy versus conventional CT-guided lung biopsy: a prospective controlled study to assess radiation doses and diagnostic performance. *Eur Radiol.* 2011;21(2):232-239. [\[CrossRef\]](#)
48. McCollough CH, Rajiah PS. Milestones in CT: Past, present, and future. *Radiology.* 2023;309(1):e230803. [\[CrossRef\]](#)



Computed tomography-guided irreversible electroporation for a pubic bone metastasis: a technical note and early experience

Claudio Pusceddu¹

Eliodoro Faiella²

Claudio Cau¹

Pierluigi Rinaldi¹

Paolo Cossu³

Salvatore Marsico⁴

¹Mater Olbia Hospital, Clinic of Radiology, Olbia, Italy

²Campus Bio Medico, Department of Radiology, Rome, Italy

³Mater Olbia Hospital, Clinic of Anesthesiology, Olbia, Italy

⁴Hospital del Mar, Clinic of Radiology, Barcelona, Spain

ABSTRACT

Bone metastases are common in advanced solid tumors and often require local control strategies in addition to systemic therapy. Although thermal ablation is an established method for selected lesions, its use may be limited in anatomically complex or heat-sensitive locations. Irreversible electroporation, a non-thermal ablative technique widely used in visceral oncology, has not yet been reported for the treatment of bone metastases.

KEYWORDS

Ablation, bone, interventional, metastases, oncology

Bone metastases are a frequent and challenging complication of advanced malignancies, particularly in patients with breast, prostate, or lung cancer. These lesions often cause severe pain, impaired mobility, and pathological fractures, considerably reducing patients' quality of life and functional autonomy. In the multidisciplinary management of such patients, local tumor control remains a key objective, especially for symptomatic, progressive, or weight-bearing lesions.

Traditional local therapies include external beam radiotherapy, surgical stabilization, and image-guided percutaneous ablation. Among these, thermal ablation methods—radiofrequency ablation (RFA), microwave ablation (MWA), and cryoablation—have been widely adopted due to their efficacy, minimal invasiveness, and rapid recovery profiles. These techniques are recommended by current practice guidelines for treating painful or oligometastatic bone lesions and are particularly useful when systemic options are exhausted or contraindicated.^{1,2}

However, thermal ablation has important limitations. It is contraindicated in anatomical regions where adjacent critical structures—such as nerves, vessels, hollow organs, or joint capsules—are susceptible to thermal injury. The anterior pelvic ring, sacrum, spine, and skull base are examples of areas where thermal techniques pose a substantial risk of collateral damage. Moreover, thermal spread can be difficult to control, especially in heterogeneous or poorly vascularized tissues such as bone.

In this context, irreversible electroporation (IRE) represents a promising alternative. It is a non-thermal technique that induces apoptosis by delivering high-voltage electric pulses across cell membranes, creating permanent nanopores that disrupt cellular homeostasis.^{3,4} Its primary advantage lies in the preservation of the extracellular matrix and surrounding connective tissues. Unlike thermal energy, electrical fields do not denature collagen, elastin, or basement membranes, enabling tumor ablation near neurovascular bundles or urogenital organs with a reduced risk of collateral injury.⁵

IRE has already been validated in visceral oncology, particularly for pancreatic, hepatic, and renal tumors located in anatomically complex regions. Despite these promising applications, its use in the treatment of bone metastases has not been previously reported.

Corresponding author: Salvatore Marsico

E-mail: salvatore.marsico@hotmail.it

Received 14 April 2025; revision requested 21 April 2025; last revision received 24 May 2025; accepted 22 June 2025.



Epub: 21.07.2025

Publication date: 02.01.2026

DOI: 10.4274/dir.2025.253402

You may cite this article as: Pusceddu C, Faiella E, Cau C, Rinaldi P, Cossu P, Marsico S. Computed tomography-guided irreversible electroporation for a pubic bone metastasis: a technical note and early experience. *Diagn Interv Radiol*. 2026;32(1):115-118.

In this case, the lesion's proximity to the urethra and pubic symphysis rendered it unsuitable for thermal techniques. The procedure demonstrated technical feasibility, safety, and early oncologic efficacy, supporting the potential role of IRE in musculoskeletal oncology.

Technique

A 55-year-old woman presented with a history of hormone receptor-positive, human epidermal growth factor receptor 2-negative breast cancer, diagnosed in 2013 and initially managed with radical mastectomy, axillary dissection, adjuvant chemotherapy, radiotherapy, and long-term endocrine therapy. She later developed widespread osseous metastatic disease, managed palliatively with capecitabine.

During restaging, pelvic magnetic resonance imaging revealed a 21 mm osteolytic lesion in the right pubic bone. Fluorodeoxyglucose (FDG) positron emission tomography/computed tomography (PET/CT) showed intense uptake, confirming the lesion's metabolic activity. The tumor was located in immediate proximity to the distal urethra and the anterior capsule of the pubic symphysis. Due to these anatomical constraints, further thermal ablation (previously attempted at another site) was contraindicated (Figure 1).

The patient was referred for percutaneous ablation and, after interdisciplinary tumor

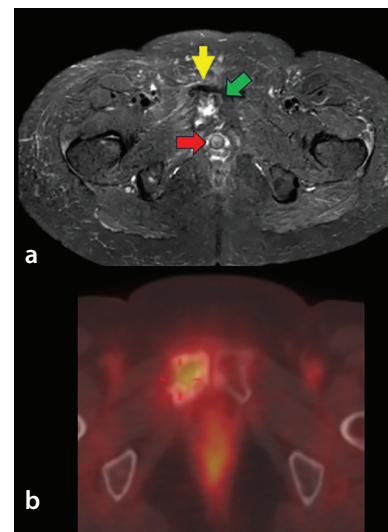


Figure 1. (a) Axial fat-suppressed T2-weighted (DP-FS) MRI of the pelvis demonstrating a hyperintense osteolytic lesion (yellow arrow) involving the right pubic bone. The anatomical relationship to adjacent critical structures, including the urethra (red arrow) and pubic symphysis (green arrow), was a key factor in selecting a non-thermal ablation approach (IRE). (b) Axial fused PET/CT image of the pelvis showing intense FDG uptake in a lytic lesion of the right pubic bone, consistent with metabolically active bone metastasis. DP-FS, dual phase fat suppression; IRE, irreversible electroporation; PET/CT, positron emission tomography/computed tomography; FDG, fluorodeoxyglucose; MRI, magnetic resonance imaging.

board discussion, was selected for CT-guided IRE as a non-thermal, structurally preserving approach.

The pubic metastasis was selected for treatment due to intense localized pain that severely impaired ambulation and its close proximity to the urethra, which posed a risk of urinary obstruction and functional decline.

Radiotherapy was excluded following a multidisciplinary team consensus evaluation due to the anatomical proximity of critical structures and the associated risk of collateral damage. Surgical resection was not indicated given the patient's advanced disease burden and limited functional reserve.

All procedures performed in studies involving human participants were in accordance with the ethical standards of the institutional and/or national research committee and with the 1964 Helsinki declaration and its later amendments or comparable ethical standards. Written informed consent was obtained for both the procedure and publication of data.

The patient was positioned supine on the CT table, with slight abduction of the legs to optimize access to the anterior pelvic region. General anesthesia was induced to ensure complete immobility during pulse delivery and to minimize discomfort. Electrocardiogram gating was employed to synchronize electrical pulses with the cardiac cycle (R-wave), minimizing the risk of arrhythmia during high-voltage delivery.

A contrast-enhanced pelvic CT was obtained to delineate tumor margins, measure safe access corridors, and plan the needle trajectory. The target lesion extended into both the cortical and medullary components of the right pubic bone and was in direct contact with the distal urethra.

Access was obtained via a percutaneous transseosseous route using two Bonopix[®] (Apriomed, Upsala, Sweden) biopsy systems. The systems were drilled into the anterior cortical bone under CT guidance, creating stable channels for subsequent electrode insertion.

Two 19-gauge monopolar IRE electrodes (NanoKnife[®], AngioDynamics[®]) were inserted through the coaxial access. The electrodes were positioned in parallel, flanking the lesion with an inter-electrode distance of 1.0–2.2 cm, adjusted according to lesion size and geometry. Positioning was confirmed in axial, coronal, and sagittal CT planes (Figure 2).

A test phase with 20 low-voltage pulses was performed to assess impedance. After confirming acceptable impedance (<1,500 ohms), full ablation was conducted with 70 pulses at 1,500 V/cm, 90-microsecond pulse duration, and a frequency of 1 Hz.

The electrode exposure length was 15 mm, and no pullbacks or repeat ablations were necessary.

Following ablation, a CT scan was acquired to exclude complications such as hemorrhage, pneumoperitoneum, or injury

Main points

- This is the first reported clinical case of irreversible electroporation (IRE) applied to a bone metastasis, specifically in the pubic bone.
- IRE enabled safe and effective ablation in an anatomically complex site where thermal techniques were contraindicated due to proximity to critical structures such as the distal urethra and pubic symphysis.
- The procedure was technically successful and well-tolerated, with no peri-procedural complications and complete metabolic response on positron emission tomography/computed tomography at 3-month follow-up.
- IRE preserved surrounding connective and neurovascular tissues, demonstrating its potential advantage in musculoskeletal oncology for lesions near heat-sensitive areas.
- This pioneering case provides proof-of-concept for the use of IRE in skeletal tumors and highlights the need for further clinical investigation and protocol development.

to adjacent organs. The patient awoke from anesthesia without complications or pain and was discharged the following day.

At 3-month follow-up, whole-body PET/CT showed complete metabolic response with no residual FDG uptake in the treated area (Figure 3). The patient reported a baseline visual analog scale pain score of 7/10, which improved to 2/10 at 48 hours post-procedure and 0/10 at 3-month follow-up, with preserved mobility and no new symptoms related to the ablation.

No delayed complications or local recurrence were identified, confirming both the safety and early efficacy of the procedure.

Two supporting procedural videos are available: Supplementary Video 1 illustrates transosseous CT-guided cannula placement and electrode deployment; Supplementary Video 2 demonstrates real-time pulse delivery using the IRE system interface.

Discussion

This case represents a pioneering application of IRE in the field of musculoskeletal interventional oncology. Pubic metastasis was prioritized due to its symptomatic burden, risk of functional compromise, and accessibility for safe percutaneous intervention.

The successful ablation of a pubic bone metastasis without thermal damage to adjacent urogenital structures highlights several important technical and clinical considerations.

First, IRE's non-thermal mechanism makes it particularly valuable in regions where heat or cold could cause unacceptable damage. The preservation of connective tissue, vasculature, and neural structures is a unique feature not shared by any other ablation modality.^{3,4} In the pelvis, this translates into potential applications near the bladder, urethra, sacral plexus, or neurovascular bundles—areas commonly involved by metastatic disease.

Second, the centripetal geometry of IRE allows for the precise definition of the ablation zone. Unlike the radial energy propagation of thermal techniques, IRE confines ablation to the area between the electrodes, enabling better control in irregular or constrained anatomical regions.⁴

Third, the mechanical integrity of bone may be better preserved with IRE compared with thermal methods. Although RFA and MWA are known to affect trabecular struc-

ture and increase fracture risk, IRE preserves bone scaffolding,⁶ potentially reducing the need for cementoplasty or other reinforcement procedures.

Preclinical studies have shown some risk of nerve injury with IRE—particularly in spinal or paraspinal locations—but also evidence of subsequent axonal regeneration.⁷ In our case, no neurological symptoms were observed post-procedurally; however, caution is warranted when planning procedures near major nerves.

Another interesting aspect is IRE's immunogenic potential. Several studies have shown that IRE-induced cell death may promote antigen presentation and immune activation, supporting possible synergy with immunotherapy or immune-modulating agents.⁷ This could be especially valuable in metastatic disease, where systemic control is also desired.

Although one case of IRE for a primary malignant bone tumor (Ewing sarcoma) has been reported, to our knowledge, this represents the first clinical application of IRE for

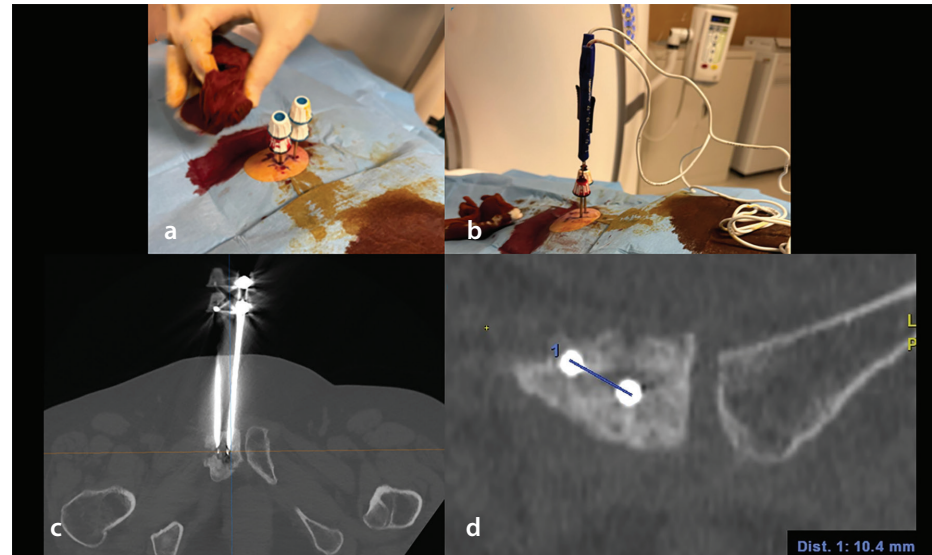


Figure 2. (a) Intraoperative view of the sterile setup showing the insertion of two Bonuity® 12-gauge coaxial bone access cannulae (Primed®) for a transosseous approach to the right pubic bone under CT guidance. (b) Intraoperative view showing coaxial insertion of the 19-gauge Nanoknife® IRE electrodes (AngioDynamics®) through the Bonuity® bone access cannulae. (c) Axial MIP reconstruction showing aligned placement of the right-sided 19-gauge IRE electrode targeting the osteolytic metastasis. (d) Coronal CT reconstruction demonstrating that the two IRE electrodes are positioned at an appropriate distance from each other, ensuring correct inter-electrode spacing for optimal electric field distribution. CT, computed tomography; IRE, irreversible electroporation; MIP, maximum intensity projection.

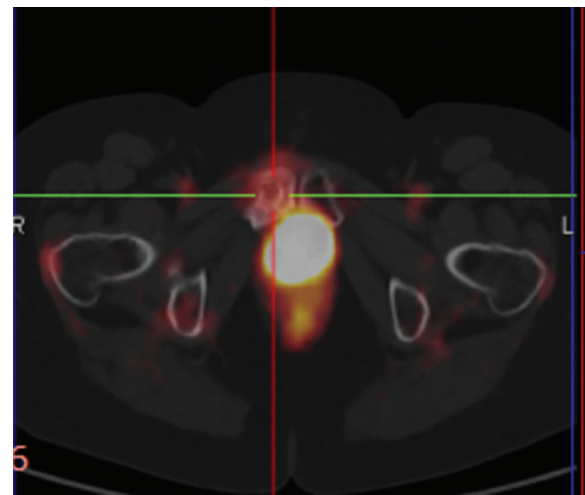


Figure 3. Axial fused PET/CT image obtained 3 months after IRE treatment showing complete metabolic response of the previously treated pubic bone metastasis. No residual FDG uptake is observed at the ablation site, consistent with successful local tumor control. PET/CT, positron emission tomography/computed tomography; IRE, irreversible electroporation; FDG, fluorodeoxyglucose.

a metastatic bone lesion.⁸ This distinction is important in terms of anatomical context, procedural planning, and therapeutic intent.

However, large-scale data are lacking, and this application remains investigational.

In conclusion, standardization is urgently needed for musculoskeletal IRE procedures, including optimal electrode design, energy delivery parameters, patient selection, and integration with other therapies. Prospective multicenter registries or trials would help define long-term outcomes and safety profiles.

Footnotes

Conflict of interest disclosure

The authors declared no conflicts of interest.

References

1. Callstrom MR, Charboneau JW, Goetz MP, et al. Image-guided ablation of painful metastatic bone tumors: a new and effective approach to a difficult problem. *Skeletal Radiol.* 2006;35(1):1-15. [\[Crossref\]](#)
2. Ryan A, Byrne C, Pusceddu C, Buy X, Tsoumakidou G, Filippiadis D. CIRSE standards of practice on thermal ablation of bone tumours. *Cardiovasc Interv Radiol.* 2022;45(5):591-605. [\[Crossref\]](#)
3. Davalos RV, Mir IL, Rubinsky B. Tissue ablation with irreversible electroporation. *Ann Biomed Eng.* 2005;33:223-231. [\[Crossref\]](#)
4. Scheffer HJ, Nielsen K, de Jong MC, et al. Irreversible electroporation for nonthermal tumor ablation in the clinical setting: a systematic review of safety and efficacy. *J Vasc Interv Radiol.* 2014;25(7):997-1011; quiz 1011. [\[Crossref\]](#)
5. Martin RC 2nd, Kwon D, Chalikonda S, et al. Treatment of 200 locally advanced (stage III) pancreatic adenocarcinoma patients with irreversible electroporation: safety and efficacy. *Ann Surg.* 2015;262(3):486-494; discussion 492-494. [\[Crossref\]](#)
6. Bazzocchi A, Aparisi Gómez MP, Taninokuchi Tomassoni M, et al. Musculoskeletal oncology and thermal ablation: the current and emerging role of interventional radiology. *Skeletal Radiol.* 2023;52(3):447-459. [\[Crossref\]](#)
7. Tam AL, Figueira TA, Gagea M, et al. Irreversible electroporation in the epidural space of the porcine spine: effects on adjacent structures. *Radiology.* 2016;281(3):763-771. [\[Crossref\]](#)
8. Steinbrecher K, Arslan B, Nassif ML, Kent P. Irreversible electroporation in the curative treatment of Ewing's sarcoma. *BMJ Case Rep.* 2016;2016:bcr2016216585. [\[Crossref\]](#)



Supplementary Video 1. Axial CT-guided procedure showing percutaneous insertion of irreversible electroporation electrodes into a lytic pubic bone lesion. Accurate intralesional positioning is confirmed by sequential axial imaging prior to electrical pulse delivery. CT, computed tomography.



Supplementary Video 2. Irreversible electroporation procedure: visualization of electrical pulse delivery with electrodes already positioned within the pubic lesion. Muscle contractions (involuntary spasms) induced by irreversible electroporation are clearly visible during pulse application.



Factors affecting the difficulty of transurethral double J stent removal in patients with renal transplants

✉ Elisabeth R. Seyferth
 ✉ Gregory J. Nadolski
 ✉ Jeffrey I. Mondschein
 ✉ Ryan M. Cobb
 ✉ Scott O. Trerotola

Division of Interventional Radiology, Department of Radiology, University of Pennsylvania Perelman School of Medicine, Philadelphia, United States of America

PURPOSE

This study aimed to identify factors affecting the difficulty of transurethral double J (JJ) stent removal in patients with renal transplants, using fluoroscopy time as a surrogate for procedural difficulty.

METHODS

Between January 2016 and November 2023, transurethral stent removal was attempted in 996 procedures (342 women, mean age 53.1 years). The following potential predictors of fluoroscopy time were investigated using bivariate analysis: patient age, sex, performance of the procedure by an attending physician alone, time from stent placement to removal, configuration and location of stent loop in the bladder, and device used for removal. For each stent retrieval device type, a multi-variable model was created, including covariates of interest.

RESULTS

Stent removal was technically successful in 99.2% of procedures. The mean fluoroscopy time for successful removals was 4.9 minutes (range 0.1–39.6 minutes). There were 5 adverse events (5/996, 0.5%), consisting of 3 moderate and 2 mild severity events. A complex snare was used in 72.5% of procedures, a simple snare in 6.0%, a looped guidewire in 31.6%, and forceps in 2.5%; multiple devices were used in 11.9% of procedures. Patient sex, number of intravesicular stent loops, and use of a simple snare, looped guidewire, and forceps predicted fluoroscopy time in bivariate analyses. In multivariable models, mean fluoroscopy time was estimated to be 0.78 minutes less when a complex snare was used ($P = 0.018$), 1.87 minutes greater when a simple snare was used ($P = 0.002$), and 0.86 minutes greater when a looped guidewire was used ($P = 0.014$); the use of forceps was not significant. When procedures using multiple devices were excluded, only the use of a complex snare and looped guidewire remained significant.

CONCLUSION

Transurethral JJ stent removal has a high success rate and can be performed with a single device in most cases. Use of complex snares and looped guidewires is associated with decreased and increased fluoroscopy time, respectively, suggesting that use of these devices may impact procedural difficulty.

CLINICAL SIGNIFICANCE

These results demonstrate that fluoroscopically guided transurethral JJ stent retrieval is an efficient technique that may be offered instead of cystoscopic stent removal. Careful choice of removal device may improve speed and ease of transurethral stent retrieval.

KEYWORDS

Renal transplantation, renal, double J stent, snare

Corresponding author: Elisabeth R. Seyferth

E-mail: Elisabeth.seyferth@pennmedicine.upenn.edu

Received 12 August 2025; revision requested 08 September 2025; accepted 15 October 2025.



Epub: 12.11.2025

Publication date: 02.01.2026

DOI: 10.4274/dir.2025.253520

You may cite this article as: Seyferth ER, Nadolski GJ, Mondschein JI, Cobb RM, Trerotola SO. Factors affecting the difficulty of transurethral double J stent removal in patients with renal transplants. *Diagn Interv Radiol*. 2026;32(1):119-124.

Double J (JJ) ureteral stent placement has become commonplace in renal transplantation, as data show that stent placement results in reduced rates of post-operative urinary leakage and ureteral obstruction.¹⁻³ A Cochrane systematic review found that the incidence of major urologic complications in renal transplants is reduced with routine prophylactic stenting, with a number needed to treat of 13 to prevent such a complication.⁴

Stents are typically removed within several weeks following transplant, either under fluoroscopic guidance via a sheath inserted into the urethra or using cystoscopy; removal by tying the stent end to a Foley catheter and then removing both by retracting the Foley, as well as other techniques not guided by imaging, may also be used.⁵⁻⁹

When performed under fluoroscopy via a transurethral approach, several different stent capture devices for the removal or exchange of JJ stents have been used, including complex (multi-lobed) snares, simple (single-lobed) snares,^{10,11} grasping devices (forceps),¹² a guidewire that is looped and bent to form a lasso ("looped guidewire"),¹²⁻¹⁴ and a "modified snare" technique in which a guidewire is advanced around the stent and then captured with a snare to form a lasso.⁵ Sometimes, a variety of these devices and techniques is required, particularly in the era of supply chain disruptions due to the COVID-19 pandemic and other global events. Understanding how the choice of removal device and other controllable factors affect procedural difficulty is important in maintaining procedural efficiency despite

Main points

- Double J (JJ) ureteral stents are routinely placed at the time of renal transplantation, and stent removal is required postoperatively. In 996 patients with renal transplants in this study, JJ stent removal performed as an outpatient procedure by interventional radiology via a transurethral approach had a >99% technical success rate, with a mean fluoroscopy time of <5 minutes.
- Complex snares, simple snares, looped guidewires, and forceps were used to capture JJ stents, and a single removal device was successful in the great majority of procedures.
- The use of a complex snare and the use of a looped guidewire were associated with decreased and increased fluoroscopy time, respectively, suggesting differences in procedural difficulty when these stent capture devices were used.

these challenges. The goal of this study is to assess the technical success of the procedure and factors that affect fluoroscopy time, using this variable as a surrogate for procedural difficulty.

Methods

Data collection and baseline characteristics

Patients with renal transplants who underwent transurethral JJ stent removal at a single academic center between January 2016 and November 2023 were identified retrospectively using a procedural database. The study was approved on July 8, 2024 by the Institutional Review Board of the University of Pennsylvania (protocol #829470), and a waiver of informed consent was obtained. Data were collected from the patient chart, imaging dictation, and the database of devices used in each procedure (QSight, Owens & Minor, Inc., Richmond, VA, USA). Procedures in which the intent was to remove a renal transplant JJ stent via a transurethral approach were included. The exclusion criteria for analysis of predictors of fluoroscopy time were removal of multiple stents in the

same procedure, performance of another procedure using fluoroscopy in the same encounter, inconsistency of the removal device noted in the imaging dictation and that noted in the procedural device database, the distal stent terminating in the ureter or urethra, use of ultrasound only, or technical failure. Technical success was defined as the complete removal of the JJ stent from the patient. Adverse events were identified and classified using the Society of Interventional Radiology guidelines.¹⁵

A total of 996 patients underwent stent removal in this period; 116 were excluded from the analysis of factors correlating with total fluoroscopic time (Figure 1). After exclusions, transurethral JJ stent removal was performed in 880 procedures. Patient age ranged from 20 to 77 years, with a mean age of 53.1 ± 12.9 years (Table 1). A total of 61.1% of the patients were male (538 of 880), and 38.7% were female (342 of 880). The attending physicians' years of experience ranged from <1 year to >35 years, with a mean of 14.4 ± 9.6 years. The time to stent removal ranged from 4 to 211 days, with a mean of 33.6 ± 10.8 days.

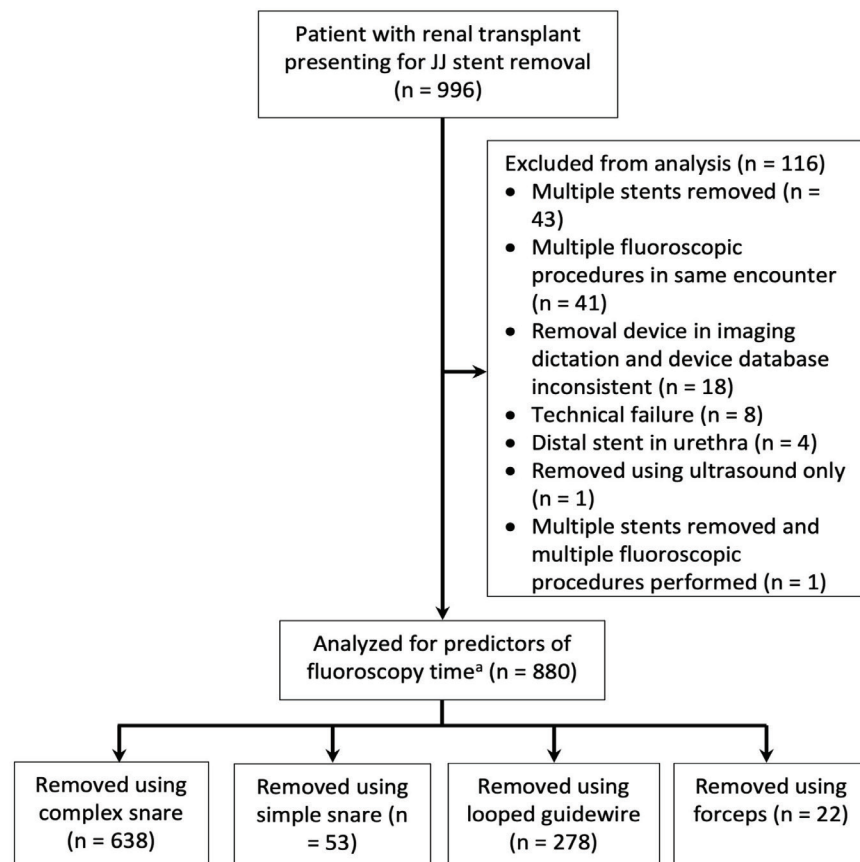


Figure 1. Flowchart of the study population. ^a, note that multiple devices were used in some procedures; JJ, double J.

Table 1. Baseline characteristics of patients and procedures, and bivariate associations between characteristics and fluoroscopy time

Variable	Mean (SD) or count (%) (n = 880)	P value
Sex (female)	342 (38.9%)	< 0.001
Age (years)	53.1 (12.9)	Not significant
Performed by attending physician alone	166 (18.9%)	Not significant
Attending physician years of experience	14.4 (9.6)	Not significant
Time to stent removal (days)	33.6 (10.8)	Not significant
Double J loops in the bladder		0.016
No complete loop	58 (6.8%)	
Single	523 (61.7%)	
Double	267 (31.5%)	
Double J loop bladder quadrant		Not significant
12 to 3 o'clock	92 (10.9%)	
3 to 6 o'clock	348 (41.2%)	
6 to 9 o'clock	219 (25.9%)	
9 to 12 o'clock	81 (9.6%)	
Central	105 (12.4%)	
Double J loop located in bladder half opposite from kidney	572 (67.7%)	Not significant
Use of complex snare	638 (72.5%)	Not significant
Use of simple snare	53 (6.0%)	< 0.001
Use of looped guidewire	278 (31.6%)	< 0.001
Use of forceps	22 (2.5%)	< 0.001
Use of multiple devices	105 (11.9%)	< 0.001

SD, standard deviation.

Procedural technique

Prophylactic pre-procedural intravenous antibiotics were administered, and the procedure was performed under moderate sedation. After insertion of a sheath through the urethra and into the bladder over a wire, the tip of the JJ stent was captured with a complex snare [i.e., a multi-lobed or three-dimensional snare, such as an EN Snare® (Merit Medical, South Jordan, UT, United States)], simple snare [i.e., a single-lobed or goose-neck-type snare, such as a ONE Snare® (Merit Medical, South Jordan, UT, United States)], looped guidewire, or forceps and was removed through the sheath or together with the sheath (Figure 2). The looped guidewire technique has been previously described;¹³ in brief, a 0.018" or 0.025" guidewire was bent into a lasso shape and advanced through the sheath and then maneuvered around the distal tip of the JJ stent before being retracted to capture the stent between the lasso and the sheath tip. The guidewire, sheath, and JJ stent were then removed together, and a final fluoroscopic image was obtained to document complete removal.

Statistical analysis

Initially, technical success was calculated from all 996 procedures performed. After ex-

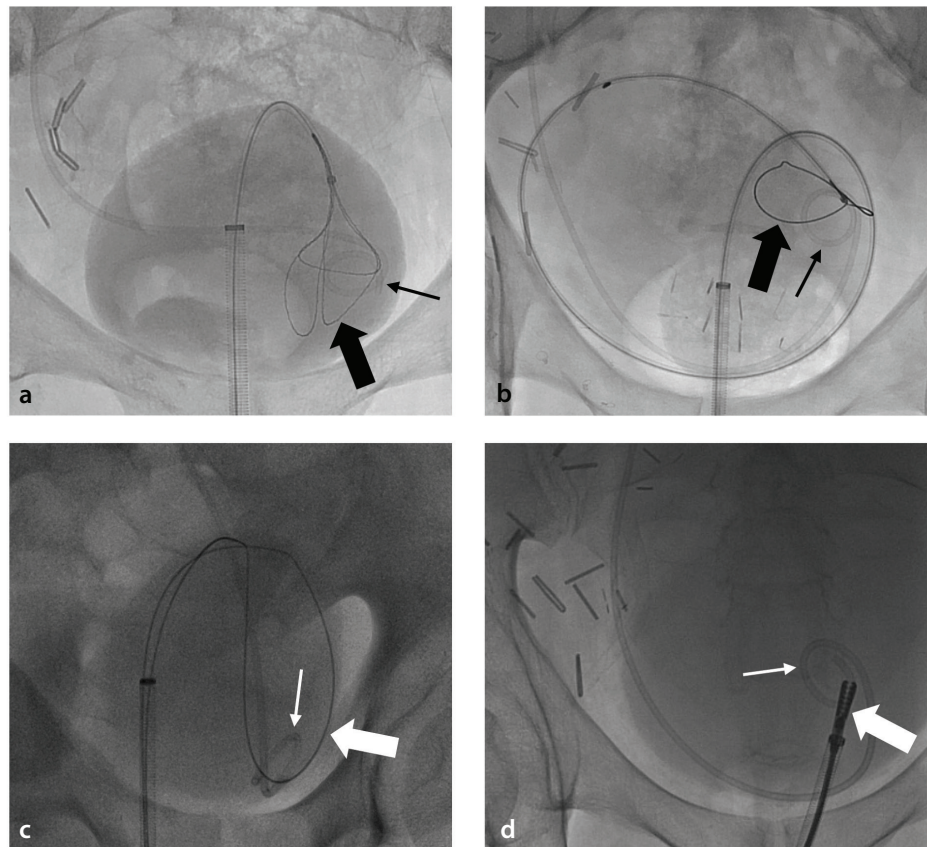


Figure 2. Four methods of transurethral double J (JJ) stent removal performed via a sheath positioned in the bladder. In each frame, the removal device is denoted by the thick arrow and the end of the JJ stent by the thin arrow. Removal with (a) complex snare (i.e., multi-lobed or three-dimensional snare), (b) simple snare (i.e., single-lobed or gooseneck-type snare), (c) looped guidewire, and (d) forceps are shown.

clusions, summary statistics were computed as means and standard deviations for continuous variables. Percentages and frequencies were used to summarize categorical measures. Bivariate associations between each predictor variable and the fluoroscopy time outcome measure were obtained using linear regression. Next, a separate multivariable linear regression model was constructed for each removal device type to assess the extent to which device types were predictive of fluoroscopy time while adjusting for covariates of interest. Each of these separate models was adjusted for patient sex, performance of the procedure by an attending physician alone (i.e., without a resident/fellow trainee), the attending physician's years of experience, number of complete JJ stent loops in the bladder, location of the distal JJ loop within the bladder, time from stent placement to stent removal, and use of multiple devices in a single procedure. In addition, a sensitivity analysis was conducted in which procedures with multiple devices were excluded from multivariable models. Statistical analysis was conducted using SAS Version 9.4 for Windows. An alpha level of 0.05 was used to determine statistical significance.

Results

Technical success was achieved in 99.2% of procedures (988/996). The most common cause of failure was heavy encrustation of the stent, resulting in the inability to remove it. In three such patients, the stent was captured and pulled to the perineum, but the proximal loop could not be dislodged from the renal pelvis; the distal loop was then replaced in the bladder. In all three patients, the stents were ultimately removed using percutaneous nephrolithotomy after failed cystoscopic removal. In another patient, the intravesicular portion of the stent fractured as it was pulled; the fractured portion was removed and was found to be heavily encrusted. The

retained stent portion was then successfully removed using cystoscopy. The times between stent placement and stent removal in these four patients with encrustation were 28 days, 36 days, 69 days, and approximately 15 years (this patient had had renal transplantation performed at an outside institution). The other failures consisted of one patient who did not tolerate placement of a sheath through the urethra; one in whom the procedure was aborted due to perforation at the proximal urethra during wire and catheter placement into the bladder; one in whom the distal JJ loop was found to be in the ureter on the initial image; and one patient, who had a preexisting percutaneous nephrostomy tube, in whom multiple initial attempts to capture the JJ loop with various snares failed, and therefore the stent was captured via the existing nephrostomy access. There were five adverse events (5/996, 0.5%), consisting of three moderate and two mild severity events (Table 2). There were no severe or life-threatening adverse events.

After exclusions, fluoroscopy time for successful cases ranged from 0.1 minutes to 39.6 minutes, with a mean of 4.9 ± 4.8 minutes. A single device was successful in 88.1% of cases, with multiple devices used in 11.9% of procedures (Table 1). A complex snare was used in 638 (72.5%) procedures, a simple snare in 53 (6.0%), a looped guidewire in 278 (31.6%), and forceps in 22 (2.5%). A 27–45 mm EN Snare® was the most used complex snare, accounting for 96.2% (614/638) of cases in which a complex snare was used; 4–8 mm, 12–20 mm, and 18–30 mm EN Snares® were used in 0.2% (1/638), 1.6% (10/638), and 2.7% (17/638) of cases in which a complex snare was used, respectively. The most used simple snare was a 35 mm snare (92.5%, 49/53 cases); a 5 mm snare was used in 1.9% (1/53) and a 25 mm snare in 5.7% (3/53) of cases in which a simple snare was used. A 0.025" wire was used in 93.2% (259/278) of

cases in which a looped guidewire was used, and a 0.018" wire was used in 9.7% (27/278) of these cases.

Bivariate analysis

Patient sex ($P < 0.001$), JJ loops in the bladder ($P = 0.016$), and the use of a simple snare ($P < 0.001$), looped guidewire ($P < 0.001$), or forceps ($P < 0.001$) were identified as predictors of fluoroscopy time in bivariate analyses (Table 1). Male patients had a mean fluoroscopy time of 5.4 ± 0.2 minutes, and female patients had a mean fluoroscopy time of 4.1 ± 0.3 minutes. JJ stents with no complete pigtail loop in the bladder were associated with increased fluoroscopy time compared with those with single and double loops in the bladder, with mean differences of 1.3 minutes ($P = 0.041$) and 1.9 minutes ($P = 0.005$), respectively. The time from stent placement to stent removal, performance of the procedure by an attending physician alone without a trainee, attending physician years of experience, location of the distal JJ loop in the bladder, positioning of the distal JJ loop in the bladder half opposite from the transplant kidney, and use of a complex snare were not found to be significantly associated with fluoroscopy time ($P > 0.05$).

Multivariable analysis

Multivariable models by device type adjusted for potential confounders estimated mean fluoroscopy time to be 0.78 ± 0.33 minutes less when a complex snare was used ($P = 0.018$), 1.87 ± 0.61 minutes greater when a simple snare was used ($P = 0.002$), and 0.86 ± 0.35 minutes greater when a looped guidewire was used ($P = 0.014$) (Table 3). The use of forceps was no longer significantly associated with fluoroscopy time in this model. Patient sex remained significantly associated with fluoroscopy time within each model, with female sex associated with a decreased mean fluoroscopy time ranging

Table 2. Adverse events associated with double J (JJ) stent removal in 996 procedures

Event severity	Description and outcome
Mild	Perforation of hydrophilic wire through bladder during sheath placement. Foley catheter was placed after JJ removal due to hematuria. Urine cleared in recovery and Foley was removed. Patient voided without issue.
Mild	Perforation of hydrophilic wire through urethra during sheath placement. Foley catheter was placed after JJ removal. After discussion with transplant team, Foley was removed in recovery area. Patient voided without issue.
Moderate	Perforation of wire through proximal urethra/bladder neck. JJ removal aborted, Foley left in place. Patient returned 1 week later for repeat attempt and JJ stent was removed. Foley catheter removed at that time. Following this, patient had acute urinary retention requiring outpatient Foley replacement, removed after 1 day.
Moderate	JJ removal was performed while patient was on oral antibiotics for urinary tract infection (UTI). Single dose of ceftriaxone was also given pre-procedure. Patient was admitted to hospital for fever and nausea 8 days after JJ removal, found to have pseudomonas UTI. Sent home the next day on course of oral antibiotics.
Moderate	Fracture of stent during removal; removed portion found to be heavily encrusted. Retained portion removed through cystoscopy.

Table 3. Multivariate associations between device used and fluoroscopy time^a

Variable	Change in estimated mean fluoro time (minutes)	Standard error	P value
Use of complex snare	-0.78	± 0.33	0.018
Use of simple snare	1.87	± 0.61	0.002
Use of looped guidewire	0.86	± 0.35	0.014

^aEach model was adjusted for the following covariates of interest: patient sex, whether the procedure was performed by an attending physician alone, the attending physician's years of experience, number of complete loops at the distal end of the double J (JJ) stent in the bladder ("JJ loops in bladder"), location of the distal JJ loop within the bladder, time from stent placement to stent removal, and use of multiple devices in a single procedure.

from 0.95 ± 0.29 minutes ($P = 0.001$) in the model assessing the effect of simple snare use to 1.07 ± 0.29 minutes ($P < 0.001$) when assessing looped guidewire use. The number of complete JJ stent loops in the bladder was no longer significant in these multivariable models.

Sensitivity analysis

Due to the underrepresentation of procedures using multiple devices (11.9%), a sensitivity analysis was conducted where procedures in which multiple devices were used were excluded. When these multiple device procedures were excluded from the multivariable models, the use of a complex snare remained significantly associated with decreased fluoroscopy time ($P = 0.019$), with a mean fluoroscopy time decreased by 0.69 ± 0.29 minutes, and use of a looped guidewire remained significantly associated with increased fluoroscopy time ($P = 0.014$), with a mean fluoroscopy time greater by 0.76 ± 0.31 minutes. However, the use of a simple snare was no longer significant.

Discussion

This study demonstrates a technical success rate of 99.2% for transurethral JJ stent removal following renal transplant, with a mean fluoroscopy time of <5 minutes and an extremely low adverse event rate. This is in line with previous studies, which have reported technical success rates of 95.7%–98.2% in large series assessing JJ stent removal or removal and replacement and a mean fluoroscopy time of 12.7 minutes in a study assessing removal alone.^{10,11,16} Half of the eight failures in this study were related to heavy encrustation causing difficulty dislodging the stent from the renal pelvis. Interestingly, the time from stent placement to stent removal in three of these patients was well within the range of time to stent removal in successful cases, and in two patients was within one standard deviation of the mean time to stent removal in successful cases. Overall, encrustation leading to procedural failure was extremely rare among stents removed within and beyond the approxi-

mately 30-day timeframe typically utilized at our institution. Additionally, time from stent placement to stent removal did not correlate with fluoroscopy time in bivariate analysis. The formation of significant encrustation causing difficult stent removal may be more related to differences in patient physiology than to the timing of stent removal.

Successful transurethral JJ stent removal required only a single removal device in approximately 90% of patients. Multivariable analysis demonstrated that the use of a complex snare was associated with decreased fluoroscopy time, and the use of a looped guidewire was associated with increased fluoroscopy time; each remained significantly associated with increased fluoroscopy time when procedures in which multiple devices were used were excluded. Choosing to use a complex snare as the initial removal device may increase procedural efficiency, whereas choosing to use a looped guidewire may reduce efficiency and increase procedural difficulty compared with other devices. Despite this, looped guidewires remain a viable option, an important consideration when the availability of preferred devices may be disrupted by supply chain issues or in low-resource environments. Loopided guidewires do have the advantage of lower equipment cost compared with snares; further studies could investigate whether this may partially offset the increased cost of greater mean procedural time.

Use of a simple snare was also associated with fluoroscopy time in a multivariable model; however, this relationship did not persist when procedures in which multiple devices were used were excluded from the model. This finding was likely due to the relatively rare use of simple snares as an initial removal device at our institution; these snares were the device of choice in only 4.0% (31/775) of procedures in which a single device was used. Additionally, 41.5% of procedures using simple snares were procedures in which multiple devices were used, compared with only 33.5% of procedures using looped guidewires and 13.3% of those using complex snares.

Few previous studies have assessed factors influencing fluoroscopy time in transurethral JJ stent removal. One study found that the distal stent loop position in the bladder and the number of loops in the JJ stent were significantly associated with fluoroscopy time.¹⁰ In contrast, we found no association of JJ loop position with fluoroscopy time, and although we did find a bivariate correlation of the number of JJ loops in the bladder with fluoroscopy time, this did not persist in a multivariable analysis. In this prior study, time from stent placement to removal was not predictive of fluoroscopy time, which was corroborated in our study. Our study also found female patient sex to be associated with decreased fluoroscopy time in both bivariate and multivariate analyses; this may be due to differences in anatomy requiring more fluoroscopic guidance during placement of the transurethral sheath prior to stent removal. One prior study of de novo retrograde ureteral stent placement found that use of ultrasound to guide the sheath to the ureteral orifice during the procedure was associated with a significant decrease in fluoroscopy time.¹⁷ Although we used ultrasound for stent removal in only 1 of 996 procedures, it is possible that using ultrasound as an adjunct imaging technique could reduce fluoroscopy time in cases where engaging the end of the stent with the capture device is difficult, and this could be considered for future study.

This study is by far the largest in existence to examine transurethral JJ stent removal due to our institution's high volume of renal transplants, as well as referral pattern to interventional radiology for stent removal rather than to urology for cystoscopic removal. The size of the cohort increases the accuracy of our estimation of technical success and peri-procedural adverse events. Additionally, the inclusion of only a relatively homogeneous population by limiting the study to patients with renal transplants allows more precise analysis of technical factors that may affect procedural difficulty. Although two prior studies focused on factors affecting procedural time in transurethral JJ stent removal, one only used snares – therefore,

different removal methods were not compared¹⁰ – and one only compared the use of forceps to a modified loop snare technique.⁵ In contrast, our study includes four different methods of stent removal while examining a variety of other factors that could affect the difficulty of stent removal.

Patients with renal transplants are a unique population with key differences from other populations that typically require JJ stent removal or replacement. JJ stents in these patients are placed during surgery and typically left in place for only 4–6 weeks before removal, rather than the 3–6 months that JJ stents are usually left in place before exchange in patients requiring chronic stenting. Stenting at the time of transplant is associated with a lower rate of urinary obstruction and leak than in non-stented groups; however, there is an increased risk of urinary tract infection if the stent is left in place for >30 days.^{3,4} Despite this finding and the immunosuppressed nature of these patients, our data show that periprocedural infection-related adverse events are exceedingly rare with transurethral JJ removal.

Our study has several limitations. Although it has a large sample size, the fact that it is retrospective makes it difficult to fully account for inherent biases – even through using multivariable regression and a sensitivity analysis – such as the preferential use of devices as a first-line choice among different interventionalists. Use of forceps was relatively uncommon, occurring in only 2.5% of procedures; therefore, the lack of a significant association of forceps use with fluoroscopy time is difficult to interpret. Similarly, the sample is unrepresentative of cases with multiple devices, which were only used in 11.9% of procedures. Additionally, the medical record does not document which device was first used, which device was ultimately successful in removing the stent, or how long each device was used during multiple device procedures, limiting the conclusions that may be drawn. Finally, other factors that may have an influence on the difficulty of stent removal, such as the exact brand and size of the stent and the years of experience of the resident or fellow who assisted with the procedure, were not assessed.

In conclusion, transurethral JJ stent removal in patients with renal transplants has a high technical success rate and short mean fluoroscopy time and requires only a single device in most patients. The use of a complex snare is associated with decreased fluoroscopy time, and the use of a looped guidewire is associated with increased fluoroscopy time, suggesting decreased and increased procedural difficulty with these removal devices, respectively.

Footnotes

Conflict of interest disclosure

The authors declared that there is no conflict of interest.

References

1. Buttigieg J, Agius-Anastasi A, Sharma A, Halawa A. Early urological complications after kidney transplantation: an overview. *World J Transplant.* 2018;8(5):142-149. [\[Crossref\]](#)
2. Kumar A, Verma BS, Srivastava A, Bhandari M, Gupta A, Sharma R. Evaluation of the urological complications of living related renal transplantation at a single center during the last 10 years: impact of the double-J* stent. *J Urol.* 2000;164(3 Pt 1):657-60. [\[Crossref\]](#)
3. Tavakoli A, Surange RS, Pearson RC, Parrott NR, Augustine T, Riad HN. Impact of stents on urological complications and health care expenditure in renal transplant recipients: results of a prospective, randomized clinical trial. *J Urol.* 2007;177(6):2260-2264; discussion 2264. [\[Crossref\]](#)
4. Wilson CH, Rix DA, Manas DM. Routine intraoperative ureteric stenting for kidney transplant recipients. *Cochrane Database Syst Rev.* 2013;(6):CD004925. [\[Crossref\]](#)
5. Grasso RF, Faiella E, Cazzato RL, et al. Retrograde fluoroscopy-guided trans-urethral exchange of ureteral stents: comparison of direct grasping vs. modified snare. *Indian J Radiol Imaging.* 2013;23(4):347-350. [\[Crossref\]](#)
6. Nadjafi-Semnani M, Simforoosh N, Basiri A, Tabibi A, Nadjafi-Semnani A. Comparison of removing double-J stent with and without cystoscopy in kidney transplant patients: a randomized clinical trial. *Urol J.* 2020;17(2):173-179. [\[Crossref\]](#)
7. Simforoosh N, Obeid K, Javanmard B, Rezaeetalab GH, Razmjoo S, Soltani MH. Stent removal in 200 kidney transplant recipients: nonoperative versus endoscopic removal. *Exp Clin Transplant.* 2016;14(4):385-388. [\[Crossref\]](#)
8. Yu C, Wei C, Dong J, et al. Transurethral retrograde fishing the double J urethral stent: a tertiary children hospital's experience with a new technical strategy. *Front Pediatr.* 2022;10:802741. [\[Crossref\]](#)
9. Kawahara T, Ito H, Terao H, Yamagishi T, Ogawa T, Uemura H, Kubota Y, Matsuzaki J. Ureteral stent retrieval using the crochet hook technique in females. *PLoS One.* 2012;7(1):e29292. [\[Crossref\]](#)
10. Chen CS, Shin JH, Li HL, et al. Analysis of the factors influencing retrograde removal of double J ureteral stents using a simple snare technique in female patients. *Ann Transl Med.* 2021;9(8):674. [\[Crossref\]](#)
11. Carrafiello G, Coppola A, De Marchi G, et al. Trans-urethral ureteral stent replacement technique (TRUST): 10-year experience in 1168 patients. *Cardiovasc Interv Radiol.* 2018;41(4):610-617. [\[Crossref\]](#)
12. de Baere T, Denys A, Pappas P, Challier E, Roche A. Ureteral stents: exchange under fluoroscopic control as an effective alternative to cystoscopy. *Radiology.* 1994;190(3):887-889. [\[Crossref\]](#)
13. Park SW, Cha IH, Hong SJ, et al. Fluoroscopy-guided transurethral removal and exchange of ureteral stents in female patients: technical notes. *J Vasc Interv Radiol.* 2007;18(2):251-256. [\[Crossref\]](#)
14. Akinci D, Ünal E, Çiftçi TT, Özkan OŞ, Akhan O. Management of single double-J stent failure in malignant ureteral obstruction: tandem ureteral stenting with less frequent stent exchange. *Diagn Interv Radiol.* 2023;29(2):312-317. [\[Crossref\]](#)
15. Khalilzadeh O, Baerlocher MO, Shyn PB, et al. Proposal of a new adverse event classification by the Society of Interventional Radiology Standards of Practice Committee. *J Vasc Interv Radiol.* 2017;28(10):1432-1437.e3. [\[Crossref\]](#)
16. McCarthy E, Kavanagh J, McKernan S, et al. Fluoroscopically guided transurethral removal and/or replacement of ureteric stents in women. *Acta Radiol.* 2015;56(5):635-640. [\[Crossref\]](#)
17. Ünal E, Çiftçi TT, Akhan O, Akinci D. Imaging-guided de novo retrograde ureteral access and stent placement without cystoscopy in women. *J Vasc Interv Radiol.* 2023;34(5):902-909. [\[Crossref\]](#)



Gastrostomy tube check radiographs: performance of an alternative diagnostic exam

✉ Muhammad Y. Hameed¹

✉ Charles A. James²

✉ Kevin Wong²

✉ Paul S. Lewis²

✉ Paula K. Roberson³

✉ Kelli R. Schmitz⁴

✉ Sateesh Jayappa²

✉ Amy C. Rowell²

✉ Marcene McVay-Gillam⁵

✉ Mary B. Moore²

¹University of Arkansas for Medical Sciences, College of Medicine, Little Rock, USA

²University of Arkansas for Medical Sciences, Arkansas Children's Hospital, Department of Radiology, Little Rock, USA

³University of Arkansas for Medical Sciences, Department of Biostatistics, Little Rock, USA

⁴University of Arkansas for Medical Sciences, Arkansas Children's Northwest Hospital, Department of Radiology, Springdale, USA

⁵Arkansas Children's Northwest Hospital, Department of Surgery, Springdale, USA

Corresponding author: Charles A. James

E-mail: JamesCharlesA@uams.edu

Received 18 April 2025; revision requested 02 June 2025; accepted 27 July 2025.



Epub: 15.09.2025

Publication date: 02.01.2026

DOI: 10.4274/dir.2025.253399

PURPOSE

The traditional imaging exam to check a gastrostomy tube (G-tube) used fluoroscopy, which requires the presence of a radiologist. Evaluate the effectiveness of an alternative 2-view abdominal radiograph exam protocol instituted to replace the prior fluoroscopic G-tube contrast check exam and provide 24/7 coverage at 2 affiliated hospitals.

METHODS

An alternative 2-view G-tube check radiograph exam following stratified contrast administration was introduced at 2 affiliated children's hospitals. Gastrostomy-tube radiograph exams performed between December 2019 and May 2022 at 2 affiliated hospitals were identified, and a retrospective chart review was performed to delineate exam test yield, accuracy, sensitivity, specificity, positive predictive value (PPV), and negative predictive value (NPV). Additional data collected included exam adherence to the protocol, 30-day adverse events, reporting time, and the years of experience of the reporting pediatric radiologist.

RESULTS

A total of 227 exams were performed among 186 patients. The 2-view radiograph protocol was followed in 81.9% (186/227). Additional radiograph views were performed for 18.1% (41/227) of cases, and additional contrast volume for 9.3% (21/227) of cases. A fluoroscopic G-tube contrast check was requested for 7 of 13 indeterminate readings with high clinical suspicion. Following the reclassification of indeterminate exams based on clinical suspicion, exam performance results were as follows: test yield, 94.3%; accuracy, 97.8%; sensitivity, 90.0%; specificity, 98.2%; PPV, 69.2%; NPV, 99.5%. The 1 false negative exam required a second hospital visit 7 days after the initial exam to detect and correct G-tube malposition. Reporting time under 1 hour occurred in 79.7% (181/227). Delayed radiology reporting in 1 patient led to endoscopic confirmation of abnormal G-tube alignment. Furthermore, 5.7% (13/227) exams were reported as indeterminate, adding a median time delay of 40 minutes (interquartile range, 90). Indeterminate exam reporting did not correlate with the years of experience of the reporting pediatric radiologist ($P = 0.189$). Reporting time over 1 hour occurred more often in the after-hours group ($P = 0.032$).

CONCLUSION

This alternative diagnostic exam performed well in terms of high test yield, accuracy, sensitivity, specificity, and NPV. The exam mostly followed protocol, allowed for the timely and safe resumption of G-tube use, and provided the remote coverage needed for a new satellite hospital.

CLINICAL SIGNIFICANCE

This diagnostic radiograph exam replaced the on-site fluoroscopic exam as the initial imaging exam for G-tube checking in our pediatric population.

KEYWORDS

Fluoroscopy, G-tube check, gastrostomy, pediatrics, radiographs

You may cite this article as: Hameed MY, James CA, Wong K, et al. Gastrostomy tube check radiographs: performance of an alternative diagnostic exam. *Diagn Interv Radiol.* 2026;32(1):125-131.

Shortages in the pediatric radiologist and technologist workforce in North America have increased the remote reading of diagnostic imaging exams.^{1,2} Concurrently, healthcare leaders have demanded increased evening/overnight final reads of diagnostic imaging exams.³ To avoid peritoneal leakage complications, imaging checks of a replaced or malfunctioning gastrostomy tube (G-tube) are often requested to ensure appropriate tube alignment prior to resuming tube use for hydration, nutrition, and medications. Imaging verification of G-tube alignment has traditionally been a fluoroscopic exam performed by an on-site pediatric radiologist. An alternative approach is a diagnostic abdominal radiograph exam following protocoled contrast administration.⁴ An unpublished survey from the Society of Chiefs of Radiology at Children's Hospitals (SCORCH) in 2019 provided support for this alternative approach, but clinical validation is needed to support practice implementation. The following report describes our experience using a 2-view abdominal radiograph exam with stratified contrast administration for 2 affiliated children's hospitals, as the satellite hospital lacked after-hours radiologist availability for an on-site fluoroscopic exam.

Methods

Institutional Review Board (IRB) approval (protocol number: 263194) was obtained to collect retrospective data of all G-tube abdominal radiograph exams performed using an alternative protocol between December 2019 through May 2022 at an established central children's hospital and a new satellite children's hospital with a shared Epic electronic health record (Epic Systems, Verona, WI, USA). Need for informed consent was waived by the IRB for this retrospective study. Both hospitals had pediatric radiology staff coverage during daytime hours; the satellite hospital lacked after-hours pediatric

radiologist or radiology resident coverage. Radiograph examinations ordered with the description "XR G-tube CHECK W CONTRAST ABD 2 VW" were identified in a shared picture archiving and communications system (PACS, Fuji Synapse, FUJIFILM, Lexington, MA, USA); a Research Electronic Data Capture (REDCap, Vanderbilt University, Nashville, TN, USA) database was created. Study inclusion criteria comprised a completed radiograph exam for a G-tube check. Exclusion criteria were cancelled radiograph exams or the use of this radiograph exam for enteric tubes other than G-tubes [e.g., nasojejunal or gastrojejunostomy (GJ) tube] (Figure 1).

The radiograph exam protocol (Figure 2) was developed in consultation with physicians from the emergency department and pediatric surgery service; a collaborating radiology department supervisor ensured protocol understanding of the existing and new radiology technologists (RTs). Our approach included a 2-view abdominal radiograph exam following contrast administration [Cysto-Conray II, 17.2% (Guebert, Princeton, NJ, USA)] by the RT, stratified by patient age: 10 mL for patients under 1 year, 15 mL for 1–5 years, and 20 mL for patients over 5 years old.⁵ A cross-table lateral radiograph (Figure 3a) was followed by a frontal radiograph with the patient in a right lateral decubitus position (Figure 3b). Upon exam completion, the RT contacted the pediatric radiologist covering the fluoroscopy work assignment or the on-call pediatric radiologist via a phone call, beeper page, or a Secure Chat message in Epic. The reviewing radiologist could request additional views and/or additional contrast as needed. Overnight radiology residents at the central hospital reviewed some exams

and provided a preliminary report note in Epic, which was subsequently reviewed by the reporting pediatric radiologist.

Report results were classified as positive (abnormal exam with abnormal G-tube retention component alignment, peritoneal air, or extraluminal contrast leakage; see Figure 4), negative (normal exam with normal intraluminal contrast flow and normal G-tube retention component alignment; see Figure 3), or indeterminate (equivocal G-tube retention component alignment or uncertainty of intraluminal contrast; Figure 5a). To determine exam sensitivity and specificity, indeterminate exams were reclassified based on clinical suspicion, a method suggested by several researchers.^{6,7} Specifically, when an indeterminate exam was accompanied by low clinical suspicion of G-tube malposition/malfunction by the consulted pediatric surgery team or other referring service, no further imaging was performed, and the study was reclassified as a negative (normal) radiograph exam. When there was high clinical suspicion of G-tube malfunction (such as pain with G-tube use) by the consulted pediatric surgery team or requesting service, a fluoroscopic G-tube contrast check was requested, and the radiograph study was reclassified as a positive (abnormal) radiograph exam.

Fluoroscopic exam protocol

For indeterminate radiograph exams with high clinical suspicion, a referring physician ordered a fluoroscopic G-tube contrast check, and the RT contacted the pediatric radiologist to perform an on-site exam. The pediatric radiologist traveled to the fluoroscopy suite from off-site or an on-site assignment

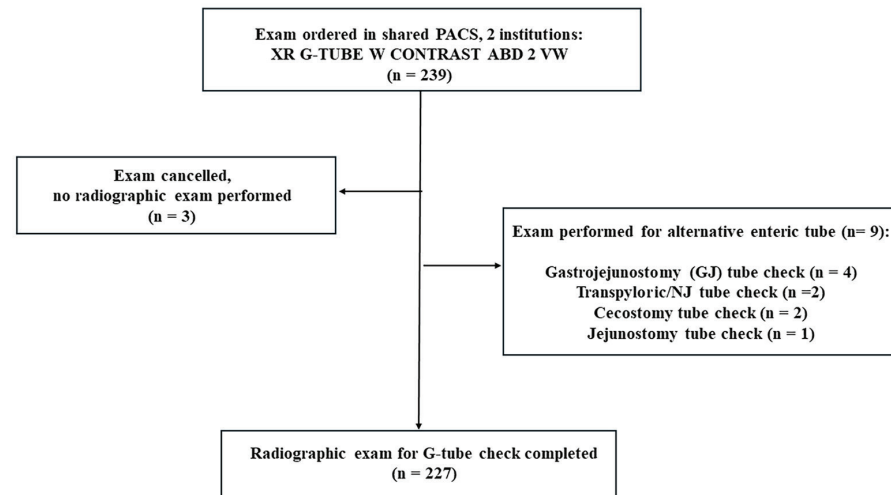


Figure 1. Study flowchart. PACS, picture archiving and communications system; XR, X-ray; G-tube, gastrostomy tube; W, with; ABD, abdomen; VW, view; GJ, gastrojejunostomy; NJ, nasojejunal.

and protocoled the exam contrast in Epic [favoring a water-soluble contrast: Cysto-Conray II, 17.2%, or Cystografin-Dilute, 18% (Bracco Diagnostics, Princeton, NJ, USA)]. This pediatric radiologist then obtained fluoroscopic images following the injection of a contrast through the G-tube in both lateral and frontal positions. The exam was tailored to confirm intraluminal contrast flow (gastric or gastroduodenal per the pediatric radiologist's judgement), confirm appropriate G-tube retention component alignment within the gastric lumen, and detect any extraluminal contrast leakage. The G-tube was then flushed with 10 mL of sterile water, and the images were sent to the PACS.

Epic data collection included demographics (age, weight, biological sex), clinical indication, referral location (Table 1), number of radiograph views, contrast volume administered, and exam reporting times (under or over 1 hour). Reporting time was defined as the time from exam uploading into PACS to pediatric radiologist report completion; for after-hours exams, reporting time was defined as the time of the radiology resident's preliminary report completion. Reporting times over 1 hour were compared between exams performed during daytime hours (Monday–Friday, 08:00–17:00) and those performed after-hours.

Any additional time delay for indeterminate exams was calculated as the time between the reporting of the radiograph exam as indeterminate to the onset of a fluoroscopic exam or resumption of G-tube use. After-hours exams performed at the satellite hospital and read remotely by the pediatric radiologist at the central children's hospital were identified, as a lack of this radiograph exam may have required an ambulance transport to the established children's hospital 3 hours away. Indeterminate exam readings by a pediatric radiologist with less experience (5 years or less) were compared to indeterminate exam readings by pediatric radiologists with greater experience (more than 5 years).

To confirm a negative radiograph exam, a chart review was performed to identify any 30-day adverse events, a standard used by the Society of Interventional Radiology.⁸ Positive (abnormal) G-tube radiograph exams were acted on accordingly by a subspecialist

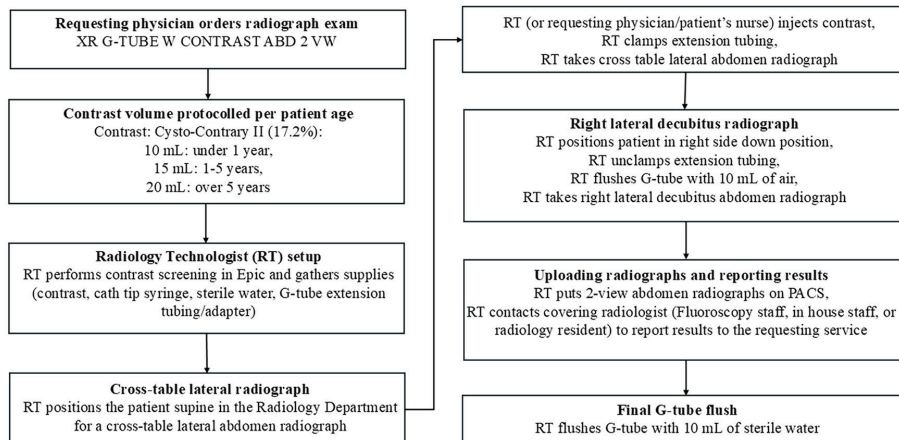


Figure 2. G-TUBE checks using radiographs: exam protocol.⁵ XR, X-ray; G-tube, gastrostomy tube; W, with; ABD, abdomen; VW, view; PACS, picture archiving and communications system.

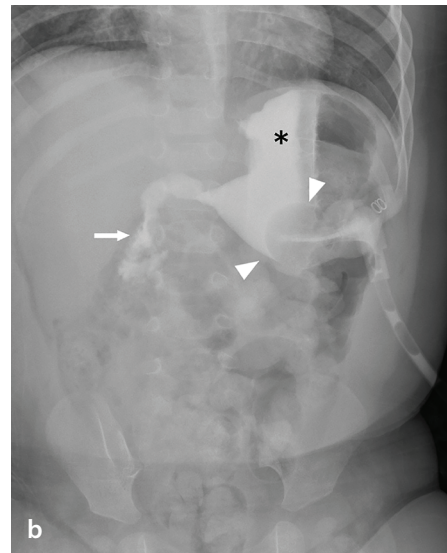
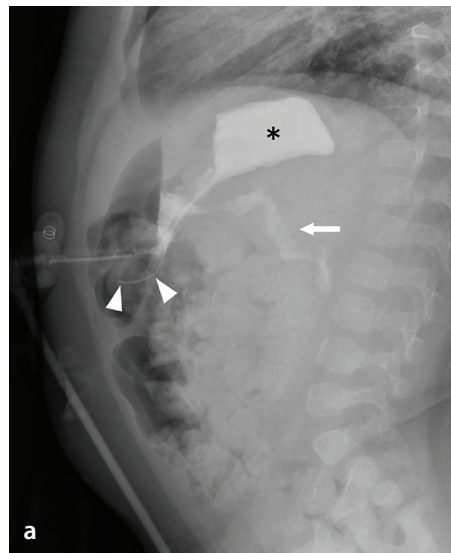


Figure 3. A 17-month-old male had gastrostomy tube (G-tube) dislodgement 4 months following surgical placement. After the surgery team placed a new G-tube button, a G-tube check radiograph exam was ordered, which was observed to be normal. (a) A cross-table lateral abdomen radiograph shows intraluminal contrast flow into the gastric lumen (*) and duodenum (arrow). Intraluminal gastric contrast outlines the tube retention balloon (arrowheads). (b) A right-lateral decubitus radiograph shows gastric luminal contrast (*) and contrast flow into the proximal duodenum (arrow). Gastric luminal contrast outlines the G-tube retention balloon (arrowheads) on this normal exam.



Figure 4. Cross-table abdominal radiograph shows the gastrostomy tube (G-tube) retention component appears to be within the gastric lumen (arrowheads), and gastric luminal contrast flow (*) is seen. However, a large pneumoperitoneum is seen (arrows) in this patient with pain and tenderness at the G-tube site 2 days after percutaneous endoscopic gastrostomy tube placement. This patient required surgical revision of a loose G-tube gastric entry site that was leaking into the peritoneal cavity.

[pediatric surgery team, pediatric interventional radiology (IR) team] to obtain a normal G-tube alignment and resume G-tube use.

Statistical analysis

Diagnostic test characteristics [yield, accuracy, sensitivity, specificity, positive predictive value (PPV), and negative predictive value (NPV)] were calculated according to a standard formula,⁹ excluding the 13 exams reported as indeterminate, and again after reclassifying the indeterminate exams based on clinical suspicion, as described in the "Methods" and "Discussion" sections. Confidence intervals (CI) for sensitivity and specificity were calculated according to the score CI formulae of Agresti and Coull⁹ as described in Zhou et al.¹⁰ The association between indeterminate reports and staff experience (5 years or less vs. more than 5 years), as well as the association of after-hours exams with reporting times (less than 1 hour vs. more than 1 hour), was assessed by chi-square using the software package StatXact-12 [v.12.0; Cytel Studio, 2019 (Cytel, Cambridge, MA, USA)]. A value of $P \leq 0.05$ was considered statistically significant.

Results

A total of 239 G-tube check exams were identified, and 12 were found to meet exclusion criteria, leaving 227 exams among 186 patients over the 2.5-year study period (Figure 1). Patient demographic details, referral location, and clinical indication are provided in Table 1.

The overall test yield was 94.3% (214/227), with a normal or abnormal exam reported. Normal exams (true negative) were found in 93.8% (213/227) of cases (Table 2); all negative exams were confirmed at a 30-day chart review. Five of the 227 radiograph exams (2.2%) were positive (abnormal) at the initial (primary) analysis. Findings on true positive exams at the initial analysis included a G-tube retention component in the abdominal wall or superficial gastrostomy tract anterior to the stomach ($n = 3$), intraperitoneal contrast leakage ($n = 1$), and large pneumoperitoneum ($n = 1$). Free extraluminal (peritoneal) air was seen on 3 exams, all within 7 days of the primary G-tube placement. In one of these cases, free air was a large volume in a symptomatic patient, and surgical revision was required. In the 2 other cases, the post-operative free air was minor and of no clinical significance.

Thirteen exams were reported as indeterminate, predominantly due to uncertain-

ty related to G-tube retention component alignment within the gastric lumen. The indeterminate exams had a median time delay of 40 minutes [interquartile range (IQR): 90]. Indeterminate exam reporting did not correlate with years of experience as a pediatric radiologist ($P = 0.189$). Of the 13 indeterminate exams, 5 had no follow-up imaging (low clinical suspicion) and were reclassified as true negatives. Seven indeterminate exams with high clinical suspicion underwent flu-

roscopy, 4 of which confirmed normal G-tube placement and were reclassified as false positives. An additional 3 indeterminate exams with high clinical suspicion revealed malpositioned G-tubes at fluoroscopy and were reclassified as true positive exams. The remaining indeterminate exam was particularly challenging to re-classify due to a delayed radiology report and differing clinical suspicion of the surgery and intensive care referring services. Specifically, the radiograph re-

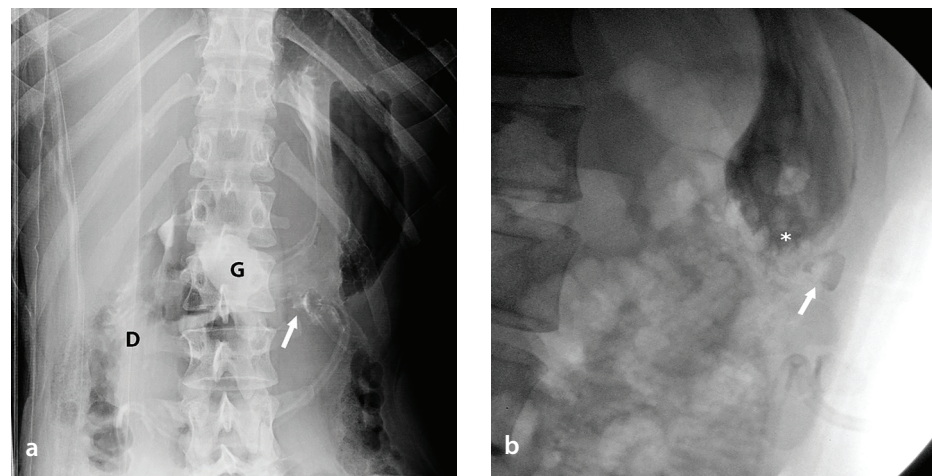


Figure 5. A 17-year-old female with an indeterminate abdomen radiograph exam and high clinical suspicion who underwent a fluoroscopic gastrostomy tube (G-tube) contrast check exam confirming a true positive (abnormal exam).⁵ (a) Right lateral decubitus abdomen radiograph shows definitive intraluminal contrast flow into the gastric lumen (G) and duodenum (D). However, alignment of the G-tube retention component (arrow) within the gastric lumen is uncertain. (b) Left posterior oblique view during a fluoroscopic G-tube contrast check shows the G-tube retention component (arrow) outside of the gastric luminal contrast (*).

Table 1. Patient characteristics

Variable	Overall (n = 227)
Age (years), median (IQR)	1.5 (8.3)
Weight (kg), median (IQR)	10 (16.8)
Biological sex	
Female – n (%)	98 (43.2%)
Male – n (%)	129 (56.8%)
Indications	
G-tube dislodged with routine replacement, n (%)	90 (40.1%)
G-tube dislodged with difficult replacement, n (%)	40 (17.6%)
G-tube leaking, n (%)	32 (14.1%)
Pain with G-tube feeds, n (%)	23 (10.1%)
Vomiting with G-tube feeds, n (%)	23 (10.1%)
G-tube partially dislodged, n (%)	9 (4%)
G-tube malfunction (not specified), n (%)	4 (1.8%)
Resistance to G-tube flush/infusion, n (%)	2 (0.9%)
Other, n (%)	26 (11.5%)
Referral location	
Emergency department	154 (67.8%)
Inpatient	57 (25.1%)
Outpatient	16 (7%)

IQR, interquartile range; ... G-tube, gastrostomy tube.

port described the presence of a small bowel contrast but no visualization of gastric luminal contrast and raised suspicion of transpyloric malposition of the distal G-tube segment (note: this patient had a longer G-tube type that was atypical for this study cohort with a variable tract length). This indeterminate exam was reported 2 hours after the exam was uploaded into PACS; the surgery team had already completed their consultation, had low clinical suspicion, and concluded that the radiograph exam was normal (no fluoroscopic exam recommended). However, the intensive care team remained concerned due to high gastric residuals via the nasogastric tube and requested an endoscopy, which confirmed gastric obstruction due to migration of the retention balloon of the G-tube. This indeterminate radiograph exam was, therefore, reclassified as a true positive exam.

The one 30-day adverse event involved a patient with autism, where the initial radiograph exam was read as normal. This patient returned to the emergency department 7 days later with increased abdominal pain and leakage at the ostomy site, and G-tube retention component malposition was confirmed on a repeat G-tube abdominal radiograph exam. Subsequent peer review of the initial G-tube check exam demonstrated G-tube retention component tract malpositioning, resulting in reclassification of this exam as a false negative exam (Figure 6).



Figure 6. A 14-year-old male with autism and abdominal pain at the gastrostomy tube (G-tube) site. The right lateral decubitus radiograph shows separation between the G-tube retention component (arrow) and gastric luminal contrast (arrowheads). This exam was reclassified as a false negative exam on pediatric radiology group peer-review assessment.⁵

Excluding indeterminate results, the exam performance metrics were as follows: sensitivity, 83.3%; specificity, 100%; PPV, 100%; NPV, 99.5%; accuracy, 99.5%. After reclassifying the indeterminate exams based on clinical suspicion, the performance metrics were as follows: sensitivity, 90.0%; specificity, 98.2%; PPV, 69.2%; NPV, 99.5% (Table 2); [95% CI for sensitivity (59.4%, 98.1%); 95% CI for specificity (94.5%, 98.4%)]. Test accuracy (true positives + true negatives/total exams) was 99.5% when excluding indeterminate results and decreased slightly to 97.8% after reclassification of the indeterminate exams.

Table 3 provides data on protocol adherence and shows that the standard 2-view radiograph protocol was followed in 81.9% (186/227) of cases. On a retrospective review of additional radiograph views, a majority appeared to have been performed for diagnostic purposes (to confirm G-tube retention component alignment or duodenal contrast flow) and less commonly for technical factors (radiograph coverage, faintly administered contrast, radiograph exposure issue). Furthermore, 78.9% (179/227) of the exams adhered to the contrast volume protocol. A contrast volume greater than the stratified volume was administered in 9.3% (21/227) of the studies.

Exam reporting time occurred under 1 hour in 79.7% (181/227). Reporting times longer than 1 hour occurred more often in the after-hours group ($P = 0.032$). Radiology resident preliminary readings were found in 36.1% (82/227) of the exams and concurred with the final pediatric radiologist report in 96.3% (79/82) of the exams. Conversely, 5.7% (13/227) exams were reported as indeterminate, adding a median time delay of 40 minutes (IQR: 90). Ten exams, performed after-hours at the satellite hospital, were interpreted remotely at the central children's hospital, thereby potentially avoiding an inter-hospital ground transport.

Discussion

In this retrospective study of 227 G-tube radiograph exams, we found a high overall exam yield (94.3%), with high accuracy (97.8%), sensitivity (90.0%), specificity (98.2%), and NPV (99.5%). These results demonstrate that a 2-view abdominal radiograph exam with stratified contrast administration can reliably evaluate G-tube positioning. With a shared PACS workstation, 2 affiliated hospitals received 24/7 reporting, despite limited on-site pediatric radiologist and radiology resident coverage.

The current shortage of pediatric radiologists is expected to continue into future

Table 2. G-tube check radiographs: exam performance

Primary analysis		
	+	-
	(G-tube malfunction)	(G-tube in normal position)
+	5 (Positive)	0 True positive False positive
Indeterminate (13)		
-	1 (Negative)	208 False negative True negative
Secondary analysis (indeterminate exams re-classified with clinical suspicion)		
	+	-
	(G-tube malfunction)	(G-tube in normal position)
+	9 (Positive)	4 True positive False positive
-	1 (Negative)	213 False negative True negative
Test yield	94.3%	
Accuracy	97.6%	
Sensitivity*	90.0%	
Specificity**	99.2%	
Positive predictive value	69.2%	
Negative predictive value	99.5%	

*Sensitivity: 95% confidence interval (59.4%, 98.1%); **Specificity: 95% confidence interval (94.5%, 98.4%); G-tube, gastrostomy tube.

years, as the number of pediatric radiology fellowship trainees has been decreasing for several years and the advancing age of pediatric radiologists nearing retirement.^{11,12}

This shortage comes at a time when the leadership of children's hospitals has greater expectations of 24/7 final reads of imaging exams, as well as expectations of coverage for a greater number of affiliated institutions.^{13,14} During the coronavirus disease 2019 pandemic, the remote reporting of pediatric radiology exams experienced a marked increase, as evidenced by a SCORCH survey; 95.8% of groups now incorporate remote reading work assignments into their staffing schedules, up from 50% prior to the pandemic.¹

At our institution, a change from the traditional fluoroscopic contrast checking of a G-tube by an on-site pediatric radiologist was necessitated after a new affiliated satellite children's hospital opened that lacked after-hours pediatric radiologist availability for an on-site fluoroscopic exam. Prior to this alternative protocol, such after-hours exams usually required a pediatric radiologist traveling to the hospital for an on-site fluoroscopic G-tube check. This study validates the prior single institution report of a radiograph exam performance where patients received either a radiograph exam or a fluoroscopic exam for both G-tube and GJ-tube checks, based on the availability of an attending radiologist in the hospital.⁴ At our institution, the radiograph exam was the initial imaging exam for all G-tube checks; potential GJ-tube malfunctions at our institution are assessed by the IR service and were not intended to be included in this radiograph exam protocol.

Regarding the 2-view abdominal radiograph exam, the cross-table lateral view was chosen to look for pneumoperitoneum, G-tube alignment relative to the gastric lumen (Figure 3a), and intraluminal contrast flow. The subsequent right lateral decubitus radiograph was chosen to optimize detecting the duodenal contrast flow (Figure 3b). An age-based protocol for the volume of contrast to administer was devised to simplify this step for the RT performing the study, as an up-to-date weight may be lacking in the medical record at the time the study is ordered.

Indeterminate exams were mainly related to the uncertainty of the position of the G-tube retention component in the gastric lumen or the gastrostomy tract (Figure 4). Publications reporting the performance of a diagnostic study often exclude or mishandle

Table 3. Protocol adherence/variance

Correct radiograph views per protocol, 81.9% (186/227)

Additional radiograph views, 18.1% (41/227)

View	Total
Cross-table lateral	27
Right lateral decubitus	16
Frontal supine	11
Left-lateral decubitus	5
Total	59*
Potential reasons for additional radiograph views on retrospective review	
Diagnostic interpretation	31
Retention component alignment	15
Duodenal contrast flow	14
Interpreter judgement (need more definitive findings)	2
Technical exam factors	15
Radiograph coverage incomplete	6
Faint contrast on radiograph	5
Exposure issue (radiograph too light/too dark)	4
RT protocol deviation	6
Incorrect initial view	4
Scout view incorrectly obtained	2
Correct contrast volume per protocol documented, 79.3% (180/227)	
Additional contrast documented, 9.3% (21/227)	
Administered contrast not documented, 11.5% (26/227)	

*59 additional radiograph views were performed in 41 radiograph exams; RT, radiology technologist.

the indeterminate exams. One study found that only 35% of the published studies reviewed reported indeterminate results accurately.⁶ Excluding indeterminate exams may falsely elevate exam performance parameters, as observed with the PPV of this cohort, which decreased from 100% to 69.2% when including the indeterminate exams on secondary analysis. Handling of indeterminate results is a complex issue, and clinical suspicion is considered a reasonable approach to reclassify indeterminate exams⁶ and is supported by the Standard for Reporting Diagnostic Accuracy 2015 guidelines.⁷ Specifically, if an indeterminate exam had high clinical suspicion (such as pain during G-tube use), a fluoroscopic G-tube contrast check exam was performed, and the abdominal radiograph exam was reclassified as a positive (abnormal) exam. If the indeterminate abdominal radiograph exam had low clinical suspicion, no fluoroscopic exam was performed, and the radiograph exam was reclassified as a negative (normal) exam. After this secondary analysis, including all exams, the new abdominal radiograph exam performed well, with particularly high accuracy (97.8%), sen-

sitivity (90.0%), specificity (98.2%), and NPV (99.5%). This study builds on a prior report of G-tube radiograph exam performance (75% sensitivity and 100% specificity) in a larger number of patients (227 vs. 126), while effectively managing indeterminate exams.⁴ To improve the sensitivity of the exam, our group intermittently reviewed abnormal exam findings at our monthly peer-review meetings.

Deviations from the prescribed 2-view exam protocol occurred when the interpreting radiologists asked for additional radiographs or contrast to improve the diagnostic information of the exam, or exam technical factors (exposure issue, RT error). Given the equivocal gastric intraluminal alignment of the G-tube retention component on all 13 indeterminate exams, consideration of a different view (left lateral decubitus view) may be a helpful consideration, providing a different view to potentially outline the G-tube retention component with contrast. This alternative radiograph exam replaced fluoroscopy as the initial imaging exam for G-tube checking, which was well received by our pediatric radiologists providing after-hours

fluoroscopy call coverage. This transition was also well-received by our RTs, who were also short-staffed during the study period. Only one 30-day adverse event (repeat hospital visit to detect and correct G-tube malposition) occurred with this diagnostic exam transition.

Exam reporting time was studied, given its relation to the resumption of G-tube use for nutrition, hydration, and medications in a timely fashion. Here, 79.7% (181/227) of exams were reported under 1 hour, allowing for the timely resumption of G-tube use for hydration, medications, and nutrition in a majority of patients. Delayed reporting (over 1 hour) of exams occurred more often in the after-hours group, when pediatric radiologist coverage was reduced. Delay in reporting time can impact clinical management, as described for the patient with a delayed radiology report entry (after surgery team consult entry), leading to endoscopic (not fluoroscopic) confirmation of transpyloric G-tube malposition, causing gastric outlet obstruction.

The limitations of this study start with the inherent limitations of a retrospective chart review. For instance, when reviewing the reason for additional radiograph views, a given patient may have had an overlapping need for more diagnostic information in addition to the technical limitations of the initial 2-view exam (faintly administered contrast). Regarding protocol adherence, the contrast volume was not documented in Epic in 26 of the 227 exams. A limitation affecting exam reporting time occurred as the study period was before our pediatric radiology group converted to 24/7 attending pediatric radiologist reads of diagnostic radiology exams; a portion of study exams included an overnight preliminary reading made by radiology residents. Following completion of this study, our institution eliminated the beeper paging system. Epic Secure Chat is now used to message pediatric radiologists, a factor that could also influence reporting times in the future. A limitation regarding adverse events would be if a patient presented to a different institution during that 30-day period for any G-tube-related issue; this scenario should be

infrequent, as the 2 affiliated hospitals comprise the only comprehensive pediatric care system across the state. Comparison of radiation doses among the alternative radiograph exam and the traditional fluoroscopic exam is not addressed, but was reported using the limited data of this study cohort.⁵

This new exam was efficiently incorporated by RTs and pediatric radiologists (as well as radiology residents) on 2 campuses. The same standard of care was maintained, despite reductions in the number of pediatric radiologists and RTs.

In conclusion, this alternative diagnostic exam performed well with a high test yield, accuracy, sensitivity, specificity, and NPV. The exam mostly followed protocol, allowed for the timely and safe resumption of G-tube use, and provided the remote coverage needed for a new satellite hospital.

Footnotes

Conflict of interest disclosure

The authors declared no conflicts of interest.

Funding

Clinical and Translational Science Awards to the University of Arkansas for Medical Sciences [National Institutes of Health (NIH) grants: UM1TR004909 and UL1TR003107] partially supported the statistical analysis and Research Electronic Data Capture (REDCap) database creation/management for this study.

References

1. Seghers MC, Seghers VJ, Sher AC, et al. Working from home during the COVID-19 pandemic: surveys of the Society for Pediatric Radiology and the Society of Chiefs of Radiology at Children's Hospitals. *Pediatr Radiol.* 2022;52(7):1242-1254. [\[Crossref\]](#)
2. Culbertson J, Jennings, Culp M, Faguy, K. Mapping the Future of Medical Imaging and Radiation Therapy: White Paper on the 2024 Consensus Committee Meeting Outcomes. American Society of Radiologic Technologists, 2024. [\[Crossref\]](#)
3. Rosenkrantz AB, Hanna TN, Steenburg SD, Tarrant MJ, Pyatt RS, Friedberg EB. The current state of teleradiology across the United States: a national survey of radiologists' habits, attitudes, and perceptions on teleradiology practice. *J Am Coll Radiol.* 2019;16(12):1677-1687. [\[Crossref\]](#)
4. Tompe AP, Lee GM, Noel-Macdonnell JR, Chan SS. Retrospective cohort comparison between fluoroscopic and radiograph-only exams for evaluation of gastrostomy and gastrojejunostomy tubes. *Pediatr Radiol.* 2023;53(10):2021-2029. [\[Crossref\]](#)
5. Hameed M, James C, Wong K, et al. G-tube contrast check: transition from fluoroscopy to abdominal radiographs. *Res Sq [Preprint].* 2024:rs.3.rs-5632134. [\[Crossref\]](#)
6. Shinkins B, Thompson M, Mallett S, Perera R. Diagnostic accuracy studies: how to report and analyse inconclusive test results. *BMJ.* 2013;346:f2778. [\[Crossref\]](#)
7. Cohen JF, Korevaar DA, Altman DG, et al. STARD 2015 guidelines for reporting diagnostic accuracy studies: explanation and elaboration. *BMJ Open.* 2016;6(11):e012799. [\[Crossref\]](#)
8. Baerlocher MO, Nikolic B, Sze DY. Adverse event classification: clarification and validation of the society of interventional radiology specialty-specific system. *J Vasc Interv Radiol.* 2023;34(1):1-3. [\[Crossref\]](#)
9. Agresti A, Coull B. Approximate is better than "exact" for interval estimation of binomial proportions. *Am Stat.* 1998;52:119-126. [\[Crossref\]](#)
10. Zhou XH, Obuchowki NA, McLish DK. Statistical Methods in Diagnostic Medicine. John Wiley & Sons, Inc., New York, 2002.
11. Farmakis SG, Chertoff JD, Barth RA. Pediatric radiologist workforce shortage: action steps to resolve. *J Am Coll Radiol.* 2021;18(12):1675-1677. [\[Crossref\]](#)
12. Dinh ML, Pfeifer CM, Gokli A. Promoting pediatric radiology at multiple levels. *Pediatr Radiol.* 2021;51(9):1556-1558. [\[Crossref\]](#)
13. Aquino MR, Maresky HS, Amirabadi A, et al. After-hours radiology coverage in children's hospitals: a multi-center survey. *Pediatr Radiol.* 2020;50(7):907-912. [\[Crossref\]](#)
14. Taylor GA, Ayyala RS, Coley BD. How did we get here? Thoughts on health care system drivers of pediatric radiology burnout. *Pediatr Radiol.* 2022;52:1019-1023. [\[Crossref\]](#)